8-17-2021

Characterization of Application-Driven Sol-Gel Coated Meshes and Composites

Armaghan Naderi
Louisiana State University and Agricultural and Mechanical College

CHARACTERIZATION OF APPLICATION-DRIVEN SOL-GEL COATED MESHES AND COMPOSITES

A Dissertation

Submitted to the Graduate Faculty of the
Louisiana State University and
Agricultural and Mechanical College
in partial fulfillment of the
requirements for the degree of
Doctor of Philosophy

in

The Department of Mechanical and Industrial Engineering

by
Armaghan Naderi
B.S., Amirkabir University of Technology, 2014
M.S., Sharif University of Technology, 2016
December 2021

To my mom, who is 7257 miles away, in travel ban and corona virus pandemic.

And to my future children, who I do everything for them.

Acknowledgements

I would like to thank colleagues from the Department of Biological and Agricultural Engineering, the Department of Mechanical and Industrial Engineering at LSU, and LSU Shared Instrumentation Facility for sharing their expertise and for helpful discussions.

I also would like to thank my mom for her support during last four years and my husband for his support in last months of my PhD study.

Table of Contents

Abstract

Surface engineering is a multi-disciplinary research area that encompasses disciplines such as materials science, chemistry, mechanical engineering, and electrical engineering. Coating is a surface modification technique in surface engineering, applied on the surface of a substrate (i.e., bulk material), to cover/protect it from environmental degradation or to modify/improve surface properties for specific applications. This PhD research presents an in-depth investigation of sol-gel ceramic coatings to modify surface characteristics of bulk materials for two specific applications: 1) antistatic/antidust applications, and 2) biomaterial implant applications.

First, zirconia antistatic thin films on glass substrates, and their application to polymer-based composites, was studied. Zirconia antistatic coatings were synthesized by a low cost dip coating sol-gel route on glass substrates, then applied to polymer-based composites to potentially improve their dust or water repellent capabilities for aesthetic purposes. The optimized coating with antistatic and dust repellent capability was derived in 50% humidity from a solution containing 15 g $ZrCl_4$/l for all substrates.

Second, hydroxyapatite (HA) coating on various mesh substrates was studied as a composite biomaterial implant, mainly for cranioplasty. In this study, we proposed the design of biocompatible, flexible composite implants by using mesh substrates and customized HA coating as bone regenerative stimulant, derived from a simple sol-gel method.

For metallic mesh substrates, HA-coated stainless steel 316 with mesh size of 200 (1 layer, dip coated by general HA solution) is a good replacement for pure titanium grade 1 regarding biomechanical, biocompatibility, and electrochemical properties. While polymeric or fabric substrate still cannot be used as a replacement for current cranioplasty implants.

Finally, based on observations acquired during HA powder synthesis, the effect of drying bed material on the amount of residue and powder crystalline characteristics was studied. The smallest residue percentage was 1.8%, for pure HA powder dried on aluminum bed. Bed material (glass, aluminum and titanium mesh) did not affect HA powder crystal structure and size. Wetting angle, which relates to surface tension between liquid HA and solid drying bed, was a key factor for the amount of leftover residue.

Chapter 1 . Introduction

1.1. Background on surface engineering and coatings

Surface engineering is a sub-disciplinary field in materials science, related to the surface of solid, bulk matter. It is a multi-disciplinary topic that encompasses chemistry, mechanical engineering, and electrical engineering fields toward surface matter improvements for different applications and properties, such as mechanical and electrical properties, wear-resistance, corrosion-resistance, and fatigue [1].

Coating is a surface modification technique in surface engineering, applied on the surface of a substrate, a bulk material, to cover/protect it from environmental degradation or to modify/improve the surface properties of the material for a specific application. Environmental degradation of a surface is any chemical or physical reaction between the surrounding environment and the surface itself, which affect the surface properties and decrease the life of the surface and bulk material [2].

Various coatings have been used for several decades to protect objects for decorative or functional purposes. For instance, using coatings at room temperature are usually provided in the jewelry industry (apply at high temperature, but used at room temperature) (to improve appearance), enameling in ceramic industry (to improve appearance and provide impermeability), and in the automotive industry for corrosion protection [3].

Functional coatings can be applied as liquids, gases, or solids. They can change the surface properties or add new properties, such as electrical resistivity or conductivity, ferroelectric properties, and magnetic properties in electronics and devices used in automotive, aerospace and missile industries [4,5]. Changing the chemical and mechanical properties of the surface by interacting with the surface material or covering the surface with an adhesive coating different

from the substrate, can affect a wide range of properties for the substrate, including wettability, biocompatibility, corrosion and wear resistance. Such improvements in physical and chemical properties of the surface are useful in the chemical industry and for biomedical implants [5].

Ceramic and bioceramic coatings are both decorative and functional coatings, which have seen a wide variety of industrial uses in the last decades. They are compatible with different environments and mediums under high temperature, as they are non-corrosive, heat resistant, erosion resistant with low degradation rates, and act as electric isolators[6–8]. They also possess good wear resistance, resulting from their high hardness. The main problem with ceramic materials is their brittleness; however, this limitation is mitigated when used as thin film coatings [9].

Ceramic coatings can be applied on substrates using various techniques, such as sol-gel methods, atomic layer deposition (ALD), chemical vapor deposition (CVD), plasma treatment, and magnetron sputtering [10]. Sol-gel methods are low cost and have been shown to produce coatings with good adhesion and uniformity. The coating's thickness and morphology may be controlled (from a few nm to mm) on different substrates of various shapes, based on the coating technique parameters and precursor solution or powder, which influence resulting coating and substrate properties. Thus, understanding how the coating process parameters affect coating characteristics and performance is primordial for appropriate design toward specific applications. In this PhD research, two specific applications for ceramic coatings applied by simple sol-gel method were targeted and investigated: 1) antistatic/antidust applications, and 2) biomaterial implant applications. Low cost materials and coating methods were prioritized, while focusing on thin film adhesion on the substrates and modification of application-specific properties.

1.2. Antistatic/antidust applications

Ceramic coatings using transition metals with ionic structure have potential for antistatic coating applications. Transition metals have different capacities, meaning their oxide is a compound with electrical resistivity in antistatic range (10^{10}-10^{12} ohms/square). In particular, zirconium (Zr) has different capacities as a transition metal and zirconium dioxide coatings should possess electrical resistivity in the antistatic range, as it has an ionic matrix with ionic defects. Antistatic coatings are used for either prevention of electrostatic discharge or antidust application on different substrates. Antistatic coatings can prevent sudden spark between two surfaces (electrostatic discharge), which leads to fire hazards, in the worst cases. These types of coatings are widely used in clothing manufacturing and missile industries.

Applying ceramic coating to polymer-based composites to impart antistatic, dust or water repellent properties is a particular application for which limited research has been carried out in the literature. For instance, lightweight carbon fiber (CF)/epoxy composites, increasingly used in the aerospace, automotive and sports industries, due to their excellent specific stiffness and strength, are often popular for their visual appearance. In addition, there is a need to develop antistatic composite structures in applications such as aircraft systems [11]. Currently, polymer or metal-based coatings or films are under investigation, but their downsides include alteration of surface finish or appearance, potentially high cost, and poor adhesion to the substrate, making them easy to remove manually [12,13].

1.2.1. Main goal and research questions

The goal of this study is to understand the effect of coating parameters on the performance of zirconia antistatic thin films on glass substrates, as well as demonstrate their application to

polymer-based composites. This goal can be further divided into the following bresearch questions:

Can low-cost materials and coating methods be used to apply zirconia thin film coating on glass and polymer-based composites?

How do coating method parameters (i.e., relative humidity and solution concentration) affect thin film coating characteristics and properties:

1. Morphology and microstructure on the substrates;
2. Thickness, hardness, and wettability;
3. Surface electrical resistivity required for antistatic/antidust applications?

In Chapter 2, a literature review on antistatic materials and coatings provides a perspective on the following topics: current applications of various antistatic coatings, manufacturing methods and parameters influencing coating characteristics, ceramic transitional coatings, and coating methods for zirconium, zirconium compounds and zirconia on different substrates. Based on the results and conclusions of those previous studies, research gaps were identified and targeted for further study in this thesis.

In Chapter 3, the experimental methods to answer the research questions posed above are presented. Glass and polymer composite substrates were coated with zirconium dioxide thin film via sol-gel method under various conditions (relative humidity and solution concentration). The substrates were dried at low temperature and the characteristics of the films, such as chemical composition, surface morphology, hardness, and surface electrical resistivity, were studied with respect to coating method parameters.

Research contribution: this work resulted in a published paper entitled “A simple route to synthesize zirconia antistatic thin films on glass substrates and their application to polymer-based composites” in *Materials Chemistry & Physics*[14].

1.3. Biomaterial implant applications

A second application of ceramic coatings investigated in this research work is biomaterial implants, with a focus on bone regeneration for cranioplasty. A ceramic coating on metallic or polymeric substrates with similar chemical, physical and mechanical properties to natural bone can be used to promote healing, osteointegration and bone formation. Coatings of calcium and calcium compounds are employed as biomaterials to promote osteointegration. Calcium orthophosphate coatings such as hydroxyapatite can be used on metallic or polymeric implants to promote bone regeneration and prevent issues such as biodegradation and implant exposure [9].

Mesh substrates have shown promising potential for tissue engineering applications, but their design is not well understood in terms of architecture, porosity and mechanical properties [15,16]. Combining mesh substrates and hydroxyapatite (HA) coating as a bone regenerative stimulant derived from a simple sol-gel method would lead to flexible, customizable implants.

1.3.1. Main goal and research questions

The goal of this study is to understand the parameters affecting hydroxyapatite (HA) coating and performance of biomaterial mesh composites, used mainly as cranioplasty implants. To reach this goal, the following research questions were established:

Can a low-cost hydroxyapatite solution processed at low temperature (< 300 ^{o}C) be used to apply HA coating on metallic and polymeric mesh substrates?

How do coating process parameters (i.e., HA solution, coating technique, number of HA layers, drying temperature) and substrate design characteristics (i.e., mesh size, open area/porosity, material) influence the implant's performance with respect to:

1. HA coating's chemical composition;
2. HA coating's morphology, microstructure, and coverage on substrates;
3. HA composites' electrochemical properties;
4. How does HA coating affect mechanical behavior of coated mesh substrates (nano-indentation and tensile behaviors)?
5. Which coating factors and substrate design characteristics have the most important effect on biocompatibility (including cell adhesion and proliferation) of mesh implants?
6. How does bed material type affect HA powder crystalline structure, morphology and manufacturing process efficiency?

In Chapter 4, a literature review provides an overview of the following topics: biomaterials and orthopedic implants, with a focus on cranioplasty implants, manufacturing methods and parameters, applications of various biocompatible substrates and coatings, as well as HA ceramic coatings and main parameters affecting bone regeneration. Based on the results and conclusions of those previous studies, research gaps were identified and targeted for further study in this thesis.

In Chapter 5, the experimental procedures to answer research questions outlined above are presented for metallic substrates. Mesh substrates were coated with HA using a sol-gel method to create thin, flexible, biocompatible combined cranioplasty implants. Composition, microstructural, morphological, and HA coverageanalyses were performed to gain a better understanding of the effect of coating process parameters. Corrosion resistance, modulus of

elasticity and hardness were characterized to ensure strength and adhesion of the coating on the mesh substrates.

Research contribution: this work resulted in a published paper entitled "Improved biocompatible, flexible mesh composites for implant applications via hydroxyapatite coating with potential for 3-dimensional extracellular matrix network and bone regeneration" in *ACS Applied Materials and Interfaces*.

In Chapter 6, polymer/ceramic implants were investigated. Hydroxyapatite coatings were applied on polymeric mesh and cellulose substrates (fabrics and mats) to potentially improve osteoinductivity and bone regeneration. Tensile behavior was studies to assess the effect of HA coating on mechanical properties.

Research contribution: this work has been submitted as a journal manuscript entitled "Comparison of microstructure and tensile behavior of hydroxyapatite-coated polymeric mesh, fabrics, and mats" to *Materials Science and Engineering C*.

In Chapter 7, biocompatibility studies for both metallic and polymeric woven mesh substrates are presented. In vitro studies on biocompatibility of uncoated and HA-coated implants are presented to better understand how HA coating coverage and substrate design characteristics (i.e., mesh size, open area/porosity, material) influence the implant's performance.

In Chapter 8, based on the results and experience gained with HA coating research, low temperature, short-time synthesis of HA powder on various bed substrates was investigated. In this research, the effect of the drying bed material (aluminum, titanium, and glass) on the crystalline characteristics of HA powder and the amount of powder residue was investigated for HA synthesis at low temperature without cooling systems [17].

Research contribution: the work was presented as a poster titled “Low-cost synthesis of hydroxyapatite on different bed materials: crystalline structure, morphology and process efficiency” at the *11th World Biomaterials Congress (WBC)*, United Kingdom, December 11-15, 2020.

In Chapter 9, conclusions based on the results from Sections 1.2 and 1.3 presented in this thesis. Finally, in Chapter 9, recommendations for future work are provided.

Chapter 2 . A Review on Antistatic Materials and Coatings

2.1. Introduction

This chapter presents a review on antistatic materials and coatings with a focus on ceramic antistatic coatings. First, a short history of static charge accumulation phenomenon and its invention is provided in Section 2, leading to electrostatic discharge (EDS) definition its importance. In Section 3, electrical properties of materials, such as electrical conductivity and resistivity, are discussed and a simple method to explain conductivity is provided. Section 4 presents a review on materials and coatings commonly used for antistatic applications, their manufacturing methods, advantages, and disadvantages. In Section 5, characterization techniques for antistatic coatings are summarized. Finally, Section 6 highlights the main gaps identified in the literature regarding coating methods and parameters, and their applications.

2.2. History of electrostatic charge and discharge

Static electricity is a phenomenon that dates back to 600 BC, when collecting amber on coastlines. Any shiny stone or glass was examined by drying them, then rubbing them on clothes. If the stone attracted a piece of dry paper, then it was amber. As known today, this phenomenon was electrostatic charging caused by friction. In 600 BC, Greek scientist Thales of Miletus found out that when amber was rubbed to animal fur, it could attract dust particles. “Elektron” is a Greek word, which means “amber”, and negatively charged elemental particles were called “amber” in ancient Greek [18].

The origin and nature of electrostatic charging was discovered in the 16^{th} century by William Gilbert. He found out that different materials could be charged to attract various objects, such as dust particles. Therefore, he divided all materials into two groups: “electriks” and “noelectriks”, in which electriks were defined as displaying an attracting force “vis electrica”.

More discoveries about electrostatic charge date back to the 17th century, when developer of the first electric generator, Otto von Guericke, produced static electricity by rubbing any object to a sulfur ball. Later, Francis Hauksbee developed a device to generate light by electrification of a glass tube and named it the “light globe”. This led to various discoveries by other scientists, such as conductors and insulators, earth wires, and electrical conductivity of wet surfaces [19].

During electrification tests, sparks are generated. At first, those sparks wereused as harmless entertainment, but later, it was discovered they could ignite together. In the 18th century, it was shown that the nature of the sparks was the same as lightning by Benjamin Franklin and William Watson. Positive and negative charges were introduced by Georg Christoph Lichtenberg in the 18th century. Finally, in 1785, the theory of repulsion between similarly charged bodies and attraction between oppositely charged bodies, and its relation to the distance between the two bodies was proposed by Charles Auguste Coulomb, known as Coulomb’s law [19].

Nowadays, it is known that electrostatic charging is a surface phenomenon, and it is sensitive to material sample history, preparation conditions, environmental conditions, and impurities. However, electrostatic charges exhibit unstable behavior, and the attractive or repulsive forces generally disappear over time. The discharge rate depends on material type, relative humidity, and environmental and surface conditions, such as surface topography. Factors influencing electrostatic charging include time and intensity of contact between bodies, contact area, rubbing intensity, and grounding of the material. Simple contact between bodies may allow electrons to flow from one specimen to the other, leading to oppositely charged surfaces. Even in the absence of contact, specimens can be charged by induction. Electron capacity is a material parameter that represents the maximum possible quantity of charges on a body. Critical breakdown potential is the maximum voltage, under atmospheric pressure, carried by an object. When the

voltage of a body exceeds this value, accumulated charge is dissipated in the form of a spark. The critical breakdown potential depends on environmental factors, such as temperature, humidity and pressure [19].

2.2.1. Importance of electrostatic discharge (EDS)

Electrostatic discharge, EDS, is defined as the flow of electricity between two electrically charged bodies or specimens. It may result from contact, dielectric breakdown, or electrical short. Tribocharging, or electrostatic induction, may lead to a buildup of static electricity. "Tribocharging" is defined as a contact electrification process. It leads to buildup of static electricity caused by touching or rubbing of surfaces of two different materials. The study of tribocharging is important because the tribocharge may create sparks in some cases, which can lead to ignition of fuels and chemicals during transportation. Therefore, mitigation strategies are required [20]. Electrostatic induction results from non-contact processes using high voltage power sources [21].

As previously mentioned, when ESD occurs, it often creates a visible spark [22]. Small sparks caused when the human body touches a synthetic or metallic material are generally not dangerous by themselves. At atmospheric conditions, the maximum charge on the specimen's plane is around 3.3×10^{-9} C/cm^2 with low current density. If under any explosive conditions, such as flammable atmosphere or ignitable materials, sparks can result in serious accidents [19,23,24].

ESD and sparks are dangerous common phenomena potentially causing damages in various industries: electronics, aerospace, petrochemical, oil paint, textile, etc. Statistics show the annual economic loss due to electrostatic hazards in the electronics industry in the United States was estimated at over 10 billion dollars. In the U.K., it was around 2 million pounds, and 45% of dangerous hazards in the Japanese electronics industry resulted from static electricity, according

to a study published in 2017 [25]. Therefore, ESD is an important issue to address and mitigate through the use of antistatic agents, as will be described in the next sections.

2.3. Electrical properties classification of materials

Materials can be divided into four major categories, according to their electrical conductivity: 1) insulators, 2) semiconductors, 3) conductors, and 4) superconductors. Figure 2.1 shows the range of electrical conductivity values with examples of corresponding materials. It should be noted that temperature can affect electrical conductivity in metals, while impurities, composition, and doping degree mostly affect polymers and doped conductive polymers [19].

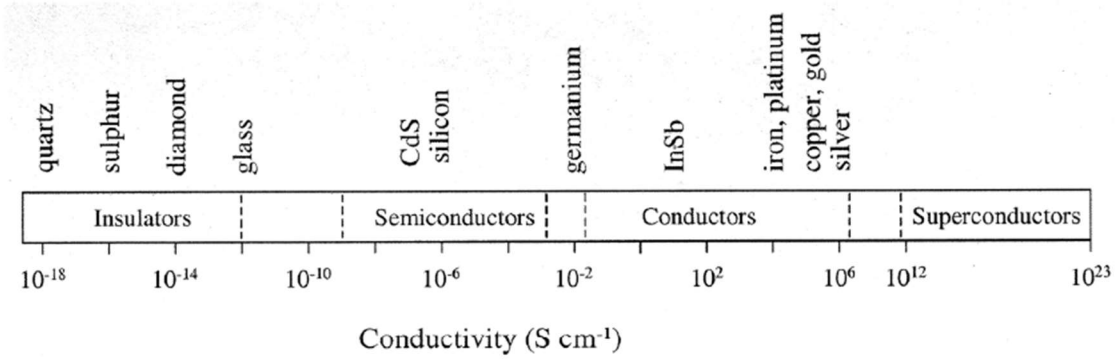

Figure 2.1. Electrical conductivity range for materials [19].

Electrical resistivity (surface and volume), is defined reversely to electrical conductivity ($\rho = 1/\sigma$). Based on recent standards for antistatic materials, a material with a surface resistivity range from 10^5 to 10^9 Ω/■ is static dissipative, while it is antistatic if surface resistivity ranges from 10^{10} to 10^{12} Ω/■ (volume resistivity from 10^9 to 10^{11} Ω cm) [25]. The ESD region includes part of conductive, and all dissipative and antistatic regions, from 10^0 to 10^{11} Ω cm (Figure 2.2).

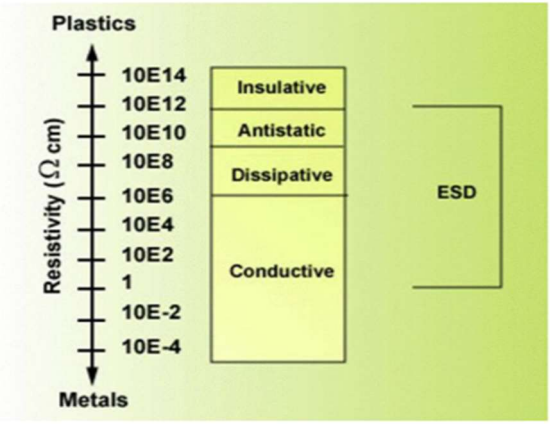

Figure 2.2. Electrical resistivity range for materials [26].

Electronic conduction based on band theory is a simple model describing conductivity (Figure 2.3). Based on this model, various energy levels include free electron, filled, valence, and conductive bands. While electrons exist in valence and conductive bands can contribute to conductivity, the bands should be partially filled to allow conductivity, as the electron velocity is above zero in this case. In metals, electrical conduction is always related to partially filled bands. In insulators, there are no energy gaps between the bands. Therefore, the region of forbidden energy level cannot be occupied, and electrons cannot travel between full valence and empty conductive bands. Thus, conductivity for insulators is impossible. In semiconductors, the energy gap is small enough so that electrons can jump from valence to conductive bands and render the material conductive by small thermal or charge activation.

In metals, conductivity decreases when increasing temperature (because of this, metals are superconductors at very low temperature, ~77 K). In semiconductors and insulators, conductivity increases with temperature as electrons gain thermal energy and can move or jump to the conductive band. However, at ambient temperature, insulators' conductivity is caused by impurities in the material's matrix. In semiconductors, positive or negative charge carriers can be doped to highly increase the conductivity [19].

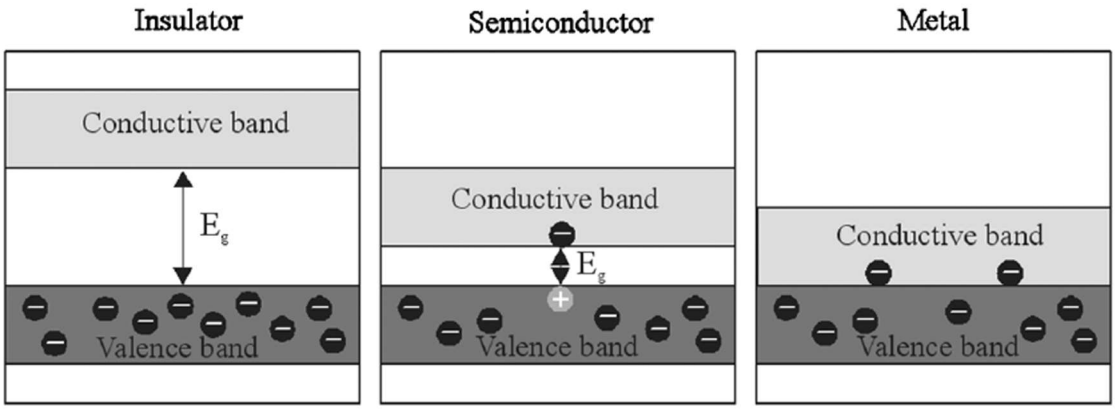

Figure 2.3. Band theory model [19].

2.4. Antistatic agents

As mentioned in previous sections, static charge can be induced without any contact by high voltage power source or by triboelectric effect. An antistatic agent is a compound which can be mixed with a material's matrix (internal agent) or be applied on its surface (external agent) in order to decrease or eliminate buildup of static electricity. It is used to increase the conductivity of the surface of the material or its bulk, by being conductive or antistatic itself, or by absorbing moisture in the air [21]. Two main categories of antistatic agents will be discussed in this section: migratory additives and permanent agents.

2.4.1. Antistatic migratory additives

Traditional migratory additives as antistatic agents areadded to a polymer matrix during manufacturing (melt mixing, compounding, etc). They migrate to the surface of the polymer after a short time. They are molecules like surfactants, and mostly have both hydrophobic and hydrophilic parts. The hydrophobic side attaches to the surface of the material, while the hydrophilic side binds to the water molecules in the air moisture (Figure 2.4). Migrating antistatic agents are used for short-term, cost-effective protection. They cannot be used for spark protection

or electronic protection from electrostatic dissipation because they do not lower electrical resistivity below the resistivity of the material itself for long-term applications [27].

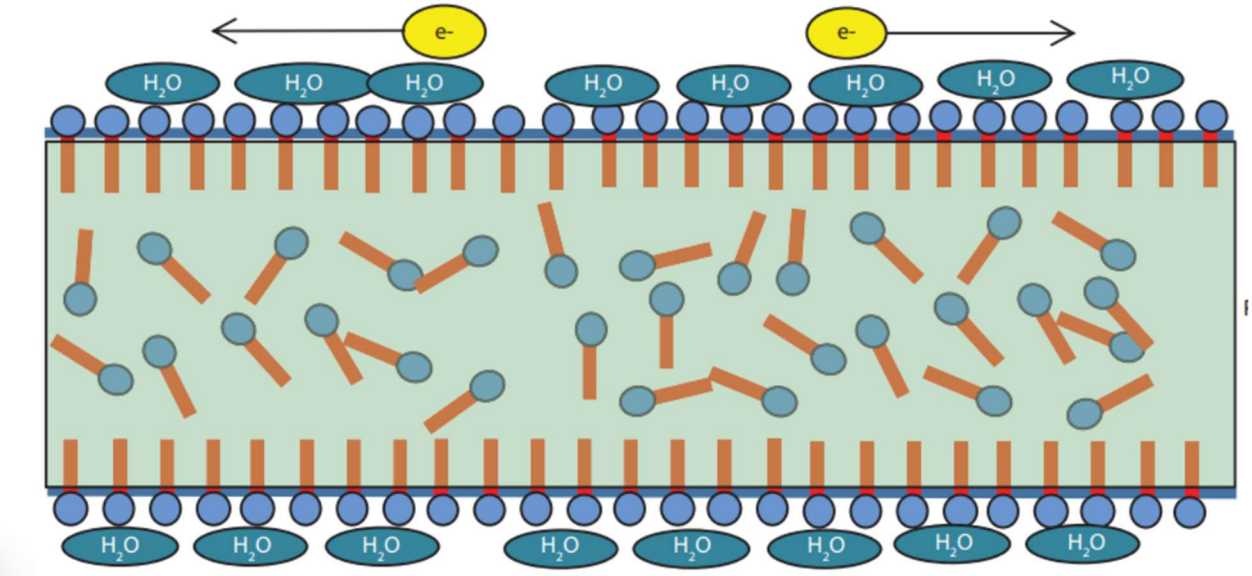

Figure 2.4. Mechanism of additive migration to the surface and static electricity dissipation [28].

2.4.2. Permanent antistatic agents: polymer composites and glazes

Permanent antistatic agents used in engineering recently can be divided into two categories: polymer composites (as bulk or coating) and antistatic glazes. Polymer composites or coatings are manufactured by adding a conductive material, such as carbon nanotubes (CNTs), graphite, carbon black, conductive fibers, or mica powder, to a polymer matrix. Figure 2.5 shows an example of conductive network created in a polymer matrix (poly ether ether ketone, PEEK with CNTs. The main disadvantage of polymer composites for antistatic applications is the non-homogeneous dispersion of conductive particles or fibers in the polymer matrix [29,30]. Issues with durability, temperature resistance and wear resistance have also been reported in the literature [31].

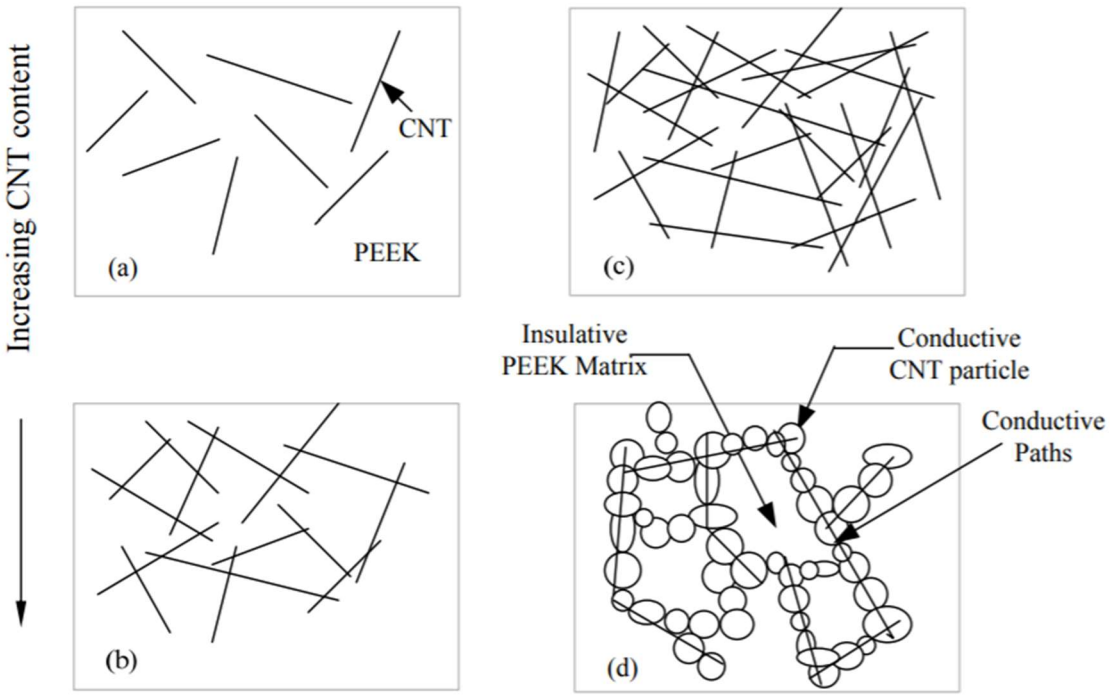

Figure 2.5. Formation of conductive paths in polymer composite antistatic agent (CNT-PEEK) without any externally applied pressure [32].

Adding conductive or semiconductive oxide powders or fibers into glaze (thick ceramic coating, commonly used in applications like pottery) to create an antistatic glaze is mainly employed in the construction industry, such as floor tiles, walls, and antistatic plaster [33]. However, glazes display a limited range of applicability beyond construction materials, as well as poor mechanical properties [25].

2.4.3. Permanent antistatic agents: ceramic coatings

For applications under harsh conditions (e.g., aerospace industry), such as high temperature, high friction, and high corrosive environment, polymer composites, glazes or migratory additives are generally not well-suited due to low temperature resistance and durability. Ceramic materials are compatible with such environments, as they possess good mechanical properties, high temperature, corrosion and wear resistance, good durability, and stability [25]. Ceramics can be divided into three categories: 1) oxides, such as metal oxides (alumina, zirconia,

beryllia, etc.), 2) non-oxides (carbide, boride, silicide, etc.), and 3) composite materials (combination of oxides and non-oxides, or reinforced materials) [34]. Metal oxides are semi-conductors, while non-oxides and composite materials are typically not.

Considering electrical properties of ceramic materials, they can be categorized into semiconductors, ferroelectrics, and thermally affected ceramics. For instance, lead zirconate titanate and barium titanate display ferroelectric effect while being pyroelectric. Rising temperature after critical transition temperature can make grain boundaries act like an insulator in a mixture of heavy metal titanates. These titanates with critical temperature below room temperature are ceramic capacitors at room temperature [35]. In ceramics, free electrons cannot move through the material because of ionic bonds. Instead, impurities and different valence can work as donors or acceptors of free electrons, which turn ceramics into semiconductors [36]. Semiconductor ceramics are mostly transition metal oxides. As previously shown in Figure 2.1 and Figure 2.2, semiconductors are between conductors and insulators, and fall under the antistatic category. From this comparison, semiconductors can be used as antistatic materials or coatings, depending on the required mechanical properties. Using a ceramic semiconductor as an antistatic material requires it to be hard, stable, and have good mechanical properties.

Considering all transitional metal oxides, Zirconium (Zr) is one that displays different capacities. Thus, zirconium dioxide (ZrO_2, or zirconia) can be used as semiconductor bulk material [37]. It is a p-type semiconductor with wide band gap, which has several oxygen vacancies on its surface [38]. Its pure form can also go through phase changes between room temperature and sintering temperature, but it can be chemically stabilized. Having a stable structure can provide transformation toughening in mechanical properties, as most ceramic knife blades are made of

zirconia [34]. Zirconia also has been used as doping agent with other metal oxides, such as ZnO, ATO (antimony tin oxide) and ITO (indium tin oxide), to reduce surface resistivity [39–42].

Given zirconia's mechanical properties, semiconductive behavior and its application as a surface resistivity reductant doping element, zirconia thin films have potential to modify insulator materials, such as glass and polymers, into antistatic range [4,43,44]. It has been shown in the literature that a thin film coating solves brittleness problems, while applicable to the surface of different material types and geometries.

2.4.4. Summary of permanent antistatic agents manufacturing methods

Table 2.1 lists a summary of different permanent antistatic agents discussed in the previous sections, their common applications, manufacturing methods, advantages, and disadvantages. By looking at the table, a good antistatic coating should be adhesive, inexpensive, durable, and provide long-term surface conductivity. Those characteristics are found in antistatic metallic coatings, where ZrO_2, in addition to the advantages mentioned in the paragraph above, shows potential for cost effectiveness through simple sol gel methods.

Table 2.1. Summary of permanent antistatic agents.

Permanent antistatic agents		Industrial application	Manufacturing method	Advantages	Disadvantages	References
Antistatic additive	Silver copper, nickel powder	Adhesives and sealants	Powder metallurgy, nano powder	High production rate	Heterogenous distribution	[27,45,46]
	Potassium sulfate	Adhesives and sealants	Hydrogel	Adhesive	Decrease impact strength	
	Graphite and Carbon fiber	Adhesives and sealants, automotive	Suffused into bedliner	Weight reduction	Decrease surface adhesion, Heterogenous distribution	
	Stainless steel and any metal fibers	Textile, polymer	Mixed with molten matrix	High durability	Affect material strength,	
	Conductive metal (Ag, Ni, Cu) coated fibers	Textile	Mixed with molten matrix		Dark appearance	
	Carbon black	Automotive, agriculture, bottle and plastic containers	Mixed with coating primer	Inexpensive	Rapid discharge	
	Carbon nanotube	Adhesives and sealants, aerospace	Mixed with melted polymer or solution, film applicator	High aspect ratio	Heterogenous distribution	[47]
Antistatic metallic coating	Ag	Adhesives and sealants	Electroplating	High durability, Long-term surface conductivity	Expensive, health issues, consistency issues	[45]
	Al	Automotive	PVD			
	SnO_2	Solar cells	Film applicator			[48]
	ITO (In_2O_5Sn)	Optics, electronics, solar cells	Sol-gel, pulsed laser deposition, vacuum evaporation			[49]
	ATO ($Sb_2O_3.SnO_2$)	Optics, electronics, solar cells	Sol-gel, plasma spraying, sputtering			[50]
	ZnO	Electronics, optics	Magnetron sputtering			[51]
	ZrO_2	Electronics, optics	Sol-gel, plasma spraying, film applicator	Consistent, stable, Long-term surface conductivity	High relative humidity, could be both inexpensive or expensive	[4,52–54]

2.5. Manufacturing and characterization methods for zirconia antistatic coatings

2.5.1. Coating methods

Several methods, such as film applicator followed by ultraviolet (UV) irradiation, plasma spraying, and wet chemical processing (sol-gel), were studied in the literature to apply zirconia (ZrO_2) antistatic coatings on a variety of substrates, such as polymers and glass [11–13]. A comparison between different coating methods showed that the sol-gel method was promising as it is effective, simple and low-cost for zirconia coatings, eliminating the cost disadvantage mentioned in Table 2.1. Moreover, it is applicable to a wide range of substrates' dimensions and geometries [43].

The sol-gel method was used in the literature to synthesize ZrO_2 solutions with different precursors, such as zirconium n-propoxide, zirconyl nitrate and zirconium tetrachloride, for ZrO_2 powder and coatings with applications for powder synthesis, thin films, and corrosion protection [14–20]. Sol-gel methods assisted by high power ultrasound (sonochemical-assisted) and precipitation routes are popular to synthesize amorphous, cubic, monoclinic and tetragonal zirconia nanostructured powders [21–25]. In general, synthesis of solids and metal alcoxides (which needs hydrolysis and polycondensation reactions) can be controlled more easily using the sol-gel process. The latter can be used to control the microscopic structure and film functions on the coating's surface. Figure 2.6 shows metal alkoxide chemical reactions in the sol-gel process and the 2D structure of zirconia coatings after completed reactions.

(a) Hydrolysis reaction :

$M—(OR)_x + H—O—H \rightarrow HO—M(OR)_{x-1} + H—OR$

(b) Polycondensation reaction:

$(OR)_{x-1}—M—OH + RO—M—(OR)_{x-1} \rightarrow (OR)_{x-1}—M—O—M—(OR)_{x-1} + ROH$ (alcoxolation)

$(RO)_{x-1}—M—OH + HO—M—(OR)_{x-1} \rightarrow (RO)_{x-1}—M—O—M—(OR)_{x-1} + HOH$ (oxolation)

M: Si, Ti, Hf, Zr, Ta, Nb, Al

R: CH_3, C_2H_5, C_3H_7

(c)

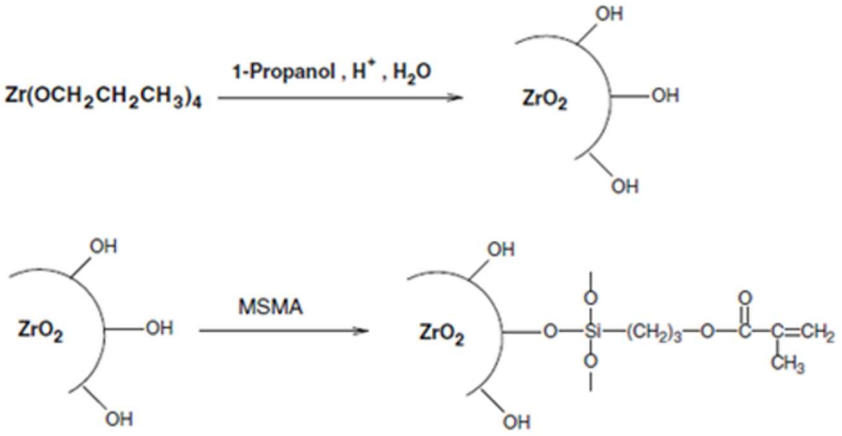

Figure 2.6. Reactions in the synthesis of metal alkoxide by sol-gel method: a) hydrolysis reaction, b) polycondensation reaction, and c) 2D structure of zirconia coating after the reactions [4].

2.5.2. Parameters affecting coating characteristics and performance

Zirconium compounds, or ZrO_2 powder, and thin films have been used for different applications on various substrates, such as glass and polymers, to improve dielectric, antiferroelectric, optical, photocatalytic, and photoluminescence properties, as well as to synthesize conductive coatings for ESD applications [1–9]. Coating method parameters, such as solution concentration and additives, can affect the chemical structure, surface morphology,

thickness, and surface properties (e.g., hardness and electrical conductivity) of thin films. As those are related to the coating performance for a given application, it is important to understand how they are affected by coating parameters.

It was shown that thickness and morphology of ZrO_2 thin films mostly depend on the solution composition, i.e., precursor concentration and additives, and coating process. For instance, it was observed, for the spin-coating process, that increasing the zirconium precursor concentration increased film thickness and created a more porous structure on glass substrates, as shown in Figure 2.7 [54]. Solution composition and ZrO_2 weight fraction for UV-curable sols applied on polymer substrates (polymethyl methacrylate, PMMA) was shown to influence surface resistivity in the 10^8 to 10^{10} Ω/■ range [4]. The effect of solution concentration was not clearly shown on film hardness and adhesion, as those characteristics did not vary significantly within the range of solution parameters investigated.

As temperature and relative humidity are two of the most important environmental conditions changing condensation and hydrolysis rates during the formation of thin films, it is expected they would influence their morphology as well [54]. However, there is limited research on the effect of relative humidity. Its relation to morphology of zirconia thin films has not been investigated as previous studies were conducted under constant humidity conditions.

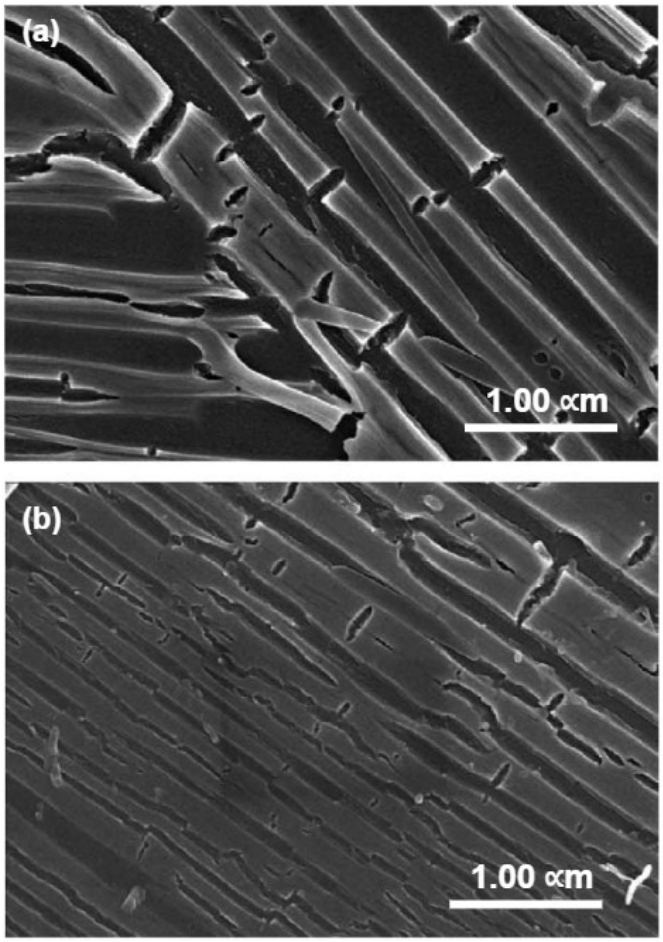

Figure 2.7. Controllable morphology and thickness of ZrO_2 thin films obtained from different concentrations of $ZrCl_4$ in solutions: (a) 75 and (b) 30 g $ZrCl_4$/l [54].

Zirconia thin films can have both crystalline and amorphous structures, but it has been observed that they do not necessarily rely on the substrate's morphology and structure [4,54,55]. Additional procedures after the coating process, such as drying at low temperatures or calcinating at high temperatures, are often used to increase the film adhesion to the substrate by solvent evaporation. If the film undergoes high temperatures, new morphological patterns may be formed, which can change the characteristics of the thin film [56]. A method to enhance zirconia film adhesion on substrates is the use of 3-(Trimethoxysilyl) propyl methacrylate (MPTS), a silane coupling agent. This coupling agent consists of hydrolysable and organofunctional groups. The hydrolysable group can form strong bonds with zirconium oxide while the organofunctional group

can enhance the wetting and adhesion characteristics of the surface [11,27]. This was demonstrated on metal-thermoplastic welded joints, where silane was used as a coupling agent between the two materials [28]. Grafting silanes onto the metal surface increased its adhesion with organic materials, resulting in an improved shear strength of the welded joints by more than 30%. However, the effect of coupling agent on other film characteristics, such as surface electrical resistivity, morphology, and thickness, has not been studied in the literature.

2.5.3. Application to polymer-based composites

In the literature, the majority of applications for ZrO_2 thin films involve metals or unreinforced polymers as substrates. Coating polymer-based composites to impart antistatic, dust or water repellent properties is a particular application. This is the case for lightweight carbon fiber (CF)/epoxy composites, increasingly used in the aerospace, automotive and sports industries, due to their excellent specific stiffness and strength [57]. CF/epoxy composites are often popular for their visual appearance, based on the transparency of the epoxy matrix combined with various fiber patterns, as exhibited in the automotive and sports industries, as well as for architectural purposes [58–60].

To preserve aesthetic appeal and improve water and dust repellent capabilities, protective coatings or films may be used, such as electrostatic spray deposition (ESD) of polyester-based powder coatings [13,58]. Additionally, there is a need to develop antistatic structures to give polymer composites further prevalence in applications such as aircraft systems [11]. Some of the more recent solutions include polymer or metal-based coatings or films to enhance manufacturing flexibility and reduce weight. So far, downsides from those solutions include alteration of surface finish or appearance, potentially high cost, and poor adhesion to the substrate [12,13]. Sol-gel ZrO_2

thin films, which have not been investigated for polymer composites (CF/epoxy), could lead to low cost, transparent thin films with antidust/antistatic properties.

2.5.4. Characterization techniques for antistatic coatings

The following sub-sections provide an overview of the main characterization techniques used in research literature for metal oxide coatings. They cover chemical composition analysis, morphology, hardness, film thickness, electrical resistivity, and contact angle measurements.

2.5.4.1. Chemical composition

Chemical structure and phase analysis are investigated by Fourier-transform infrared spectroscopy (FTIR), X-ray diffraction spectroscopy (XRD), and Energy dispersive x-ray spectroscopy (EDX). FTIR is a characterization technique to determine chemical bonds in solid, liquid, and gas. For zirconia powder and coatings, it could be applied to both sol and powder. The results can show emission or absorption of (OH), (ZrO), (ZrOZr) and (OC) bonds in powder or solution [4,61,62].

XRD is a technique in materials science to determine the crystallographic structure of a material. The material is subjected to x-ray, then the diffraction angle and intensity of each scattered rays are measured by the machine. For powder of zirconia, XRD is a better technique than FTIR because it can determine exactly the plane indices and the crystal structure of the material and any intermediate phases or compounds [63,64].

EDX in field emission electron microscopy (FESEM) is another technique to be applied on the surface of the substrate or coating under FESEM microscope. It can investigate and present the existence of most elements in the periodic table. The analytical results could be reported as elemental analysis, point analysis, and mapping distribution. It also can be used to distinguish and

study unknown compounds. For zirconia coating, this technique is mostly used to investigate or confirm uniform elemental distribution in the coating.

2.5.4.2. Morphology and structure

Microscopy techniques and imaging provide specimen surface morphology and structure. Optical microscopy is used for general observation while scanning electron microscope (SEM) and field emission scanning electron microscope (FE-SEM) presents more detailed images with higher quality [4,54]. Surface topography, crack, porosity, the quality of coating adhesion and all detailed surface properties can be investigated with FE-SEM, in two different imaging modes with high resolution. Secondary electron (SE) imaging mode is used to present surface topography while backscatter electron mode (BSE) is used to distinguish between various chemical structures on the specimen.

2.5.4.3. Surface characteristics

Coating hardness shows the resistance of the coating to surface deformation. It can be measured by many techniques, from indentation to scratching methods. Hardness test method should be selected by considering the application of the coating. Pencil hardness test is operated based on ASTM D3363-05(2011)e2 and shows the hardness of the coating compared to the corresponding pencil hardness, if it can scratch and remove the coating from the surface [65].

Film thickness can be measured by visual techniques, such as microscopy methods, or by surface roughness. Contact profilometer is a technique to measure surface roughness while it can be used to measure the height of the step between coated and uncoated substrate from the roughness profile of the surface.

The surface electrical resistivity of a coating is measured based on ASTM D257-07 [66]. The shape and number of electrodes used for the measurement should be defined based on the coating application, surface topography, and covered area.

Contact angle measurements of distilled water on the top of the coated and uncoated substrates determine the potential for dust adhesion on the surface. Higher wetting angles of liquids indicate lower adhesion of dust particles on the surface. Therefore, wettability measurements can be related to antidust properties of coatings [13].

2.6. Literature review summary and knowledge gaps

Accumulation of electric charges on the surface of a body is called the electrostatic discharge (ESD) phenomenon. The growth of the electronics industry, in particular, has increased damages related to ESD, which require low cost solutions to prevent loss of materials, capital, and human resources. Transition metal oxide semiconductor ceramics are a promising solution, as not only they have similar antistatic properties to conventional antistatic materials, but also are hard and stable. The major disadvantage of ceramic materials is their brittleness, which can be solved by using them as a coating on a range of substrates.

The literature review showed that zirconia has been successfully used to create stable, antistatic thin films on metallic and polymeric substrate materials. However, two main research gaps were identified regarding coating process parameters and application to new substrate materials, as summarized below:

1. While relative humidity is expected to affect hydrolysis and polycondensation during the coating process, its effect on coating morphology and surface characteristics (e.g., thickness, hardness, surface resistivity) has not been investigated. Moreover, its coupled

effect with solution concentration and coupling agent, both of which have been shown to influence coating morphology and/or properties, remains unknown.

2. To date, there is no research on application of ZrO_2 coatings to polymer composites (such as carbon fiber/epoxy) using simple, low cost sol-gel methods. Antistatic properties, related to antidust behavior, are of interest to polymer composites to preserve aesthetic appeal by improving water and dust repellent capabilities. Furthermore, application of polymer composites in aircraft systems demands improved antistatic solutions, as limitations of recent advances (polymer or metal-based coatings/films) include alteration of surface finish or appearance, and potentially high cost.

Chapter 3 . Synthesis and Characterization of Zirconia Antistatic Thin Films on Glass Substrates and Their Application to Polymer-based Composites.

3.1. Introduction

The aim of this study is to make a transparent antistatic coating through a simple dip-coating sol-gel method, from low cost, commercially available materials on glass and polymer composite substrates. Based on literature review presented in chapter 2, it is expected that coating parameters (i.e., relative humidity and solution concentration) will affect chemical composition, morphology, surface, and antistatic properties of derived zirconia thin films. Therefore, this chapter seeks to understand how coating parameters affect the performance of zirconia antistatic thin films on glass substrates, as well as to demonstrate the coating application to polymer-based composites. First, the dip-coating method was developed to form ZrO_2 thin films on glass substrates. Homogeneous and transparent solutions with long stability were prepared at room temperature. Second, the effects of changing solution concentration and relative humidity, as well as adding coupling agent (MPTS), were studied separately with respect to films surface characteristics. Transparent zirconia thin films with high adhesion to glass substrates were obtained from the solution with the lowest concentration of precursor without any additive. The surface resistivity of all samples was in antistatic range. Third, based on the characterization results on glass substrates, a solution concentration was selected and applied to CF/epoxy substrates by dip-coating. Finally, morphology, surface resistivity, film thickness, hardness and contact angle measurements were analyzed to evaluate potential for antistatic, dust and water repelling capabilities of polymer-based composites.

This chapter was previously published as A. Naderi, A. Dolati, A. Afshar, G. Palardy, A simple route to synthesize zirconia antistatic thin films on glass substrates and their application to polymer-based composites, Mater. Chem. Phys. 244 (2020) 122696. doi:10.1016/j.matchemphys.2020.122696. reprinted by permission of Elsevier Publication. https://www.sciencedirect.com/science/article/abs/pii/S025405842030078X

3.2. Materials and methods

3.2.1. Materials

Zirconium tetrachloride 99.9% ($ZrCl_4$), chelating (coupling) agent MPTS 98% (3-(Trimethoxysilyl)propyl methacrylate, $C_{10}H_{20}O_5Si$), acetic acid 98% (CH_3COOH), sulfuric acid 98% (H_2SO_4) and anhydrous oxalic acid 99% ($C_2H_2O_4$) were purchased from Sigma-Aldrich. Isopropanol 98% (C_3H_7OH) was purchased from VWR International. Commercial grade sodium hydroxide (1 mol/l) was used. All materials were used as received. The glass substrates were microscope slides from Eisco Scientific. Polymer composite substrates were made from two different types of carbon fiber/epoxy prepregs: (1) twill weave AS4/Newport 301 prepreg with 55% fiber volume fraction (Rock West Composites) and (2) plain weave T650/Cycom® 5320 prepreg with 64% fiber volume fraction (Cytec Solvay Group, provided by The Boeing Company). Composite panels were manufactured using vacuum bagging followed by oven cure according to the manufacturer's recommendations and the procedure described in Ref. [37]. The AS4/Newport 301 prepreg had a layup of 6 plies with orientation [(0/90)3]s, where (0/90) denotes a single ply. The laminate had a final thickness of 1.62 ± 0.04 mm. The T650/Cycom® 5320 layup consisted of 8 plies with orientation [(0/90)4]s with a final laminate thickness of 1.63 ± 0.02 mm. Samples measuring 20 mm ± 10 mm were cut out of the panels with a PACE Technologies PICO 155P precision diamond saw. In this paper, to simplify the text, "AS4" and "T650" will be used to refer to AS4/Newport 301 and T650/Cycom® 5320 prepregs, respectively.

3.2.2. Synthesis of zirconia solutions and antistatic coatings

A stock solution containing 1.5 g $ZrCl_4$ as precursor in 10 ml isopropanol was prepared with vigorous stirring for about 2 h. The solution was kept in batch iced water with a temperature around 4 °C during preparation. Other solutions with different concentrations of $ZrCl_4$ were

obtained by diluting the stock solution with appropriate amount of isopropanol. After dilution, the new solution was vigorously stirred again for 2 h. As a result, four different solutions with 150, 100, 50, 15 g $ZrCl_4$/l were prepared (see Table 1 for details). The activated coupling agent MPTS was added only to the stock solution (1.5 g $ZrCl_4$ in 10 ml isopropanol). Distilled water (3 ml) and acetic acid (0.1 ml) were added to 0.1 ml MPTS to activate the chelating agent. Then, this activated MPTS was dissolved in 40 ml of isopropanol and added to 10 ml of stock solution to prepare a new one.

All prepared solutions were kept in sealed penicillin bottles and aged at room temperature for one week in a dark room to get homogeneous solutions. Figure 3.1 illustrates the general coating process. Prior to coating, the glass substrates were degreased with 1:1 vol ratio of oxalic acid (0.3 mol/l) to sulfuric acid solution. Then, the glass surface was activated by immersion in sodium hydroxide solution (1 mol/l) for 5 min. Finally, all samples were washed with distilled water and calcined at 40 °C.

There was no specific preparation for the composite samples (AS4 and T650). An area of 2 cm^2 of substrate was coated by dip-coating process (withdrawn rate: 1.4 mms^{-1}, immersion time: 50 s) at room temperature. Immediately after immersion, the samples were dried in air with different relative humidity values from 20% to 60% (see Table 3.1 for details). Then, all coated samples were heated at 80 °C for 1 h to evaporate isopropanol solvent and increase the coating adhesion to the substrate.

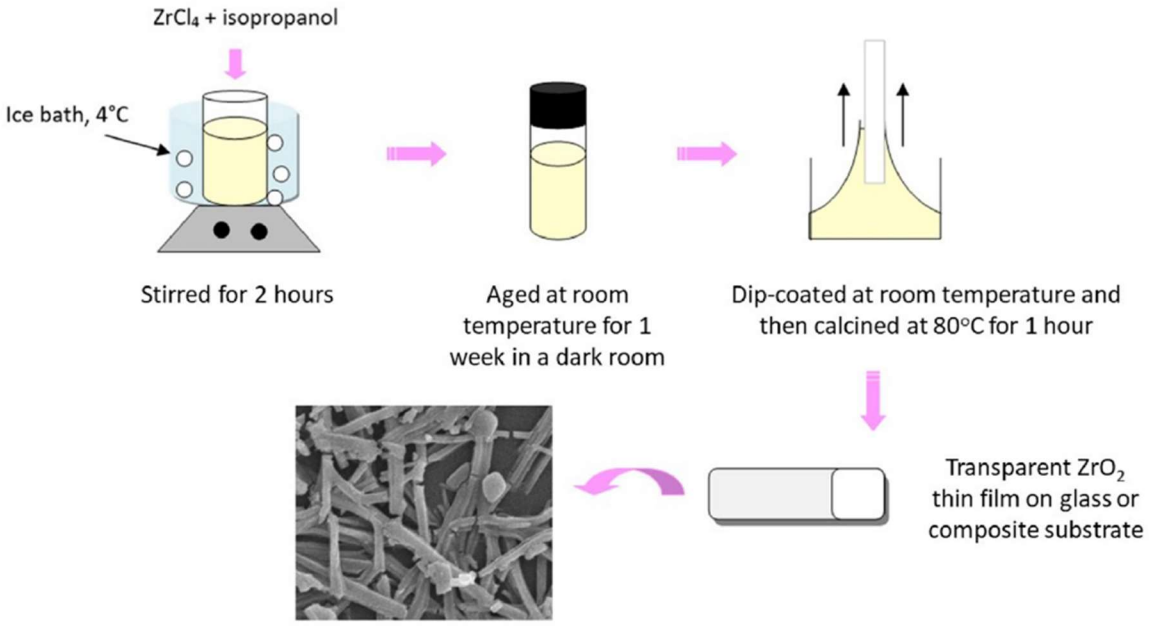

Figure 3.1. Sol-gel derived zirconia antistatic coating process.

3.2.3. Characterization

Fourier-transform infrared spectroscopy (FTIR) absorption spectra of stock solution and powder of its coating were recorded over the wave number range of 400–4000 cm^{-1} by FTIR spectrophotometer (PerkinElmer, spectrum RxI). X-ray diffraction (XRD) patterns for the powder of solutions and coatings were taken by X-ray diffractometer (PANalytical Empyrean) over 2θ range of 5°–90° to determine the crystal structure of thin films. The process operated at continuous CuKα radiation (0.1540598 nm) with a step size of 0.02°, generator voltage of 45 kV and tube current of 40 mA.

The morphology of thin films was analyzed by focused ion beam (FIB) with a high-resolution field emission gun scanning electron microscope (FE-SEM, FEI QUANTA 3D FEG FIB/SEM) using an accelerating voltage of 5 kV. The elemental distribution of ZrO_2 thin films was determined with energy-dispersive X-ray spectroscopy (EDX) with field emission electron

source (FEI QUANTA 3D FEG FIB/SEM) using an accelerating voltage of 20 kV in statistical imaging mode.

Film thickness was measured with a Tencor P2 contact profilometer. The measurements were taken from the surface roughness profile between uncoated and coated areas on each sample. Film hardness was examined by pencil hardness test up to 6H with a speed of 1 mm/s and 5 N load, according to ASTM D3363-05(2011)e2. Then, the samples surfaces were analyzed by optical microscope (Meiji Techno MT8100F) with 20x magnification to detect scratches made by different pencils.

The surface electrical resistivity of zirconia antistatic films was measured with a Keithley 2604B SourceMeter® unit at 100 mV (current limitation of 1 A) and 60 s electrification time, direct measurement with copper electrodes, based on ASTM D257-07. Finally, contact angle measurements were carried out to analyze wettability with distilled water on the top of the surface of coated and uncoated substrates. Higher wetting angles of liquids indicate lower adhesion of dust particles on the surface. Therefore, wettability measurements can be related to antidust properties of coatings [67]. Measurements were taken after one, seven and 15 min on 10 samples (n = 10) for each coating condition as listed in Table 3.1. and for each composite substrate.

Table 3.1. Coating conditions and sample codes for all coated glass substrates.

Sample code	$ZrCl_4$ concentration in solution (g/l)	Relative humidity % during air drying
Z1.20	150	20
Z1.30	150	30
Z1.40	150	40
Z1.60	150	60
Z1	150	50
Z2	100	50
Z3	50	50
Z4	15	50
Z.MPTS*	30	50

*$ZrCl_4$ (1.5 g) + isopropanol (50 ml) + diluted water (3 ml) + acetic acid (0.1 ml) + MPTS (0.1 ml)

3.3. Results and discussion

3.3.1. Chemical structure and crystallinity

FTIR spectra were recorded to determine the composition of the stock solution and its coating (Figure 3.2). Figure 3.2a shows a representative spectrum for ZrO_2 powder of the coating (sample Z1 from Table 3.1). The broad band at 538 cm^{-1} indicated the presence of Zr–O–Zr in $(OR)_{x-1}Zr–O–Zr(OR)_{x-1}$ [61,68,69]. The bands around 1600 cm^{-1} and 3300 cm^{-1} correspond to O–H bending and stretching vibrations, respectively, in adsorbed water and residual isopropanol [4,61,62]. Figure 3.2b represents the spectrum of stock solution (150 g $ZrCl_4$/l). The bands from 423 cm^{-1} to 816 cm^{-1} correspond to Zr–O vibrations in the ZrO_2 structure [70,71]. The sharp band at 951 cm^{-1} exhibits Zr—OC stretching vibrations [62]. The unbranched C–C is displayed at 1128 cm^{-1} [70]. The O–C band in isopropanol is observed at 1162 cm^{-1} [72]. The band at 1379 cm^{-1} is related to vibration O–H due to Zr–OH and isopropanol [4,73]. The bands at 2970 cm^{-1} and 3336

cm^{-1} are assigned to stretching vibrations of C–H and O–H in isopropanol, respectively [4,61,70]. The main difference between Figure 3.2a and b is the total amount of specified bands. It suggests that more Zr–O bonds could be formed in the coating due to high solution concentration. All related bands to Zr–O, Zr–O–Zr, Zr—OC and Zr–OH in Figure 3.2 shows the complete formation of zirconium compounds in the solution and film. XRD patterns were analyzed to determine amorphous or crystal structure of the coatings (Figure 3.3). The broad peak before 30° for stock solution (150 g $ZrCl_4$/l) dried at 80 °C (blue line (c) on Figure 3.3) shows an amorphous structure for ZrO_2, as reported in the literature [74]. The spectrum for powder of scratched coating (green line (b) on Figure 3.3) displays the same general pattern as the stock solution dried at 80 °C (blue line (c)). By comparing the green (Figure 3.3b) and blue spectra (Figure 3.3c), it can be concluded that the ZrO_2 thin films possess an amorphous structure. Another spectrum was obtained for powder of stock solution dried at 700 °C to analyze the crystal structure at higher temperature and confirm the presence of zirconia. As the spectrum shows, nearly all plane indices are for ZrO_2 monoclinic crystal structure and few of them are for tetragonal crystal structure (orange line (a) on Figure 3.3). By raising the temperature, there is a transition between amorphous structure to monoclinic and tetragonal crystal structure [8,64,68,71,75,76].

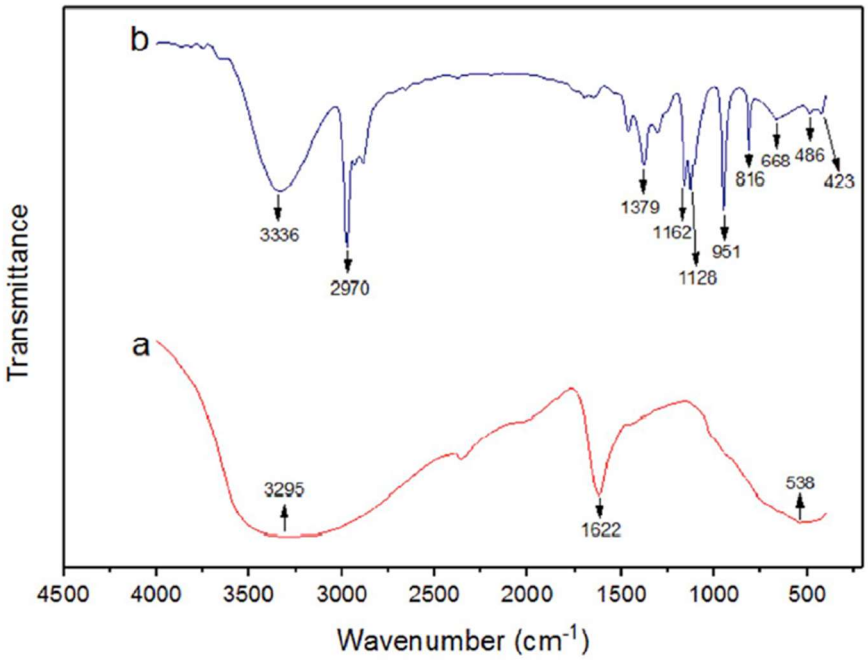

Figure 3.2. Representative FTIR spectra: (a) powder of coating Z1, and (b) stock solution (150 g $ZrCl_4$/l), in 400–4000 cm^{-1} region.

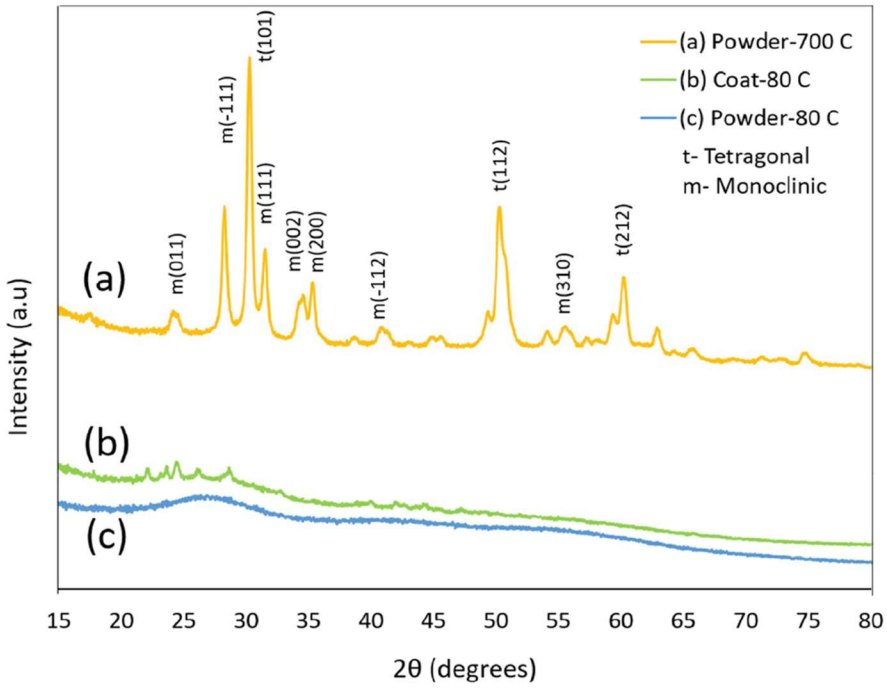

Figure 3.3. XRD patterns for: (a) powder of calcined solution at 700 °C, (b) coating Z1 scratched off with a razor blade (dried at 80 °C on glass substrate), and (c) powder of calcined solution at 80 °C.

EDX analyses of all samples were performed to confirm the relationship between Zr concentration in solutions and Zr wt% in derived coatings. As seen in Table 3.2, Zr wt% is directly related to solution concentration. As the concentration decreases, so does Zr wt%. Relative humidity, on the other hand, does not affect Zr wt% for coatings derived from the same solution, within the parameters investigated in this work.

Table 3.2. EDX analysis, hardness, and surface resistivity of prepared films on glass substrates.

Sample code	ZrO_2 content (EDX analysis ZrL) (wt.%)	Hardness	Surface resistivity (Ω/■)
Z1.20	12	4H	1.33×10^{10}
Z1.30	12	4H	1.34×10^{10}
Z1.40	11	4H	1.33×10^{10}
Z1.60	12	4H	1.33×10^{10}
Z1	9	4H	1.33×10^{10}
Z2	5	3H	1.70×10^{10}
Z3	3	H	1.80×10^{10}
Z4	2	6H	1.35×10^{10}
Z.MPTS	7	6H	2.37×10^{10}

3.3.2. Thin film microstructure and morphology

FE-SEM images were captured to investigate the effect of precursor concentration in solution and relative humidity during coating drying on the microscopic structure of thin films (Figure 3.4). The branched texture of ZrO_2 fibers is known to be related to the rate of hydrolysis and condensation. If hydrolysis and condensation occur separately at a slow reaction rate, a smooth morphology with thick fibers is formed [54]. The hydrolysis reaction rate can be increased with an increase in precursor concentration in solution or relative humidity during coating drying. On the other hand, the condensation reaction rate during coating drying decreases with an increase in

relative humidity. In this study, hydrolysis occurred in two steps: 1) in solution, according to FTIR spectra that showed Zr–OH compounds (Figure 3.2), then 2) on the substrate surface after the dip-coating process when the remaining $ZrCl_4$ was exposed to the moisture in the air. Consequently, the rate of hydrolysis has a direct relationship with the precursor concentration in solution. Condensation also formed on the surface of the substrate due to solvent evaporation [54]. Figure 3.4a–e show the effect of $ZrCl_4$ concentration in zirconia solutions and MPTS additive on the microscopic texture and structure of thin films. These samples were dried at 50% relative humidity at room temperature (Z1 to Z.MPTS in Table 3.1). For sample Z1 (Figure 3.4a), a uniform film with sharp cracks was obtained from immersion in stock solution. The hydrolysis and condensation reaction rates were low and therefore, small fibers formed on the glass surface. As the humidity was high enough (50%) to form several fibers, it resulted in a dense and multilayered film. The large cracks stemmed from high internal stresses caused by the shrinkage of the coating after drying in air and oven.

These fibers intertwined into a dense network and sharp cracks in uniform texture can be seen. By decreasing the precursor concentration from 150 to 15 g/l (Figure 3.4c, d and e), cracks disappear: ZrO_2 fibers are more visible with an increase in porosity, and the multilayered film becomes one layer with increasingly thick fibers. This is observed for sample Z4 (Figure 3.4e), in which the film is made of thick fibers separated by large gaps [54]. Figure 3.4b shows the effect of adding MPTS as a coupling agent. Compared to sample Z1 (without MPTS), the coating is more uniform and dense due to Si–Zr bonds [4]. The sharper and larger cracks reveal higher internal stresses in the coating. The silane additive increased the coating/substrate adhesion and uniformity for larger areas of the coating. The depth of the cracks suggests the coating has a very low thickness, as transparency on the glass substrate was visually observed. As the majority of

hydrolysis occurs in solution during aging time, the rate of condensation has the most significant effect on the thickness of ZrO_2 fibers in thin film. The rate of condensation on the surface of samples can be lessened if the relative humidity increases. Figure 3.4f–i show the effect of relative humidity on the texture of ZrO_2 thin films derived from the stock solution, from 20% to 60%, while drying in air. The coating has a fiber-like structure for lower humidity values (20% and 30%) (Figure 3.4f and g). It suggests that the fibers backbone is forming in lower humidity, but the fibers themselves start to form and appear around 40% humidity, becoming thicker from 40% to 60% (Figure 3.4h, a and i, respectively). Figure 3.5 represents FE-SEM EDX mapping images for thin films to locate the surface distribution of the Zr element. The Zr element content decreased with $ZrCl_4$ concentration in solution (Table 3.2), but it uniformly covered the surface for different samples (Figure 3.5a and b). As adding MPTS enhanced the thin film coverage by reducing cracks, a uniform distribution of Zr element on the substrate surface can be seen for sample Z.MPTS (Figure 3.5c and d).

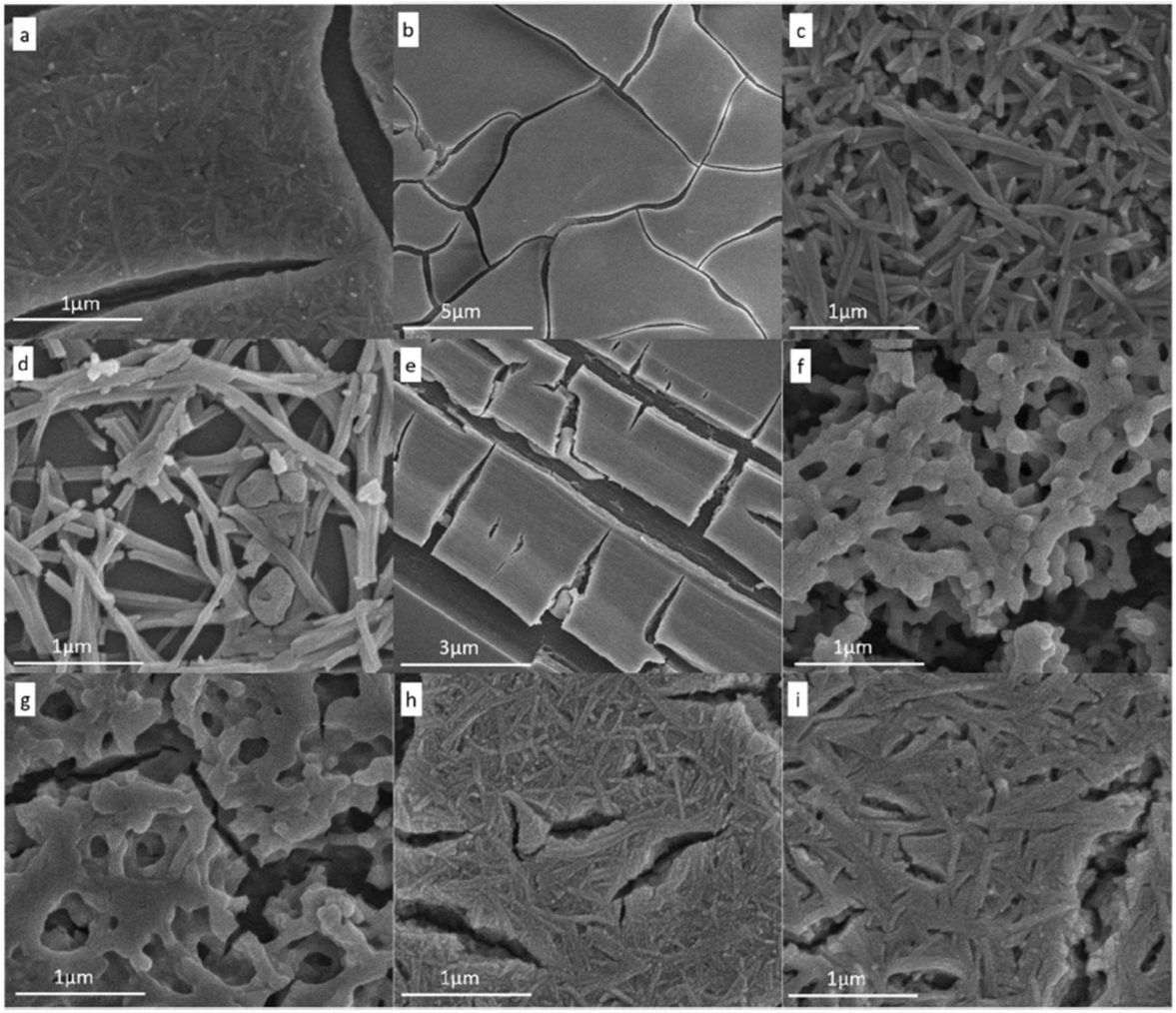

Figure 3.4. FE-SEM images of ZrO_2 coatings: (a) Z1, (b) Z.MPTS, (c) Z2, (d) Z3, (e) Z4, (f) Z1.20, (g) Z1.30, (h) Z1.40 and (i) Z1.60. Scale bar is 5 µm in (b) and 3 µm in (e), and 1 µm for all others. Coating conditions are described in Table 3.1.

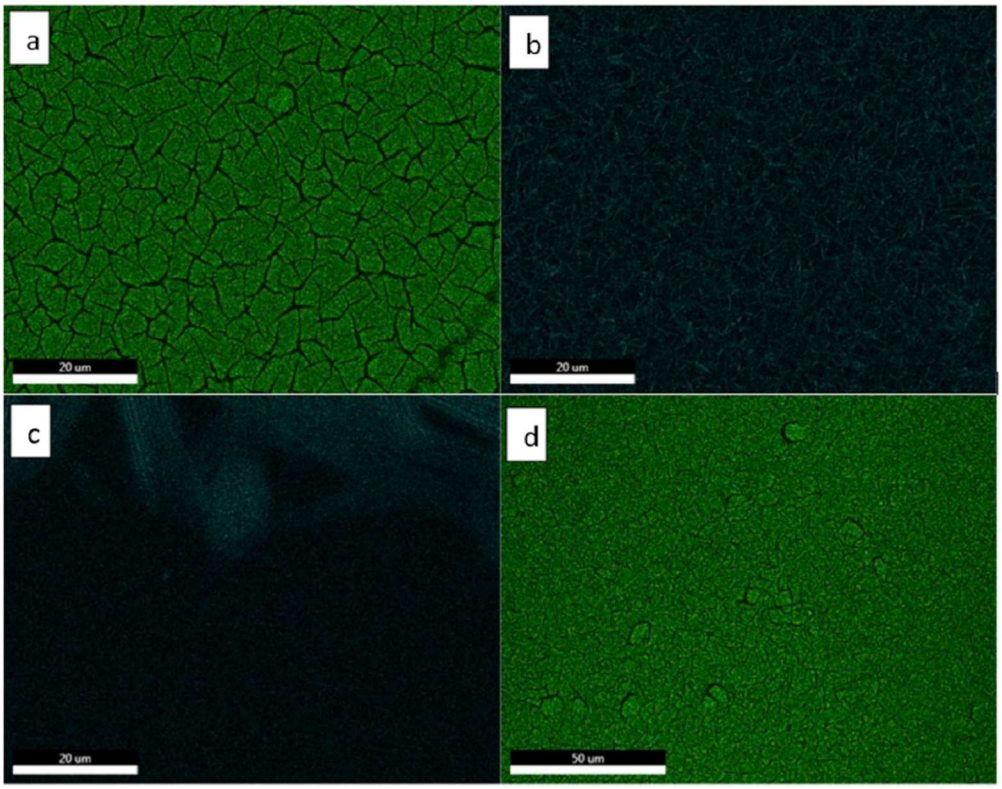

Figure 3.5. FE-SEM-EDX mapping images of elemental distribution for Zr in ZrO_2 coatings: (a) Z1, (b) Z3, (c) Z4 and (d) Z.MPTS. Coating conditions are described in Table 3.1 and ZrL wt% values in Table 3.2.

3.3.3. Antistatic film surface characteristics

Figure 3.6a and Figure 3.6b show the effect of humidity and solution concentration on film thickness, respectively. For the same parameters in the dip-coating process, film thickness fluctuated between 494 nm and 839 nm for samples derived from stock solution in different relative humidity values (20%–60%, illustrated in Figure 3.6a). The thickness did not follow any specific trend with respect to humidity percentage for the parameters investigated in this study. The lowest thickness value, 494 nm, was for sample Z1.50 dried in 50% relative humidity. In contrast, film thickness decreased when reducing solution concentration. The results are shown in Figure 3.6b, where all samples were dried in 50% relative humidity. Thickness values for samples Z1 to Z4 were between 494 nm and 13.5 nm, displaying a consistent decrease. This behavior is in

accordance with previous studies in the literature for the spin coating process. The thickness for sample Z4 is close to the thickness of samples derived from a solution with the same concentration by spin coating (11 nm) [54]. On the other hand, the thickness values for zirconia thin films on glass substrates, derived from other precursors by dip-coating process, were higher than 100 nm [62,71]. Even though the solution concentration for Z.MPTS is 30 g $ZrCl_4$/l (more than sample Z4), the film thickness is 7.7 nm (lower than sample Z4). This means a thinner film (in the order of 10 nm) with the same properties as sample Z4 can be formed by adding MPTS. However, it was observed that MPTS cannot be added to solutions with higher $ZrCl_4$ concentration because of a risk of coagulation or precipitation.

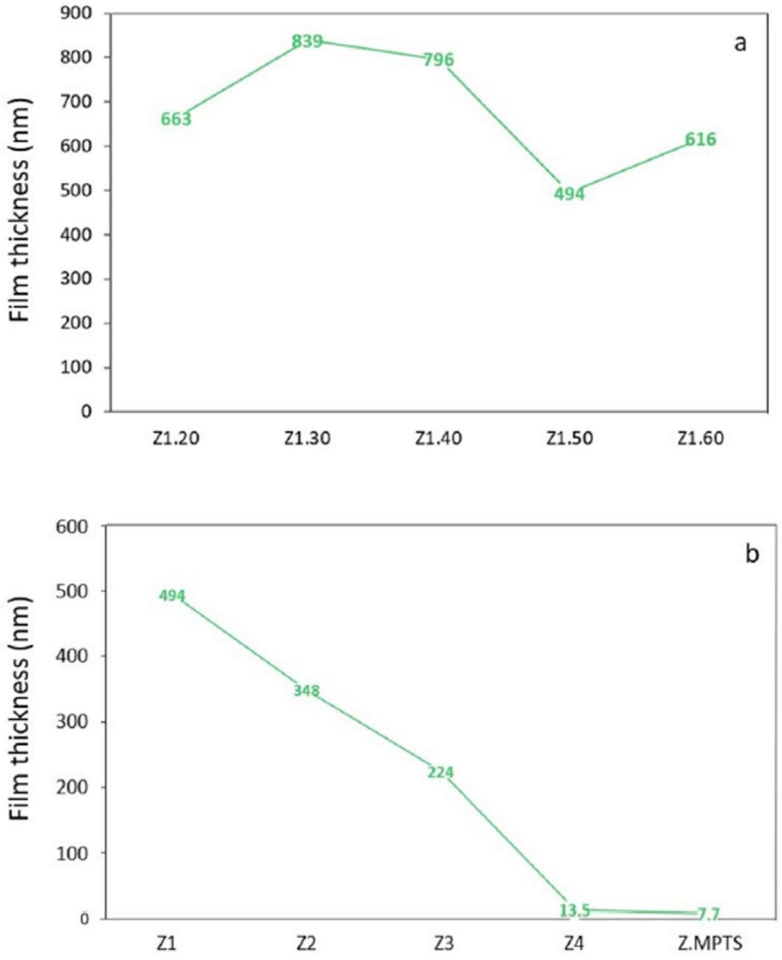

Figure 3.6. Thin film thickness related to: (a) relative humidity during drying in air (20%–60%), and (b) solution concentration (150–15 g $ZrCl_4$/l).

According to all results for thickness measurements, film thickness may be controlled by changing solution concentration, but it does not follow a specific trend over the range of relative humidity values investigated in this study. Furthermore, the additive MPTS can reduce the thickness of zirconia thin films without changing solution concentration or relative humidity.

The adhesion and stability of the thin films on the glass substrates was characterized through hardness tests, as summarized in Table 3.2. The hardness range was between H and 6H. As all samples coated with stock solution and dried in different relative humidity values remained unchanged (4H), it suggests that humidity does not have any effect on hardness. Similar to the

thickness, the hardness decreased when reducing the solution concentration (150 g–50 g $ZrCl_4$/l) from 4H to H. However, the highest value, 6H, was measured for samples Z4 and Z. MPTS, with the lowest $ZrCl_4$ and MPTS concentrations, respectively. Samples Z4 and Z.MPTS led to thin, transparent and uniform films, on which the hardest pencil left no noticeable scratch. It may be related to the smoother surfaces observed under FE-SEM (Figure 3.4b and e). The hardness values for these two samples are as high as those obtained for zirconia thin films with MPTS and curing agent on PMMA (polymethyl methacrylate) substrates [4]. Therefore, the most cost-effective sample for hardness, in terms of reagents, is Z4, without any additive.

Surface electrical resistivity tests were carried out to characterize the antistatic property of the zirconia thin films. All results, shown in Table 3.2, were in the order of 10^{10} Ω/■ (compared to uncoated glass substrate, 10^{13} Ω/■) and therefore, in static dissipative range. As there is coverage of zirconia fibers without any large crack or gap between them (which creates a better running path for electrons) on the surface for all samples without MPTS, as shown in Figure 3.4, the numbers for surface resistivity should be in the same range. The change in relative humidity during drying made no difference in surface electrical resistivity as the solution concentration (150 g $ZrCl_4$/l) was the same between Z1.20 and Z1. Although a reduction in $ZrCl_4$ concentration in solution decreases the Zr content on the surface, as observed in Fig. 5, it did not change surface electrical resistivity for different samples (1.33×10^{10} Ω/■ to 1.8×10^{10} Ω/■). The result for Z.MPTS was in same range (2.37×10^{10} Ω/■), which indicated that adding MPTS in stock solution (Z1 versus Z.MPTS) can improve static dissipativity as it has ionic silanes integrated with ZrO_2 [4].

Contact angle measurement results (with distilled water) are shown in Figure 3.7 for both coated and uncoated samples. Values were taken over a duration of 15 min. For glass substrates, there was a difference in contact angle, θ_d, by at least 30° between uncoated and coated samples.

Generally, the average contact angle decreased as the coating smoothness increased (as seen in Figure 3.4) by either increasing the humidity or, to a lesser extent, decreasing the precursor concentration [70]. It indicates that the most hydrophobic coating was sample Z1.20 with θ_d=88.6±8.0°. This value is on the lower-end range of contact angle measurements for ZrO_2 coatings on stainless steel AISI 316L substrates, θ_d=91.8±4.9° to 120±4.8° [70,77]. While a direct comparison may not be accurate because of the different substrates, reagents and coating conditions, it demonstrates that the proposed coating can achieve a similar performance to previous studies using dip coating. For all other coated glass substrate samples, the contact angle remained within a 55°–70° range on average, showing a tendency to repel water or dust well above the uncoated glass substrate.

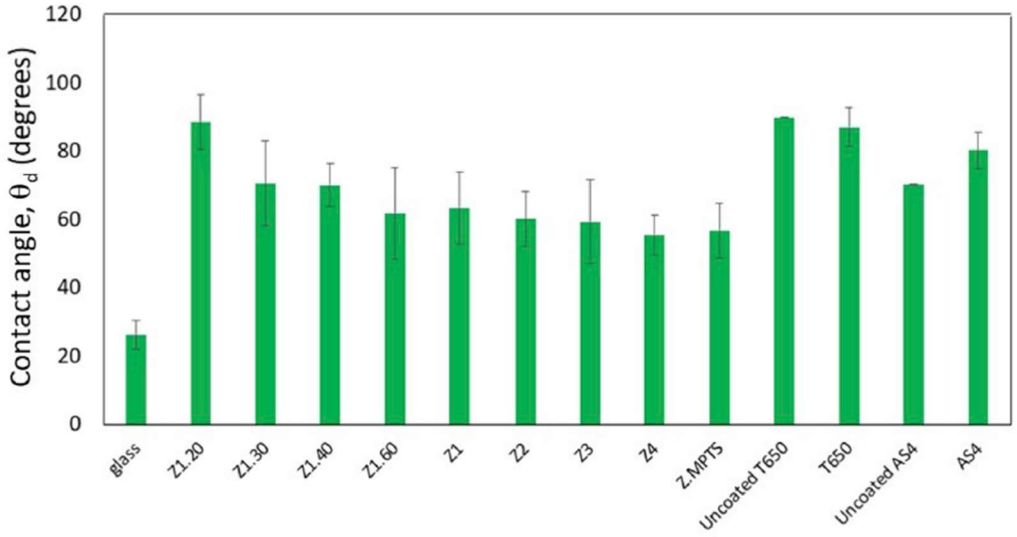

Figure 3.7. Contact angle (θ_d) of uncoated and ZrO_2 coated samples obtained in various conditions on glass and composite substrates for distilled water (average±standard deviation after 15 min, n=10). Coating conditions are described in Table 3.1. Composite substrates T650 and AS4 were coated with Z4 solution.

3.3.4. Application to carbon fiber/epoxy composite substrates

Based on the results presented for glass substrates, coating condition Z4 was selected for the CF/epoxy composite substrates (15 g $ZrCl_4$/l and drying at 50% relative humidity, as listed in

Table 3.1). All coating and drying procedures were the same as the glass substrates. This coating condition was chosen based on the following three criteria: 1) hardness, 2) film thickness, and 3) wettability. A high hardness and low film thickness are preferred as they are related to high film adhesion to the substrate and transparency to preserve surface appearance, respectively [64]. While Z4 did not display the highest hydrophobic behavior (Figure 3.7), it was nonetheless higher than the uncoated glass substrate (56^{o} vs 26^{o}) with the lowest standard deviation among coated substrates, indicating potential to repel dust particles and liquids on the surface [67].

Figure 3.8a and Figure 3.8b show the thin film structure on both composite substrates, T650 and AS4. The morphology of the coatings was different from the one observed on the glass substrates (Figure 3.4), but the boundary between coated and uncoated regions was clearly noted. There were no fibers, entangled network or cracks visible on the surface, but the coating appeared uniform and transparent across the entire area. This reveals that the morphology of ZrO_2 thin films may depend on the substrate's material and composition. Zr elemental distribution confirmed the existence of Zr in the coating for both samples (Figure 3.8c and d). Film surface characteristics for composite samples are summarized in Table 3.3. The hardness for both T650 and AS4 coated composites was 6H, confirming good adhesion and resistance to manual removal. The coatings were transparent, allowing to preserve the visual appearance of the composites. The surface electrical resistivity for T650 and AS4 was 0.90 and 1.00×10^{10} Ω/■, respectively, similar to the glass samples. Uncoated samples had a surface electrical resistivity of 0.80×10^{10} Ω/■, indicating that the zirconia coating increased its value by up to 25%, but remained in the static dissipative range.

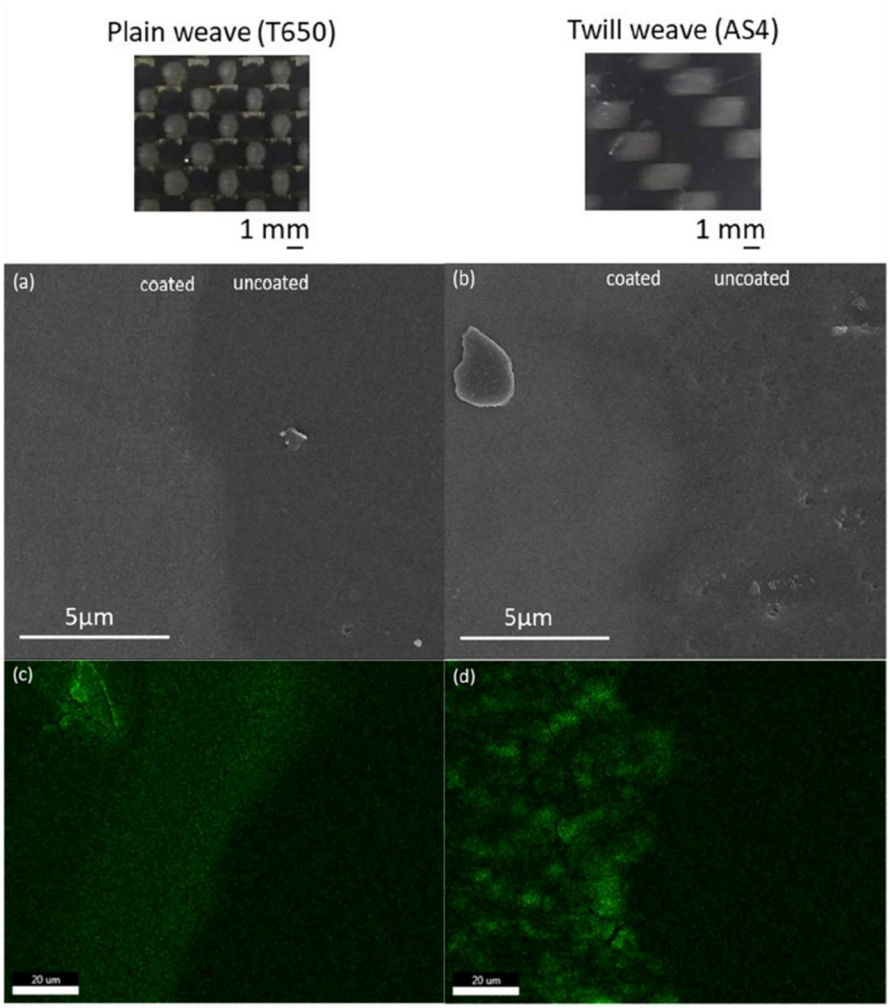

Figure 3.8. FE-SEM images of coatings derived from solution Z4 (15 g $ZrCl_4$/l): (a) T650 and (b) AS4, and FE-SEM EDX mapping images of elemental distribution for Zr in ZrO_2 coatings for (c) T650 and (d) AS4 (ZrL wt% shown in Table 3.3). Scale bar is 5 µm for (a) and (b), and 20 µm for (c) and (d). Fiber pattern for each sample type is shown at the top (1 mm scale).

Table 3.3. Coating conditions and surface characteristics for prepared films on carbon fiber/epoxy composite substrates.

Sample code	$ZrCl_4$ concentration in solution (g/l)	Relative humidity % during air drying	ZrO_2 content (EDX analysis ZrL) (wt%)	Hardness	Surface resistivity (Ω/■)	Thickness (nm)
T650	15	50	27	6H	0.90×10^{10}	2340
AS4	15	50	21	6H	1.00×10^{10}	1530

By comparison with the literature, zirconia thin films on PMMA substrates led to a surface electrical resistivity in the order of 10^8–10^{10} Ω/■ [4]. Film thickness, on the other hand, was higher than the glass substrates: 2340 nm (2.34 μm) and 1530 nm (1.53 μm) for T650 and AS4, respectively. This suggests that the CF/epoxy substrates absorbed the solution after coating and did not let the isopropanol evaporate completely on the surface. As a result, solvent remained on the surface, which led to a thicker film in the order of micrometers. The absorption by the substrates and thicker film may explain the morphology differences in Figure 3.8 when compared to the glass substrates (Figure 3.4).

Thickness values for the proposed coating are lower than what was previously presented in the literature for zirconia thin films on PMMA substrates, and ESD polyester-based coatings on CF/epoxy and polyamide 6,6 substrates: above 10 μm for all cases [4,13,58]. For lightweight composite applications, lower thickness is preferred to minimize weight. Wettability results, presented in Figure 3.7, showed that the contact angle θ_d for T650, stable after 15 min, was around 90° with and without coating. For AS4, the contact angle for the coated samples increased by approximately 10° compared to the uncoated substrates. The main differences between T650 and AS4 were examined to explain those θ_d values: i) their fiber weave (plain weave and twill weave, shown in Figure 3.8), and ii) their fiber volume fraction, V_f, from 64% (T650) to 55% (AS4). Both may affect their surface roughness and create non-polar groups on the surface, thereby reducing wettability and increasing hydrophobicity [48]. However, as the uncoated T650 samples already exhibited high contact angles ($\theta_d > 90°$) similar to the highest glass substrate value (Z1.20), the zirconia coating did not further increase the contact angle.

It is suggested that the contact angle increased between uncoated and coated AS4 samples because of their lower fiber volume fraction and surface roughness compared to T650 samples. In

the literature, it was observed that poly (styrene-co-acrylonitrile)-modified epoxy matrix could reduce wettability of glass fiber composites by increasing the contact angle from approximately 60° to 75°, similarly to the proposed coating [78]. While surface resistivity did not decrease after coating, indicating it may not be specifically suited for antistatic applications for composites, contact angle measurements showed promising results for wettability. The proposed coating method is simple and has potential to be cost-efficient, when compared to techniques such as electrostatic spray deposition. It could facilitate cleaning of CF/epoxy specimens used for aesthetic purposes, taking V_f and weave pattern into consideration.

3.4. Conclusion

ZrO_2 antistatic thin films were prepared by a simple dip coating sol-gel route using different concentrations of $ZrCl_4$ precursor (15–150 g/l) and relative humidity values during air drying (20%–60%). FTIR spectra showed the presence of ZrO and ZrO_2 bonds in solution and powder of the coating. The XRD patterns revealed that the ZrO_2 coating possessed an amorphous structure. Both methods confirmed zirconia thin films were successfully synthesized on the substrates. For coatings on glass substrates, relative humidity and solution concentration affected coating surface morphology. FE-SEM pictures showed thicker ZrO_2 fibers were obtained by either increasing the relative humidity (from 20% to 60%) during drying or decreasing $ZrCl_4$ concentration in solutions (from 150 g to 15 g ZrCl4/l). Relative humidity did not affect surface resistivity, ZrO_2 content, and hardness, while lower solution concentration decreased ZrO_2 content and hardness.

A transparent ZrO_2 thin film with 13.5 nm thickness, 6H hardness and 1.35×10^{10} Ω/■ surface resistivity with a smooth surface was obtained with the lowest precursor concentration in solution and 50% relative humidity. Generally, the average contact angle decreased, from

approximately 90° to 60°, as the coating smoothness improved by either increasing the humidity during drying or, to a lesser extent, decreasing the precursor concentration.

The MPTS coupling agent was found to further reduce the film thickness to 7.7 nm while maintaining all desired antistatic characteristics of zirconia thin films. However, the addition of MPTS might not be recommended if cost efficiency is a concern. As a second step, solution Z4 was used to coat plain weave and twill weave carbon fiber/epoxy samples, and assess their antistatic and dust or water repellent properties. It was found that thin films morphology, hardness (6H), thickness (1.53 μm–2.34 μm) and surface resistivity (antistatic range) were similar for both types of composite substrates. While surface resistivity did not decrease after coating, indicating it may not be suited for antistatic applications for composites, contact angle measurements showed promising results for wettability. Contact angle increased by approximately 10° for twill weave AS4 substrates containing 55% fiber volume fraction. It was suggested that contact angle was related to lower fiber volume fraction and surface roughness, compared to the plain weave samples. This improvement of hydrophobicity makes the proposed zirconia coating a simple, low cost solution to impart dust and water repellent properties to preserve the composites' visual appearance.

Chapter 4 . Literature Review on Orthopedic Implants: Materials, Manufacturing Methods, and Bone Regeneration Mechanisms

4.1. Introduction

This chapter is a review on orthopedic implants, with a focus on cranioplasty (CPL) application, and the related biological and biomaterial terms. First, a brief review of the definition and types of orthopedic biomaterials is provided to show the origin of cranioplasty implants (Section 4.2). Second, ancient and modern definitions, and the history of cranioplasty surgery and cranioplasty implants are presented in Section 4.3 to summarize surgery complications and difficulties with current implants. Section 4.4 includes a review on materials commonly used as cranioplasty implants, current implant designs, and their advantages and disadvantages. In Section 4.5, a review of surgical meshes are presented to draw inspiration from for implant designs. Different manufacturing methods for hydroxyapatite coating are presented in Section 4.6, followed by characterization techniques in Section 5.7. Human cell behavior on implants is discussed with the perspective of stem cells differentiation to bone cells in Section 4.8. Finally, Section 4.9 highlights the main gaps identified in the literature regarding materials selection, implant design, and characterization.

4.2. Orthopedic biomaterials definition

Orthopedic biomaterials are used to facilitate the healing process or to fill the lack or loss of bone tissue by implantation into or near a bone fracture [79]. The global orthopedic biomaterial market in 2019 was about $12.46 billion with an expected growth rate of 10.3% by 2025 [80]. These materials are generally used for fracture fixation enhancement, joint replacement, or dynamic stabilization. Cranioplasty implants fall under the fracture fixation enhancement category, as they provide plates and fixation devices, such as wires, pins, and screws [81]. Improving bone healing by using orthopedic implants falls under the tissue engineering discipline.

Tissue engineering considers both engineering and scientific methods to maintain existing tissue or to promote new tissue formation. The three essential components in tissue engineering are: 1) scaffold, 2) cells, and 3) signaling biomolecules [82].

Orthopedic biomaterials can be used as scaffold or reinforcing scaffold in tissue engineering, while providing good chemical and physical properties for cell attachment, proliferation and differentiation to form new tissue by the body itself.

4.3. Cranioplasty definition and background

Although it has been suggested that cranioplasty dates back to 7000 BC by archeological evidence [9], the proof of earliest cranioplasty operations were found next to skulls in graveyards dating back to 3000 BC, Inca civilization, South America. This evidence contained metals, gourds and shells, with a thin plate of gold covering a cranial defect on a skull, dating back to 2000 BC, Peru. In Polynesian Islands in the South Pacific Ocean, defective skull remains from archeological studies contained coconut shells or palm leaves [83]. In each ancient tribe, the most suitable resources were used as medical implants, whether they were metal or organic compound.

The earliest modern definition for cranioplasty is related to a surgeon from the Ottoman Empire in 1505, where he mentioned the use of xenografts from Kangal dogs or goats as implants in his surgical book [84]. The cranioplasty operation was an open wound dressing and surgical skills until the 16th century, when Fallopius, an Italian anatomist, stated that "[…] the fractured cranium should be removed and be reinserted with a gold plate if the dura was damaged". The first and successful cranioplasty was reported by a Dutch surgeon in Russia, where a canine cranium was used as a xenograft [83]. From the first cranioplasty operation (in the 16th century), various xenografts from different animals were used until the introduction of modern materials, autografts, allografts, and synthetic materials [83,85]. Autografts were harvested from different

parts of the patient's body, from leg bone to shoulder blade, along with fat tissue and fascia. Allografts for cranioplasty were first collected from human cadaver cartilage, followed by cadaver skull in the subsequent years. The use of cadaver allografts ended as they led to a lack of significant calcification or to infections.

Synthetic materials, such as polymers and metals, were employed during World War II and afterwards, when the number of patients with head injuries increased drastically. Methyl methacrylate (MMA) was one of the first synthetic materials for cranioplasty implants with good malleability, durability, high strength, and low cost. High infection rate, brittleness and lack of adjustability and calcification further limited its use in operations [9,86]. Metallic materials, including titanium, stainless steel, and cobalt-chromium alloys, were later introduced for cranioplasty. Hydroxyapatite is another material often used in modern cranioplasty as it has a similar chemical structure to bone and improves osteointegration [87]. Hydroxyapatite is often used with a titanium mesh to prevent fractures and for better osteointegration [9,86].

In the last twenty years, head injuries and traumatic brain injuries (TBI) are the first cause of death and disability in adults in the United States. Motor vehicle accidents, falls, and violence as a result of child abuse can lead to head injuries in both children and adults. Although it seems that senior adults are more exposed to head injuries, reports showed children from 0 to 4 years old, and young adults from 15 to 24 years old, had the most cases in the United States between 2001 and 2010. Adults above 65 years old are fourth [88].

Skull fracture, intercranial hematoma (ICH) and concussion are major types of head injury. Skull fracture includes linear skull fracture, depressed skull fracture, diastatic skull fracture, and basilar skull fracture. Depressed skull fracture is a kind of fracture with or without a cut in the scalp. Typically, a part of the skull is recessed from a trauma or injury and needs to be fixed by

surgery [89]. ICH or blood clots in or around the brain could constitute a mild head injury to a severe, potentially life-threatening one. Epidural hematoma (usually related to skull fractures), subdural hematoma (sometimes related to skull fractures), contusion or intracerebral hematoma (which can cause TBI), and diffuse axonal injury (DAI) (patient is in a coma for a long period of time with damage to many areas of the brain) are types of intercranial hematoma. Any kind of bump, blow or jolt to the head, which disintegrates the normal function of the brain, can result in a mild (concussion) to severe (unconsciousness or memory loss) TBI [90].

Today, cranioplasty is a follow up surgery as a bone flap replacement for decompressive craniotomy (DC) in any case of loss of bone in scalp due to head injuries, TBI or corrected skull malformations [91]. Complications in cranioplasty can make it a risky operation and increase the mortality rate. The result of the cranioplasty surgery depends on many factors, such as surgical skills and repair method, fit of contiguous soft tissues, as well as size and location of the skull defect [92,93]. A list of general cranioplasty complications correlated with the choice of alloplastic graft include infections, bone resorption, wound dehiscence, poor cosmetic results, a need for reoperation, and surgery-related complications, such as duration of the surgery. Other complications could be hematoma, seizures, hygroma and cerebro-spinal fluid (CSF) collection [91,94].

Regarding cranioplasty complications, a good graft should be low cost, non-corrosive, non-toxic to avoid infection, malleable, osteoconductive, durable, radiolucent, and display good fitting and contouring for aesthetic purposes [92]. Bone grafts, osteoinductive growth factors, and medical biomaterials are the most common repair methodologies developed in the past few years [7]. All materials for cranioplasty have some drawbacks. Thus, cranioplasty surgery and treatment still need improvements in materials, implant designs and surgical methods.

4.4. Materials for cranioplasty implants

4.4.1. Bone grafts

An autograft consists of bone from a patient's body, transferred from healthy tissues to the injury site. An allograft is bone transplanted from another human body to a patient's body [9]. Growth factors or |osteoinductive stimulators can be added to the fractured bone or bone graft to speed up bone regeneration on the wound. Osteoinductive growth factors can stimulate other parts of a patient's body, including cartilage, such as hip and elbow joints, to form a new bone. However, the new bone can tear through the muscles in extreme cases and lead to heterotopic ossification (HO) in other joints [95]. Bone donor shortage, complexity of reshaping the harvested bone, bone graft resorption, and risks of harvesting bone grafts are limitations to bone grafts as implants in cranioplasty [7].

4.4.2. Biomaterial definition

Biocompatibility of a material is defined as "the ability of a material to be used in close connection with living tissues without causing adverse effects to them [6]." Biomaterials for cranioplasty can reconstruct cranial defects, while presenting advantages with regards to biocompatibility, non-toxicity and aesthetics without major side effects. There are four general categories of biomaterials used for cranioplasty: metals, polymers, bioceramics, and composite materials made from two or more aforementioned materials.

4.4.3. Metallic biomaterials

Metals were used extensively from the 19th century as they are strong, malleable and can be sterilized [6,9]. Although gold and silver were used for cranioplasty in the Inca Empire, their use as cranioplasty implants were discontinued in recent times. Gold is too expensive, even though it has good strength and no infection risk. On the other hand, silver was too soft and oxidized easily

under the skin [86]. In modern age, aluminum was the first material used for cranioplasty implants, but was later discontinued because of high infection rate and epilepsy in patients [9,86]. Tantalum was another metallic material used for cranioplasty, as a substitute during World War II. High heat conductivity, difficulty in procurement and high cost were tantalum's main disadvantages, thus it was abandoned [6,9,86].

A limited number of metals and alloys are appropriate for cranioplasty implants. Metals frequently used for specific cranioplasty applications are stainless steel, cobalt based alloys (with chromium, nickel, molybdenum), titanium and titanium alloys (with aluminum, vanadium, nickel) [6,86,96–98]. Although there are a few reports on cranioplasty surgeries using stainless steel mesh [99], stainless steel and cobalt−chromium alloys have limited application after 1980s, as they possess poor corrosion properties as biomedical implants (Figure 4.1) [6].

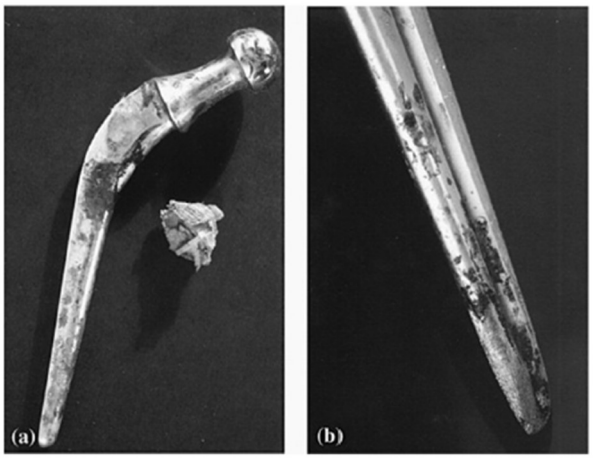

Figure 4.1. Corroded stainless steel implant for hip after implant removal a) stem, and b) pitting [6].

In recent years, titanium and titanium alloys (Ti−6Al−4V) have gained popularity because of their excellent corrosion resistance [100]. They are mostly used as bulk or plate implants for hip and joints, and custom-made or mesh-like implants (Figure 4.2) for cranioplasty [9]. However, the lack of isoelasticity of skeleton and bone, as well as cytotoxicity from the release of ions (e.g.,

Ti4+, aluminum (Al), and vanadium(V)), are potentially harmful to the human body's immune system. Additionally, some metallic implants restrict the use of magnetic resonance imaging (MRI) and cone beam X-ray imaging for medical diagnosis, are heat conductive and have issues in long-term [98,101,102].

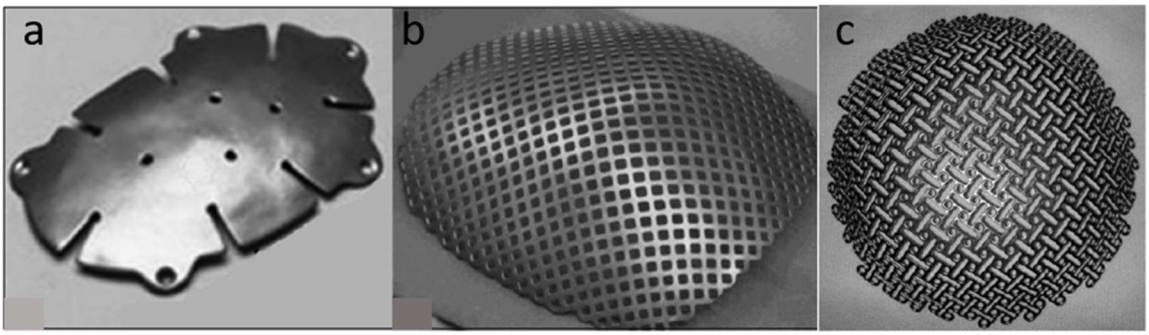

Figure 4.2. Cranioplasty implants: titanium plate (a) and titanium mesh (b, c) [9,86]

Metallic mesh implants are typically fabricated by CNC machining, weaving wires into mesh patterns, or, more recently, various additive manufacturing technologies [103]. Cranioplasty implants usually need to be custom designed to fit the patient's anatomy. This implies to use of 3D imaging (computed tomography or 3D scanners), followed by computer-assisted design (CAD), and computer-assisted manufacturing (CAM) or 3D printing. Thus, the process is lengthy and is not suitable for emergency use.

In summary, metallic biomaterials are strong enough to be used as bone substitute for cranioplasty, but have some drawbacks, such as cost (for titanium and alloys), lengthy manufacturing process, lack of osteointegration, poor connections with surrounding tissue [104], and some medical imaging restrictions [101].

4.4.4. Polymeric biomaterials

The first synthetic polymer material used as a cranioplasty implant was acrylic resin, methyl methacrylate (MMA), during and after World War II, until today. For larger skull defects,

cellulose-based materials [105], and polymers have demonstrated potential for bone regenerative tissue engineering. For the latter, acrylic [106], polyethylene (PE) [107], poly(methyl methacrylate) (PMMA) [108], and polyether ether ketone (PEEK) [109], are common polymers or matrices that have been successfully used as implants.

In contrast with metals, polymer implants are radiolucent and mainly used for large skull defects. For instance, PEEK is a biocompatible, semi-crystalline polymer with excellent mechanical properties, non-toxicity, and natural radiolucency [110]. It has been widely used as orthopedic implants, with a complication rate similar to Ti, but better than autologous bone grafts based on surgical meta-analysis results [111]. PEEK has high chemical resistance [112], and higher tensile strength (100-115 MPa) and flexural modulus (4-4.2 GPa) [113] than most other polymers like PMMA (tensile strength: 70 MPa, flexural modulus: 2.9 GPa) [114]. However, the smooth surface of PEEK implants typically needs to be modified to improve osseointegration or incorporated with fillers, such as hydroxyapatite (HA) [115].

Acrylic and acrylic resin-based materials such as PMMA are other long chain polymers, which can be constructed preoperatively (customized graft) or added as a curing cement during surgery [116]. PMMA is amorphous with strength at least equal to cranial bone [117], but it is generally brittle [118]. Different kinds of curable acrylic polymers (bone cement) have also been used on skull defects for good contour below the skin. However, heat generation during polymerization can affect the brain and neighboring tissues [104,116]. The complication rate for PMMA is similar to other implants in surgical meta-analysis results [104]. Polymeric implants should be custom-made using computed tomography (CT) imaging (Figure 4.3 and Figure 4.4). Die casting, molding, and 3D printing are common manufacturing methods for polymeric bulk implants [103,119].

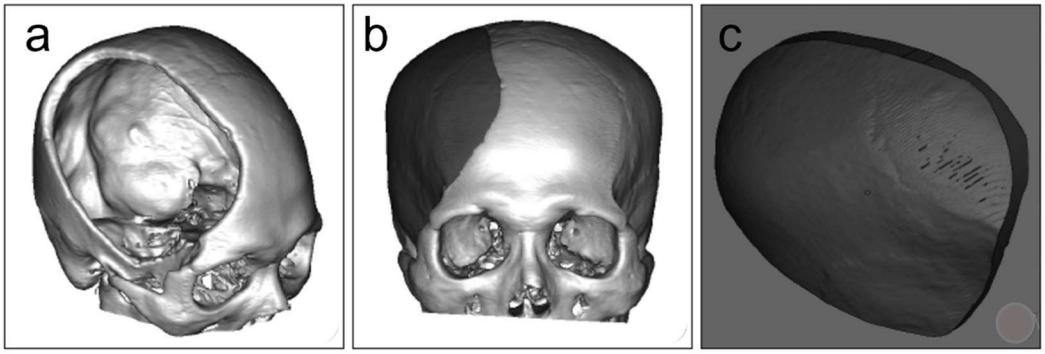

Figure 4.3. The steps of 3D imaging and design of PMMA cranial implants: a) CT data is converted to 3D image, b) 3D image of the implant generated by digital subtraction mirror-image process, and c) 3D implant model [108].

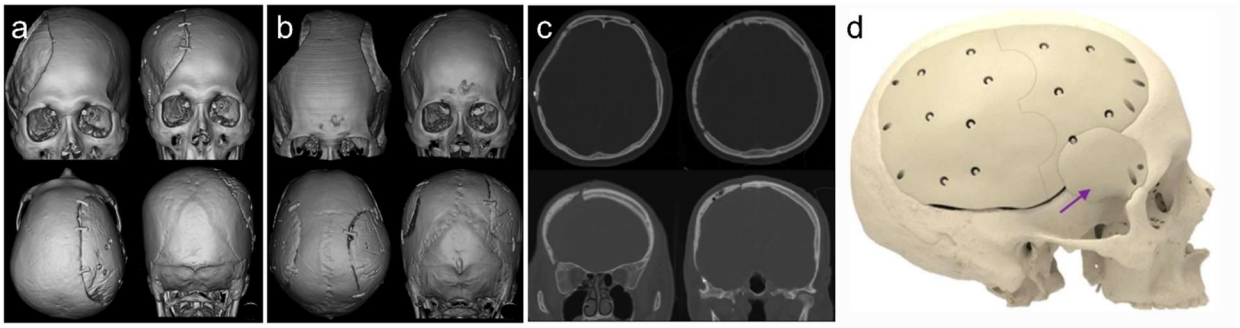

Figure 4.4. 3D CT image illustrations of a) unilateral and b) bilateral for reconstruction of large cranial defects, c) postoperative CT scan shows symmetric contour of cranium using custom-made implant (right) compared to contralateral normal one (left) [108], and d) actual PMMA implant [120].

Natural and synthetic cellulose $(C_6H_{10}O_5)_n$-based fabrics and scaffolds have been used for different biomaterial applications, from wound dressing to tissue engineering applications to bone repair [105,121–123]. A biodegradable 3D scaffold can be obtained from cellulose fabrics or mats as it is biocompatible, and has low cytotoxicity and good biochemical properties [124,125]. As cellulose fabrics and mats are porous and consist of thin fibrils [126], they are flexible and the open areas between fibrils can hold liquids, for instance, cell suspension or any human body fluids [126].

Overall, polymers or polymer composites can exhibit complications due to potential inflammation, infection, implant exposure, skin penetration, and radiolucency [7,101,127,128]. Another problem is that custom-made implants are time-consuming and costly to design and manufacture. They need to be designed according to CT scans or other 3D images and manufactured by molding, die casting, or 3D printing [9,106,129]. All these processes require several months to be carried out by authorized suppliers.

4.4.5. Bioceramics

Bioceramics are another type of promising materials for cranioplasty. They can be used as bulk, scaffold, powder, cement, filling for bone fractures, and coating on bioinert materials [112,130–132]. Alumina was considered in 2000s, because of its strength, tissue compatibility, low infection rate, and aesthetic properties. However, as customized ceramics are very expensive, the use of alumina implants was halted for major cranioplasty implants [9].

Tricalcium phosphate (TCP) and hydroxyapatite (HA, $Ca_{10}(PO_4)_6(OH)_2$) are the most commonly used bioceramics because of their chemical structure (Figure 4.5). HA is an inorganic part of bone and tooth, which can initiate bonding with surrounding bony tissues [130]. Thus, it naturally possesses good osteoinduction and osteoconduction. Several histological studies in the literature presented formation of bone in-growth on different forms of porous and nonporous HA implants and calcium phosphate scaffolds [7,73,131,132].

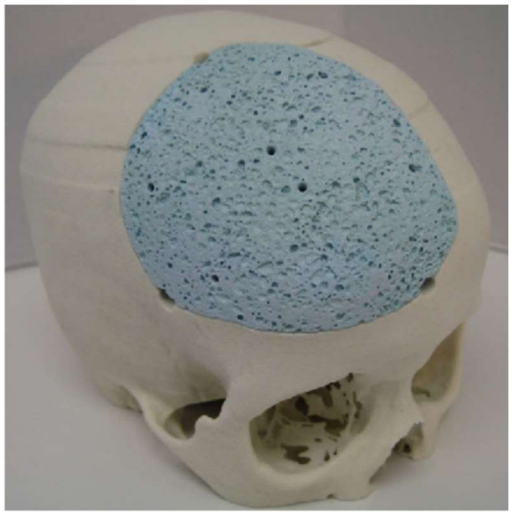

Figure 4.5. Hydroxyapatite implant in child cranium [133].

However, their low strength and brittleness limit their application to non-load-bearing human body skeleton, such as cranial and mandible bone [101,130]. Fragmentation due to head injuries or external loads can cause infection and inflammation even for cranial implants [9,101]. The design process for custom-made bioceramics implants is similar to metallic and polymeric implants, requiring CT scans and CAD.

4.4.6. Combined or composite biomaterials

The first combined biomaterials consisted of metal mesh or plate as reinforcing scaffold, covered by polymeric or ceramic fillings or cements, such as MMA resins or HA. Combining bioceramics and metallic substrates by using HA cement has shown promising advantages, such as an increase of implant strength and aesthetic properties (Figure 4.6) [101,134,135]. HA coating is expected to improve biocompatibility, while displaying optimal porosity, good adhesion to the substrate, high crystallinity, and proper stoichiometry (Ca/P ratio of 1.67) [134,136].

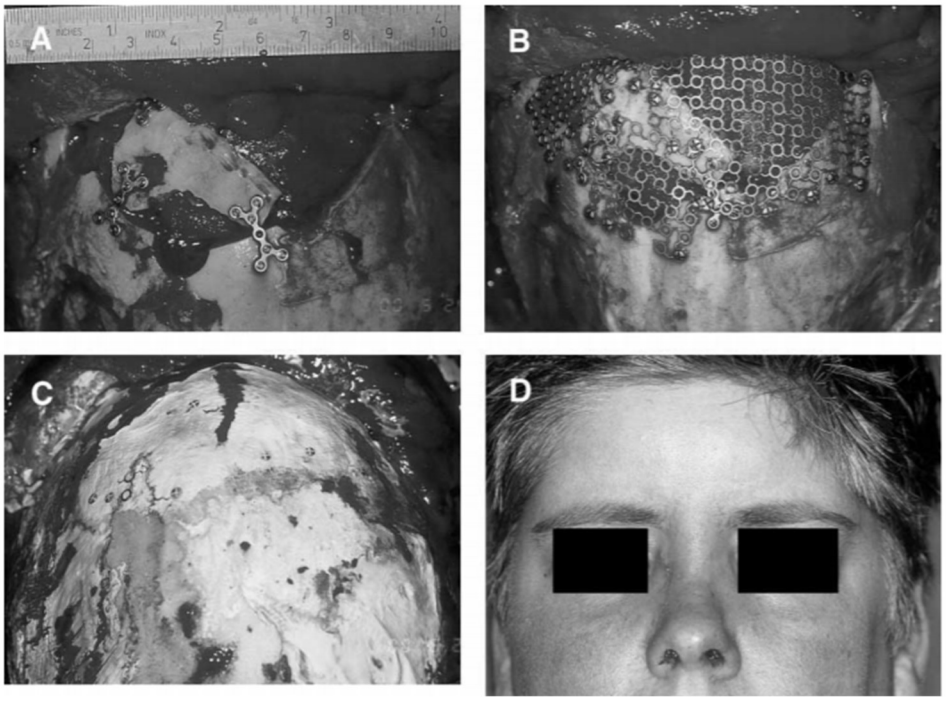

Figure 4.6. The stages of applying cranial implants for a patient: a) showing a small part of the fractured skull is covered by remained bone after tumor removal and b) titanium mesh covered the whole defect. c) hA cement covered titanium mesh; d) patient after surgery [137].

By themselves, pure polymeric biomaterials are not bone regenerative in human body (in vivo) [101], but they can be coated by osteoinductive factors [138,139]. Bioceramics are osteoinductive according to their chemical structure. Therefore, they can be used as a coating on flexible scaffolds to circumvent the brittleness issue, while promoting osteoinduction and adhesion to nearby tissues. Cement biomaterials may be used to create composite implants. They are curable compositions that should be set or hardened after covering the implant substrate. MMA paste setting is an exothermic reaction, while calcium phosphate cements set in minutes under isothermic condition and controlled pH [140]. Using cement biomaterial can increase the duration of surgery or hurt the surrounding tissue due to heat release during crosslinking.

4.5. Surgical meshes for tissue engineering applications

While surgical meshes are not specifically used for cranioplasty, a brief review of their advantages and limitations may provide guidance for novel implant designs. Porous scaffolds, such as meshes, woven fabrics and mats, have potential for implant and bone repair applications, and they possess additional benefits (over bulk, custom-designed implants), such as flexibility and customizability. Surgical meshes typically provide additional support to a weak tissue. They were initially used in the 1950s for hernia repair applications. Afterwards, surgical meshes have been used to manage various conditions, such as pelvic floor dysfunctions, breast surgery, periodontal surgery, and wound healing [15,16].

Materials used as surgical meshes are divided into four categories: non-absorbable synthetic materials, absorbable synthetic materials, absorbable natural materials, and grafts. Among all the materials used in those categories, titanium and cellulose are common orthopedic bone implants. Titanium is widely used as cranioplasty implant, while the properties of cellulose and cellulose-based materials for cartilage and bone regeneration is still under investigation [15,122].

Surgical meshes have the potential for support cell growth and collagen production, which is the main goal for cranioplasty implants. The main problems with surgical meshes are related to materials and geometric design. Even biocompatible materials can activate the human body's immune system and cause infections. Mechanical properties of the surgical meshes should be close to the surrounding tissue. If the material is very stiff or too soft, biomechanical mismatch between the implant's mechanical properties and the surrounding tissue can prevent integration of the implant with nearby tissue [15,16,122]. Some examples of promising, strong, flexible mesh designs for tissue engineering include woven and 3D printed PEEK scaffolds [141]. Woven

monofilament or multifilament PEEK fabrics have been shown to lead to good levels of cell attachment, even without surface modification (Figure 4.7). It was suggested that weave pattern, open area dimensions and exposed surface area could play an important role in biocompatibility behavior, but no studies were carried out to further investigate the effect of mesh parameters, including 3D printed meshes.

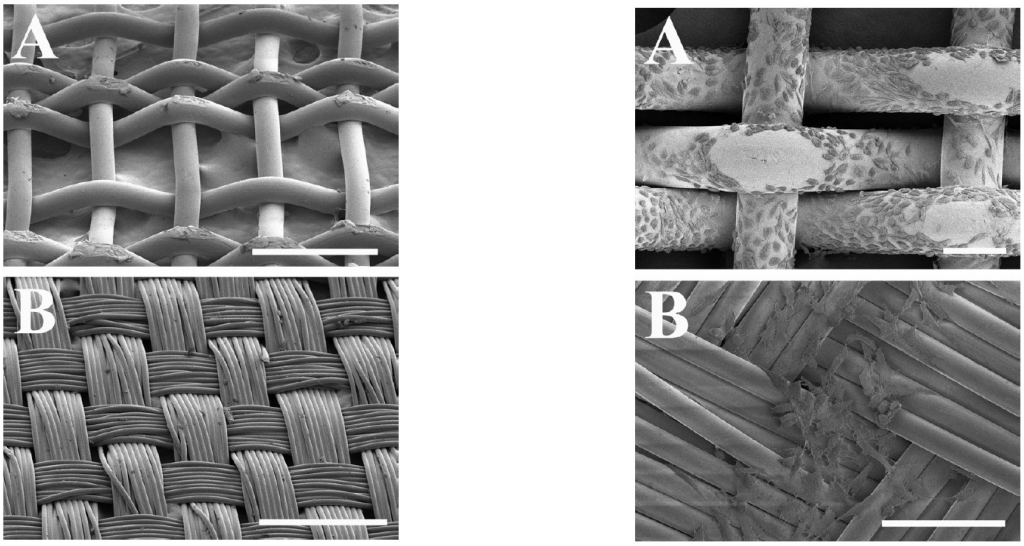

Figure 4.7. LEFT: SEM micrographs of woven PEEK (a) monofilament and (b) multifilament scaffold. Scale bar is 500 μm. RIGHT: SEM micrographs of fibroblasts on (a) PEEK monofilament and (b) multifilament scaffolds on day 8 of culture. Scale bar is 100 μm [141].

Considering common issues between surgical meshes and cranioplasty mesh implants, the requirement for better understanding between mesh design (weave pattern, porosity/open areas) and resulting properties is apparent. A mesh with appropriate material, tailored design and mechanical properties compatible with human body tissue could be promising as a true biocompatible device.

4.6. Hydroxyapatite (HA) coating process for biomedical implants

4.6.1. Main coating processes

Ceramic coatings were initially introduced as protective coatings, mostly for bulk metals or substrates [14,96]. These thin coatings have all the characteristics of ceramic, but are more flexible than bulk ceramics, which can solve fragility issues. The coating usually has good adhesion to different substrates and can be manufactured with different procedures.

There are several methods to deposit HA coating on a substrate: electrophoretic deposition (EPD), electrochemical deposition, pulsed laser deposition (PLD), hot isostatic pressing, plasma spraying, biomimetic coating, sputter coating, spin coating, and sol-gel deposition [136]. EPD is a material coating technique in which charged particles in a stable colloidal suspension are deposited on an oppositely charged conductive substrate, by moving through the solution due to an electric field [142]. Electrocoating, anodic electrodeposition, cathodic electrodeposition, and electrophoretic coating (electrophoretic painting) are specific industrial processes under the EPD category [143]. This technique needs high sintering temperatures and creating crack-free coatings is a challenge as the coating thickness ranges from 0.1 to 2.0 mm [144].

Electrochemical deposition is a coating process in which a thin metal layer, derived from a solution, contains the metal ions or chemical complex on a conductive substrate [145]. The main disadvantage of the process is its very low deposition rate, a few angstroms per minute [146].

PLD is a physical vapor deposition (PVD) technique, in which a laser is used as a source for material vaporization. The laser has high power density and narrow frequency bandwidth, and the technique is used when any other techniques cannot create a film on the substrate [147]. Plasma spray coating process uses high temperature in which the material powder is injected into a plasma flame. The material melts around 10,000 K (9,726.85 ^{o}C) and is sprayed on the surface of the

substrate [148]. Sputter coating is another type of PVD, in which the sputtering cathode is electrically charged, and targeted by plasma to eject material from the cathode's surface [149]. Hot isostatic pressing operates at high temperature, high pressure and low strain rate to create a compact material from powder metallurgy [150]. All these techniques require high temperatures, which increases manufacturing costs. In addition, they are not suitable for polymeric substrates with generally low melting or glass transition temperatures (< 200 ^{o}C) [118,151].

Biomimetic coating is a technique for specific coating of bone chemicals on an implant, in which the latter is soaked in simulated body fluid (SBF) after surface preparation. The process is lengthy and typically takes three weeks [152].

Sol-gel process is a wet chemical process, in which a colloidal solution (sol) is made by adding elemental precursors into a solvent. The sol transforms to gel phase after solvent evaporation. Thus, in the sol-gel coating technique, sol is used for the coating, while gel is formed by solvent evaporation at different temperatures. The coated substrates undergo calcification after the coating to enhance hardness, adhesion, and stability of the coating. Spin coating is a type of sol-gel coating, which is used to cover the top surface of flat substrates by centrifugal force [96,134,153,154]. The main drawback of this process is that it can only cover one side of the substrate at a time. The dip-coating and drop casting processes are other types of sol-gel coating techniques. In their case, the whole substrate can be coated by soaking it in the sol for various durations. Unlike spin coating, dip-coating and drop casting are suitable for substrates with complex geometries. They are inexpensive, low processing temperature methods leading to good adhesion for substrates made from a range of materials (metals and polymers). Dip-coating is better suited than drop casting to achieve superior surface uniformity and multi-layer coating at different

temperatures. It can create thin coating thickness from hundreds of nanometers to a few millimeters [134,135,155].

4.6.2. HA-coated mesh scaffolds

As previously mentioned, HA is commonly used as a coating on implants to promote osteoinduction and adhesion to nearby tissues. Coating parameters (e.g., solution concentration, number of layers) are expected to affect coating coverage and morphology [156], especially for mesh or porous substrates. For instance, HA coating has been used on various cellulose-based mats and cellulose nanofibers to demonstrate their potential for bone regeneration [123,157]. Figure 4.8 shows examples of HA coating for two types of cellulose mats, for which coating solution affected morphology. However, there are limited studies on HA coating coverage and its effect on porosity for low cost, low temperature coating methods on mesh scaffolds. Additionally, it is expected HA fillers incorporated into the bulk substrate (usually a polymer) can reduce mechanical properties above a certain wt % [158], but the effect of HA coating on porous structures is not widely investigated, especially for various mesh patterns, such as monofilament weaves, multifilament fabrics, and mats.

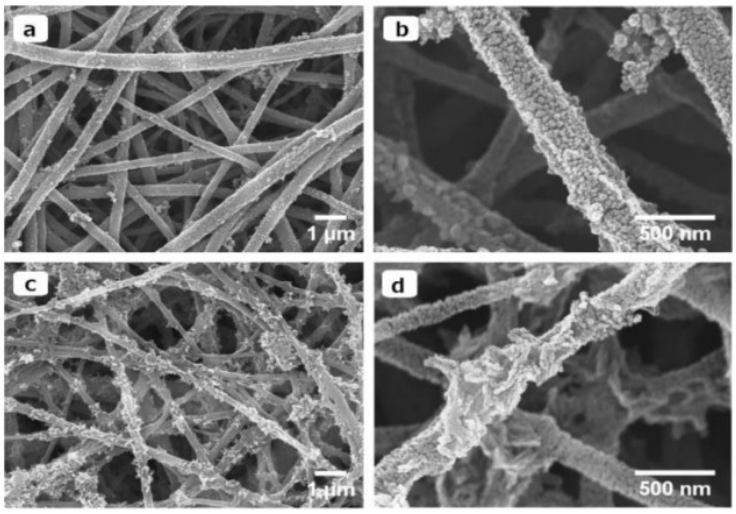

Figure 4.8. FE-SEM images of HA coating on nanofibers (a, b) cellulose and (c, d) CMC (carboxy methyl cellulose) soaked in 1.3 M NaOH [123].

4.7. Characterization methods for cranioplasty implants

4.7.1. Chemical properties

X-ray diffraction spectroscopy (XRD) is a technique in materials science to determine the crystallographic structure of a material. The material is subjected to X-rays, then the diffraction angle and intensity of each scattered ray are measured by the machine. For powder of hydroxyapatite, XRD is a better technique because it can determine exactly the plane indices and the crystal structure of the material, as well as any intermediate phases or compounds [159–161].

Transmission electron microscopy (TEM) can be used to determine the crystal structure, atomic planes' distance, and relative diffraction pattern of HA powders. This technique can show crystal structure size and shape, atomic plane arrangements and coordinates visually [162–164].

Energy dispersive X-ray spectroscopy (EDX) in field emission electron microscopy (FE-SEM) is another technique to be applied on the surface of the substrate or coating under FE-SEM microscope. It can investigate and confirm the existence of most elements in the periodic table. The analytical results can be reported as elemental analysis, point analysis, or mapping

distribution. It can be used to distinguish and study unknown compounds. For hydroxyapatite coating, this technique is mostly used to investigate or confirm uniform elemental distribution in the coating.

4.7.2. Mechanical properties

Tensile strength or compression strength of hydroxyapatite bulk materials can be measured by general tensile or compression test, according to ASTM D638 IV [165]. The adhesion of calcium phosphate or hydroxyapatite coating on any substrate can be determined according to ASTM F1147 [166], which is a standard test method for tension testing of calcium phosphate and metallic coatings. Porosity percentage measurements may be acquired from optical microscopy images or difference in sample's occupied liquid volume [159].

The coating hardness shows the resistance of the coating to surface deformation and stiffness. Indentation tests can be done to measure coated or uncoated surface hardness. Nanoindentation hardness tests can also be used for specimens for which the hardness cannot be measured by general indentation tests because of low coating thickness, or specimen size. Related elastic modulus can be calculated based on Oliver-Pharr method from load-indentation curves [167].

4.7.3. Morphology and structure

Microscopy techniques and imaging provide specimen surface morphology and structure. Optical microscopy is used for general observation while scanning electron microscope (SEM) and FE-SEM presents more detailed images [98,159,167]. Coating thickness, surface topography, crack, porosity, quality of coating adhesion, and all detailed surface properties can be investigated with FE-SEM, in two different imaging modes with high resolution. Secondary electron (SE)

imaging mode is used to present surface topography, while backscatter electron mode (BSE) is used to distinguish between various chemical structures on the specimen.

4.7.4. Electrochemical properties

Corrosion behavior and coating protection is studied by electrochemical measurements. Potentiodynamic polarization measurement is used to determine the corrosion potential and corrosion current for coated and uncoated samples. Electrochemical impedence spectroscopy (EIS) with bode and Nyquist plots analyze the coating protection of specimen by means of coating corrosion resistance. An equivalent electrical circuit model should be developed for each coated sample to show the outline of protection [6].

4.7.5. Biocompatibility

Biocompatibility and biocorrosion can be determined in various ways. Degradation can be measured via soaking in human body simulated solutions, such as Hank's balanced salt solution or simulated body fluid (SBF), at 37 °C for various durations [98,168]. Observation with optical microscope to find any defect or change in morphology and structure after soaking of uncoated or coated specimen is a method to assess degradation. Another test is to weigh samples before and after soaking and measure the degradation rate. Swelling ratio is another test to examine water absorbent capacity of coated and uncoated samples, after soaking in SBF for various times at human body temperature [159]. The samples should be weighed before and after immersion. The difference between these two tests is that the reduction in sample weight is measured in degradation, while the increase of weight is measured in swelling ratio. Another difference is the test duration, which is about a week for degradation tests, but up to 90 minutes for swelling ratio.

Cell culture is a test to investigate the reaction of human cells to the samples [169–172]. Cytotoxicity is a cell viability measurement in which samples toxicity to cells is measured in terms

of cell viability after various periods of human cells in contact with coated or uncoated samples. Cell proliferation and growth can show the capability of samples to be accepted by human cells as a growing substrate. The test depends on the results of cell number measurements after various times and optical microscopy images. Cell differentiation shows the capability of samples to provide a human tissue like substrate for cells to transform from one type to another type by adding relative serum. Immunohistochemistry test is based on immunofluorescence imaging of the interaction between osteogenesis differentiated cells and fluorescence antibodies. It shows the progress of osteoblastic differentiation versus time.

FE-SEM imaging of fixed samples after 21 days of osteogenesis cell culture can provide the coverage and morphology of the coated and uncoated samples. TEM imaging of harvested cells and tissue of the samples can prove the existence of different cell types, differentiated and non-differentiated ones, on the sample.

4.8. Human cell behavior on orthopedic implants

This section provides a brief summary about bone cells and their bonding mechanisms to implants.

4.8.1. Bone cells and matrix

Bone is a mineralized connective tissue, which includes four types of cells: 1) osteoblasts, 2) osteocytes, 3) osteoclasts, and 4) bone lining cells. It is a dynamic organ, which is continuously resorbed by osteoclasts and reformed by osteoblasts. The replacement of old bone by new bone is called bone remodeling, which is required for fracture healing, skeleton adoption to mechanical use, and calcium homeostasis. Bone remodeling has three steps: 1) bone resorption by osteoclasts, 2) transition from resorption to new bone formation, and 3) bone formation by osteoblasts [173].

Osteoblastic differentiation in cell culture starts from mesenchymal progenitor, while osteoclastic differentiation initiates from hematopoietic progenitor (Figure 4.9).

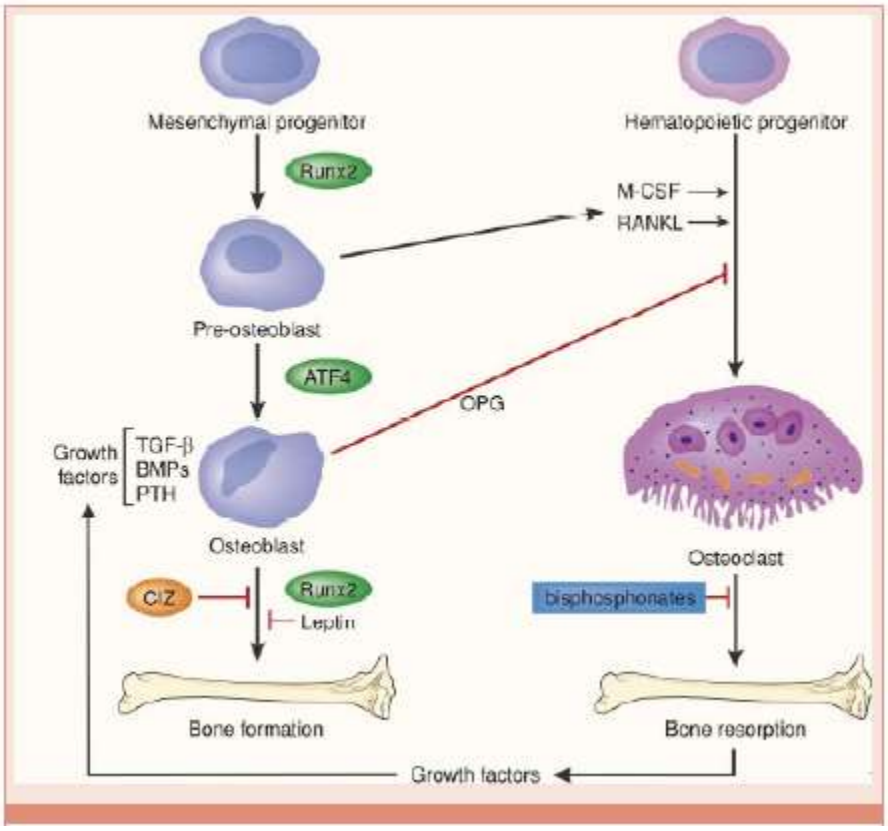

Figure 4.9. Bone formation, remodeling and repair from two different progenitor [174,175].

Osteoblasts are crucial for bone formation. They are made from cuboidal cells located on the bone surface and consist of 4 to 6% of the total existing bone cells. Osteoblasts secrete the osteoid toward the bone matrix. The differentiation process from osteoprogenitor cell to osteoblast needs specific gene secretion. These gene expressions include Runtrelated transcription factors 2,Distal-less homeobox 5 (Dlx5), and osterix (Osx) for osteoblast differentiation. The most important gene among those are Runx2, which upregulates osteoblast-related genes, such as ColIA1, ALP, BSP, BGLAP, and OCN. With an increase of Runx2 and CollA1, osteoblasts go through a proliferation phase. They show alkaline phosphatase (ALP) activity, which turns them into preosteoblasts. Mature osteoblasts are formed once there is an increase in the expression of

Osx and secretion of bone matrix proteins, such as osteocalcin (OCN), bone sialoprotein (BSP) I/II, and collagen type I [173–175].

Bone matrix synthesis occurs in two main steps: 1) deposition of organic matrix, and 2) mineralization. Secretion of type I collagen is mainly responsible for organic matrix deposition. Afterwards, mineralization of bone matrix takes place into two phases: 1) vesicular and 2) fibrillar phases [173–175].

In the vesicular phase, apical membrane domain in osteoblasts releases portions of matrix vesicles into the newly formed bone matrix. Osteoblasts bind to proteoglycans and other organic components in the new bone matrix. On the other hand, sulphated proteoglycans have negative ion charges. They immobilize calcium ions in the matrix vesicles. Therefore, when osteoblasts secrete enzymes that degrade the proteoglycans, the calcium ions can be released from the proteoglycans and move to the calcium channels existing in the matrix vesicles membrane. These calcium channels are formed by proteins called annexins [173–175].

Osteoblasts also secrete alkaline phosphatase (ALP), which can degrade phosphate-containing compounds and release them inside the matrix vesicles. Then, hydroxyapatite crystals are formed by the reaction between the phosphate and calcium ions inside the vesicles. Supersaturation of calcium and phosphate ions inside the matrix vesicles tends to break the calcium phosphate crystal structure. Thus, hydroxyapatite crystals released and distribute to the surrounding matrix. The process is called fibrillar phase [173–175].

Bone lining cells are flat shaped osteoblasts that cover the bone surfaces, without bone resorption or formation. The nuclear profile is thin and flat and the cytoplasm enlarged along the bone surface in bone lining cells.

Osteocytes are the main portion of total bone cells (90-95%) and can live up to 25 years. The osteocytes with a dendritic morphology are located within lacunae enclosed by mineralized bone matrix. Through osteoblast differentiation (Figure 4.9), osteocytes are derived from stem cells lineage beginning with a mesenchymal progenitor. When the bone formation cycle is complete, a subpopulation of osteoblasts transformed to osteocytes located in the bone matrix. This process includes morphological and ultrastructural changes such as the reduction is the size of round osteoblast [173–175].

Mononuclear cells of the hematopoietic stem cell lineage can differentiate to multinucleated cells under the influence of several factors. The multinucleated cells are osteoclasts, which are responsible for bone resorption. A visual summary of bone cells and matrix formation is provided in Figure 4.10.

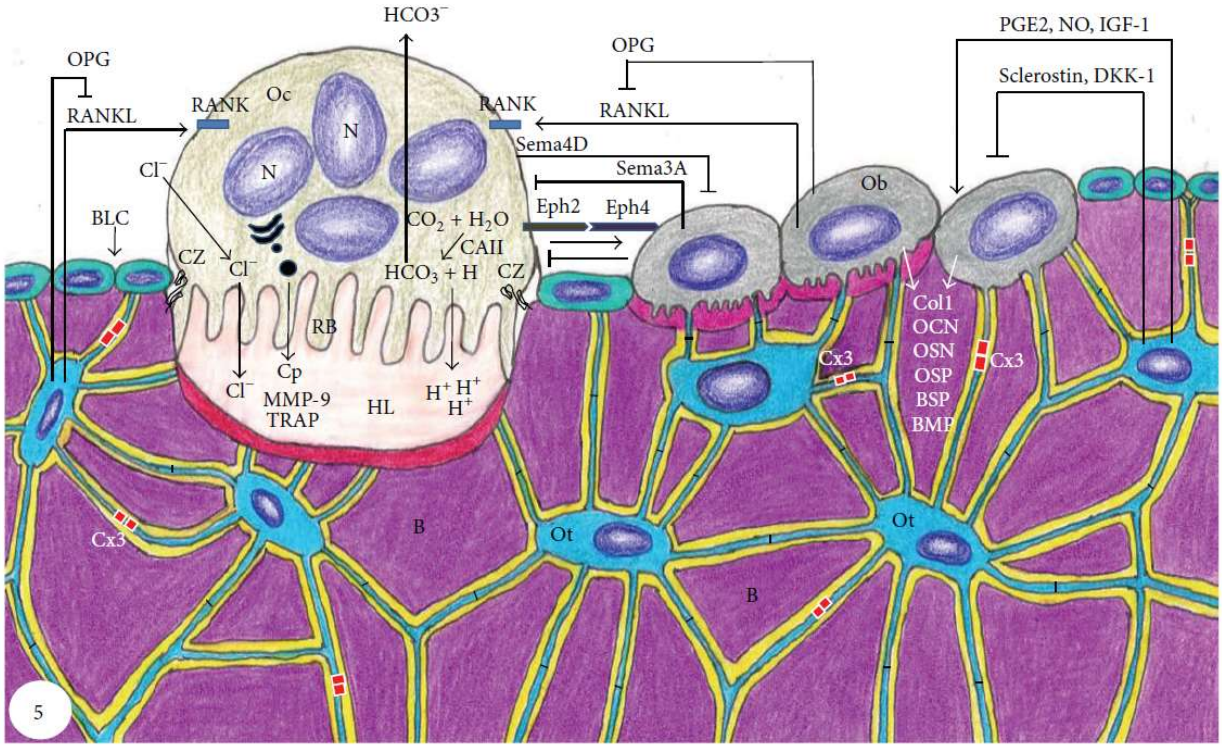

Figure 4.10. Schematic summary of bone tissue showing bone cells, bone matrix, and bone proteins. The parts of the image used in this research are: osteoblast cell (Ob), collagenous (Col1) and noncollagenous proteins such as osteocalcin (OCN) and bone sialoprotein (BSP) related to Runx2, noncollagenous protein osteopontin (OSP), Osteocytes (Ot) are located within lacunae surrounded by mineralized bone matrix (B), bone lining cells (BLC) on bone surface [173].

4.8.2. Implant-bone tissue bonding mechanisms

Although metallic biomaterials, mainly titanium and its alloys, possess biomechanical match with nearby bone tissues, they are bioinert, which shows no direct chemical bonding with the surrounding bone tissue [176]. Polymeric materials as bone implants may not be tough or strong enough, compared to natural bone tissue. Thus, they may suffer from poor bonding with the surrounding bone tissue due to high differences in biomechanical properties [177]. Calcium phosphate ceramics show good bonding to natural bone, even as bulk implants or coating on a substrate. Among all of them, HA coatings have the most similarity with human bone chemical structure. As the bioceramic replaces the bone defect in the human body, there are four different

types of ceramic-tissue bonding steps after implantation: 1) morphological fixation, 2) biological fixation, 3) bioactive fixation, and 4) resorption [82].

Morphological fixation is the attachment of ceramic implant to the nearby tissue surface via bone growth. The ceramic should be nonporous, inert, and dense to have this type of attachment. Biological fixation is the kind of attachment for porous and inert materials, in which the implant is mechanically attached to the bone or surrounding tissue, by screws, pins, or fixators. In bioactive fixation, the dense, nonporous, and bioactive ceramic implant has chemical bonding with the bone. Lastly, in the resorption process, the resorbable ceramic slowly degrades in the body and is replaced by natural bone. Knowing the various types of bone-ceramic implant attachments and their outcomes can help to design more biocompatible implants for cranioplasty [81,82].

Various types of stem cells, such as human adipose-derived stem cells (ASCs), mesenchymal stem cells (MSCs), and muscle-derived stem cells (MDSCs) are used in bone tissue engineering for osteogenic differentiation. Implant's properties affect the stimuli factor in cell differentiation. Surface chemical structure, surface roughness, and surface topography are three parameters affecting cell adhesion, proliferation, and differentiation.

Related to surface chemistry, surface charge, ionic environment, and solubility of substrate or coating can affect protein adsorption. For example, hydroxyl (-OH) on HA surface can increase the binding empathy with $\alpha_5\beta_1$ integrin, which affects the fibronectin structure. Also, hydrophilic OH provides a supplementary role for proteins (talin, a-actinin, paxillin, and tyrosine-phosphorylated) related to the cell adhesion. It has been observed for some metal ions, such as Zn2+ and Mg2+, cell proliferation and differentiation increased in presence of ions in silicon based bioceramics and TiO_2 coatings.

Surface roughness is related to the grain size and nanoparticle size. Literature shows that nanoscale or nanophase HA with grain size about 400 nm have higher protein adsorption of albumin, collagen and vitronectin, than the flat surface with a grain size of at least 1 μm. However, the effect of cell surface roughness on cell adhesion is not clear. Surface topography results in different cell behavior. Topography affects cell adhesion and alignment on the surface, which defines "contact guidance" of cells. "Contact guidance" means cell alignment on an isotropic surface which guide cells to elongate along or through ridge axes [82]". Cell shape depends on the cell alignment and can regulate cell differentiation pathways. It has been proven that microporosity promotes cell adhesion due to cytoplasmic extension in osteogenic differentiation. The results of one study showed osteoblasts were absorbed by microporous HA and nanostructures can also enhance cell proliferation. Cell migration was also affected by surface topography, but the effect cannot be determined clearly as cell migration relates to several different factors. As cell differentiation depends on protein adsorption and protein adsorption is higher in microporous structure (because of higher surface area), topography can affect cell differentiation too [82].

Knowing the chemical and physical parameters affecting cell adhesion, proliferation, and differentiation, investigating the regulatory mechanisms of development and function of bone could help to understand the mechanism of formation bone cells and extracellular matrix on the implant.

4.9. Summary of literature review and knowledge gaps

Various accidents can lead to head injuries and traumatic brain injuries, Those increase the number of patients who need cranial surgery. Cranioplasty is a follow up surgery for decompressive craniectomy, to replace removed bone part with bone graft or synthetic implants. Metallic, polymeric, ceramic, and composite biomaterials are used as cranioplasty implants.

Alongside biocompatibility of the implant, bone formation and connection with surrounding tissue to create a uniform structure under the skin are one of the most important properties required from cranial implants. The main disadvantage for metallic and polymeric biomaterials is they are bioinert and generally have a lack of bonding with enclosed bone tissue by themselves. Although ceramic implants can chemically bond with bone and induce bone formation, they are brittle which limits their application as bone implants.

This literature review highlighted that: 1) woven meshes or fabrics have potential for implant and bone repair applications, and they possess additional benefits (over bulk, custom-designed implants), such as flexibility and customizability, and 2) HA is commonly used as a coating on implants to promote osteoinduction and adhesion to nearby tissues. Therefore, mesh composite scaffolds with tailored HA coating is a promising research direction for which several topics haven not been investigated yet. Three main research gaps were identified regarding coating process parameters and application to mesh substrate materials, as summarized below:

1. The influence of HA coating process parameters (e.g., HA solution, coating technique and drying temperature, number of layers) on implant's performance (e.g., chemical composition, morphology, HA coverage, biocompatibility, etc) is not well documented. Further studies on woven mesh substrates need to be performed to understand the effect of coating parameters on resulting implant's characteristics and properties.
2. Similarly, the effect of substrate design characteristics (i.e., mesh size, open area/porosity, material) on implant's performance is not well understood, coupled with HA coating process parameters, especially for HA-coated woven mesh substrates. For instance, there is no detailed investigation on bone cell and matrix formation with complete coverage on both sides of

cranial implants. A better understanding of mesh or fabric characteristics could lead to design guidelines for customized woven substrates, also useful for 3D printed design.

3. Finally, there is a lack of research on mechanical behavior of HA-coated woven mesh substrates, as most studies consider HA-filled polymeric substrates. HA coating may increase open areas coverage and this could affect mechanical behavior of the mesh or fabric specimens.

Chapter 5 . Synthesis and Characterization of Hydroxyapatite Coatings on Metal Mesh Substrates

5.1. Introduction

This study aims to design flexible, biocompatible composite implants by using a metal mesh as substrate and hydroxyapatite coating as bone regenerative stimulant derived from a simple sol−gel method. It is expected that a thin HA layer coated on both sides of a metallic mesh substrate can improve bone regeneration by forming a 3-dimensional (3D), through the thickness extracellular matrix (ECM) network, while protecting the implant from losing ions over time. Experiments were carried out to understand the effect of the following parameters on implant's performance (i.e., coating microstructure and adhesion, stiffness, hardness, and electrochemical behavior): (1) sol−gel method (HA solution concentration, dip-coating and drop casting, and number of HA layers), (2) substrate material (titanium and stainless steel), and (3) substrate mesh characteristics (mesh size, open area and weave pattern). Although stainless steel implants are not commonly in use today, they have potential as coated biocompatible materials, as their regeneration time is higher than titanium or titanium alloys because they can possess a more stable passive layer [6,96]. Mesh characteristics were expected to affect HA coating and ECM coverage based on open areas, mesh size, and weave pattern.

Mechanical testing was performed through nanoindentation on the flexible HA/metal mesh samples, followed by biocompatibility tests to observe adipose-derived stem cells (ASCs) attachment, proliferation and osteogenic differentiation. Electrochemical behavior and protective effect of HA coating were assessed through potentiodynamic polarization and impedance

This chapter was previously published as A. Naderi, B. Zhang, J.A. Belgodere, K. Sunder, G. Palardy, Improved Biocompatible, Flexible Mesh Composites for Implant Applications via Hydroxyapatite Coating with Potential for 3-Dimensional Extracellular Matrix Network and Bone Regeneration, ACS Appl. Mater. Interfaces. 13 (2021) 26824–26840. doi:10.1021/acsami.1c09034. https://pubs.acs.org/doi/abs/10.1021/acsami.1c09034

spectroscopy tests. According to the outcomes of this study, HA-coated titanium grade 1 showed the best overall performance as a potential cranioplasty implant, but HA-coated stainless steel with the finest mesh size could constitute an adequate alternative based on electrochemical and morphology results.

5.2. Materials and methods

5.2.1. Materials

Potassium dihydrogen phosphate EMSURE ISO (KH_2PO_4) was supplied by Merck (Darmstadt, Germany); calcium nitrate tetrahydrate ≥99.0% ($Ca(NO_3)_2.4H_2O$), ammonium hydroxide solution, and ASC reagent 28.0−30.0% NH_3 basis (NH_4OH) were purchased from Sigma-Aldrich (USA). Technical grade distilled water was purchased from ChemWorld (USA). Acetone AR ACS (C_3H_6O) was supplied by Macron Fine Chemicals, Avantor (USA). Ethyl alcohol, 95% denatured lab grade (C_2H_5OH), was bought from Aldon Company (USA).

Two mesh substrate materials (stainless steel and titanium), two wire diameters, and two mesh sizes (materials and mesh dimensions were selected based on literature review presented in Chapter 4) were investigated. Stainless steel (ss) 304 and 316 mesh cloths, plain weave with 0.1 and 0.04 mm wire diameter, were purchased from McMaster-Carr (USA). The mesh sizes were 100 (i.e., 100 openings per 25.4 mm) and 200 (i.e., 200 openings per 25.4 mm) with 30% and 46% open area, respectively. Titanium mesh grade 1, twill weave with 0.1 mm wire diameter (mesh size 100), was supplied from Stanford Advanced Materials (USA). White titanium mesh (titanium + titanium oxide, brookite), twill weave with 0.1 mm wire diameter (mesh size 100), was acquired from Deze Wire (China). These mesh sizes and wire diameters were selected because of their flexibility and ease of cutting with scissors. All materials were used as received.

5.2.2. Synthesis of Hydroxyapatite Sol

Hydroxyapatite (HA) sols were prepared by mixing two precursor solutions to maintain Ca/P ratio as 1.67. First, 0.0167 mol of $Ca(NO_3)_2 \cdot 4H_2O$ [130] was dissolved in 50 mL of distilled water; 2.5 mL of NH_4OH was added dropwise to the solution to adjust pH around 12, while stirring for 30 min. Second, a solution was made by adding 0.01 mol of KH_2PO_4 in 50 mL of distilled water and stirred for 30 min. Then, the second solution was added to the first one dropwise while stirring for another hour. The sol preparation was held at room temperature. Finally, 100 mL of HA white sol (pH ≈ 9) kept in glass container at room temperature for a week.

This sol was used as general HA sol (GHA), referred to in the next paragraphs. A condensed HA sol (CHA) was derived from general HA sol. The general sol separated to transparent and white phases after aging for a week. The transparent solution was sucked by pipet to get a condensed HA white solution (pH ≈ 11).

5.2.3. Sol−Gel Coating Procedure and Samples Coding

Prior to coating, all samples were degreased by soaking in acetone, dried in air at room temperature for 5 min, and then, dried in an oven at 65 °C for 15 min. Each sol was sonicated for 15 min to get a homogeneous solution before the coating process. An area of 1.5 cm^2 on each substrate was coated by two dissimilar separate sol−gel processes to assess the best coating procedure. Samples with one, two, and three layers of coating were made to determine the effect of multilayered films on implants characterization.

Two coating procedures were investigated in this study: dip-coating and drop casting. For dip-coating sol−gel (withdrawn rate = 20 000 μm/min, immersion time = 10 s), the sol was general HA (GHA) for one group and condensed HA(CHA) for another group. For multilayer coating, the substrate was kept in air for 30 s between two immersions until reaching the desired number of

HA layers. For drop casting, a 1.5 cm^2 area, on each side of the substrate, was covered with GHA by eye dropper. The adhesion of the liquid sol was sufficient so that the sample could be flipped and the other side could be covered by sol as well. For multilayer coating, the substrate was dried in an oven for 1 h at 150 °C and cooled in the oven to room temperature between each coating until reaching the desired number of HA layers. All samples were dried at room temperature, 50% humidity, immediately after immersion, then calcined in an oven at 150 °C for 1 h. Samples for all characterization and biocompatibility tests were prepared at the same time. The samples were kept at room temperature, in Petri dish in a dark place.

For future reference in the subsequent sections of this chapter, sample coding was done in accordance with substrate material, mesh size, coating solution and procedure, and number of HA layers. Definition and examples are represented in Table 5.1.

Table 5.1. Samples coding with definition of terms used in this manuscript.

Sample code example	Substrate material	Mesh size	Coating solution and procedure	Number of layers
ss304.100.DC3 ss304.200.GS1	Stainless steel 304 (ss304)	100 200	DC (drop cast from GHA) GS (sol-gel dip-coating from GHA) CS (sol-gel dip-coating from CHA) b (uncoated bare substrate)	1, 2, 3
ss316.100.DC1 ss316.200.CS2	Stainless steel 316 (ss316)			
Tig1.100.GS2	Titanium grade 1 (Tig1)			
WTi.100.CS1 WTi.100.b	White titanium (WTi)			

5.2.4. Chemical Composition and Phase Analysis.

X-ray diffraction (XRD) patterns were obtained for HA powders derived from three methods: (1) from HA coating powders, collected from both sides of HA-coated titanium samples by scratching the coating off with a razor blade (coatings from GHA and CHA sols, dried in an

oven for 1 h at 150 °C); (2) from GHA sol dried at 700 °C in a glass beaker for 1 h to compare this data with literature and the coating powders from method 1; and (3) fromGHAsol after aging for 1.5 year to analyze the crystal structure and stability of the solution after a long storage time.

An X-ray diffractometer (PANalytical Empyrean) over 2θ range of 5−90° was used to determine crystal structure for all powders. The process operated at continuous CuKα radiation (λ = 0.1540598 nm) with a step size of 0.02°, generator voltage of 45 kV, and tube current of 40 mA.

Energy-dispersive X-ray spectroscopy (EDX) with field emission electron source (FEI QUANTA 3D FEG FIB/SEM) using an accelerating voltage of 20 kV in statistical imaging mode was used to determine Ca/P ratio in HA coating on substrate. HA crystallographic structure and the most brilliant plane spaces and indices were studied by high-resolution transmission electron microscopy (HR-TEM, JEOL JEM-2011) equipped with a bottom-mounted Gatan SC1000 CCD camera with an accelerating voltage of 200 kV.

5.2.5. Microstructure and Morphology

The morphology of HA coating on the mesh substrates was analyzed by focused ion beam (FIB) with a high-resolution field emission gun scanning electron microscope (FE-SEM, FEI QUANTA 3D FEG FIB/SEM) using an accelerating voltage of 5 and 20 kV. Images were also captured before and after polarization tests to determine the corrosive effects of simulated body fluid (SBF) [178]. Thickness of HA layers was measured from tilted images or cut sections made by FIB. Effect of coating method and number of HA layers on mesh coverage was further analyzed by quantifying the following: coverage of mesh wires (in % value with respect to total mesh area) and open mesh area (in % value with respect to total mesh area).

An image analysis software (Image J, National Institutes of Health) was used to calculate mesh coverage for three to five samples (n = 3−5) for each coating method/HA layer combination.

An example of image analysis with uncoated wire area and open mesh areas is shown in Figure 5.1.

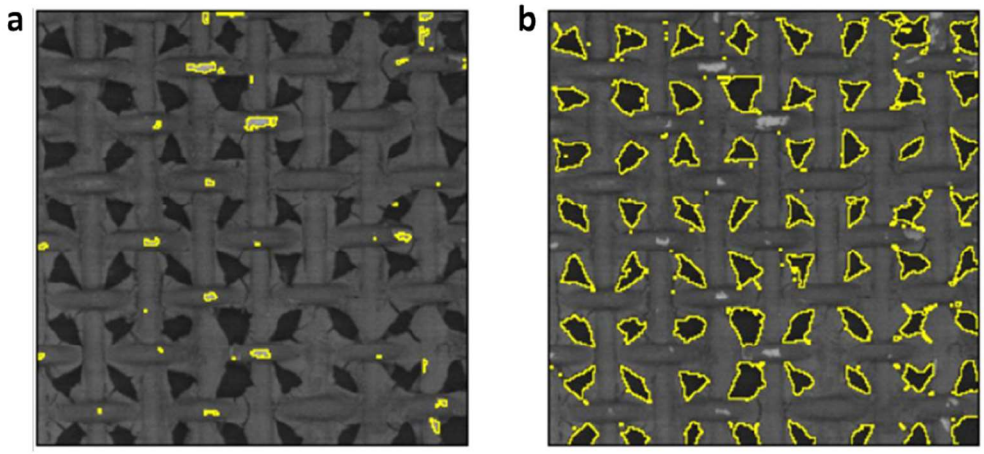

Figure 5.1. Example of image analysis to extract (a) uncoated wire area and (b) open mesh area (delineated in yellow). Mesh conditions: ss304 mesh size 200, coated by dip-coating with CHA solution and two HA layers.

5.2.6. Hardness and Modulus of Elasticity

To determine resistance to surface deformation and stiffness of HA coating on wires of the mesh substrates, nanoindentation hardness measurements were conducted on the top surface of the wires. After several preliminary trials, it was determined that samples with the thickest HA coating (DC3) were the most suitable to carry out nanoindentation tests, as it prevented the nanoindenter tip from slipping and drafting on the wires' curved surface. All samples were glued to a flat, hard surface before nanoindentation. The tests were also carried out on bare substrates as a reference. All hardness measurements were performed with a Nanoindenter XP system (MTS Systems Corp., Knoxville, TN), in a force-controlled mode with a maximum force of 10 mN and a force rate of 0.7 mN/s. For each sample, six testing points were collected, and the distance between each two adjacent points was set to 15 μm.

5.2.7. Electrochemical Behavior Analysis

To examine the corrosion behavior and the protective effect of HA coating of the chosen samples after the biocompatibility tests and to evaluate the differences between coated and uncoated samples in human body medium, potentiodynamic polarization measurements were performed.

A CHI 604C electrochemical workstation in simulated body fluid (SBF) [178] with a standard tree-electrode corrosion cell set up was used. HA-coated or uncoated sample with a surface area of 1 cm^2 was used as the working electrode, a platinum wire as the counter electrode and a saturated calomel electrode (SCE) as the reference electrode.

Polarization curves were assessed by sweeping the potential from −0.6 V_{SCE} to +0.6 V_{SCE} at a scanning rate of 1.67 mV/s at room temperature [153]. All samples were soaked in SBF solution around 1 h before potentiodynamic polarization tests to stabilize the open circuit potential (OCP). Electrochemical impedance spectroscopy (EIS) was performed to analyze the electrochemical behavior with low frequency of 0.01 Hz, high frequency of 10000 Hz, and an amplitude of 0.05 V. Nyquist and bode plots were sketched according to EIS results and an equivalent circuit was selected based on literature review of the same substrate material type (Ti or SS) [167]. All experiments were reported for three samples (n = 3) to minimize the error.

5.2.8. Statistical Analysis

In the results and discussion section, data are represented as the mean ± standard deviation (SD). Two-way analysis of variance (ANOVA), followed by Tukey's multiple comparison test, was used to compare HA and ECM coverage data at a significant level of $p < 0.05$. For biocompatibility test results, the difference between control groups and the samples (test group) was determined through two-tailed Student's t test at the significant level of $p < 0.05$. On the bar

graphs, because of the large number of different samples, the statistical significance of a limited number of pairs is indicated for clarity. Details regarding statistical analysis are provided in the figures' captions.

5.3. Results and discussion

5.3.1. Chemical composition and phase analysis

As explained in Section 2.4, HA powders were collected from both sides of HA-coated titanium samples by scratching the coating off with a razor blade. Different samples were scratched off for drop casting and dip-coating methods with GHA- and CHA-based coatings, dried in an oven for one hour at 150 °C. HA powder samples were also made from GHA sol at 700 °C for one hour in a glass beaker to compare this data with references for higher temperature calcination, and to confirm the lower temperature-made coating powders had the same crystal structure as higher temperature-made powders. A fourth powder type was made from GHA after aging for 1.5 year to analyze the crystal structure and stability of the solution after a long storage time.

X-ray diffraction patterns for all HA powders are shown in Figure 5.2. A pure crystalline hydroxyapatite phase is observed from the characteristic peaks for CHA powder, consistent with standard database (JCPDS 09-9432). For HA powders from both coated and aged GHA samples, diffraction patterns mostly show the peaks for crystalline pure HA, but also for decomposed compounds of HA, β-tricalcium phosphate (214, 217, 220) (β-TCP) and CaO (200). Characterization peaks for both powders are the same, which indicates stability of the general HA solution during long storage time (1.5 year). The diffraction pattern for GHA samples dried at 700 °C shows both pure hydroxyapatite and β-tricalcium phosphate (0210). It is observed that the structure for GHA powders made at 150 °C and 700 °C is the same, but differences about the direction of some β-TCP and CaO planes make them undetectable in XRD patterns. As the GHA

solution is calcium-deficient hydroxyapatite, which is unstable against thermal treatment with a pH ≈ 9, calcination induced decomposition of the structure into three different calcium phosphate phases: pure HA, β-TCP and CaO [160]. CHA solution was a precipitated solution and had a pH around 11, which is above 10 and preferable to produce pure HA, as observed in Figure 5.2 [179] . Since all samples were dried at temperatures lower than 1000 °C, β-tricalcium phosphate is most likely to be formed for powders from GHA sol [180]. Overall, crystal structure and characteristic peaks for powders collected from drop casting and dip-coating methods are the same. For the proposed research, no issue is expected with mixed structures of hydroxyapatite and β-tricalcium phosphate (biphasic hydroxyapatite) for bone regeneration purposes as tricalcium phosphate is a better material to stimulate bone growth [181].

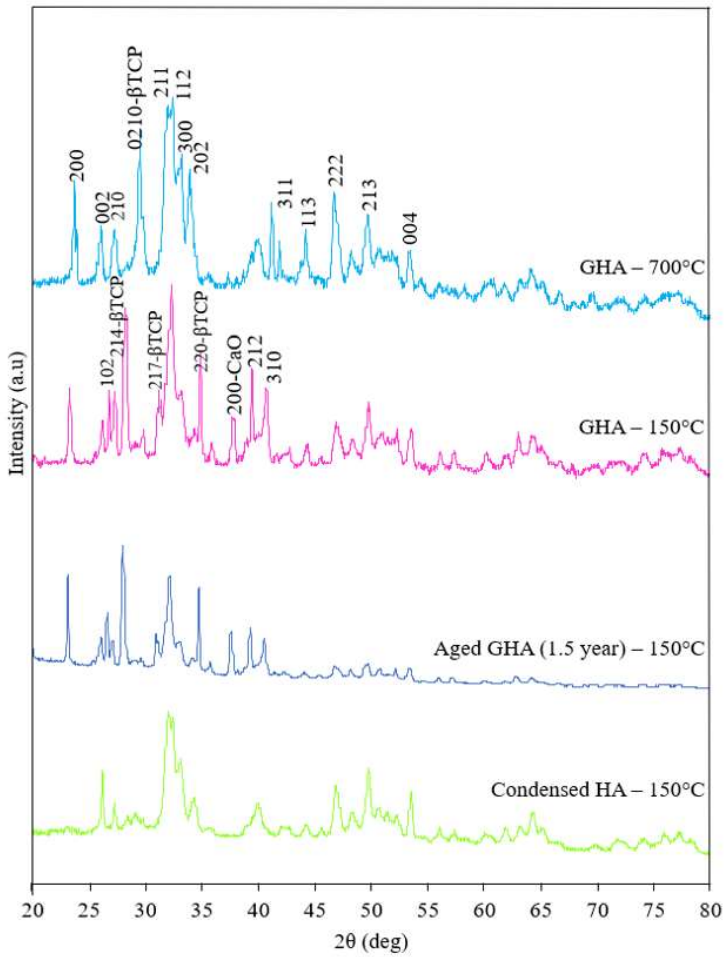

Figure 5.2**.** XRD patterns for the following powders (from top to bottom): general hydroxyapatite sol (GHA) dried at 700°C, scratched off coating powder made from GHA sol dried at 150°C, aged GHA sol (1.5 year old) dried at 150°C, and scratched off coating powder made from condensed hydroxyapatite sol (CHA) dried at 150°C.

EDX results for elemental distribution of Ca and P are presented in Figure 5.3a,b, respectively. The Ca/P was 1.67 for powders from CHA solution and 1.86 for powders from GHA. However, in GHA powders, there are three different compounds: HA, β-TCP and CaO. As those all contain calcium, it is difficult to find the accurate Ca/P ratio for HA in this powder. EDS mapping images for one layer HA coatings derived from GHA and CHA solutions by dip coating method on titanium grade 1 (Tig1) showed a homogenous dispersion of calcium (Figure 5.3a).

Figure 5.3c,d displayed the visible substrate (Tig1, pink colored areas) in mapping pictures, indicating uncoated areas.

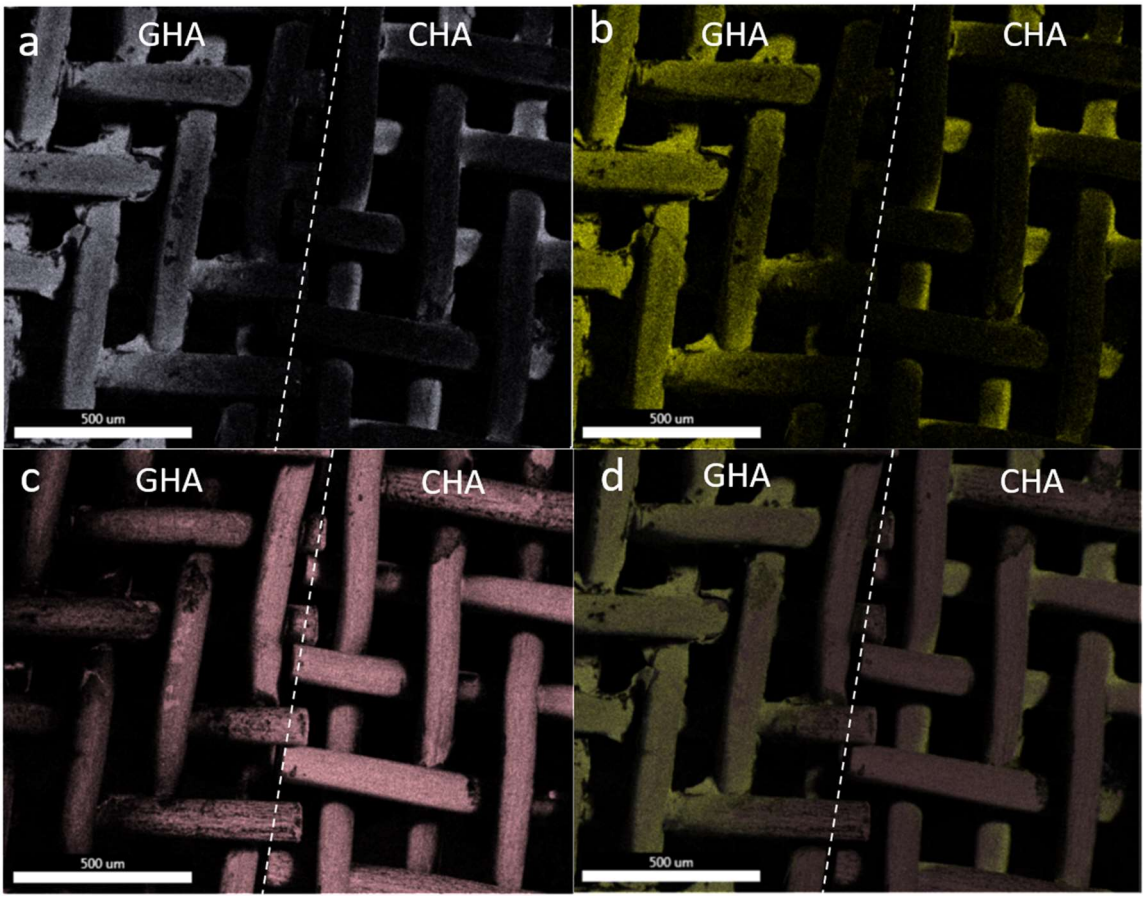

Figure 5.3**.** Representative FE-SEM mapping images (EDX) of elemental distribution for Ca and P in one layer HA coatings derived from GHA and CHA solutions by dip coating method, on titanium grade 1 (Tig1) mesh substrates: (a) Ca, (b) P, (c) Ti, and (d) merge mapping for GHA (left) and CHA (right). Scale bar is 500 µm.

HR-TEM pictures were captured to characterize the nano crystal shape of HA powders and interplanar spacing of the most intense reflections (Figure 5.4). Figure 5.4a,b show HA crystals in two different directions for GHA powder, with aged GHA in Figure 3c. HA nanorods are visible in Figure 3b,d with lengths from 30 nm to 50 nm and diameters from 10 nm to 15 nm. Figure 3e,f reveal the structure of GHA powder dried at 700 °C at two different magnitudes, which presents pure HA plane spaces equal to d = 0.81 nm (001) and d = 0.34 nm (002) [164]. Those planes were

observed for all powder samples. Different coating procedures and numbers of layers did not affect crystal structure, shape or most intense plane reflections.

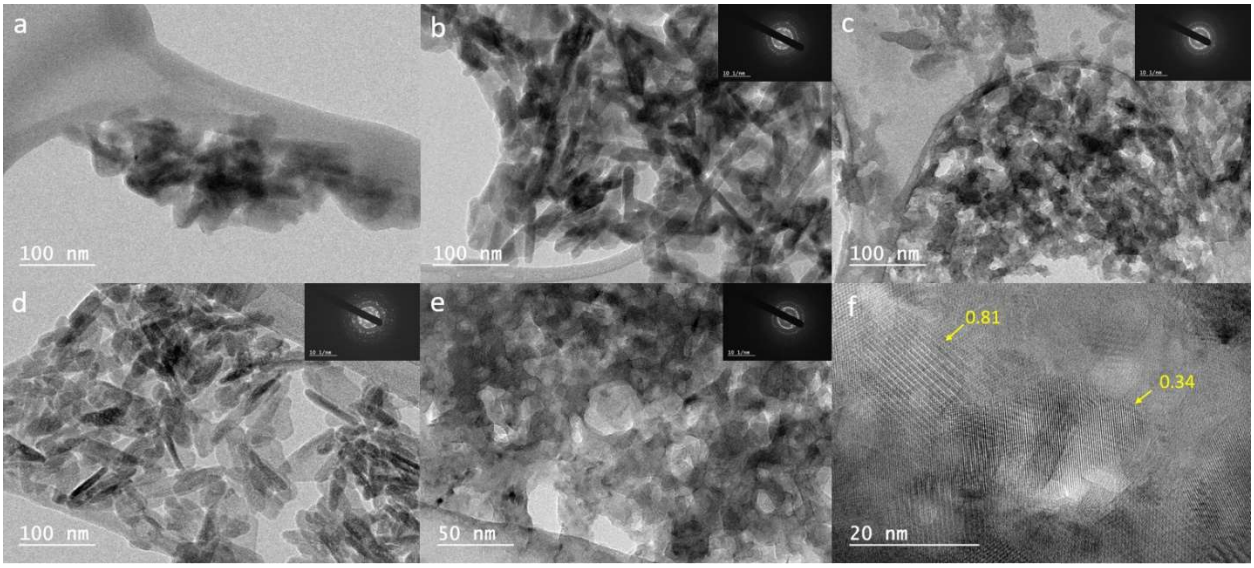

Figure 5.4**.** Representative HR-TEM images for coating powders (scratched off from substrate surface) derived from different sols, dried at various temperatures: (a, b) GHA, (c) aged (1.5 year) GHA, (d) CHA dried at 150°C, and (e, f) GHA dried at 700°C. Pure HA plane spaces of d = 0.81 nm (001) and d = 0.34 nm (002) are marked in (f). Scale bar is 100 nm for (a, b, c, d) and 50 nm for (e) and 20 nm for (f). Images in inset are related to diffraction patterns with a scale bar of 10 1/nm.

5.3.2. Microstructure and surface morphology

FE-SEM images were used to analyze the effect of substrate material, mesh size, number of HA layers, and coating solution and procedure on microstructure, uniformity and coverage of HA coating on the substrates (Figure 5.5 to Figure 5.7). Before investigating the effect of the coating procedure and number of HA layers in detail, coating quality for different substrate materials and mesh sizes was first qualitatively assessed for cracks and adhesion (Figure 5.5 and Figure 5.6). Representative FE-SEM images in back scatter and secondary electron modes (BSE and SE, respectively) were captured. However, as images in BSE mode helped differentiate between coating and substrate, as they both displayed similar gray scale in SE mode, they were

used for most observations and image analyses for all samples. A comparison between those two modes is shown in Figure 5.5a,b.

5.3.2.1. Effect of substrate material and weave pattern

The substrate material is a factor affecting adhesion and coverage of HA coating. Weaving pattern for mesh samples is another important factor impressing uniformity of coating on the surface and interface cohesion between coating and substrate. Examples of HA coating with three layers derived from drop casting method (DC3) are represented in Figure 5.5 as they are most representative for this discussion. The discussed pattern was observed for other coating solutions, procedures and number of layers on all materials. Figure 5.5b,c and Figure 5.6b show that stainless steel 304 and 316 with plain weave led to an overall more uniform coverage and adhesion of HA coating on different areas of the wire when compared to titanium samples with twill weave (Figure 5.5d,e and Figure 5.6c). It is expected that the different bending ratios of the wires in the two patterns (plain and twill weave for the same mesh size) impacted distortion and internal stresses in HA coating, leading to uncovered areas or interfacial gaps located, in particular, at the wire peaks on titanium mesh samples (yellow arrows in Figure 5.5d,e and gap in Figure 5.6c). Moreover, based on TiO_2 chemical structure and its tendency for physical or chemical bonding with calcium or phosphate ions in HA [182], adhesion of HA coating on pure titanium (Tig1) substrates is likely lower than titanium + titanium dioxide (WTi), as the HA coating completely covered some open areas in WTi samples, but not in Tig1 samples (Figure 5.5d,e). The microstructure of HA coating was similar in all samples, featuring a smooth appearance on the wires' surface, but with micro-cracks between wires or delamination seen on cross-sectional images (Figure 5.6). Overall, the microstructure of HA coating was not affected by weave pattern or substrate material.

5.3.2.2. Effect of mesh size

Regarding the effect of mesh size (100 and 200), higher mesh size (200 with wire diameter d = 0.04 mm for ss304 and ss316 substrates) led to better coverage compared to substrates with lower mesh size (100) (Figure 5.6b,c). Higher mesh size substrates have thinner wires, smaller holes, but overall more open area (46% vs 30%). It is expected the latter can promote solution's movement from one side to the other side of the substrate during coating, which leads to more contact between solution and wire's surface, resulting in more uniform coverage. The topography of the coating surface for mesh size 200 (smaller wire diameter) is smoother than mesh size 100 due to the overall flatter pattern: reduced wire bending at the junctions and smaller distance between wire peaks and valleys [183,184].

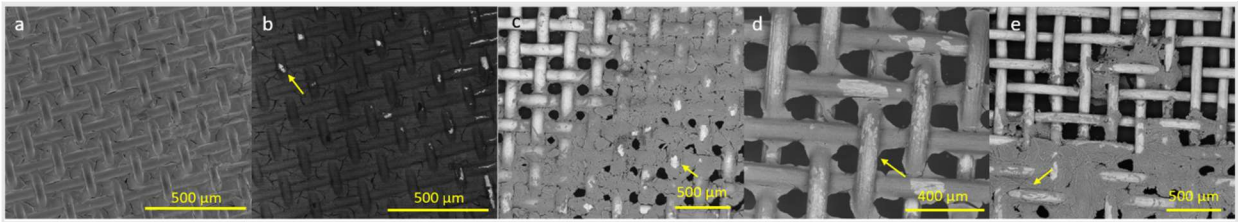

Figure 5.5**.** Representative FE-SEM images in secondary electron (SE) and backscatter electron (BSE) modes for examples of 3 layered HA coatings derived from drop casting method (DC3) on: (a) ss304.200 (SE), (b) ss304.200 (BSE), (c) ss304.100 (BSE), (d) Tig1.100 (BSE), (e) WTi.100 (BSE). Scale bar is 400 µm in (d) and 500 µm in the rest. Yellow arrows indicate wire peaks.

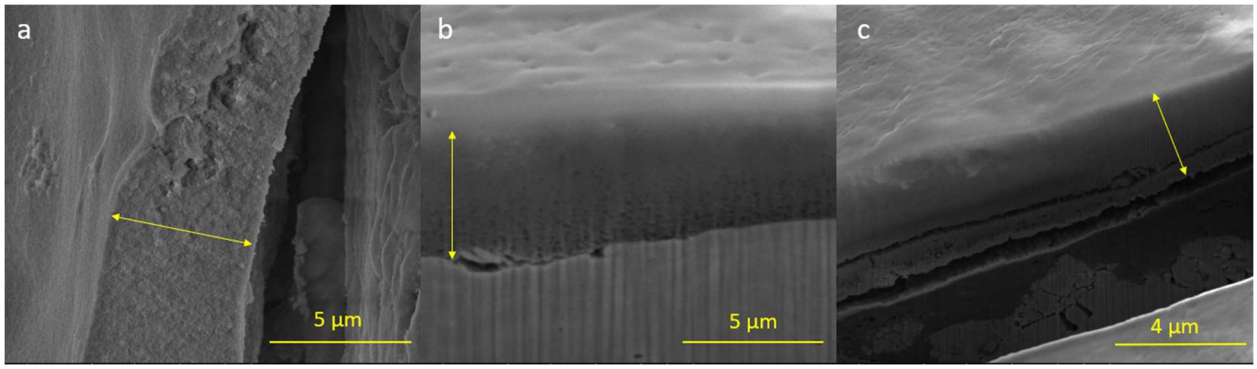

Figure 5.6**.** Representative FE-SEM (SE) images of delaminated HA coating and FIB cross-sections to measure thickness of HA coating with three layers derived from drop casting method on: (a) ss316.200, (b) ss316.100 (tilted at 52°) and (c) Tig1.100 (tilted at 52°). Yellow arrows indicate the HA coating. Scale bar is 5 µm in (a, b) and 4 µm in (c).

5.3.2.3. Coating thickness

Increasing the number of HA layers on the substrates increased coating thickness and improved coverage. However, it also multiplied cracking and delamination of HA coating, as thicker coating may crack and detach easier than thinner one. Table 5.2 summarizes the measured maximum thickness from the thickest coating (DC3 samples) on all substrate materials by FIB cross-section or coating delaminated edge in FE-SEM pictures (Figure 5.6). As the coating coverage was not uniform, the HA coating thickness on each substrate varied from none up to the reported maximum thickness. For stainless steel samples, the maximum thickness was 5.4 ± 0.9 µm, while it was 4.0 ± 0.6 µm for titanium grade 1 and 7.9 ± 0.9 µm for white titanium. The highest standard deviation value (0.9 µm) is related to the variations induced by the cylindrical shape of the wires, wire junctions and pattern waviness. All thickness values were in the same range as reported in the literature for sol-gel derived HA coating on different substrates (0.07 µm to 9 µm) [184]. The highest coating thickness value was obtained for white titanium, which contains titanium dioxide (TiO_2). As stated in Section 5.3.2.1, adhesion of HA on TiO_2 is higher than Ti [185], thus the higher thickness of HA layers on WTi samples.

Table 5.2. Thickness measurements (maximum values) based on FE-SEM pictures for all substrates with three layers of HA coating applied by drop casting method from GHA solution (average ± standard deviation, $n = 9$).

Sample code	ss304.100.DC3	ss304.200.DC3	ss316.100.DC3	ss316.200.DC3	Tig1.100.DC3	WTi.100.DC3
Thickness (µm)	5.4 ± 0.9	5.4 ± 0.9	5.4 ± 0.9	5.3 ± 0.6	4.0 ± 0.6	7.9 ± 0.9

5.3.2.4. Effect of coating solution, procedure, and number of HA layers

Figure 6 illustrates a representative summary of the effect of coating procedure, solution type and number of HA layers on mesh coverage for ss304 mesh size 200 substrates (ss304.200). For any constant mesh size, similar coverage behavior was observed for all other substrate materials (ss316, Tig1 and WTi). Figure 5.7j shows the average % area of coated mesh wires and % open mesh area for all conditions shown in Figure 5.7a-j.

GHA and CHA solutions exhibited different viscosities, which affected HA film coverage (Figure 5.7j) and uniformity on the substrates. CHA solution (CS row, Figure 5.7a-c) exhibited higher viscosity and consequently, the solution dragged the liquid on the substrate while the sample was moved out during the dip-coating process. Thus, overall, the coverage of the GHA solution (GS row, Figure 5.7d-f), which is above 50% area coverage on wires and less than 20% open areas (Figure 5.7j), was better than CHA (CS row) on all substrates with different materials and mesh sizes. The microstructure of the HA coating derived from various HA solutions was not significantly affected as their chemical composition and crystal structure are similar (see Section 3.1). The dip-coating process (CS and GS rows), compared to drop casting (DC row, Figure 5.7g-i), led to more uniform films and coverage on the wires, as this process is homogenous and controlled during the coating procedure. There was no excess solution on the substrates after the coating process or before drying. The drop casting process provided coatings with higher thickness values with micro-cracks as the excess solution remained on the substrates and was dried in the

oven. This led to high wire coverage with sealed holes in some areas (less than 1% open area with more than 52% wire coverage), while wires remained uncovered in other areas.

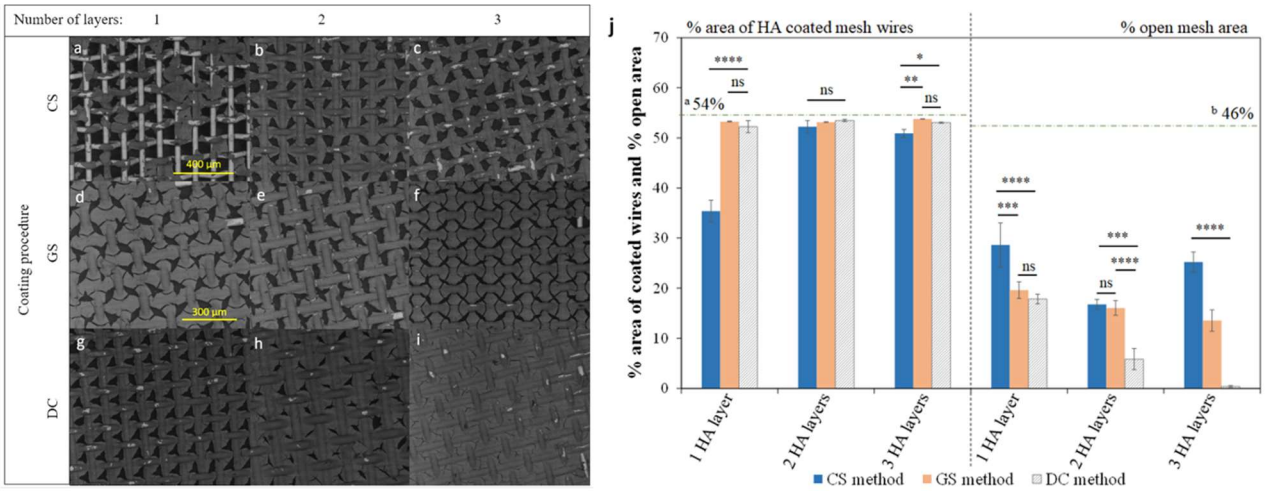

Figure 5.7. Representative FE-SEM (BSE) images for ss304.200 substrates with different numbers of HA layers, derived from different solutions (GHA, CHA) and procedures (CS, GS, DC). (a, b, c): CS – substrates coated by sol-gel dip-coating with CHA sol with 1, 2 and 3 HA layers; (d, e, f): GS – substrates coated by sol-gel dip-coating with GHA sol with 1, 2 and 3 HA layers; (g, h, i): DC – substrates coated by drop casting with GHA sol with 1, 2 and 3 HA layers. Scale bar is 400 µm in all except (d) and (e), which is 300 µm. (j) Corresponding average % area of HA-coated mesh wires and open mesh areas for all coating procedures and number of HA layers (compared to manufacturer's values, [a]54% and [b]46%). (ns: not significant, $*p < 0.05$, $***p < 0.001$, $****p < 0.0001$, $n = 3$).

By analyzing images of HA coating with various number of layers (1 to 3 in Figure 5.7), for the dip-coating process (CS and GS rows), it can be assumed that the first layer coverage depends on solution viscosity. The lower viscosity of the GHA solution led to higher coverage and drying in air for 30 s was long enough to set the layers (GS method in Figure 5.7j). For the CS coating procedure, coverage of wires and open areas after the second layer was improved. The second layer smoothed out any sections of the first layer that had not been set or bonded to the substrate. Wire coverage after the third layer remained similar for both methods, but open areas exhibited a significant difference (Figure 5.7j). GS3 samples in particular displayed a uniform HA coating pattern (Figure 5.7f). For the drop casting method (DC row), the samples were dried in

oven before adding the next layer. Adding second and third layers increased the thickness and coverage, until the layer was too thick and delaminated from the substrate. Micro-cracks mostly appeared at wire junctions due to thermal mismatch between substrate/coating and internal stress in the coating. Delamination occurred at the wire peaks, resulting from the coating internal tension related to the bent shape of the wires. In general, for all substrate materials, the highest coverage and thickness were obtained for DC3 samples, the most uniform coverage was observed for GS samples, and the lowest wire coverage was noted for samples CS1.

5.3.3. Hardness and modulus of elasticity

Hardness and modulus of elasticity are two important properties to determine mechanical performance of metal/ceramic implants. Modulus of elasticity of HA coating should be close to the modulus of natural skull bone (3.3 GPa to 6.0 GPa) for cranioplasty applications. In addition, hardness should be high enough to bear induced mechanical load after implantation [167,179].

Figure 5.8 and Table 5.3 show load-indentation curves for nanoindentation tests, as well as corresponding hardness and modulus of elasticity values. The inserting depth for bare substrates was around 500 nm, while it was more than 2500 nm for HA-coated titanium substrates and more than 1000 nm for HA-coated stainless steel substrates. Hardness values for HA-coated stainless steel substrates are higher than titanium ones as HA coating is more uniform (as seen in Figure 5b,c). The lowest hardness value (39.0 MPa) is more than double the highest value reported in the literature for HA coating on titanium substrates (17.5 MPa) [134]. Moduli of elasticity for all coated substrates were in the range of 2.2 GPa to 18.3 GPa, close to reported values for natural human skull bone (3.3 GPa to 6.0 GPa). On the other hand, the moduli of elasticity values for bare substrates were higher than natural bone. Thus, mesh substrates with HA coating are more similar to natural bone than bare metal ones. This is preferable to keep consistency between the implant

and the surrounding bone. High standard deviation values in Table 5.3 are related to the topography of the surface (cylindrical shape of wire) and the drift of the nanoindenter tip. Flat surfaces generally present fewer variations in measurements.

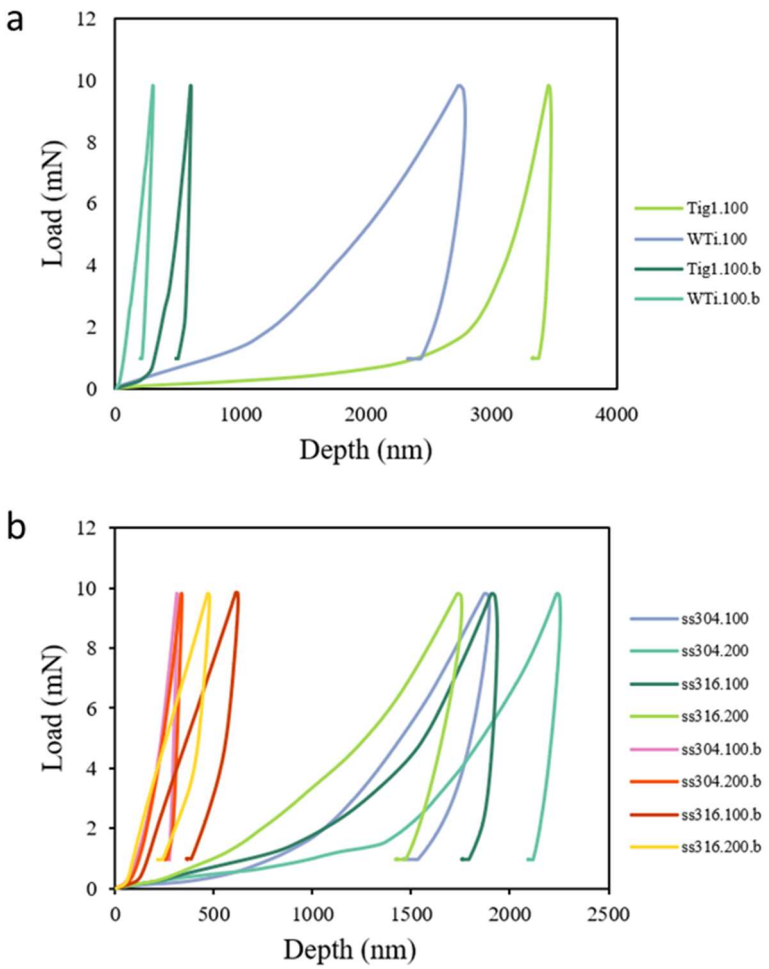

Figure 5.8**.** Load-indentation curves and release patterns for HA-coated samples (DC3) and bare substrates (.b) for (a) titanium and (b) stainless steel substrates.

Table 5.3. Hardness and modulus of elasticity calculated from Fig. 7 for HA-coated (DC3) and bare substrates (average ± standard deviation).

Sample code (HA coated, DC3)	Hardness (MPa)	Modulus of elasticity (GPa)	Sample code (bare substrates)	Hardness (GPa)	Modulus of elasticity (GPa)
ss304.100	77.8 ± 35.5	3.7 ± 1.2	ss304.100.b	4.8 ± 0.6	137 ± 16.8
ss304.200	64.4 ± 31.4	5.9 ± 2.1	ss304.200.b	4.2 ± 0.1	191 ± 14
ss316.100	111.2 ± 32.4	18.3 ± 9.0	ss316.100.b	1.5 ± 0.2	114 ± 5
ss316.200	84.2 ± 41.8	3.2 ± 1.2	ss316.200.b	1.7 ± 0.4	36 ± 6
Tig1.100	54.0 ± 17.3	11.3 ± 2.1	Tig1.100.b	0.7 ± 0.2	64 ± 9
WTi.100	39.0 ± 18.1	2.2 ± 0.6	WTi.100.b	2.6 ± 2.5	71 ± 30

5.3.4. Electrochemical behavior analysis

5.3.4.1. Potentiodynamic polarization

Potentiodynamic polarization trends were analyzed to determine the corrosion potential and current density for coated and uncoated samples for each material, in contact with SBF at room temperature (Figure 5.9). The coated samples were similar to the ones used for cell culture in osteogenic medium. Table 5.4 represents data for potentiodynamic polarization tests. Coated samples had higher E_{corr} (corrosion potential) than the uncoated onee for all materials, which shows better corrosion protection performance for HA-coated samples than the uncoated substrates. For most coated samples, E_{corr} was higher than the highest E_{corr} value for uncoated samples, -0.234 V for titanium grade 1 (Tig1). It indicates HA coating in any condition can improve corrosion protection for both stainless steel and titanium, making the corrosion resistance ability of HA-coated stainless steel similar to that of bare titanium grade 1.

Corrosion current density (i_{corr}) determines corrosion rate of metallic substrates, which has a direct relationship to material's mass loss per year (Table 5.4). I_{corr} values for coated substrates were higher than bare substrates, which is not desirable. This is explained by the non-uniform and partial coating coverage on the surface, thus uncoated areas still exist. Galvanic corrosion occurred as HA-coated areas and bare metal are coupled. Consequently, i_{corr} for galvanic corrosion would be higher than i_{corr} for each couple. The lowest i_{corr} values were 0.11 $\mu A/cm^2$ and 0.13 $\mu A/cm^2$ for uncoated and coated ss316.200, respectively. Ss316 is molybdenum-bearing grade and has better overall corrosion resistance than ss304. The mesh size 200 in both ss304 and ss316 possessed lower i_{corr} and higher E_{corr} than mesh size 100 due to its surface topography. The mesh diameter is smaller in mesh size 200 (d = 0.04 mm), thus wire beding is less significant in wire junctions. Therefore, the surface topography is more uniform and flatter, and the area with localized corrosion on the surface is smaller. In general, the lowest i_{corr} was close to the range of HA coatings with good coverage found in the literature (0.007-0.1 $\mu A/cm^2$) [50] and better than most HA films on titanium alloy and ss316 L substrates (0.07-10 $\mu A/cm^2$)[23,31].

In addition, Figure 5.9 shows that passivation occurred for all samples. $I_{passive}$ was generally lower for ss316, as a passive layer can be formed at lower current and have higher corrosion protection. No pitting was observed for titanium samples in the range of -0.6 V to 0.6 V (Figure 5.9c), but pitting and transpassive regions were observed on HA-coated ss304 (Figure 5.9a) and ss316 (Figure 5.9b) at about 0.35 V. Considering the galvanic corrosion case in which the bare substrate is the anode, passivation and pitting should happen for uncoated substrates. This means each sample has an HA film and a passive film of the metal oxide forming on its surface in contact with SBF. The results showed HA coating with semi-coverage could be acceptable for titanium substrates, as bare substrates were covered by an oxide layer without any pitting. However, this is

not desirable for ss304 and ss316 as the passive layer on bare metal pits. FE-SEM surface and cross-sectional images were taken to see the effect of the corrosive medium on bare and HA-coated samples. Figure 5.10a,b show the surface of ss304.200.CS1 after polarization tests. Pitting occurred on uncoated areas of the surface which had a passive layer (Figure 5.10a). The corresponding cross-section (Figure 5.10c) reveals that the passive layer is very thin and cannot be differentiated. There is good adhesion between HA layer and substrate as there is no delamination or formation of any other layer at the coating–substrate interface due to corrosion (Figure 5.10d).

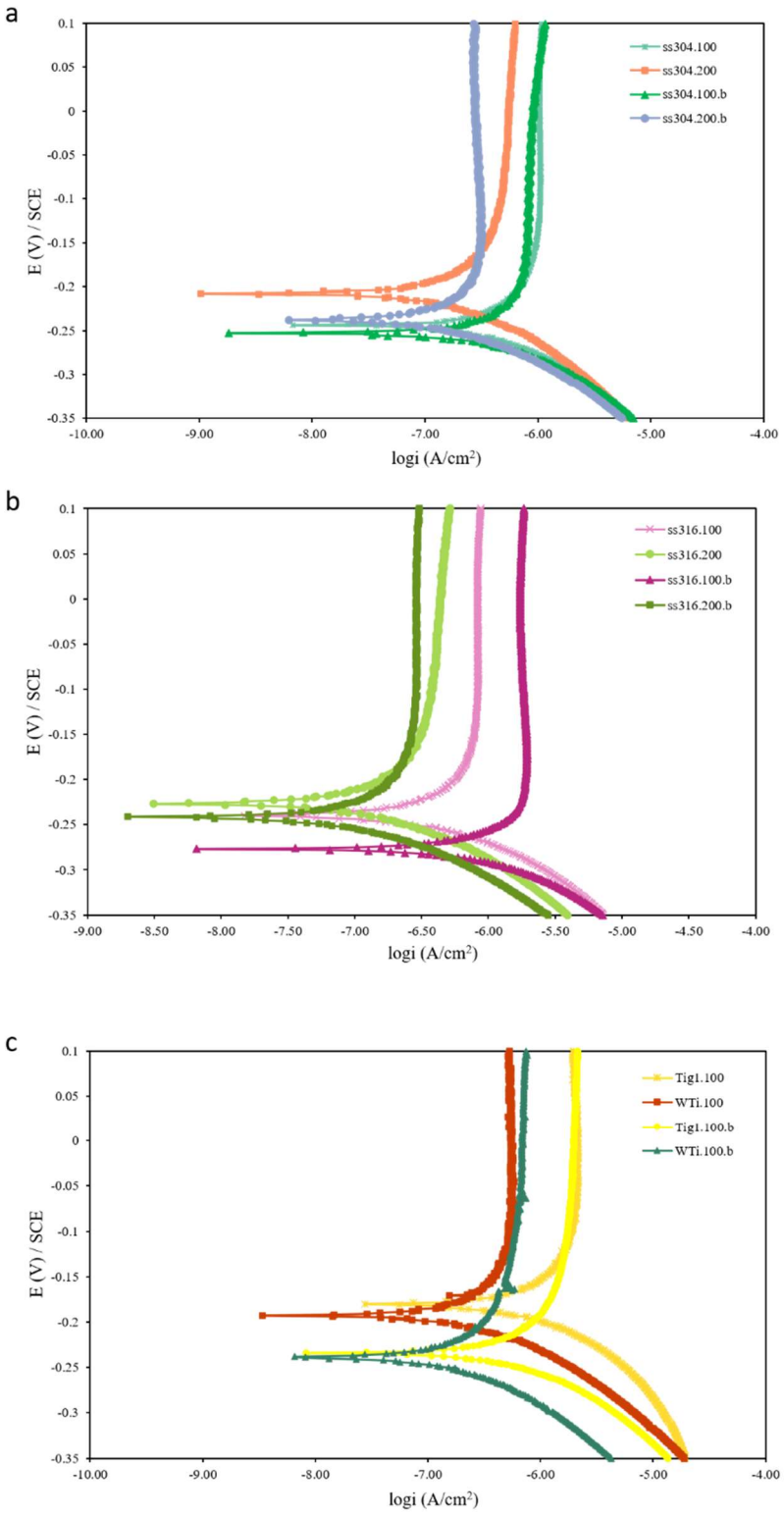

Figure 5.9**.** Potentiodynamic polarization curves for (a) ss304, (b) ss316 and (c) titanium, bare and HA-coated samples, in simulated body fluid (SBF) at room temperature. Coating conditions for HA-coated samples were the same as those chosen for biocompatibility tests.

Table 5.4. Fitting values for E_{corr} and i_{corr} in potentiodynamic polarization curves and EIS data. Samples for each material type are ordered according to i_{corr} values, from highest to lowest.

Sample code	Polarization data			EIS data				
	E_{corr} (V) vs. SCE	i_{corr}(μA/cm^2)	$i_{passive}$(μA/cm^2)	R_s (Ω.cm^2)	C_{dl}(F/cm^2)	R_{ct}(Ω.cm^2)	C_C(F/cm^2)	R_P(Ω.cm^2)
ss304.100	-0.244 ± 0.002	0.49 ± 0.11	1.07	13.21	15.00E-5	548	12.00E-5	1.67E5
ss304.100.b	-0.253 ± 0.006	0.46 ± 0.06	0.85	15.42	7.72E-5	594	68.74E-5	2.20E5
ss304.200	-0.208 ± 0.007	0.18 ± 0.10	0.53	15.51	9.57E-5	1011	9.67E-5	3.73E5
ss304.200.b	-0.238 ± 0.005	0.16 ± 0.04	0.29	14.55	2.89E-5	698	2.74E-5	5.97E5
ss316.100.b	-0.277 ± 0.005	1.00 ± 0.15	1.75	14.83	5.46E-5	831	9.36E-5	1.17E5
ss316.100	-0.240 ± 0.009	0.37 ± 0.13	0.83	13.28	7.92E-5	795	5.96E-5	2.65E5
ss316.200	-0.227 ± 0.007	0.13 ± 0.05	0.42	18.27	6.35E-5	1197	5.85E-5	3.01E5
ss316.200.b	-0.241 ± 0.004	0.11 ± 0.03	0.29	19.07	2.77E-5	6321	5.03E-5	3.11E5
Tig1.100	-0.180 ± 0.003	0.74 ± 0.15	1.99	16.01	133.0 E-5	119	74.00E-5	0.63E5
Tig1.100.b	-0.234 ± 0.005	0.47 ± 0.11	1.95	19.41	2.77E-5	609	34.00E-5	0.24E5
WTi.100	-0.193 ± 0.004	0.20 ± 0.06	0.57	16.76	22.70E-5	113	8.37E-5	1.80E5
WTi.100.b	-0.238 ± 0.004	0.16 ± 0.04	0.69	17.78	2.78E-5	1030	70.50E-5	0.66E5

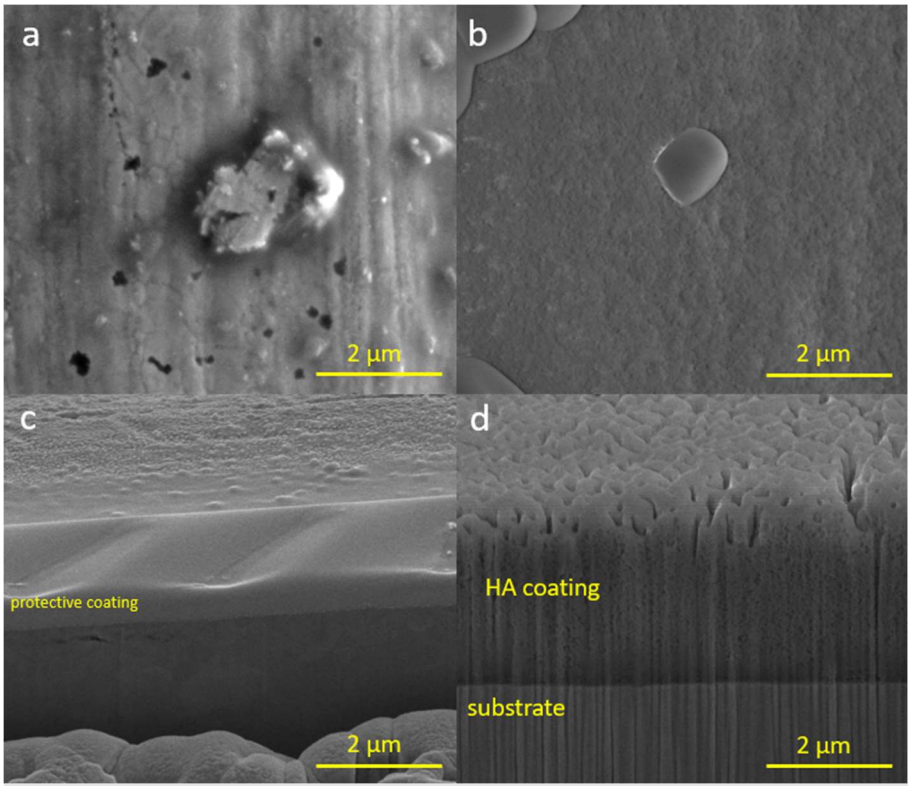

Figure 5.10. FE-SEM (SE) images for an example of corroded sample (ss304.200.CS1) after polarization in SBF, pits on passive layer (a), HA coating surface (b), and cross-sections of uncoated area (c) and HA-coated area (d). Scale bar is 2 µm for all images.

5.3.4.2. Electrochemical impedance spectroscopy

Electrochemical impedance spectroscopy was used to estimate the corrosion resistance of HA-coated samples. As the coating was not uniform, a related equivalent electrical circuit model for best fit was designed, as represented in Figure 5.11 [97,167]. R_s is the solution resistance, or the SBF resistance, C_{dl} is the double layer capacitance, and R_{ct} is the charge transfer resistance. C_c is the interfacial capacitance and R_p is the polarization resistance, inversely proportional to i_{corr} (from Table 5.4) and expressed as $R_p = B/i_{corr}$, where B depends on material (substrate and coating) and solution [167]. Here, $i_{passive}$ is assumed equal to i_{corr}, as the EIS test was done after polarization and there were both HA and oxide layers on the wire surface. Four different materials were used in this study, and the trend of change in R_p, according to $i_{passive}$, should be considered for each

material separately. Values of the circuit elements were calculated with ZSimpWin 3.20 from the Nyquist plots seen in Figure 5.12a-c, with parameters listed in Table 5.4, under the EIS data column. R_s is in the range of 13.0 $\Omega.cm^2$ to 19.5 $\Omega.cm^2$, showing solution consistency in polarization and EIS tests. C_c is in the order of 10^{-4} to 10^{-5} and R_p is in the order of 10^4 to 10^5. Lower C_c values represent lower transferring current, which means higher resistance (R_p). C_c, R_p and $i_{passive}$ follow the same trend for each material and are in the same order of magnitude as reported in previous studies in the literature for HA-coated titanium and stainless steel [96,97,167].

Bode phase angle and impedance plots are shown in Figure 18. In bode phase angle plots (Figure 18a-c), higher values at -90° indicate higher corrosion resistance, as -90° shows pure capacitance [168]. For ss304, the uncoated samples, which were covered by an oxide layer, were higher around -81°, while HA-coated titanium samples displayed higher values around -81°. The results showed the same trends in the bode impedance plots (Figure 5.13d-f), in which corrosion resistance was better for stainless steel uncoated samples and titanium HA-coated samples.

Higher impedance in bode impedance plots indicates better corrosion resistance. Higher impedance in the low-frequency region represents resistance to mass transportation, while it shows propagation of charge transfer in the high-frequency region [97]. For both ss304 and ss316, bode impedance plots for uncoated substrates reported higher values than coated ones because there is one uniform oxide layer covering the entire surface. Although pitting affected the oxide layer, the consequence was not visible in the plots. For titanium samples, the HA-coated ones led to higher values in the bode phase plot, showing higher resistance for coated samples, which is desirable.

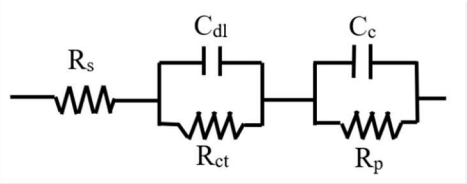

Figure 5.11. Equivalent electrical circuit for HA-coated samples used for EIS study.

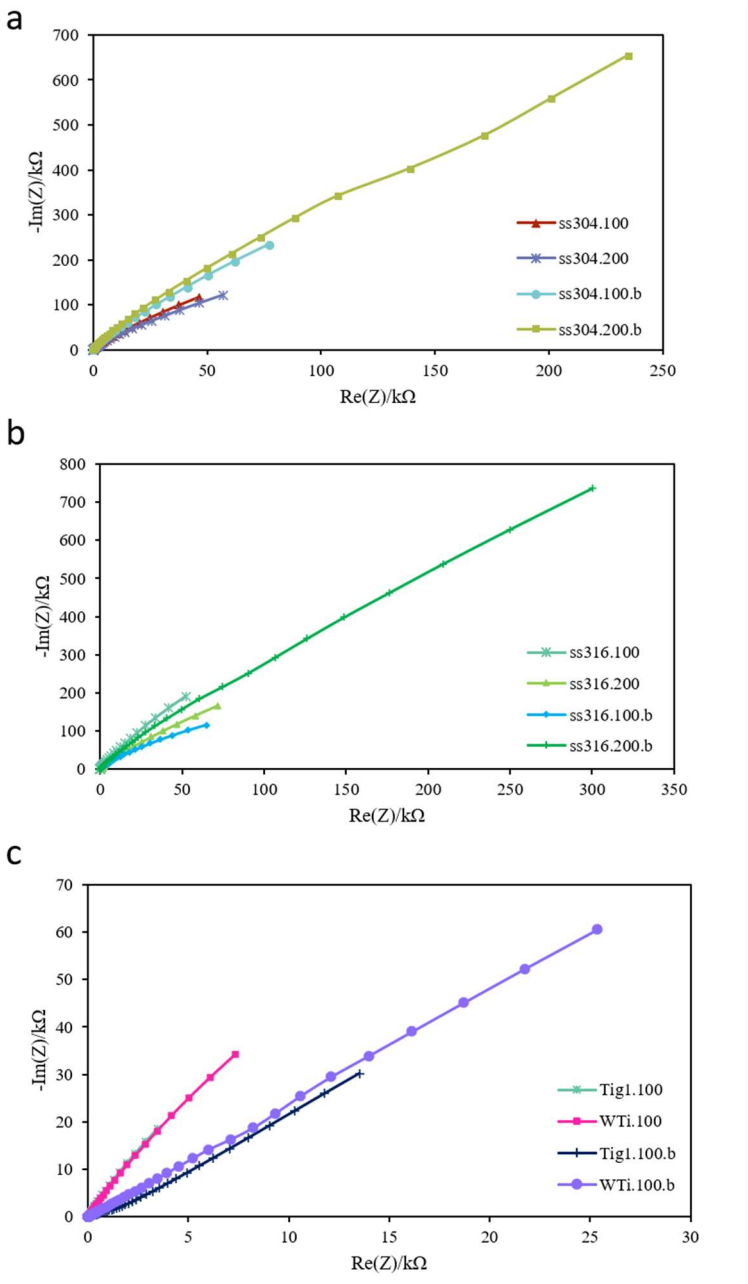

Figure 5.12**.** Nyquist plots of EIS data for (a) ss304, (b) ss316 and (c) titanium, bare and HA-coated samples, in simulated body fluid (SBF) at room temperature. Coating conditions for HA-coated samples were the same as those chosen for biocompatibility tests.

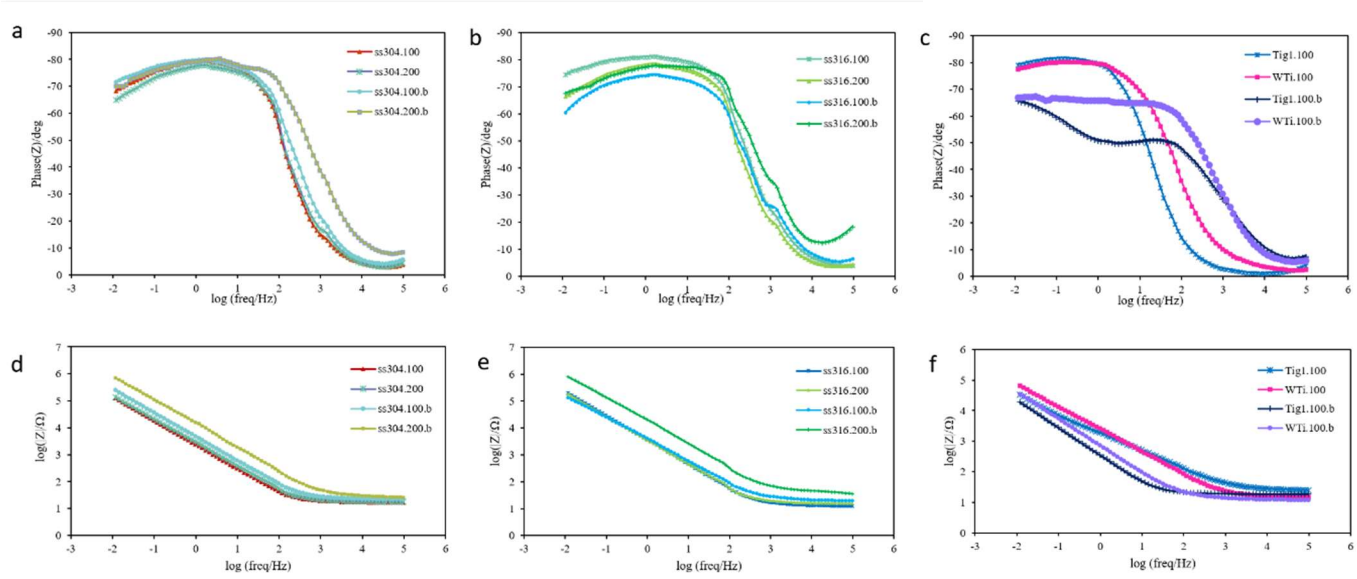

Figure 5.13. Bode phase plots (a) ss304, (b) ss316 and (c) titanium; and bode impedance plots (d) ss304, (e) ss316 and (f) titanium of EIS data for bare and HA-coated samples, in simulated body fluid (SBF) at room temperature. Coating conditions for HA-coated samples were the same as those chosen for biocompatibility tests.

5.4. Conclusion

In this study, the design of flexible, biocompatible composite implants was proposed by using a metal mesh as substrate and hydroxyapatite coating as bone regenerative stimulant derived from a simple sol-gel method. Experiments were performed to understand the effect of coating method (dip-coating and drop casting), substrate material (stainless steel and titanium) and substrate mesh characteristics on implant's performance.

Pure or biphasic nanorod hydroxyapatite coating on flexible mesh substrates were obtained through sol-gel method. All HA-coated samples dried at 150 °C in an oven possessed a crystalline structure. Different coating procedures and numbers of layers did not affect the crystal structure, shape or most intense plane reflections of the HA coating. It was observed that HA solutions with lower viscosity (GHA) led to higher wire and open areas coverage with the dip-coating process. Substrate material and wire diameter affected coating adhesion and coverage and consequently,

coating thickness ranged between 4.0 μm to 7.9 μm for all samples. Smaller wire diameter (or higher mesh size) enhanced coating coverage and adhesion due to reduced wire bending at the junctions and smaller distance between wire peaks and valleys. Overall, adding more HA layers improved wire coverage (above 50%) and reduced open areas (less than 1%). However, application of more than one layer induced defects like micro-cracks and coating delamination. Hardness values for HA-coated stainless steel substrates were higher than titanium ones as adhesion of the HA coating was more uniform. Moduli of elasticity for most HA-coated samples were in the range of human skull's modulus of elasticity (3.3 GPa to 6.0 GPa), which is preferred for potential implants. Finally, electrochemical behavior studies revealed that, even though corrosion protection for HA-coated samples was generally higher than bare samples, galvanic corrosion occurred on some samples. However, during use, a 3D ECM network covering the mesh implant could reduce the risk of galvanic corrosion.

Overall recommendations regarding design selection of mesh composite implants are summarized as follows: finest mesh size and dip-coating method to promote uniform coating on wires, and low number of HA layers to maintain open areas for 3D ECM formation. The experimental results indicated that while HA-coated titanium grade 1 showed the best overall performance as a cranioplasty implant, HA-coated stainless steel 316 with mesh size 200 constitutes an adequate, lower cost alternative (by a factor above 100 based on raw materials cost).

Chapter 6 . Comparison of Microstructure and Tensile Behavior of Hydroxyapatite-coated Polymeric Meshes, Fabrics and Mats

6.1. Introduction

The aim of this study is to assess the effect of HA coating on the morphology and mechanical behavior of polymeric meshes, fabrics, mats. Biocompatible, polymeric materials, typically suitable for biomedical applications (commercially available PEEK and cellulose), were investigated in different porous forms (mesh, fabric and mat), with and without hydroxyapatite coating. The microstructure of the substrates was first evaluated for fiber diameter distribution and porosity. Then, a low temperature sol gel coating method (< 150 ^{o}C), suitable for polymeric substrates, was developed. HA powder chemical structure and coated substrates surface morphology were studied to understand the effect of coating procedure on substrate microstructure. Finally, tensile tests were performed to assess HA coating adhesion and its effect on mechanical performance of different substrates (mesh, fabric and mat).

6.2. Materials

Hydroxyapatite solution and powder were derived through the sol-gel method. Potassium dihydrogen phosphate EMSURE® ISO (KH_2PO_4) (Merck KGaA, Germany) and calcium nitrate tetrahydrate ≥99.0% ($Ca(NO_3)_2.4H_2O$) (Sigma-Aldrich, USA) were used as hydroxyapatite precursors. Ammonium hydroxide solution (ASC reagent, 28.0-30.0% NH_3 basis (NH_4OH)) (Sigma-Aldrich, USA) was used to adjust pH. Cleaning and degreasing reagents, were acetone (AR® ACS (C_3H_6O)) (Macron Fine Chemicals™, Avantor™, USA) and ethyl alcohol (95% denatured, lab grade (C_2H_5OH)) (Aldon Company, USA). Technical grade distilled water was purchased from ChemWorld as a solvent.

Two types of materials in three different forms (mesh, fabric and mat) were investigated in this study. Table 6.1 summarizes the material types and sample coding used in this manuscript.

Materials and mesh dimensions were selected based on literature review and results with metallic meshes.

First, polyether ether ketone (PEEK) mesh with 80 μm-diameter filaments woven as a plain weave were used (FDA Compliant 21 CFR 177.2415, McMaster-Carr, USA). The open area was 56 % with 220 μm opening size and a mesh size of 86 x 86 (86 openings per 25.4 mm length), selected based on previous work on metal meshes, literature and commercial availability [186]. Second, as cellulosic fabric, a commercial grade 32 count linen cross-stitch fabric was selected (Caydo, China). This fabric was coated with poly methyl methacrylate (PMMA), using 3D printing filament with 1.75 mm diameter (Push Plastics, USA). Finally, two types of cellulose mats were investigated: 1) FDA-approved, compostable, non-biodegradable mats containing cellulose fibers (from two different suppliers, Z Natural Foods and Monterey Bay, USA); and 2) grade one cellulose mats (Whatman® qualitative filter papers, Sigma-Aldrich, USA). The latter had a pore size of 11 μm and areal weight of 87 g/m^2.

Table 6.1. Material types and sample coding used in this study.

Material and type (Supplier)	General sample coding	Uncoated (bare)	HA-coated
PEEK mesh (McMaster-CARR)	PEEK	PEEK.b	PEEK-HA
Cotton fabric (Caydo)	Cotton	Cotton.b	Cotton-HA
Cotton-PMMA fabric (Caydo and Push Plastics)	Cotton-PMMA	Cotton-PMMA.b	Cotton-PMMA-HA
Cellulose 1 mat (Z Natural Foods)	Cellulose 1	Cellulose 1.b	Cellulose 1-HA
Cellulose 2 mat (Monterey Bay)	Cellulose 2	Cellulose 2.b	Cellulose 2-HA
Filter paper cellulose mat (Whatman, Sigma-Aldrich)	Filter-paper	Filter-paper.b	Filter-paper-HA

6.2.1. Synthesis of hydroxyapatite sol

Hydroxyapatite (HA) sols were prepared by mixing two precursor solutions at room temperature to maintain Ca/P ratio as 1.67. Calcium solution contained 0.0167 mol $Ca(NO_3)_2.4H_2O$ [130] dissolved in 50 ml distilled water. 2.5 ml NH_4OH was added dropwise to the solution to adjust pH around 12, while stirring for 30 minutes. Potassium solution consisted of 0.01 mol KH_2PO_4 in 50 ml distilled water which stirred for 30 minutes. Then, potassium solution was added to calcium one dropwise while stirring for another hour. Finally, after approximately 2 hours, 100 ml of HA white sol (pH ≈ 9) was produced.

6.2.2. Coating procedures

To coat the cotton fabric with PMMA (Cotton-PMMA substrates), PMMA filaments were dissolved in acetone (10 g/L) and stirred for 24 hours at room temperature. Then, the fabric was coated with the acetone solution (10 g/L) by dip-coating process (withdrawn rate: 10000 μm/min, immersion time: 20 s, upholding time: 300 s, number of immersions: 3 times).

Prior to HA coating all samples, they were degreased by soaking in acetone, dried in air at room temperature for 5 min, then dried in an oven at 65 °C for 15 min. HA sol was sonicated for 15 min to get a homogenous solution before the coating process. An area of 20 cm^2 on both sides of each substrate was coated by drop-casting method with three consecutive HA layers, at room temperature with 50% humidity. These coating conditions were selected based on preliminary tests and previous research [186]. The adhesion of the liquid sol was high enough that the sample could be flipped, and the other side could be covered by the sol. For multilayer coating, the substrate dried in oven for one hour at 150 °C (for PEEK, cotton and cotton-PMMA), and at 90 °C (for filter paper and tea bag papers), then cooled in the oven to room temperature between each coating layer.

Between tests, the samples were kept at room temperature in a petri dish in a dark place. An area of each substrate was cut for use in different tests.

6.2.3. Chemical composition analysis

Chemical composition and crystallinity was studied by X-ray diffractometer (PANalytical Empyrean) over 2θ range of 5°- 80° for powder of coatings dried at various temperatures. The test settings were continuous CuKα radiation (λ=0.1540598 nm) with a step size of 0.02°, generator voltage of 45 kV and tube current of 40 mA. To investigate crystal structure and plane indices of powder of HA coatings, high resolution transmission electron microscopy (HR-TEM, JOEL JEM-2011), equipped with a bottom-mounted Gatan SC1000 CCD camera, was used with an accelerating voltage of 200 kV. X-ray spectroscopy (EDX) point analysis with field emission electron source (FEI QUANTA 3D FEG FIB/SEM), using an accelerating voltage of 20 kV in statistical imaging mode, was also done to find the Ca/P ratio in HA coatings on PEEK and Cellulose 1 substrates.

6.2.4. Microstructure and morphology analysis

Microstructure and morphology of uncoated and HA-coated substrates, scissor cut edge and failure surfaces resulting from tensile tests were analyzed with a field emission electron microscope (FE-SEM, FEI QUANTA 3D FEG FIB/SEM) using an accelerating voltage of 5 kV in secondary electron mode. The fiber diameter distribution for fabric and mat specimens was measured using ImageJ (version 1.53e, National Institutes of Health, USA) for n = 100. PEEK meshes exhibited consistent wire diameters as noted above in Section 2.1.

6.2.5. Mechanical testing

The tensile behavior was evaluated for uncoated and HA-coated samples by using an eXpert 2610 MTS (ADMET, Norwood, MA, USA) at room temperature. Each substrate was cut

into a dog bone shape based on ASTM D638 IV [165] and ASTM D3822-01 [187] for which the cross-sectional area was 8 mm (width) × specimen thickness in mm. This dog bone shape was selected based on preliminary tests to ensure failure occurred along the length of the gauge section for all specimen types, and not in the grips, as was the case for rectangular samples. The crosshead speed was 0.5 mm/min with a load cell of 5 kN. At least three specimens were tested for each substrate type. The stress-strain curves were plotted from the load-displacement curves using the initial cross-sectional area of the specimens (width x thickness) to establish a comparison between all substrates. Three tensile properties were calculated: Young's modulus (initial linear region of the stress-strain curves), tensile strength (maximum stress achieved during test), and elongation at break or maximum stress (strain value at maximum stress). As all substrate types behaved differently under tensile load, further considerations regarding mechanical properties calculation will be discussed in Section 3.3.

Porosity volume measured by finding the difference between the volume of bulk material and the volume of material in the water. Then porosity volume divided by bulk volume to determine porosity measurement. The measurement repeated for 3 times (n=3) for each sample.

6.2.6. Statistical analysis

In the results and discussion section, data are reported as the average ± standard deviation. All statistical analyses were performed with GraphPad Prism (version 9.1.2). For mechanical tensile test results on PEEK meshes, paired t test analysis (comparison between bare and HA-coated specimens) at the significance level of $p < 0.05$ was used. For fabric and mat specimens, to assess significance between bare and HA-coated specimens, as well as between material types, two-way analysis of variance (ANOVA), followed by Tukey's multiple comparisons test, was carried out with $p < 0.05$.

6.3. Results and discussion

6.3.1. Hydroxyapatite chemical composition and phase analysis

HA powders were collected from both sides of HA-coated substrates by lightly scratching the coating off with a razor blade. Different HA power samples were scratched off numerous substrates, dried in an oven for one hour at 90 °C or 150 °C.

X-ray diffraction patterns for all HA powders are shown in Figure 6.1. A pure crystalline hydroxyapatite phase is observed from the characteristic peaks for HA powder derived at 90 °C or 150 °C, consistent with standard database (JCPDS 09-9432). Diffraction patterns mostly show the peaks for crystalline pure HA at both temperatures, but also for decomposed compounds of HA, β-tricalcium phosphate (214, 217, 220) (β-TCP) and CaO (200). The peaks for HA-150°C have higher intensity than peaks for HA-90°C in Figure 6.1, showing higher temperature could affect crystallinity and make a crystal structure with more aligned atomic planes. As the HA solution is calcium-deficient hydroxyapatite, unstable after thermal treatment with a pH ≈ 9, calcination decomposed the structure into three calcium phosphate phases: pure HA, β-TCP and CaO [160]. Since all samples were dried at temperatures lower than 1000 °C, β-tricalcium phosphate is most likely to be formed for powders from HA sol [180]. For our study, this confirms that low drying temperatures, suitable for polymeric substrates (i.e., below glass transition temperature), can create HA coatings with the same crystalline structure as high drying temperature. [181]

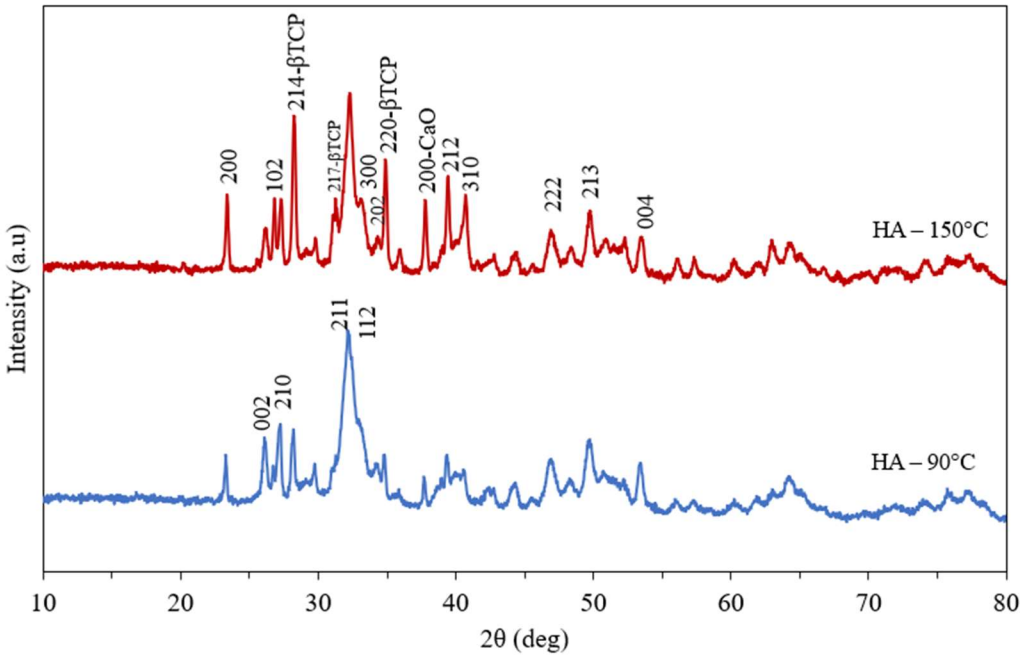

Figure 6.1. XRD patterns for powder of HA-coating scratched from surface of cellulose mat dried at 90 °C (bottom pattern) and PEEK mesh or cotton fabric dried at 150 °C (top pattern).

EDX point analysis results for elemental distribution of Ca and P on HA-coated PEEK and Cellulose 1 shows the Ca/P ratio varied from 1.38 to 1.68. As there are three different compounds (HA, β-TCP and CaO) in the coating and the substrates consist of carbon, hydrogen and oxygen, the Ca/P ratio is not a good estimate for the formed calcium compound in the coating. All three compounds contain calcium and the substrates contain a high amount of carbon. While 1.68 is close to the Ca/P ratio for pure HA (1.67), the results obtained from XRD and HR-TEM are more reliable.

HR-TEM pictures were captured to characterize the nano crystal shape of powder of HA coating dried at various temperatures, and the interplanar spacing of the most intense reflections (Figure 6.2). HA nanorods are visible in Figure 6.2a and c with lengths from 16 nm to 19 nm and diameters from 5 nm to 7 nm for dried coating at 90 °C. For dried coating at 150 °C, nanorod lengths from 40 nm to 90 nm and diameters from 8 nm to 16 nm are observed. Those values show

the effect of higher drying temperature, which result in longer HA nanorod crystals. Figure 6.2b and d reveal the structure of HA coating, which presents pure HA plane spaces equal to $d = 0.81$ nm (001), $d = 0.34$ nm (002) [164,186] for both 90 °C and 150 °C.

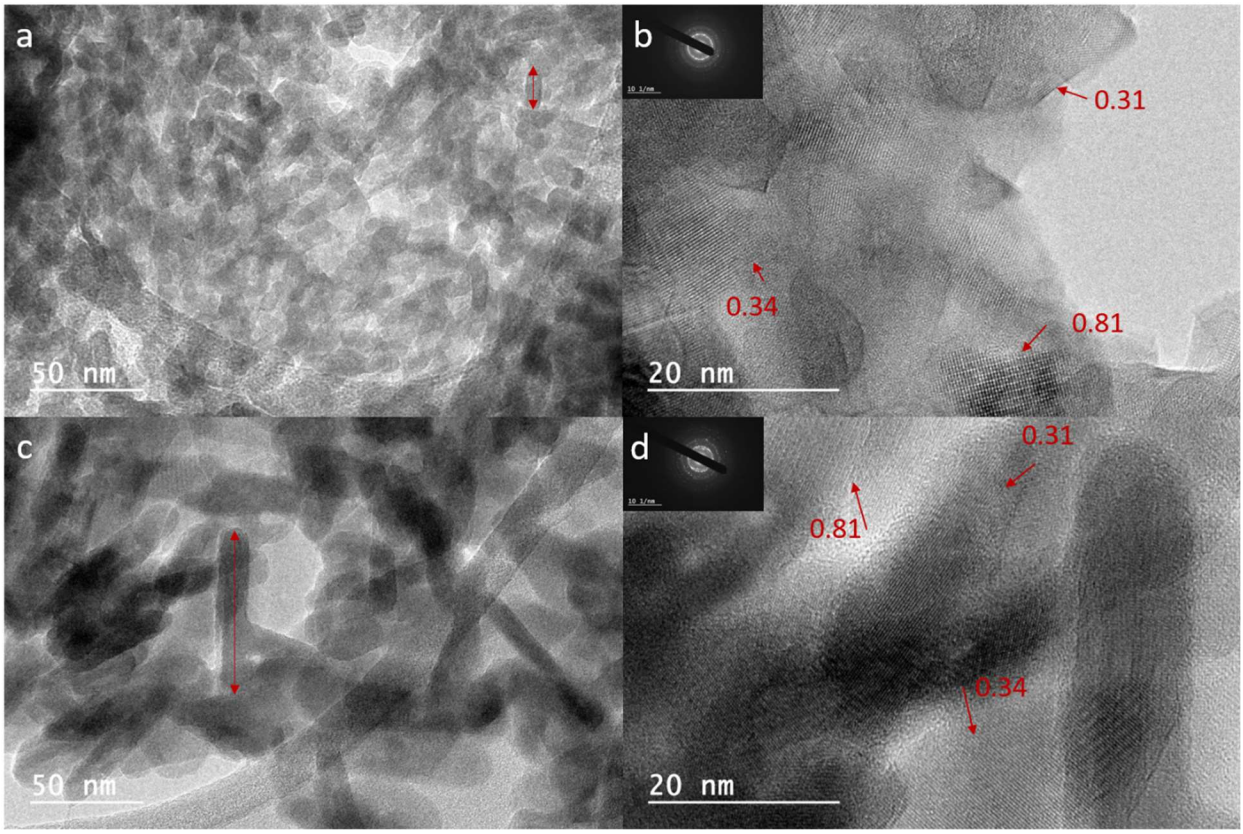

Figure 6.2. Representative HR-TEM images for HA coating powders (scratched off from substrate surface) dried at various temperatures: (a, b) 90 °C, (c, d) 150 °C. Pure HA plane spaces of $d = 0.81$ nm (001), $d = 0.34$ nm (002), and $d = 0.31$ nm (102) are marked in panels b and d. Scale bar is 50 nm for (a, c) and 20 nm for (b, d). Images in inset correspond to diffraction patterns with a scale bar of 10 nm−1.

6.3.2. Scaffold's microstructure and morphology

FE-SEM pictures were captured with various magnifications to study the differences between bare and HA-coated substrates. PEEK meshes are shown in Figure 6.3a and b, where individual PEEK filaments are clearly observed in a plain weave pattern. Based on FE-SEM images (Figure 6.3b), the filaments peaks at the wire junctions display a rougher microstructure, likely due to the weaving procedure or post-processing steps (i.e., packaging, transportation,

etc.).After HA coating (Figure 6.3c and d), coated and uncoated areas on the mesh are visible. Although back scatter imaging mode is preferable to more easily distinguish between coated and uncoated areas, the high voltage surface charging limited the imaging procedure and quality. Thus, secondary electron mode was used. HA coating coverage appears generally uniform, except for a few wire peaks (Figure 6.3c, arrow). Coating delamination occurred below the fiber junctions (Figure 6.3d), as the accumulation of HA sol at the junctions led to thicker HA coating, which would crack and delaminate due to high internal stresses during coating drying in the oven [14]. Image analysis of HA-coated PEEK meshes revealed the following average data: 1) uncoated filament area of 6.6 % ± 1.0 %, and 2) open area of 52.4 % ± 3.2 % (compared to 56 % total open mesh area, as per manufacturer's specifications) [14]. The highest thickness for the HA coating on PEEK mesh was about 4.5 μm, based on the delaminated HA coating at the fiber junctions.

Cotton fabric consists of fiber tows in a twill weave pattern, as shown in Figure 6.3e,f before coating. The fiber diameter distribution is summarized in Figure 6.5a for n = 100. Three layers HA coating partially filled the porous areas between fibers, as seen in Figure 6.3g, h. In some cases, HA blocks with a width around 50 μm formed in the areas between fibers (Figure 6.3h, arrow). For cotton-PMMA fabrics, PMMA solution was absorbed and covered individual fibers, without any visible delamination (Figure 6.3i, j). Figure 6.3l shows both adhesive and delaminated HA coating on cotton-PMMA fabric (shown by arrow), in which the porous areas between fibers is less occupied by HA blocks, compared to Figure 6.3h. This is the result of lower adsorption of HA sol by cotton-PMMA fibers, as PMMA is water repellent.

For cellulose mats, intertwined fibers with different diameters are shown in Figure 6.4 and Figure 6.5b-d Fiber mats appear dense, but HA coating is generally not uniform with the presence of several HA blocks. Lower oven drying temperature for the mats (90 ^{o}C), compared to 150 ^{o}C

for PEEK and cotton fabric, resulted in smaller HA blocks. The smallest HA block size (less than 5 µm) was observed and measured for the filter-paper substrates (Figure 6.4d, arrow). There is no visible difference between cellulose 1 and cellulose 2 mats except the range of fiber diameter is wider for the former (Figure 6.5c,d).

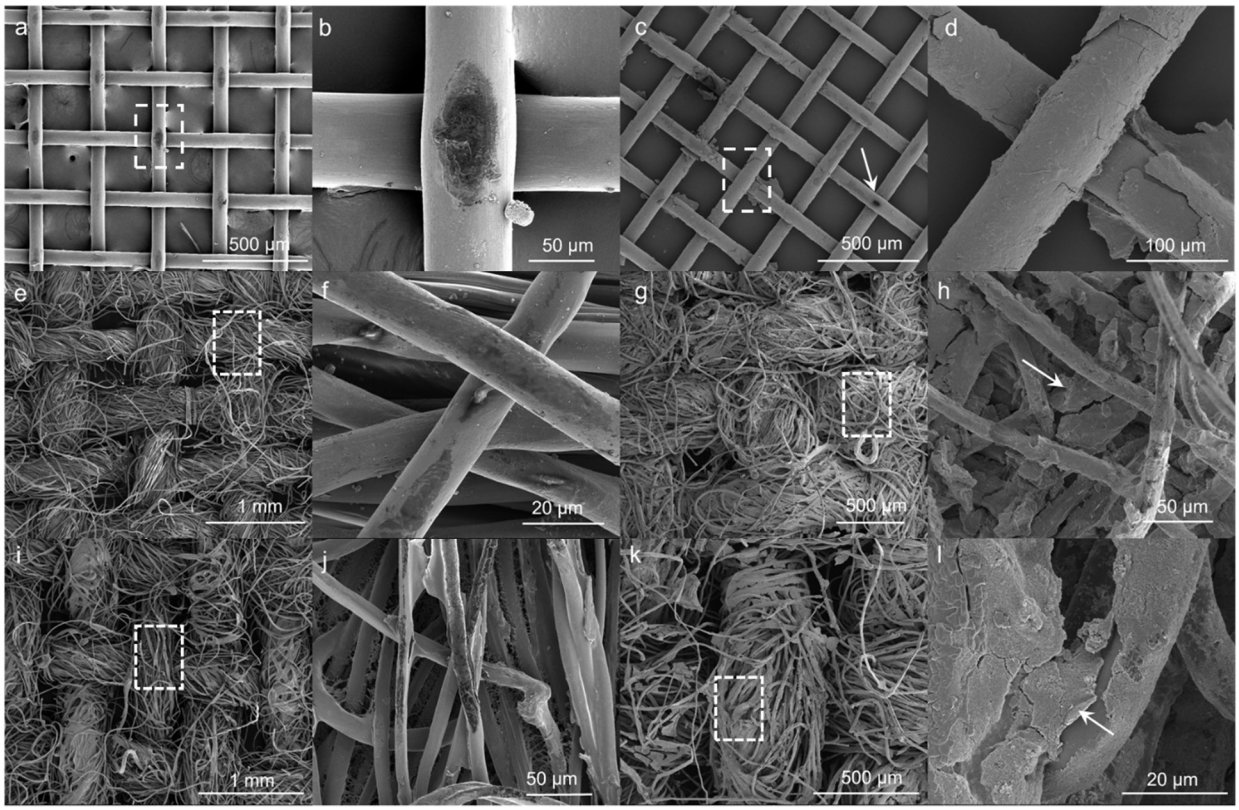

Figure 6.3. FE-SEM images in secondary electron (SE) modes for bare substrates (dashed rectangles are zoomed in areas): (a, b) PEEK, (e, f) cotton, and (i, j) cotton-PMMA; and HA-coated substrates: (c, d) PEEK (with uncoated filament area of 6.6 % ± 1.0 %, and open area of 52.4 % ± 3.2 %), (g, h) cotton, and (k, l) cotton-PMMA. Scale bar is 1 mm in (e, i), 500 µm in (a, c, g, k), 100 µm in (d), 50 µm in (b, h), 20 µm in (f, l), and 5 µm in (j).

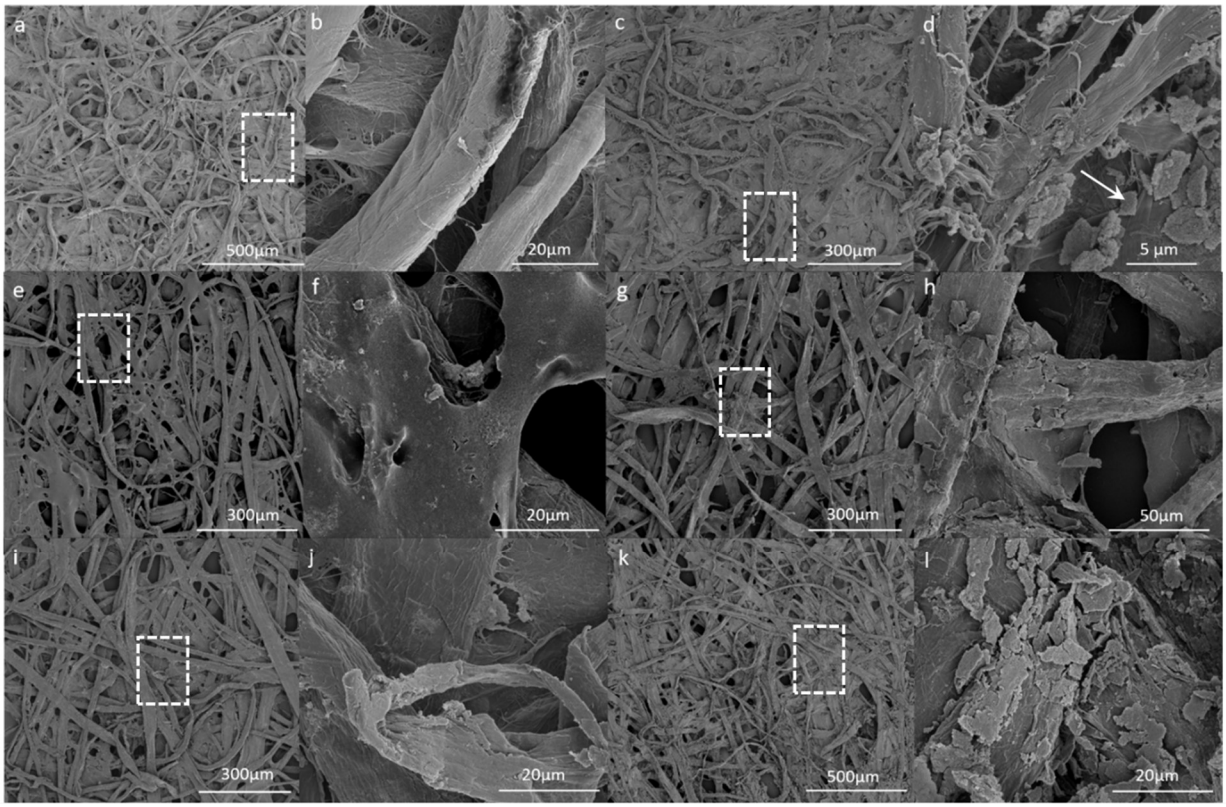

Figure 6.4. FE-SEM images (SE) for representative bare substrates (dashed rectangles are zoomed in areas): (a, b) filter-paper, (e, f) cellulose 1, and (i, j) cellulose 2; and HA coated substrates: (c, d) filter-paper, (g, h) cellulose 1, and (k, l) cellulose 2. Scale bar is 500 µm in (a, k), 300 µm in (c, e, g, i), 50 µm in (h), 20 µm in (b, f, j, l), and 5 µm in (d).

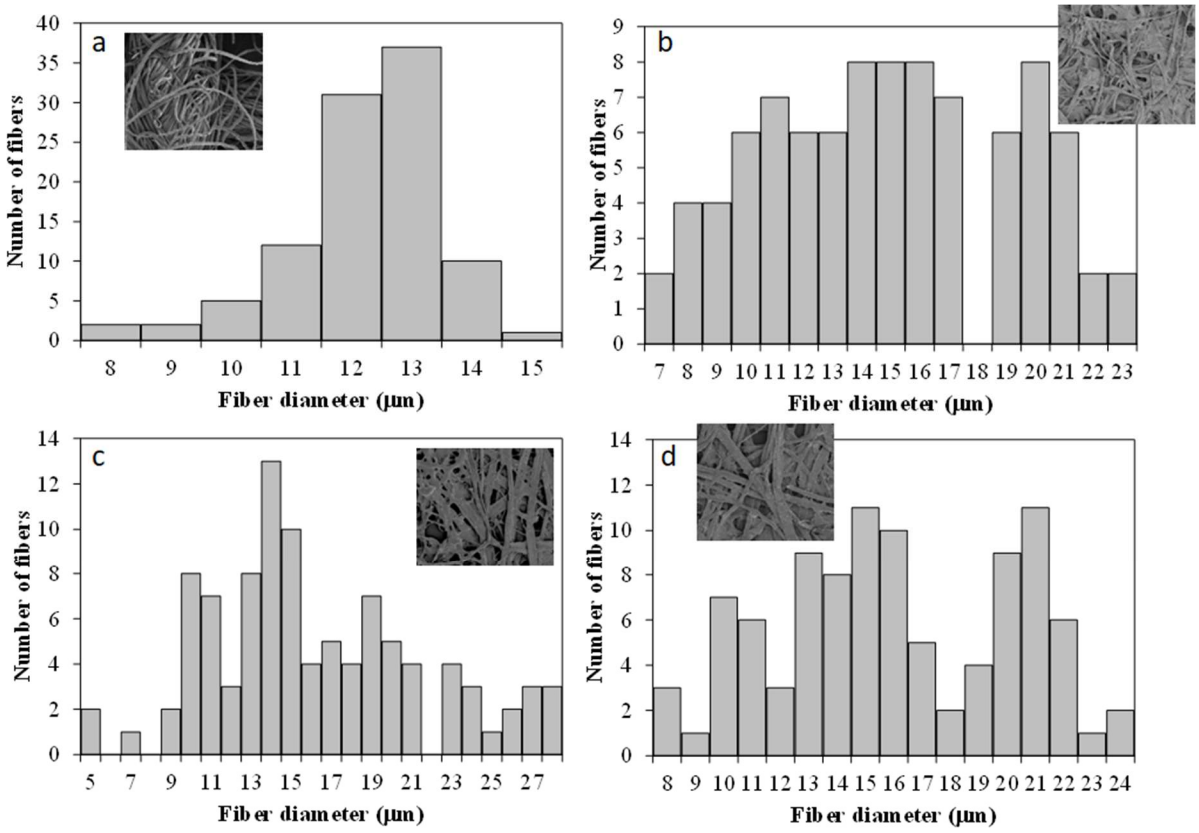

Figure 6.5. Fiber diameter distribution for (a) cotton fabric with inset image from Fig. 3e, (b) filter-paper mat with inset image from Fig. 4a, (c) cellulose 1 mat with inset image from Fig. 4e, and (d) cellulose 2 mat with inset image from Fig. 4i (n = 100 for all substrates).

Figure 6.6 shows the measured porosity before and after HA-coating on each type of substrate. PEEK mesh showed little variation after coating because it did not cover open areas, as observed and calculated based on Figure 6.3a. The porosity for fabric specimens (cotton and cotton-PMMA) decreased with both PMMA and HA coating. As PMMA impregnated the fabric, it occupied previously porous areas. Similarly, as previous mentioned for Figure 6.3h,l, HA coating further settled into porous areas, therefore reducing overall porosity of the fabric. Finally, cellulose mats, as commercially received, possessed decreasing porosity (Cellulose 1 > Cellulose 2 > Filter-Paper). After HA coating, porosity reduced for Cellulose 1 and Cellulose 2, while it slightly increased for the filter-paper. Based on statistical analysis (one sample t test, two-tailed),

the difference is significant at $p < 0.05$. This is likely due to the characteristics of the filter-paper, which should not absorb any liquid and should filter out particulate solutions. This resulted in a flaky HA coating on the surface (Figure 6.4d), which could delaminate more easily during handling.

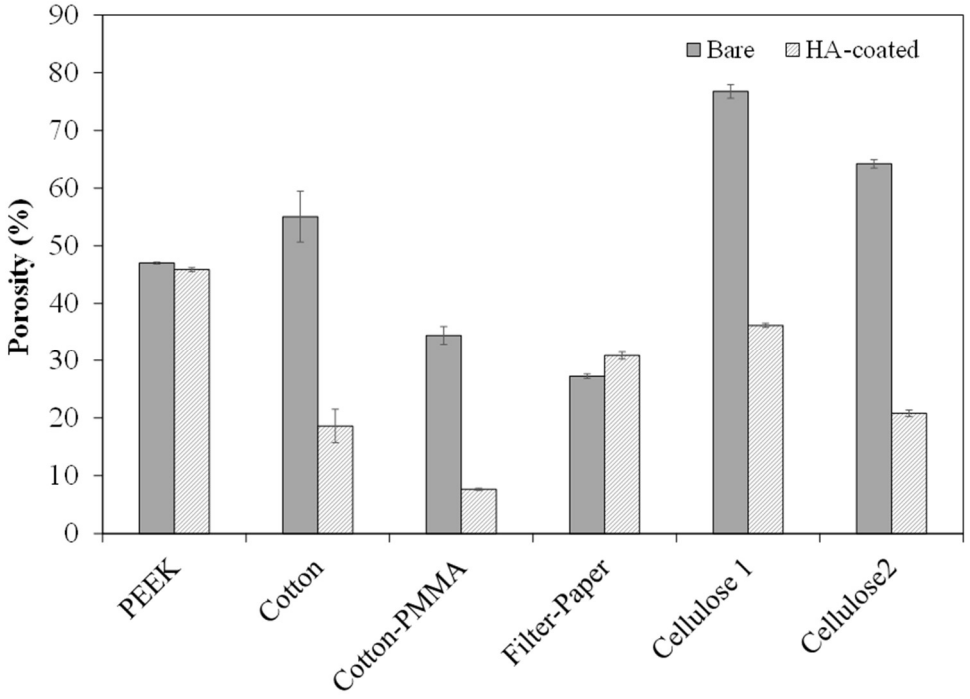

Figure 6.6. Measured porosity for each type of substrate (bare and HA-coated): PEEK mesh, and cellulose-based fabrics and mats.

6.3.3. Mechanical tests

Tensile tests were performed for all materials (mesh, fabric and mat), bare and HA-coated. Representative stress-strain curves until failure are presented in Figure 6.7a, Figure 6.8a, Figure 6.9a. Photographs of the tested samples are shown in inset with the failure location boxed in red. The curves show different behaviors depending on the material and its form. PEEK meshes exhibit a behavior similar to monofilament woven fabrics (Figure 6.7a) [141,188]: initial linear behavior followed by change of slope and linear stress increase until failure initiation, then cross-wires

slippage and progressive wires failure (in the warp direction). Fabric specimens (Figure 6.8a), due to their initial flexibility, first go through a tows straightening phase, followed by linear behavior until progressive failure of filaments. This is typically observed for woven fabrics tested under tension [189]. Finally, mats specimens (Figure 6.9a), due to the random fiber orientation and the distribution of their diameters, generally display a non-linear behavior with tearing failure.

From those curves, the following mechanical properties were calculated or determined (as described in Section 6.2.5): Young's modulus(Figure 6.7b, Figure 6.8b, Figure 6.9b), tensile strength (Figure 6.7c, Figure 6.8c, Figure 6.9c), and strain at break (Figure 6.7d, Figure 6.8d, Figure 6.9d). Direct comparison between materials and specimen types show the highest Young's modulus values were obtained for PEEK meshes (Figure 6.7b) and cellulose filter paper mats (likely due to their denser fiber packing and more consistent fiber diameter compared to cellulose 1 and cellulose 2 mats, Figure 6.5 and Figure 6.6b). Highest tensile strength and strain at break values were achieved for PEEK meshes (Figure 6.7c-d), as expected based on PEEK bulk properties [151]. The effect of HA coating appeared to be negligible for all materials, except cellulose mats, more specifically for Young's modulus (Figure 6.9b) and tensile strength (Figure 6.9c). A more in-depth discussion regarding tensile behavior and mechanical properties for each specimen type, for bare and HA-coated specimens, is presented in section 6.3.4.

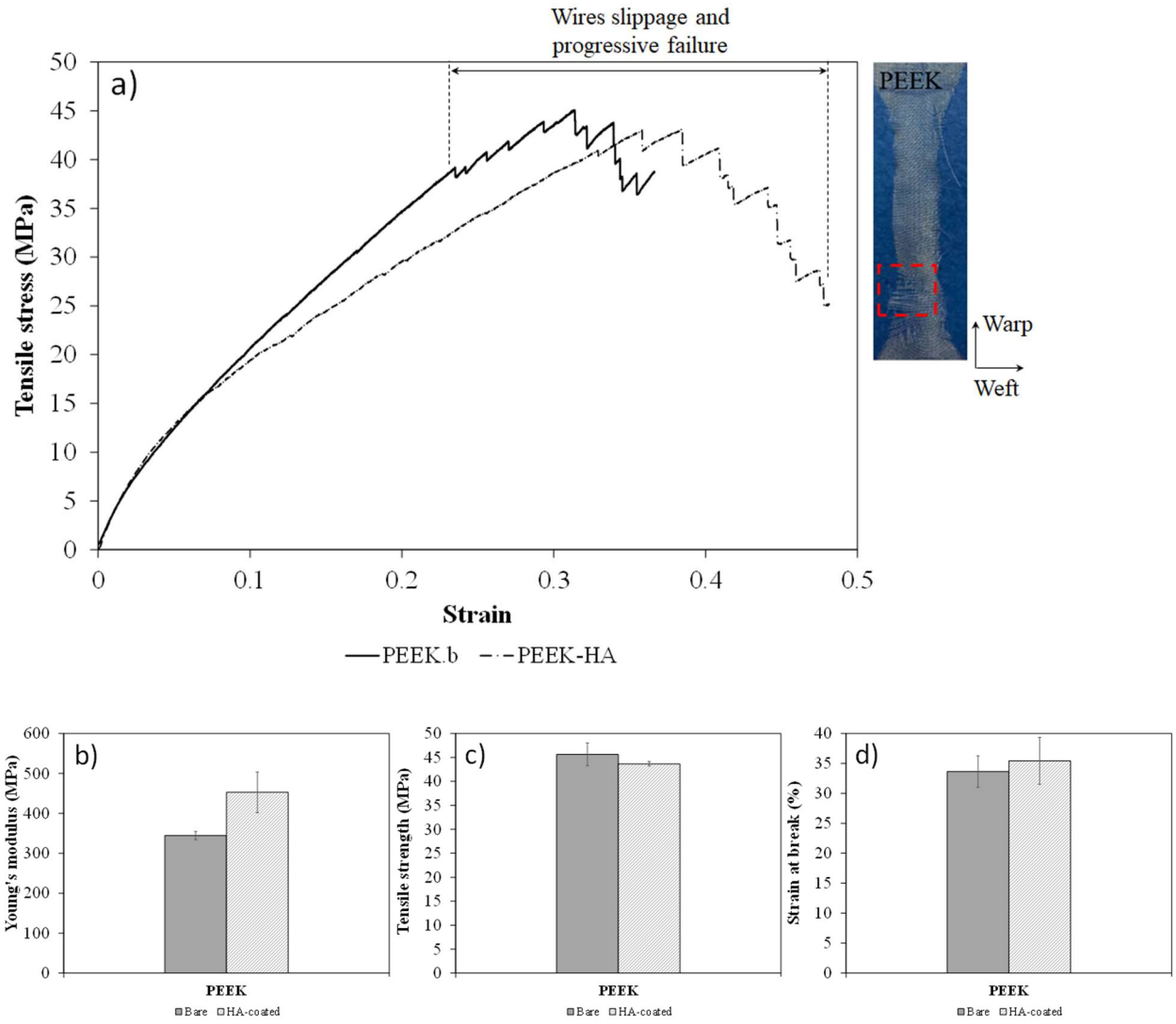

Figure 6.7. (a) Representative stress-strain curves for bare and HA-coated PEEK mesh samples, with torn region boxed in red in inset, (b) Average Young's modulus, (c) Average tensile strength, and (d) Average elongation at maximum stress.

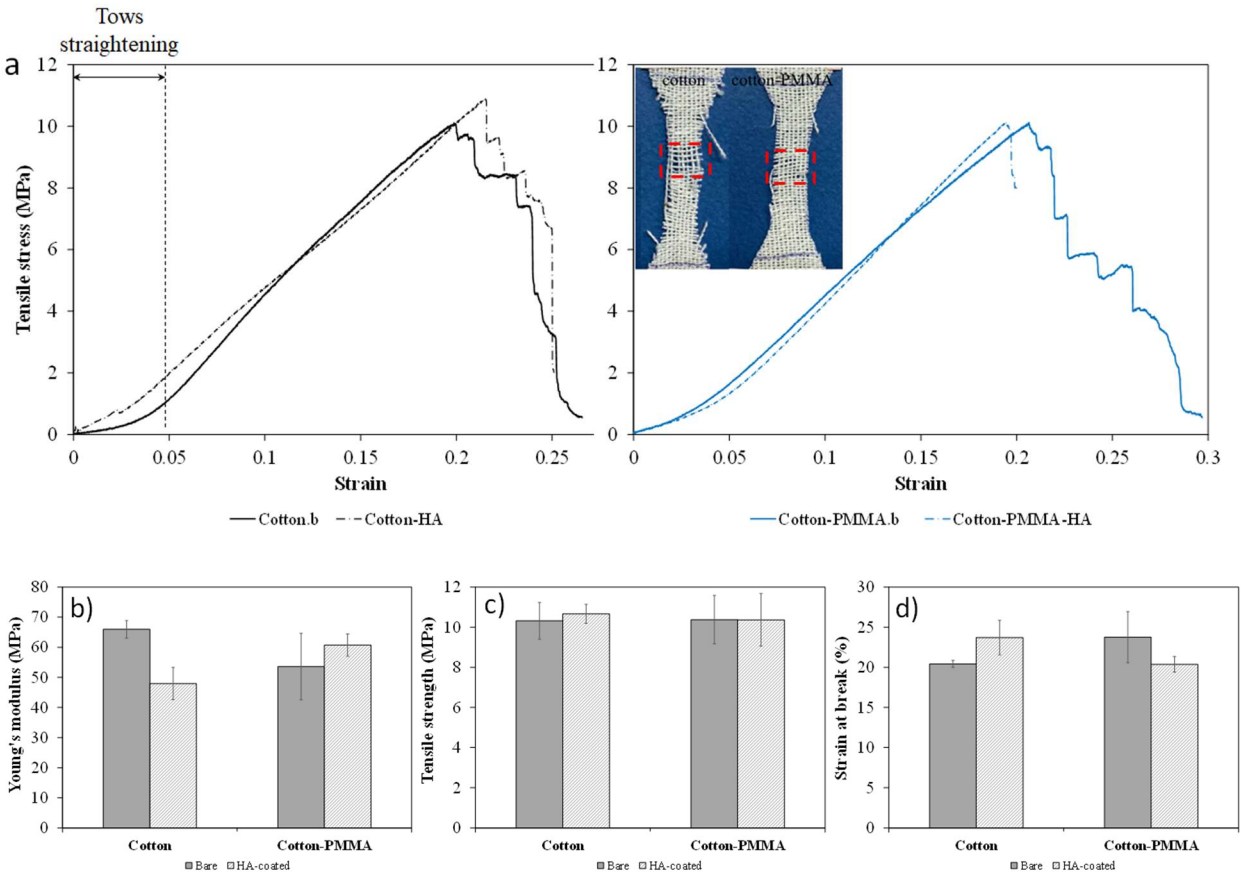

Figure 6.8. (a) Representative stress-strain curves for bare, PMMA-coated and HA-coated cotton fabric samples, with torn regions boxed in red in inset, (b) Average Young's modulus, (c) Average tensile strength, and (d) Average elongation at maximum stress.

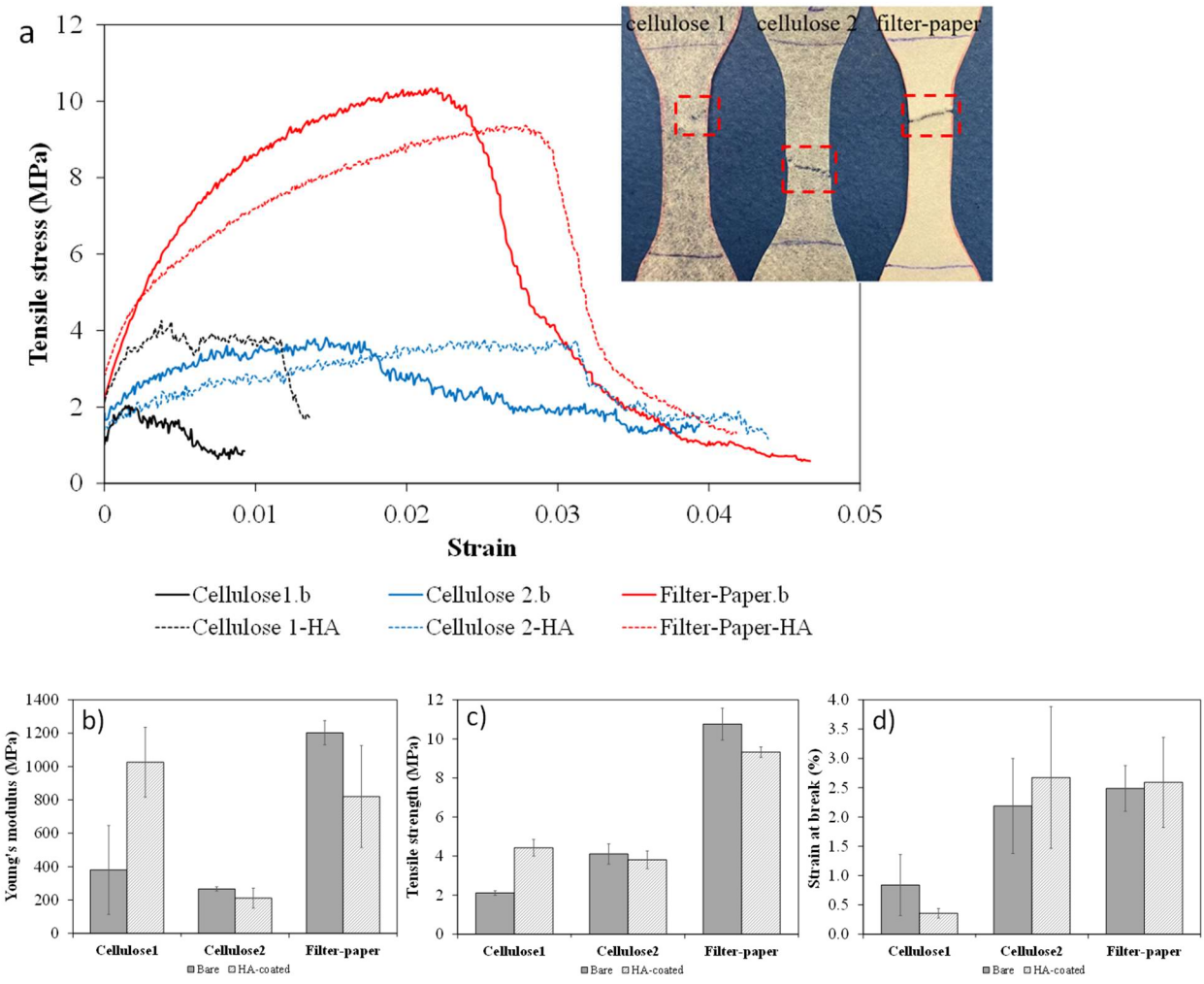

Figure 6.9. (a) Representative stress-strain curves for bare and HA-coated cellulose mat samples (Filter-Paper, Cellulose 1 and Cellulose 2), with torn regions boxed in red in inset, (b) Average Young's modulus, (c) Average tensile strength, and (d) Average elongation at maximum stress.

To assess the quality of HA coating adhesion after cutting (by scissors), FE-SEM images are presented in Figure 6.8a-f (for PEEK mesh and cotton fabrics) and Figure 6.9a-c (for cellulose mats). Similarly, after tensile tests, FE-SEM images are shown in Figure 6.8g-i and Figure 6.9d-i. In most cases, HA-coating partially remained stable on cut fibers or after tensile tests (indicated by arrows where visible). This could be a result of coating delamination or non-uniform coverage before cutting or tensile tests.

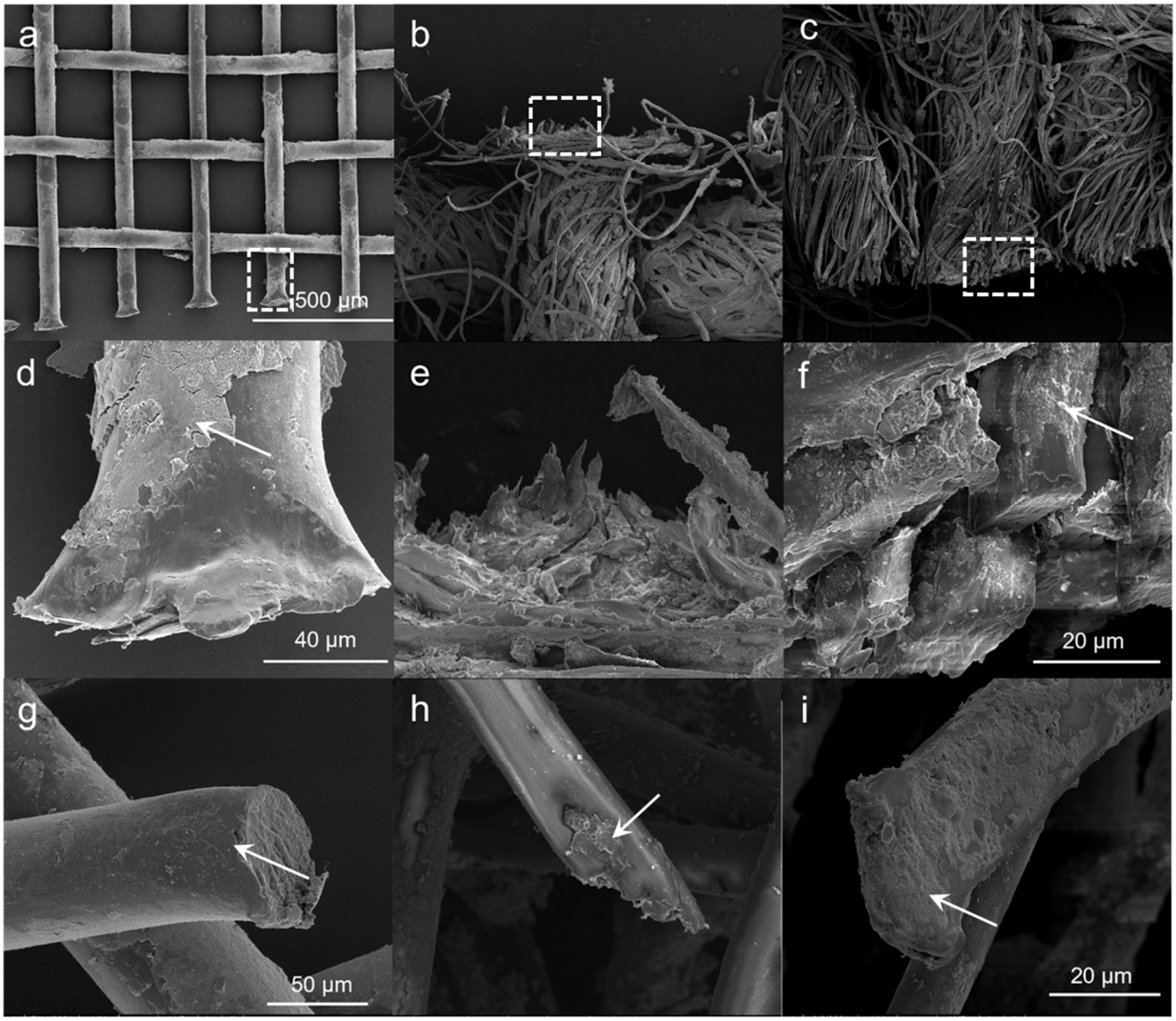

Figure 6.10. Representative FE-SEM images (SE) for HA-coated cut sections: (a, d) PEEK, (b, e) cotton-PMMA, and (c, f) cotton, and torn sections after tensile tests: (g) PEEK, (h) cotton-PMMA, and(i) cotton. Scale bar is 500 µm in (a, b, c), 40 µm in (d, e, g, h), and 20 µm in (f, i).

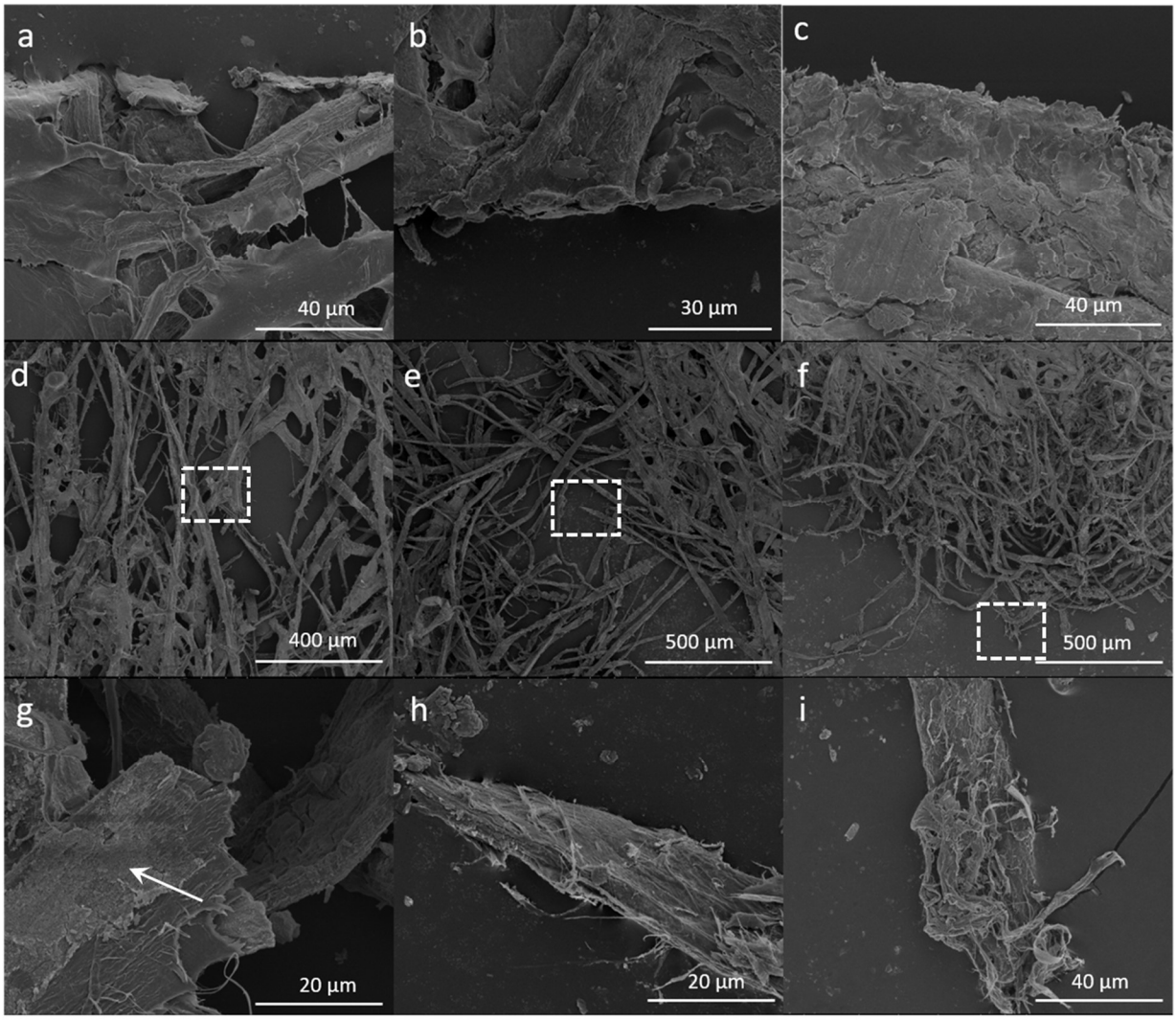

Figure 6.11. Representative FE-SEM images (SE) for HA-coated cut sections: (a) cellulose 1, (b) cellulose 2, and (c) filter-paper; and torn sections after tensile tests: (d, g) cellulose 1, (e, h) cellulose 2, and (f, i) filter-paper. Scale bar is 500 µm in (e, f), 400 µm in (d), 40 µm in (a, c, i), 30 µm in (b) and 20 µm in (g, h).

6.3.4. Discussion on tensile behavior

While cotton fabrics and cellulose mats present a wide range of mechanical properties in the literature [190–192], PEEK mesh specimens displayed the most deviation from generally expected properties for bulk PEEK [193]. This is partly based on the use of the cross-sectional area (width x thickness) to calculate properties, which ignores the actual wire areas sustaining tensile load. Corrected stress-strain curves and tensile properties were estimated based on open

area, shown in Figure 6.12. Those values are comparable to 3D printed PEEK specimens, which is a format similar to the mesh specimens, as both types are made from PEEK filaments [194,195]. In the literature, properties were found to vary from 0.25 GPa to 4 GPa for tensile modulus, from 5 MPa to 100 MPa for tensile strength, and from 2% to 135 % for strain at break. For mesh specimens, tensile strength and strain at break values are on the mid-end of those ranges, while Young's modulus is on the low-end (for bare and HA-coated specimens).

A few factors play a role in the tensile behavior of mesh specimens, compared to literature. The first one is the degree of crystallinity of the PEEK filaments [195,196]. As it increases, tensile modulus and strength are improved since polymer chains are organized and aligned along the filament axis. On the other hand, crystallinity reduces strain at break as the chains are already stretched along the filament length. The second factor is particular to mesh testing, which may affect the stress-strain curves. One challenge with tensile testing of the mesh specimens is the alignment of individual wires, even when tabs are used. This means tensile load may not be evenly distributed across all filaments, leading to consecutive failure of individual wires that were unevenly strained. This is confirmed by the progressive wire failure behavior seen in Figure 6.7a and Figure 6.12a. This behavior was also observed in the literature for tensile testing of a number of plain weave fabrics (such as polyethylene terephthalate) [188].

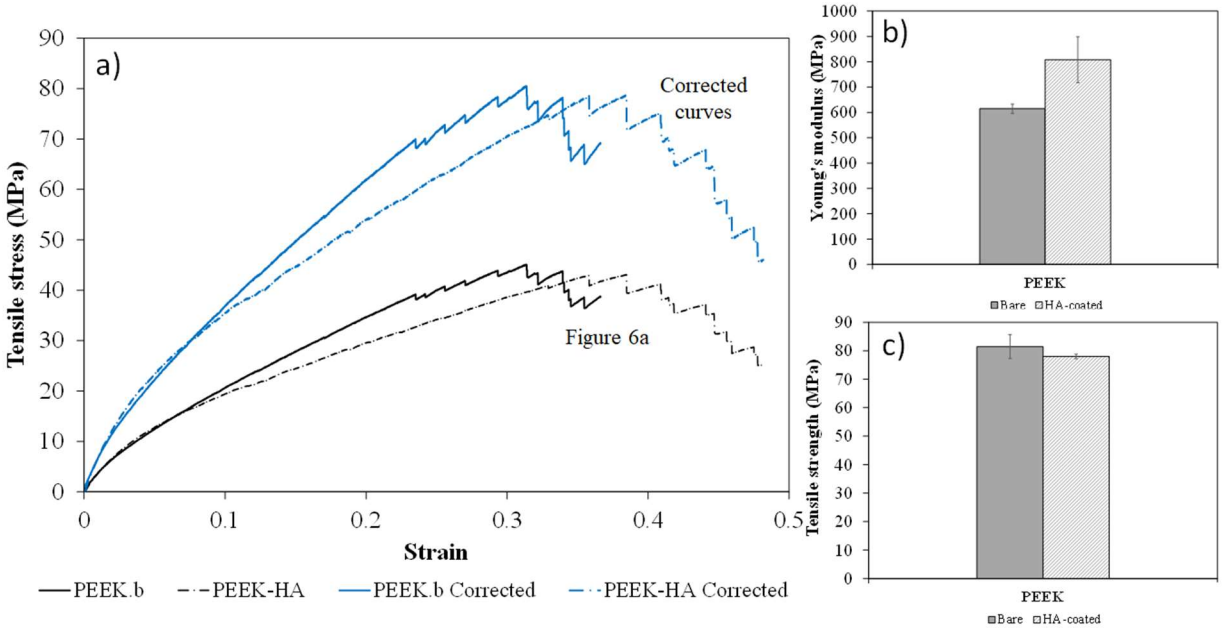

Figure 6.12. (a) Corrected stress-strain curves for bare and HA-coated PEEK mesh samples, (b) Average Young's modulus, and (c) Average tensile strength. Strain at break values are the same as presented in Fig. 6d.

Table 6.2 summarizes the statistical analysis (ANOVA) results for the main comparison pairs. The outcomes indicate that the effect of HA coating on PEEK mesh mechanical properties is not significant. Similarly, for cotton fabrics, both PMMA coating and HA coating did not have a significant effect. As was observed in Figure 6.3i,j, PMMA coated individual fibers and did not create a solid matrix around fiber bundles like a fiber-reinforced polymer. For HA coating, as seen in SEM images after tensile tests (Figure 6.10g-i), it is possible it partially delaminated during tension loading and did not play a significant role on mechanical behavior. Cellulose mats exhibited more significant effect of HA coating on mechanical properties, for the following cases: cellulose 1 (Young's modulus and strength) and filter-paper (strength). As cellulose 1 possessed the highest porosity (Figure 6.6) and the widest fiber diameter distribution (Figure 6.5c), it is expected that HA coating would have a more significant effect on mechanical properties as it reduced porosity by over 50%. Filter-paper mats, on the other hand, displayed lower tensile

strength for HA-coated specimens. This may be explained by the small increase in porosity after HA coating (Figure 6.6). While the denser structure of the filter-paper, compared to cellulose 1 and 2 mats, may have led to generally higher mechanical properties, it is not well-suited for HA-coating through a sol-gel method, as explained in section 6.3.2 for the porosity measurements. Overall, HA coating did not significantly reduce mechanical properties of the PEEK mesh, cotton fabric and cellulose mats (expect filter-paper).

Table 6.2: Summary of *p*-values from statistical analysis (ANOVA) for main comparison pairs. Highlighted gray cells indicate significance (level set to $p < 0.05$).

	Elastic modulus	Tensile strength	Strain at break
PEEK.b vs HA	0.1245	0.4315	0.5633
Cotton.b vs HA	0.0960	0.9853	0.4065
Cotton.b vs Cotton-PMMA.b	0.3078	> 0.9999	0.3940
Cotton-PMMA.b vs HA	0.7069	> 0.9999	0.3841
Cellulose1.b vs HA	0.0159	0.0014	0.8881
Cellulose2.b vs HA	0.9889	0.9125	0.8854
Filter-Paper.b vs HA	0.1893	0.0355	0.9986

6.4. Conclusions

In this study, two types of materials (PEEK and cellulose) and three different scaffold structures (mesh, fabric and mat) were investigated with respect to their mechanical behavior, with and without HA coating. First, it was demonstrated that pure HA powder can be synthesized by sol gel method at low temperature (90 ºC and 150 ºC) for compatibility with polymeric substrates (coating process below their glass transition temperature). Secondly, coating uniformity was achieved on PEEK meshes, due to their smoother surface and structure, compared to cellulose-based substrates. Nonetheless, porosity of most substrates decreased after HA coating, indicating effective coating. Filter paper cellulose mats were however not well suited for HA coating, as they filtered out the sol during the process. Finally, HA coating did not negatively affect the tensile properties of all specimen types, except filter paper cellulose mats (tensile strength decrease of 13.3 %). Overall, highest elastic modulus was obtained for PEEK meshes and filter-paper mats,

and highest tensile strength and strain at break for PEEK meshes, due to the polymer's bulk properties. As PEEK meshes exhibited high mechanical properties and uniform HA coating (6.6 % ± 1.0 % uncoated surface area), they show the most promise as scaffolds for implant applications and bone regeneration for future work.

Chapter 7 . Biocompatibility of Uncoated and HA-coated Metallic and Polymeric Woven Mesh Substrates

This chapter includes biocompatibility studies for both metallic and polymeric woven mesh substrates, as described in Chapter 5 and Chapter 6. In vitro studies of uncoated and HA-coated implants are presented to better understand how HA coating coverage and substrate design characteristics (i.e., mesh size, open area/porosity, material) influence the implant's performance with respect to: 1) biocorrosion in human body simulated media, 2) human cell-sample interactions, 3) cytotoxicity, 4) proliferation, and 5) osteogenic differentiation abilities. Statistical analysis was done as described in Chapter 5, section 5.2.8.

7.1. Materials and methods

7.1.1. Materials

The description of metallic and polymeric woven mesh substrates studied in this chapter, along with sample coding, is shown in Table 5.1 and Table 6.1, respectively.

7.1.2. Hank's Salt Solution Immersion Test for Metallic Mesh Samples

Biocorrosion test was performed by immersion in Hank's salt solution [98,168] for all HA-coated metallic mesh samples (all conditions defined in Table 5.1) for 48 h at 37 °C. The sustainability and morphology of samples in marked areas were examined by optical microscopy (Meiji Techno MT8100F) before and after immersion in Hank's salt solution.

7.1.3. Swelling Ratio and Degradation Rate for Polymeric Mesh Samples

Based on the porosity and tensile tests results (Chapter 6, section 6.3.3), three substrate types were selected for swelling ratio and degradation rate studies: PEEK, cotton-PMMA, and

---

Part of this chapter was previously published as A. Naderi, B. Zhang, J.A. Belgodere, K. Sunder, G. Palardy, Improved Biocompatible, Flexible Mesh Composites for Implant Applications via Hydroxyapatite Coating with Potential for 3-Dimensional Extracellular Matrix Network and Bone Regeneration, ACS Appl. Mater. Interfaces. 13 (2021) 26824–26840. doi:10.1021/acsami.1c09034. https://pubs.acs.org/doi/abs/10.1021/acsami.1c09034

Cellulose 1 mat (highest, medium, and lowest values for each category). Swelling ratio was determined by the difference between the substrate's weight (for both bare and HA-coated) before and after immersion in PBS (Phosphate-buffered saline, pH = 7.4) at 37 °C. The samples were weighted and immersed in PBS for 2, 4, 6, 8, 10, 15, 20, 30, 40, 50, 70, and 90 minutes. They were removed from the solution along with excess liquid, then weighted. The duration of the test was chosen based on the times provided by previous studies [159], and the times for degradation test, to prevent overlapping of swelling and degradation of samples at the same time. The amount of water absorbed by the scaffold was calculated based on Eq. (1), in which W_i is the initial scaffold weight and W_f is its weight after immersion:

$$Swelling\ ratio\ (\%) = \frac{W_f - W_i}{W_i} \times 100 \quad (1)$$

The degradation rate test was also performed for both bare and HA-coated polymeric substrates. For bare substrates, degradation rate was calculated based on the weight of samples before immersion and after immersion in PBS (pH = 7.4) at 37 °C, for 0, 1, 3, and 7 days. Samples were dried in an oven at 60 °C when they were taken out of the solution. Degradation rate was calculated with Eq. (2):

$$Degradation\ \ rate\ (\%) = \frac{Wd_f - Wd_i}{Wd_i} \times 100 \quad (2)$$

Where Wd_i is the initial substrate weight and Wd_f is its weight after immersion and drying in the oven.

7.1.4. Cell Culture

Biocompatibility for all HA-coated metallic samples (all conditions defined in Table 5.1, for a total of 54 samples) was studied by cell culture in well plates. A detailed timeline of all experiments and samples selected for each step related to cell culture (section 7.1.3), cytotoxicity

determination (section 7.1.4), osteogenic differentiation (section 7.1.5), and immunocytochemistry (section 7.1.6) is shown in . shows a summary of all initial sample conditions based on mesh substrate, mesh size and coating procedure. Human adipose-derived stem cells (ASCs) frozen at passage 0 (P0) were supplied by LaCell LLC (New Orleans, LA, USA). The vials were thawed in a water bath at 37 °C for 2 min and diluted with stromal medium (89% dulbecco's modified eagle medium (DMEM), 10% fetal bovine serum (FBS) and 1% anti−anti 100× antibiotic−antimycotic, all from Gibco) to remove cryoprotectant agent. Then, the samples were centrifuged at 1500 rpm for 5 min to obtain cell pellets and the supernatant was removed. The cell pellets were resuspended in stromal media and cultured until passage 3 (P3) in T flasks in incubator at 37 °C and 5% CO_2 and 95% humidity as described in literature [172,197,198].

For polymeric mesh substrates, uncoated and HA-coated samples from each material and substrate type were chosen: PEEK, Cotton-PMMA, and Cellulose 1. Those specimens were chosen based on tensile strength, porosity, and HA coating morphology presented in Chapter 6 (highest, medium, and lowest in each category). Cell type, media type and procedure were the same as the cell culture for metallic substrates, but osteogenic differentiation started after 3 days.

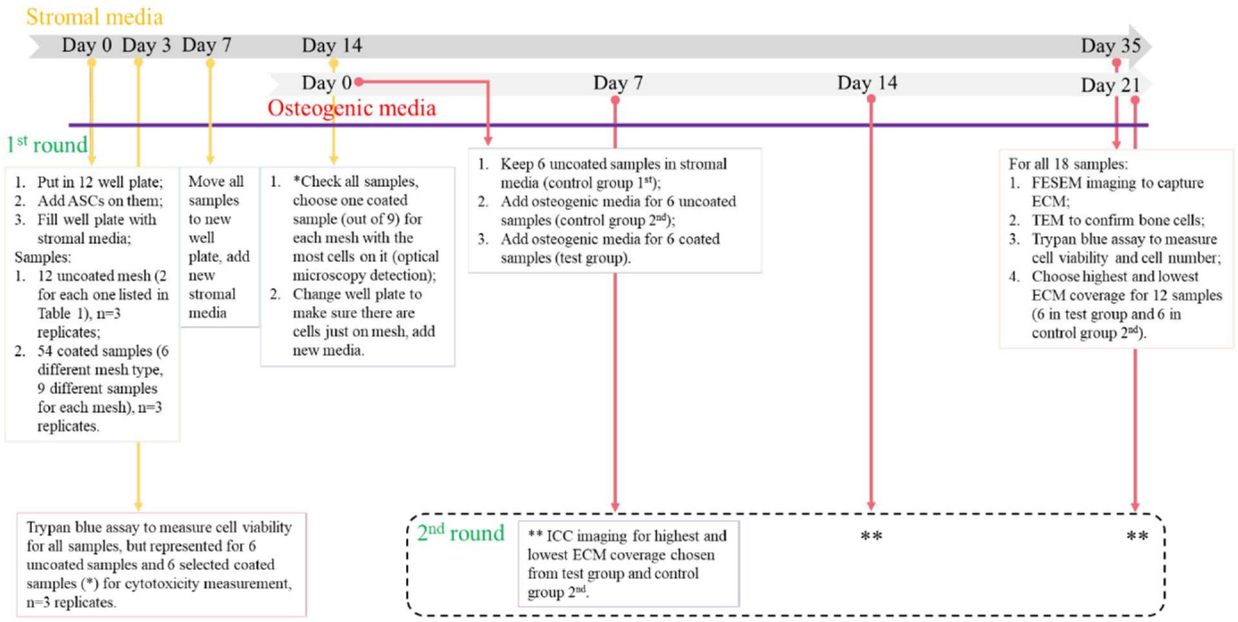

Figure 7.1. Timeline of biocompatibility experiments.

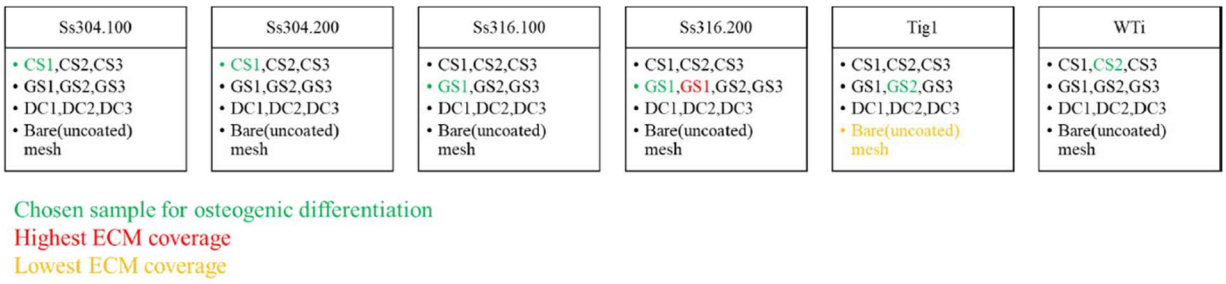

Figure 7.2. Summary of all mesh samples investigated in this study, along with those specifically selected for osteogenic differentiation (in green), and those with highest (in red) and lowest (in yellow) ECM coverage.

7.1.5. Cytotoxicity Determination

Bioactivity for all metallic bare substrates and HA-coated samples was measured by means of viability after 72 h of direct contact between ASCs and samples in 12-well plates. The test conditions were modified based on ISO 10993-5 (Biological evaluation of medical devices, Part 5: Tests for invitro cytotoxicity). Viability test was also carried out for control and test groups after 35 days to show the effect of long-time exposure of ASCs and osteogenic differentiated ASCs to

the metallic materials. Cell viability was measured by trypan blue exclusion assay [199], as other assays based on absorbance measurements (optical density, O.D.) were not accurate for metal samples. All experiments were performed for three samples (n = 3), and the results are reported for bare substrates (six samples) and the test group (six samples).

For polymeric mesh substrates, the same procedure as metallic samples was initially attempted, but failed. Therefore, live-dead staining and Almar Blue assay were used for days 1, 3, and 7 to determine cytotoxicity. The process is different from the metallic samples because of the material and structure of polymeric samples.

7.1.6. Osteogenic Differentiation

Prior to placing uncoated and coated mesh samples in well plates, they were immersed in ethanol (95%) for 72 h, then dried, and placed under UV light for 3 h in a biological safety cabinet. ASCs were transferred from T flask to 12-well plates. Each well contained one sample and 1.5×10^4 cells were placed on the sample's top surface in the well. Two control groups and one test group were defined for osteogenic differentiation tests. The first and second control groups were uncoated substrates (one for each mesh substrate material type) covered by ASCs in stromal medium. The initial study group was comprised of all samples covered by ASCs in 12- well plates in stromal media. Well plates were kept in an incubator at 37 °C and 5%CO_2 and 95% humidity during cell culture. The medium was refreshed every 3 days for all samples. All samples were moved to a new well plate after 7 and 14 days to keep cell proliferation only on the samples' surface. After 14 days, the samples with the most cells on both sides were chosen for each substrate type as the actual test group (i.e., six samples, one for each mesh substrate material type). Then, this new test group and the second control group were placed in a new 12-well plate and an

osteogenic differentiation medium (Obatala Sciences, New Orleans, LA, USA) was added to it for 21 days. The first control group was continued for 21 days in stromal media in this stage.

After day 21, a part of each metallic sample was cut and fixed for FE-SEM imaging to study the morphology and microstructure of the formed tissue layer on the sample, while the other cells were trypsinized for TEM (JEOL JEM 1400 TEM, 120 kV) and viability tests. Cell viability was measured by trypan blue exclusion assay [199]. ECM coverage on the samples was quantified in % value with respect to total area through image analysis (Image J, National Institutes of Health). All measurements were acquired for three samples (n = 3).

7.1.7. Immunocytochemistry (ICC)

As the ASCs underwent osteoblast differentiation while feeding with osteogenic differentiation medium, the bone differentiation was validated with RUNX2 and Osteopontin (OPN) genes. RUNX2 is a transcription factor induced with bone differentiation to an osteogenic lineage. It is used to direct the osteoblast and is expected to be high in the beginning of the osteogenic lineage (<14 days). Osteopontin aids in attachment of osteoclast but is not expressed in osteoclast and is used to verify mineralized bone. This gene (OPN) is mostly detectable at the end of an osteo lineage (≤21 days). It is to be noted that when a gene is detected, it can exhibit variability as different stem cells from various donors will not be induced at the same rate [200].

Immunocytochemistry was done on the surface of two samples among 12 HA-coated samples (those from the test group and second control group that had the lowest and highest ECM coverage after 21 days, identified in) and one blank well plate (ASCs only) in osteogenic differentiation medium. Using primary and secondary antibody for RUNX2 and OPN, the expression of antigen on the scaffold (mesh samples) and blank well plate was visualized for 7, 14, and 21 days of cell culture based on manufacturer protocol. RUNX2 Polyclonal Antibody with

Alexa Fluor 647 goat antirabbit IgG (H+L) and Osteopontin Monoclonal Antibody with Alexa Fluor 594 goat antimouse IgG (H+L) were used to detect osteoblast markers on the mesh samples. The nucleus and cytoskeleton of cells were dyed by Hoechst 33342 Solution (20 mM) and Phalloidin, DyLight 488, respectively. Thirty minutes after adding the last dye (Hoechst), samples were removed from the solution, washed with warm phosphate buffer saline (PBS) three times, and then, imaged using an inverted fluorescence microscope (Nikon Eclipse Ti2) and NIS Elements Advanced Research Microscope Imaging Software (NIS Elements AR, Nikon). All materials were supplied by Invitrogen, Life Technologies Corporation, USA.

7.2. Results and discussion

7.2.1. Biocorrosion and biocompatibility

Before using ASCs for cell culturing, stability and biocorrosion behavior for all samples were determined by immersion in Hank's salt solution at human body temperature (37 °C). Optical microscopy images for all samples before and after immersion for 48 hours in Hank's salt solution displayed the same morphology without any signs of coating delamination or dissolution in Hank's solution. Coating with pure or biphasic hydroxyapatite composition was stable and displayed good adhesion after contact with body fluid solution at 37 °C.

7.2.2. Swelling ratio and degradation rate of polymeric mesh samples

Swelling ratio is presented as a measurement for water absorption capacity for uncoated and HA-coated samples. shows swelling ratio (%) for all samples after 2 to 90 mins, calculated based on Eq. (1).

No clear trend is observed over time for all samples (Figure 7.3), but there are observable differences between substrate types, showing the material of the sample affects water absorbance capacity. For uncoated PEEK (PEEK.b), the swelling ratio varied between 0.61 % and 2.94 %,

while it varied from 0.05 % and 3.42 % for PEEK-HA. Swelling ratio for uncoated Cotton-PMMA was in the range of 1.16 % to 4.17 %, and 1.91 % to 3.38 % for Cotton-PMMA-HA. For Cellulose 1, the range of change was higher than PEEK and Cotton-PMMA, i.e. 3.60 % to 8.69 % for uncoated samples and 3.45 % to 9.42 % for HA-coated cellulose.

The results showed that HA coating did not affect water absorption capacity for all substrates, but the material of the scaffold was the main factor driving water absorption. PEEK, as a semi-crystalline polymer, is known to have very low water absorption capacity (in the range of 0.1 % to 0.4 %) [201]. It is however possible the mesh samples would display higher water absorption due to the porous structure. For cotton-PMMA substrates, PMMA can typically absorb up to 2 % w/w water [202]. As all cotton fibers were not fully coated with PMMA, they also contributed to the swelling ratio. Cellulose 1 had the highest water absorption capacity as its fibers are hydrophilic. Cellulose has also shown promise for wound healing applications because of its fluid absorption properties [203].

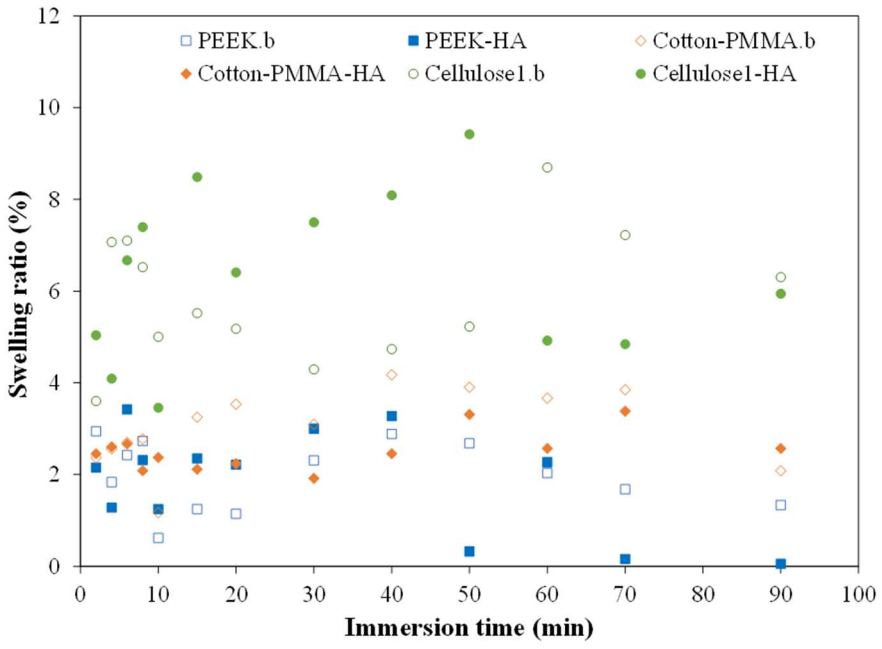

Figure 7.3. Swelling ratio (%) for uncoated and HA-coated samples after immersion in PBS at 37°C.

Degradation rate for bare and HA-coating substrates was calculated by measuring the weight of remaining material after immersion in PBS for various durations (1 to 7 days). Figure 7.4 shows the degradation rate increased by day 3 but decreased by day 7 for all uncoated and HA-coated samples. It is expected that all samples lost some fibers and sections of HA coating after day 1 and day 3, but gained ions or compounds in PBS, such as NaCl, KCl, Na_2HPO_4, and KH_2PO_4, replacing the lost mass after day 3. It is also possible for HA-coated substrates to gain compounds of calcium on the scaffold as the calcium in the hydroxyapatite coating reacted with PBS ions and deposited new calcium compounds. Degradation rate for HA-coated substrates was higher than bare ones, as HA coating can detach more easily than the substrates' fibers during the immersion.

From the results presented in Figure 7.3 and Figure 7.4, it can be concluded that substrate's material mostly affects swelling ratio, while HA coating affects degradation rate. Cellulose 1 had the highest swelling ratio, meaning it can hold more fluid than other substrates and make a hydrogel around it. Immersion time is important in degradation rate, as new compounds can deposit on scaffolds during immersion.

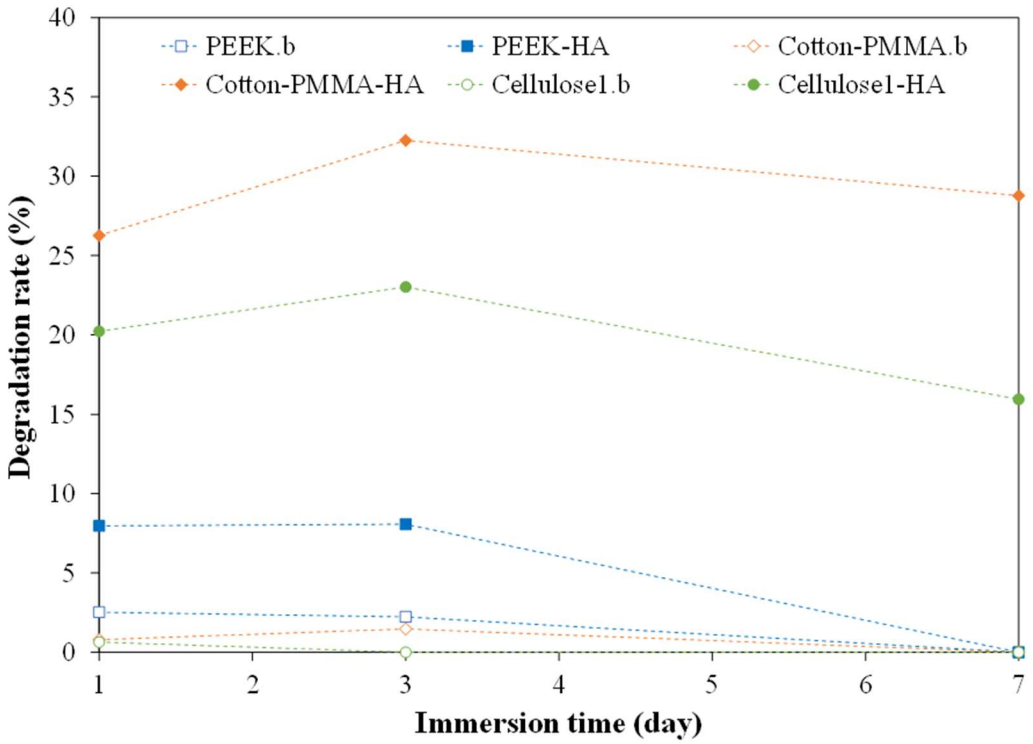

Figure 7.4. Degradation rate (%) over time for bare and HA-coated substrates after immersion in PBS at 37°C.

7.2.3. Cell viability and cell proliferation

ASCs were used based on their ease of application. They have also been used for craniofacial repair and regeneration based on a review of preclinical and clinical studies [204]. Using optical microscopy with magnification up to 10x, one HA-coated metallic sample (for each mesh substrate) with the most stem cells attached to the substrate was chosen and placed in new 12 well plates with osteogenic media for 21 days. For the test group, this resulted into the following sample selection: samples with one HA layer for stainless steel substrates and two HA layers for titanium substrates. All chosen samples were coated through the same method (dip-coating process, CS or GS). Thickness for these samples was approximately 3 μm. In the first and second control groups, the uncoated mesh for each substrate was transferred to a 12 well plate in stromal and osteogenic medium for 21 days, respectively.

For polymeric mesh samples, the control group was ASCs in stromal and osteo media cultured for 21 days, separately. The test group was uncoated or HA-coated samples in osteo media, cultured for 21 days.

7.2.3.1. Metallic mesh substrates

For cytotoxicity analysis for metallic substrates, cell viability was measured for uncoated substrates and selected HA-coated substrates (test group) after 72 hours (3 days). The timeline was chosen based on the performance of the materials, during the first days, as there were no significant changes in well plates until 48 hours. Figure 7.5a shows cytotoxic potential for uncoated/coated metal substrates is low as viability is more than 90% for the second control group (uncoated substrates) and test group (HA-coated substrates) in stromal media after 3 days. Cell viability was also calculated after 35 days for the first control group (uncoated samples in stromal media), and after 21 days for the second control group (uncoated samples in osteogenic media) and the test group (HA-coated samples in osteogenic media) at the end of the cell culture procedure. Figure 7.5b shows approximately up to 50% increase (0.5) in cell viability when using osteogenic media for control groups. Cell viability was more than 90% for all coated samples, which confirms HA coating can improve cell viability by up to 20% (0.2) in the same medium (difference between second control group and test group). The best average result (98%) was obtained for HA-coated Tig1, but all values remained within standard deviation, which suggests the material of the substrate marginally affects cell viability. There is a significant difference between uncoated and HA-coated substrates in stromal medium for ASCs and osteogenic medium for differentiated ASCs (bone cells) as $p < 0.05$ for all pairs in b.

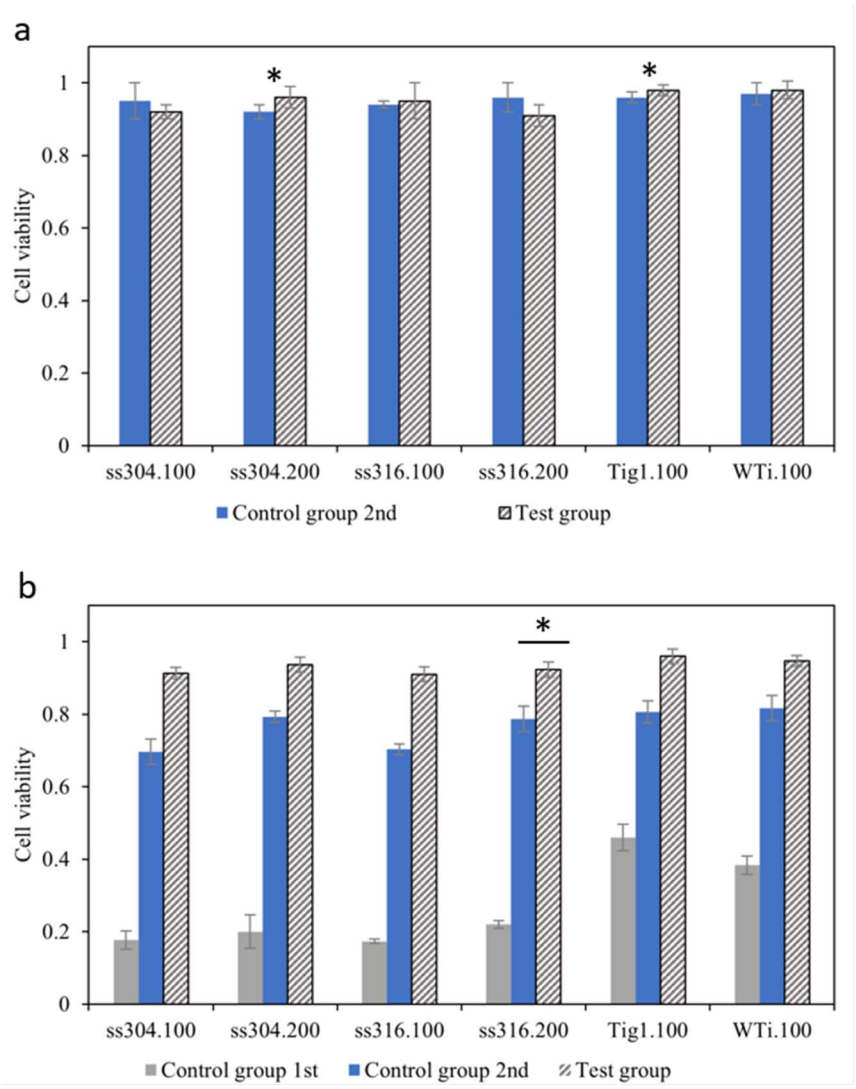

Figure 7.5. Cell viability after (a) 3 days and (b) 35 days calculated for two control groups and one test group. First control group: uncoated substrates in stromal medium for 35 days; Second control group: uncoated substrates in stromal medium for 14 days, then placed in new well plate with osteogenic differentiation medium for 21 days; Test group: HA-coated samples. Cell viability was measured using trypan blue assay. In (a), $*p < 0.05$ for two pairs, not significant for all others ($n = 3$). In (b), $*p < 0.05$ for one pair and $**p < 0.01$ for all others ($n = 3$).

After 35 days, cells were collected from the substrates' surface and counted using a hemocytometer. The values for the first control group (bare substrates in stromal media) are shown in Figure 7.6 the secondary vertical axis on the right. It can be concluded that ASCs could not survive or proliferate for 35 days in stromal media on uncoated metal mesh substrates. Although they can stay alive and differentiate on metal mesh substrates in osteogenic media, they only

exhibited partial ECM coverage after 21 days, as will be discussed in Section 7.2.4 and . HA coating increased both proliferation in stromal medium and differentiation of ASCs on metal/ceramic mesh composite substrates in osteogenic medium.

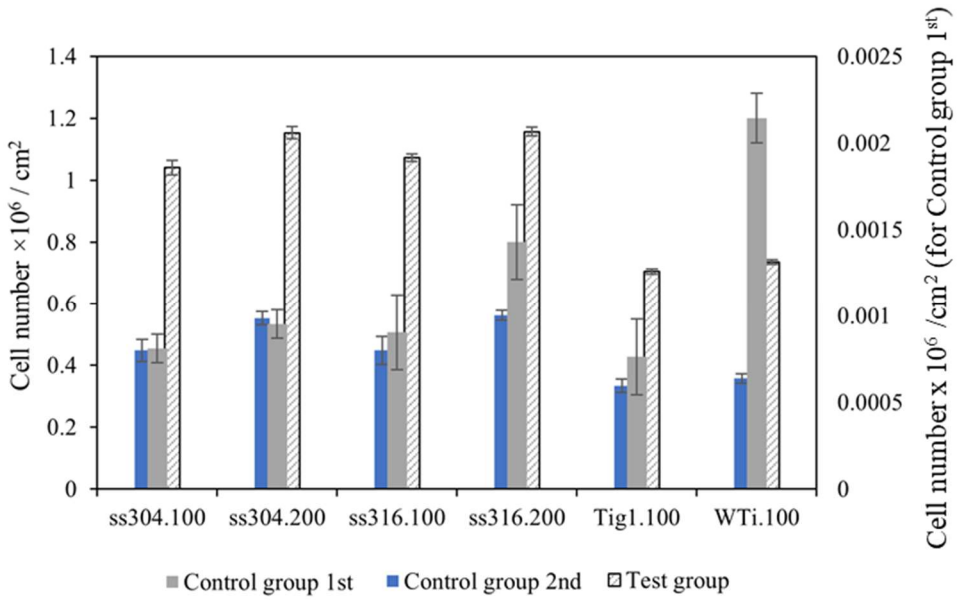

Figure 7.6. Cell numbers per substrate cm^2 after 35 days, counted for cells collected from both sides of mesh samples in two control groups and one test group. First control group: uncoated substrates in stromal medium for 35 days; Second control group: uncoated substrates in stromal medium for 14 days, then placed in new well plate with osteogenic differentiation medium for 21 days; Test group: HA-coated samples. All test group results are significant compared to both control groups (***$p < 0.001$, $n = 3$). Cell numbers were measured using hemocytometer (mean ± SD, $n = 3$).

7.2.3.2. Polymeric mesh substrates

For polymeric substrates, cell viability and cytotoxicity were analyzed visually by live-dead staining, and quantifiably by Almar Blue assay. Figure 7.7 shows live-dead staining with green and red colors for live and dead cells, respectively, for days 1, 3, and 7 of ASCs culture in stromal media. Control pictures for all days show promising results with adhesive live cell matrix and only a few dead cells. For the test samples, live or dead cells on PEEK.b or PEEK-HA are hard to distinguish. Few of them attached on the edge of the filaments. Cotton-PMMA.b shows the most live cells on day 7, while Cotton-PMMA-HA shows the most live cells on day 1. Both

uncoated and HA-coated cellulose 1 samples showed live and some dead cells for all days. Based on those pictures and visual analysis, the number of live or dead cells on all test samples are lower than the control. The results for Almar blue assay (Figure 7.8a) show the number of attached live cells on samples could not be reliably determined by this assay, as standard deviation is large (with $p > 0.05$), and there is not clear trend between days. Almar blue assay for cells attached to the bottom of the plate containing the samples, Figure 7.8b, shows the results for day 1 are not significant (with large standard deviation), as the cells are not stable after 24 hours of seeding. Day 3 and day 7 show more consistent data, with no significant difference with the control, for all uncoated and HA-coated samples.

The results show that all coated and uncoated samples are bioactive and non-toxic, as there are live cells at the bottom of the well plate after 7 days. However, there are specific issues with the polymeric substrates studied in this work for cell viability on their surface, as will be further explained in Section 7.2.4.

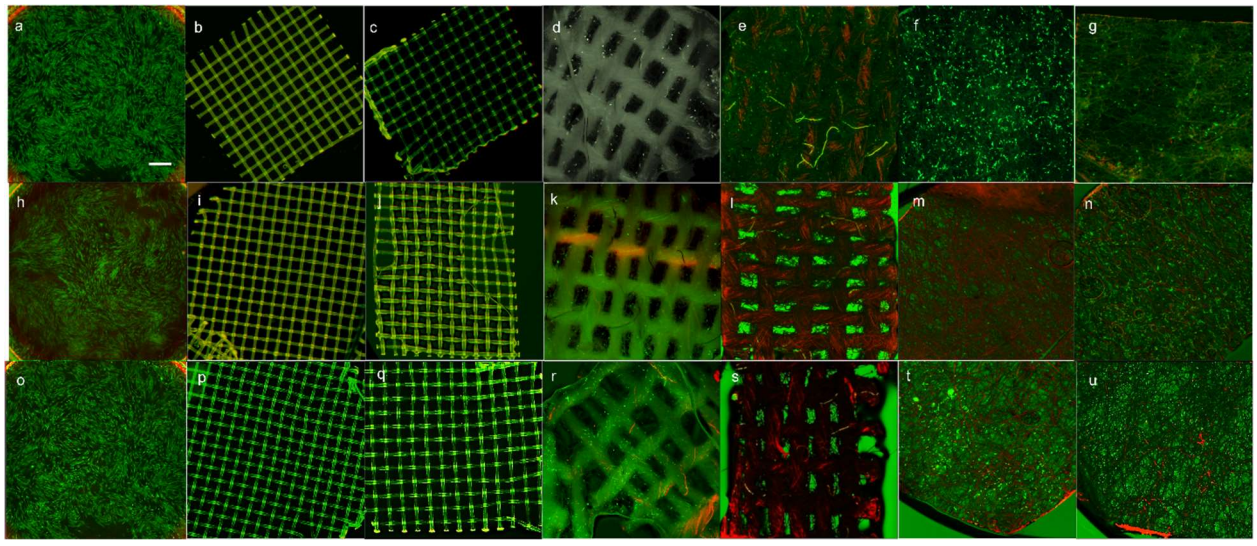

Figure 7.7. Live-dead staining for polymeric and fabric samples for ASCs in stromal media after day 1 (a-g), day 3 (h-n), and day 7(o-u). Green shows live cells, while red shows dead cells. For day 1: (a) control, (b) PEEK.b (uncoated), (c) PEEK-HA, (d) Cotton-PMMA.b, (e) Cotton-PMMA-HA, (f) Cellulose 1.b, (g) Cellulose 1-HA. The arrangement for day 3 and day 7 is the same as day 1. Scale bar is 550 µm for all images

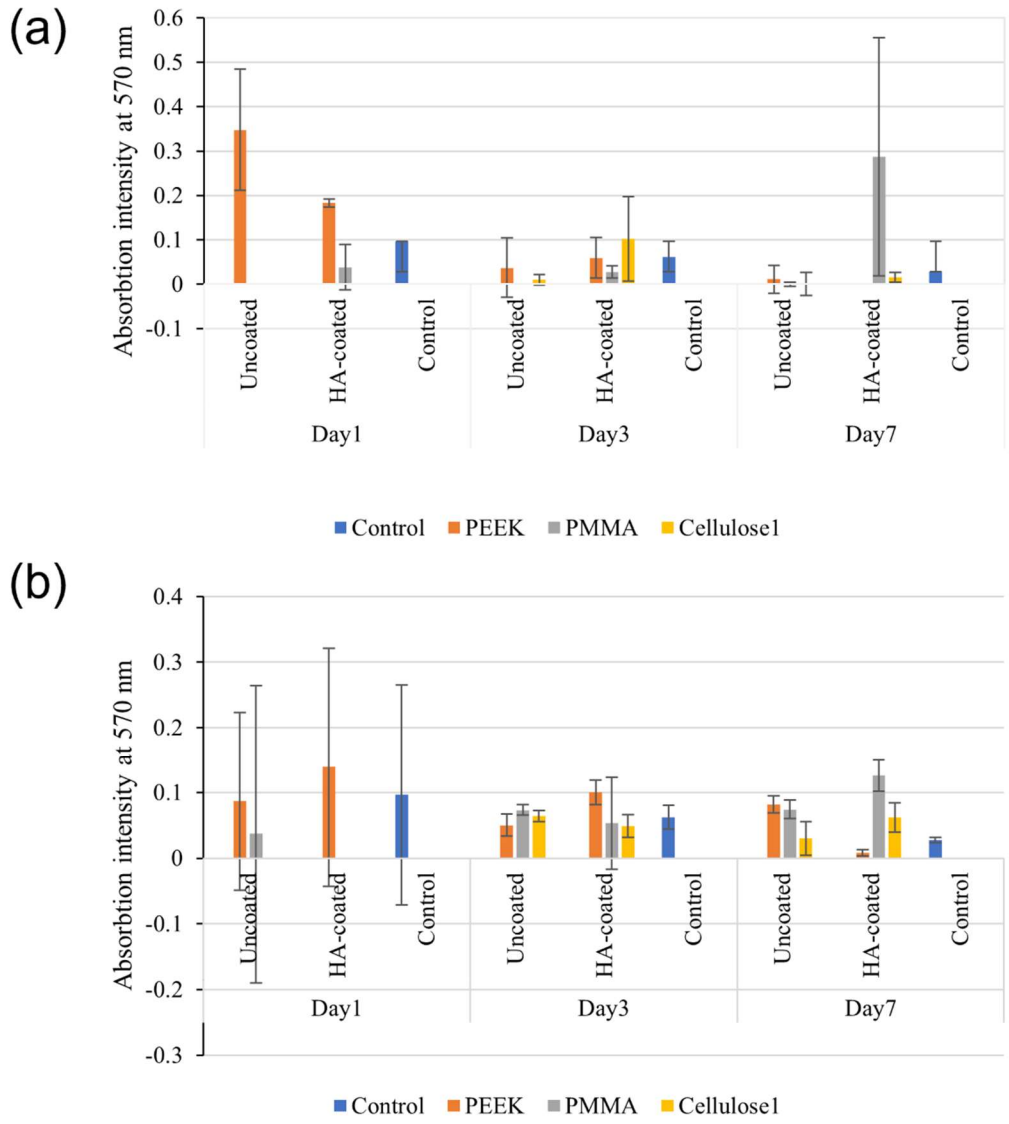

Figure 7.8. Almar blue absorption intensity (average ± standard deviation) for (a) cells attached to samples and (b) cells attached to the bottom of the well plate ($p > 0.05$).

7.2.4. Cell type and tissue surface morphology

7.2.4.1. Metallic samples

Figure 7.9a-f and show FE-SEM micrographs of ECM resulting from cell proliferation and differentiation on representative HA-coated and uncoated samples (for high and low ECM coverage). Both sides of each sample were examined under FE-SEM to confirm the 3D nature of the ECM network. Average ECM coverage % values are reported in Figure 7.9g. Overall, ECM

coverage was more uniform on ss304 and ss316 HA-coated samples with mesh size 200 (> 99.4%, a-c and g) compared to uncoated ones (< 83.1%, Figure 7.9g). ECM coverage on HA-coated ss304, ss316, titanium grade 1 and white titanium with mesh size 100 was above 93%. In those cases, the wire peaks were not covered by ECM. The ECM coverage for uncoated samples with mesh size 100 was less than 34% (Figure 7.9d,e and g). This difference shows the effect of mesh size on cell adhesion, proliferation, and ECM coverage through the mesh thickness. Collagen fibers, attached cells (Figure 7.9f and d) and porous structure of multilayered ECM (Figure 7.9b and c) were found alongside the trapped HA laminates (Figure 7.10a and b) [205–207]. The microstructure of ECM on both uncoated and coated samples was similar. In addition, apatite formed on HA films and laminates as shown in Figure 7.9f and Figure 7.10b.

Quality and coverage of ECM on HA-coated and uncoated substrates after 21 days revealed that ASCs can grow faster on substrates with HA coating for which the mesh holes remained open (as seen for % open mesh area with one or two HA layers in Figure 5.7j); cells can move from side to side and have a larger surface area to attach to and grow from. This resulted into a 3D ECM network. During imaging, it was noted that all samples were coated with nonconductive extracellular matrix. Therefore, from a design standpoint, HA-coated meshes with finer sizes and open areas above 15% would be preferable to create high ECM coverage in a 3D network.

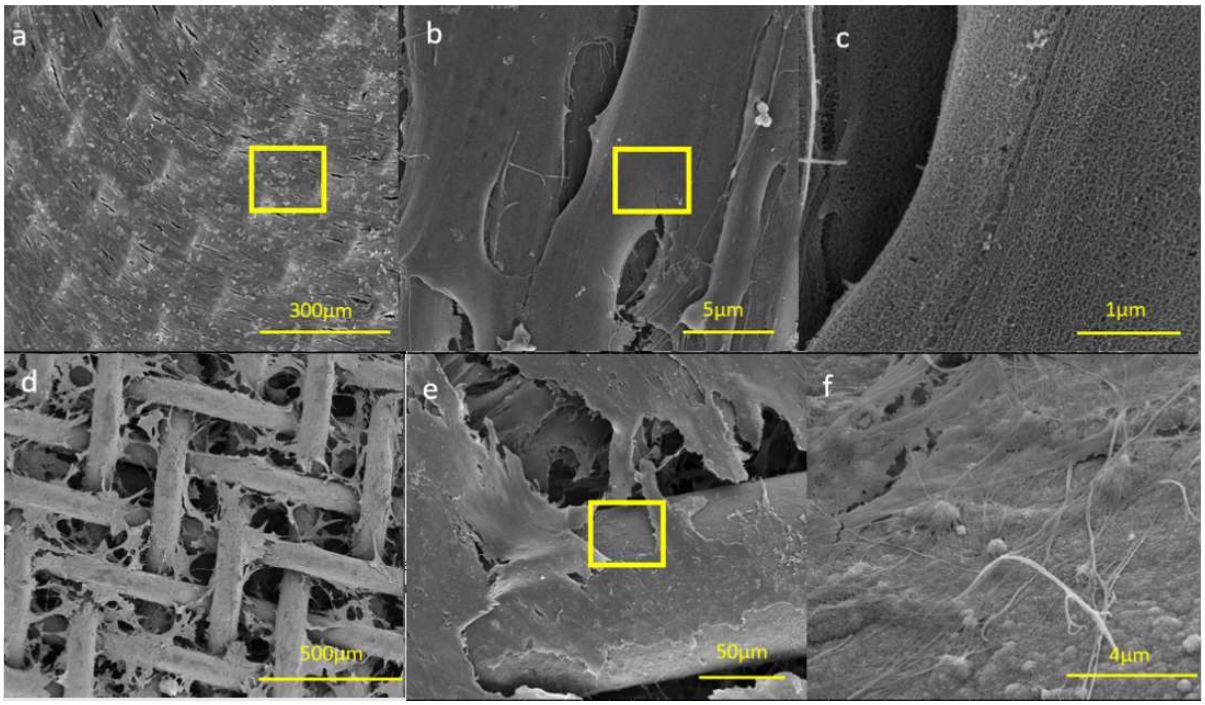

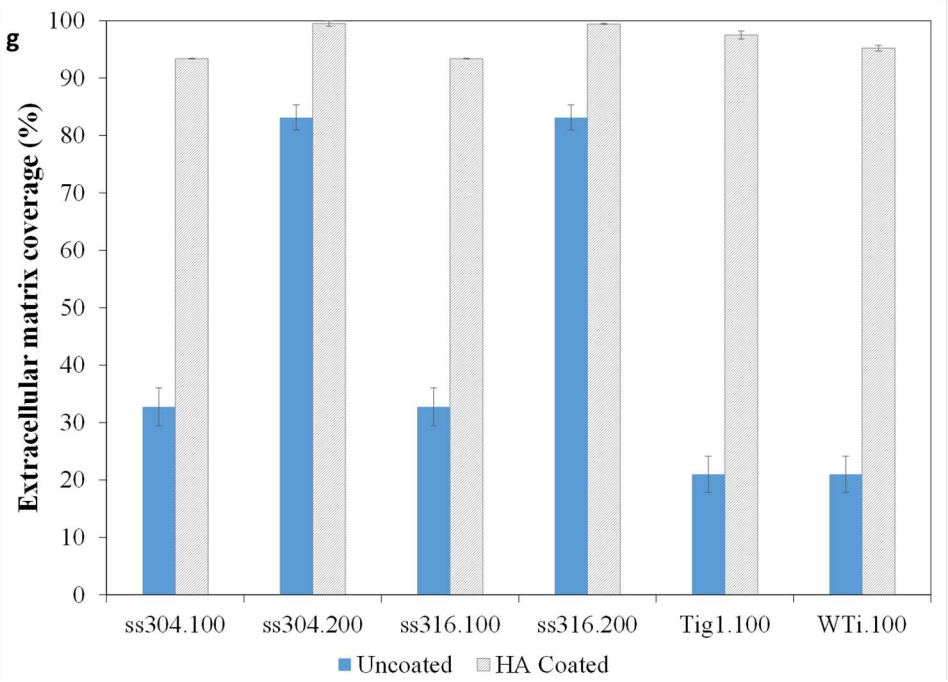

Figure 7.9**.** Representative FE-SEM images of extracellular matrix (ECM) on: (a) HA-coated mesh ss304.200 and (b, c) close ups from squared areas, (d) partial ECM coverage on bare mesh Tig1.b, (e) junction of two wires in Tig1.b, and (f) cells and apatite particle on a wire, and (g) average % coverage by ECM ($n = 3$). Scale bar is 300 µm in (a), 5 µm in (b), 1 µm in (c), 500 µm in (d), 50 µm in (e), and 4 µm in (f). All comparisons between uncoated and HA-coated pairs are significant at ****$p < 0.0001$ ($n = 3$). All comparisons among HA-coated samples are not significant (ns, $n = 3$).

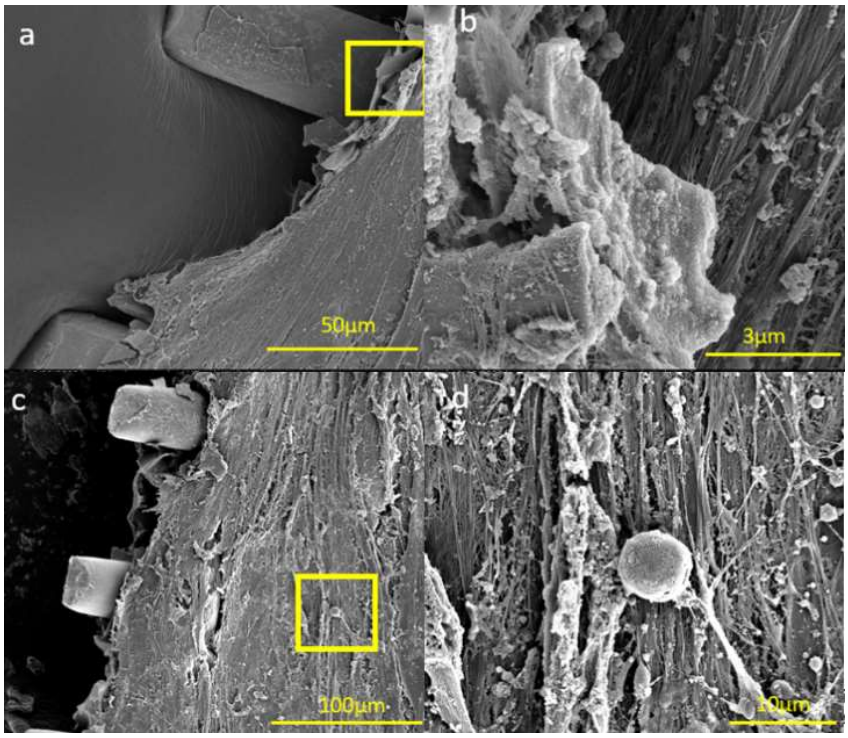

Figure 7.10**.** FE-SEM images for ECM covered mesh on both sides (a and c) and close ups of HA laminate (from squared areas) with apatite (b) and collagen fibers (d). Scale bar is 50 µm in (a), 3 µm in (b), 100 µm in (c), and 10 µm in (d).

Prior to immunocytochemistry analysis and TEM imaging, it was verified that ASCs could differentiate to bone cells by placing them into osteogenic media [169]. To observe differentiation in ASCs, antibody staining for RUNX2 (osteoblasts at beginning of culture) and OPN (osteoblasts at the end of culture) was used to confirm cellular features using DAPI (nucleus) and phalloidin (cytoskeleton).

Figure 7.11a-i show merged images for immunocytochemistry results for cells attached on the bottom of the well plate (blank well plate contained only ASCs) and on the mesh substrates for those with the lowest and highest ECM coverage (as observed in g for ss316.200 and Tig1.100). As the fluorescence images were directly acquired on the mesh substrates, some surface distortion was observed and all cells could not be captured in a single picture because of out-of-focus areas. a-c were provided as a reference for blank well plate containing ASCs only. Figure 7.11j-n show

the individual fluorescent dyes representing each part of the cells and the merged image that overlays all dyes. Fluorescent images captured for immunocytochemistry analysis showed high expression of gene RUNX2 at day 7, lower at day 14 and none at day 21 for all samples (d-f for Tig1.b and g-i for ss316.200.GS1). In reverse, OPN gene showed no presence during the first days, followed by an increased expression for day 14 and 21 for all samples. The coherency between transition from red (RUNX2) to blue (OPN) for all samples (blank well plate, Tig1.b and ss316.200.GS1) shows there is no difference in osteogenic differentiation. Thus, bare metal or HA-coated metal meshes will not affect the quality of differentiation, while HA-coated samples can have higher ECM coverage and cell attachment (Figure 7.9). The bright points in d-i indicate the position of cells on the mesh scaffold, which is mostly at the corners of the mesh openings.

TEM images (Figure 7.12) confirmed different bone cells on uncoated and HA-coated samples (second control group and test group). The diversity of cells on coated samples was higher than uncoated ones as osteogenic cells and osteoblasts were found and are represented in a-d. In d, one osteoblast is differentiating to osteocyte, but the process is not complete yet. Again, it reveals HA coating can improve cells' differentiation on metal/ceramic composite substrates. For uncoated samples, most of the cells were osteogenic cells.

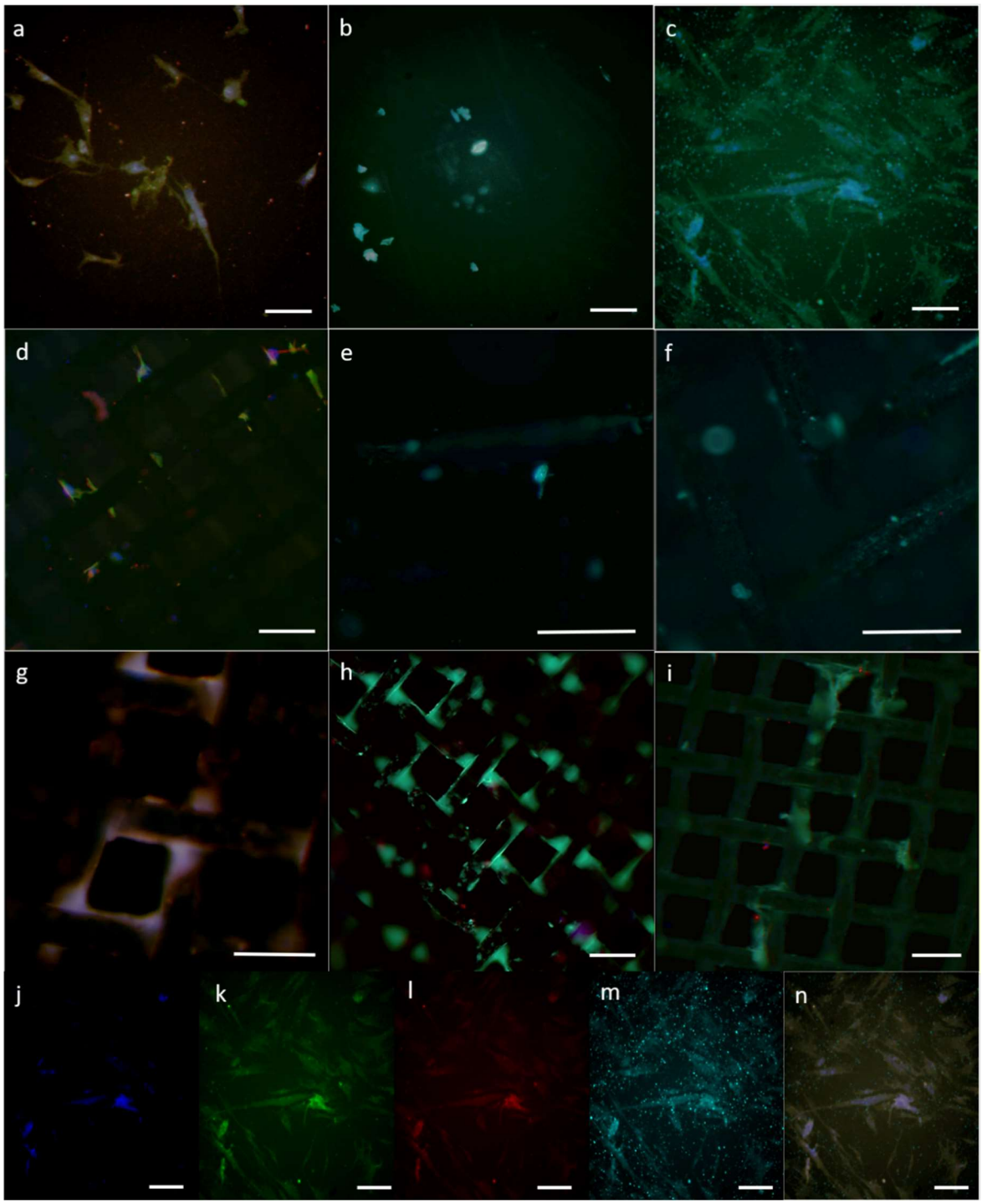

Figure 7.11. Fluorescence microscopy merged images showing nucleus, cytoskeleton, RUNX2 and osteopontin genes during osteogenic differentiation for three series of samples: blank well plate containing only ASCs for day (a) 7, (b) 14, (c) 21; bare titanium grade 1 (Tig1.b) (lowest ECM coverage) for day (d) 7, (e) 14, (f) 21; stainless steel 316. 200 (ss316.200.GS1) (highest ECM coverage) for day (g) 7, (h) 14, (i) 21. Fluorescent dyes represented for (j) nucleus, (k) cytoskeleton, (l) RUNX2, (m) osteopontin and (n) merged image from j to m. Scale bar is 200 µm for all images.

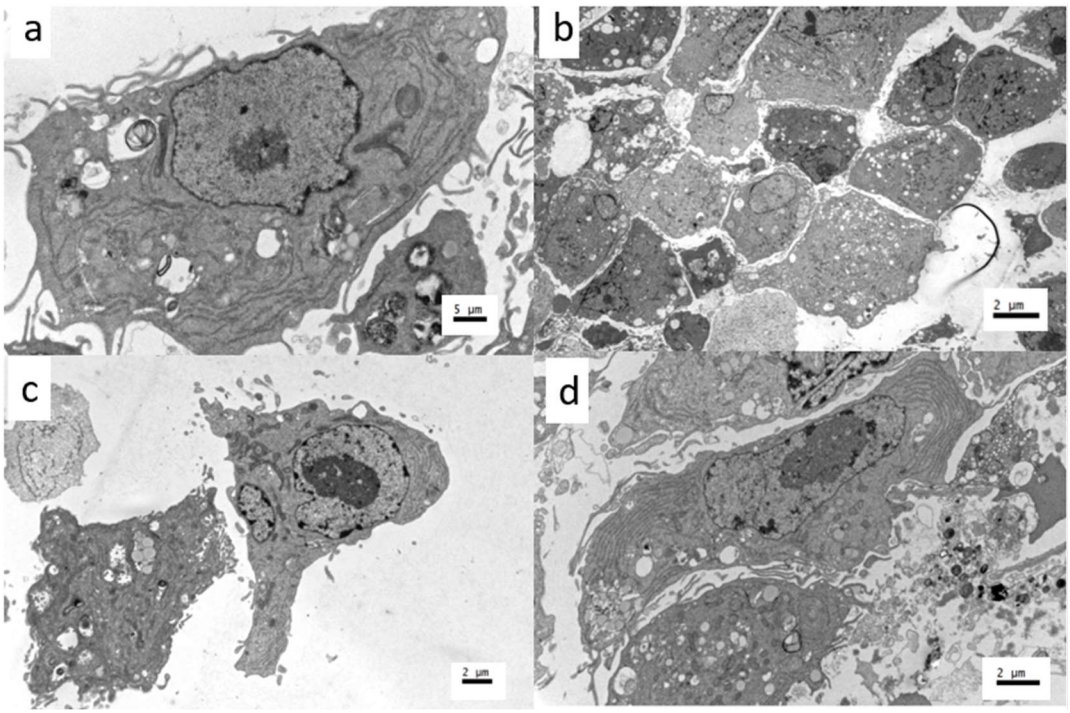

Figure 7.12**.** TEM images of bone cells collected from HA-coated samples: (a) osteogenic cell, (b and c) osteoblasts, and (d) deformed osteoblast. Scale bar is 5 µm in (a) and 2 µm in all others.

7.2.4.2. Polymeric samples

There was no ECM matrix on scaffolds for polymeric samples after day 21. Thus, no FE-SEM or TEM pictures are represented. There are a few possible reasons. First, water absorption of cellulose 1 and cotton-PMMA samples, as well as their structure, may have prevented the medium to circulate properly inside the scaffolds. Therefore, cells died because of lack of food, not necessarily cytotoxicity. Second, PEEK substrates are more rigid and less water absorbent than cotton and cellulose samples, and cells can thus feed on its surface. However, the problem with PEEK coated or uncoated mesh is that the mesh size is large (mesh 86 with 220 µm open areas), and the cells cannot attach to the scaffold while seeding. It takes time for them to move up from the bottom of the well plate after reaching confluency and to step up on the filaments. The effect

of open area size is consistent with the superior results obtained for metallic mesh, as mesh sizes were in the range of 100 to 200 (open areas between 86 μm and 152 μm). For PEEK meshes, HA coating did not reduce opening size, as was the case for metallic meshes. Another reason is that, during osteogenic differentiation, cells make bone cells, which tend to attach to hard substrates like bone. In this situation, the hardest substrate was PEEK, so they move from bottom of the well plate to PEEK, attach on it and proliferate.

Additional confirmation of cell type and presence was performed through fluorescence microscopy. Figure 7.13 shows merged images for immunocytochemistry results for cells attached on the bottom of the well plate (blank well plate contained ASCs only) as control groups and on the mesh substrates as test groups for PEEK and Cellulose 1. Results for Cotton-PMMA are not represented as the matrix interfered with fluorescence dyes and nothing could be recognized. Figure 7.13a-c show nucleus and cytoskeleton staining for all days for ASCs in stromal media, without any change in color during 21 days. The control shows there is no osteo differentiation in stromal media. The best pictures are represented in Figure 7.13d-f for ASCs is osteo media. Color change is obvious as the image shows blue and green, with some purple, after 7 days. After 14 days, the image includes all colors and shows the existence of both RUNX2 and OPN, while at day 21, it mainly shows OPN in multilayered ECM.

Comparing the images for polymeric samples with the osteo control, Figure 7.13i shows the same color tune for PEEK.b for day 21. It represents osteo differentiation contains OPN, while few cells are obvious for day 7 and 14 (Figure 7.13g,h). For PEEK-HA, on day 14 (Figure 7.13k), a thin layer containing cells with similar color as the osteo control for day 14 is observed. For Cellulose 1, it seems cells from the bottom of the well plate reached the surface of the sample for day 21, as the color tune is similar to the osteo control at day 21 (Figure 7.13o). Cells show a color

tune similar to osteo control for day 14 in Figure 7.13r for Cellulose 1-HA, which indicates a delay in osteogenic differentiation.

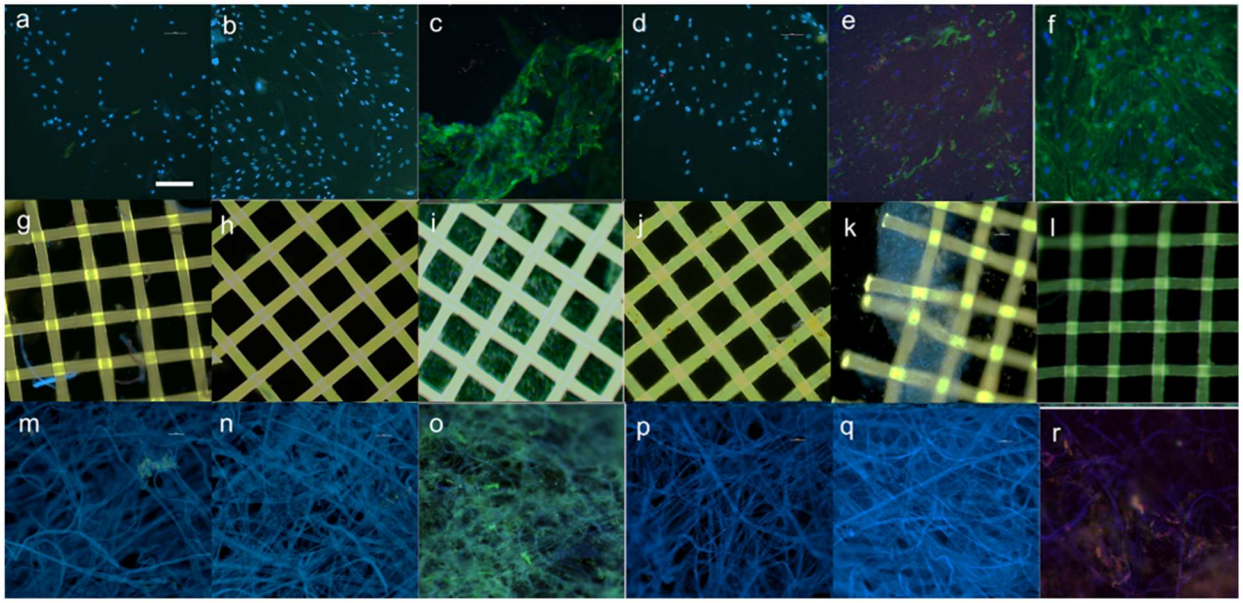

Figure 7.13. Fluorescence microscopy merged images showing nucleus, cytoskeleton, RUNX2 and osteopontin (OPN) genes during osteogenic differentiation for six series of samples: blank well plate containing only ASCs in stromal media for day (a) 7, (b) 14, (c) 21; blank well plate containing only ASCs is osteo media for day (d) 7, (e) 14, (f) 21; PEEK.b sample for day (g) 7, (h) 14, (i) 21; PEEK-HA sample for day (j) 7, (k) 14, (l) 21; Cellulose 1.b sample for day (m) 7, (n) 14, (o) 21; cellulose 1-HA sample for day (p) 7, (q) 14, (r) 21. Fluorescent dyes colors are blue for nucleus, green for cytoskeleton, purple for RUNX2 and red for OPN. The scale bar is 225 µm for all pictures.

7.3. Conclusion

Cell culture tests showed ASCs were more likely to attach and grow on samples that had open mesh areas after coating. Cell viability was higher than 90% after 3 days in stromal media and 21 days in osteogenic media. HA coating increased both proliferation and differentiation of ASCs on metal/ceramic mesh composite substrates. ECM developed into a 3D network on HA-coated samples for all mesh materials and its coverage area was between 93% and 99.5% (compared with 21% to 83% for bare substrates). Fluorescent imaging showed no antagonistic effect of the coatings on osteogenic differentiation.

For polymeric samples, uncoated and HA-coated samples are biocompatible, but their structure is not suitable for cell adhesion and growth. The effect of HA coating was not significant, and material and structure of the substrate highly affected cell behavior. Cells could not lead to ECM matrix growth on any of the polymeric mesh substrates after 21 days. There are a few possible reasons, such as water absorption and structure of cotton and cellulose substrates, which may have prevented the medium to circulate properly inside the scaffolds. Second, PEEK substrates possessed a larger mesh size than metallic meshes (mesh 86 with 220 μm open areas), preventing cells from attaching to the scaffold while seeding. This suggests mesh and open area sizes are important factors for cell adhesion.

Chapter 8 . Effect of Bed Material on Crystalline Structure, Morphology and Residue of Hydroxyapatite Powder Synthesis

8.1. Introduction

As previously described in Chapter 4, Hydroxyapatite (HA, $Ca_{10}(PO_4)_6(OH)_2$) is one of the main calcium orthophosphate compounds with excellent biocompatibility. HA powder can promote bone regeneration for implant applications, typically used alongside hydrogels, metallic/ceramic or polymer/ceramic scaffolds (Figure 8.1). Over the course of this PhD thesis, it was observed that during synthesis of HA powders, there were always powder losses or residue on the drying bed, depending on the bed type (glass beaker, aluminum cup, etc), which has potential to increase production cost and decrease production efficiency. In addition, high temperature and cooling systems for HA powder synthesis result in expensive procedures and consequently, raise the production and costumers' costs.

Figure 8.1. Hydroxyapatite powder (a), HA scaffold (b) [208,209], and titanium 3D scaffold (c) [210].

Therefore, in this chapter, a study on the effect of drying bed type and solution concentration on the characteristics of HA powder is conducted for low temperature synthesis without cooling systems. Its aim is to understand how synthesis parameters (bed material, type, solution concentration, temperature) affect HA powder crystalline structure, morphology and manufacturing process efficiency (powder residue). This will lead to identification of drying bed type for highest process efficiency with appropriate HA crystalline structure.

8.2. Materials and methods

8.2.1. Hydroxyapatite powder synthesis

HA sol was made with a calcium to phosphate precursor ratio of 1.67. HA powder was synthesized via sol-gel method as summarized in Figure 8.2. Sol preparation lasted approximately 1.5 hour. The whole process for HA sol synthesis is described in chapter 5, section 5.2.Low concentrated HA sol (LHA) was dried immediately in an oven, while the solution (LHA) was held for more than 2 hours to complete aging and gelation. Then, the supernatant solution was extracted from the beaker and a high concentrated HA sol (HHA) was made. All samples were dried in an oven at 150 °C for one hour (Figure 8.2).

LHA and HHA were dried on three types of beds:1) glass beaker, 2) aluminum cup, and 3) titanium mesh grade 1(size 100, based on Chapter 5, section 5.2). The first two bed types were chosen based on commonly available labware. The third type, titanium mesh, was selected based on substrates from Chapter 5 and its potential to act as a filter for HA powder. To collect HA powder from the titanium mesh, it was coated with LHA or HHA solution, then dried in an oven several times. The process was repeated until a thick HA coating layer could be detached from the substrate.

As the procedure was carried out at low temperature, it was hypothesized that the bed material would not affect the crystal structure of the HA powder [179], but that the physical shape of the bed could affect the crystal structure (in terms of pure HA or biphasic HA).

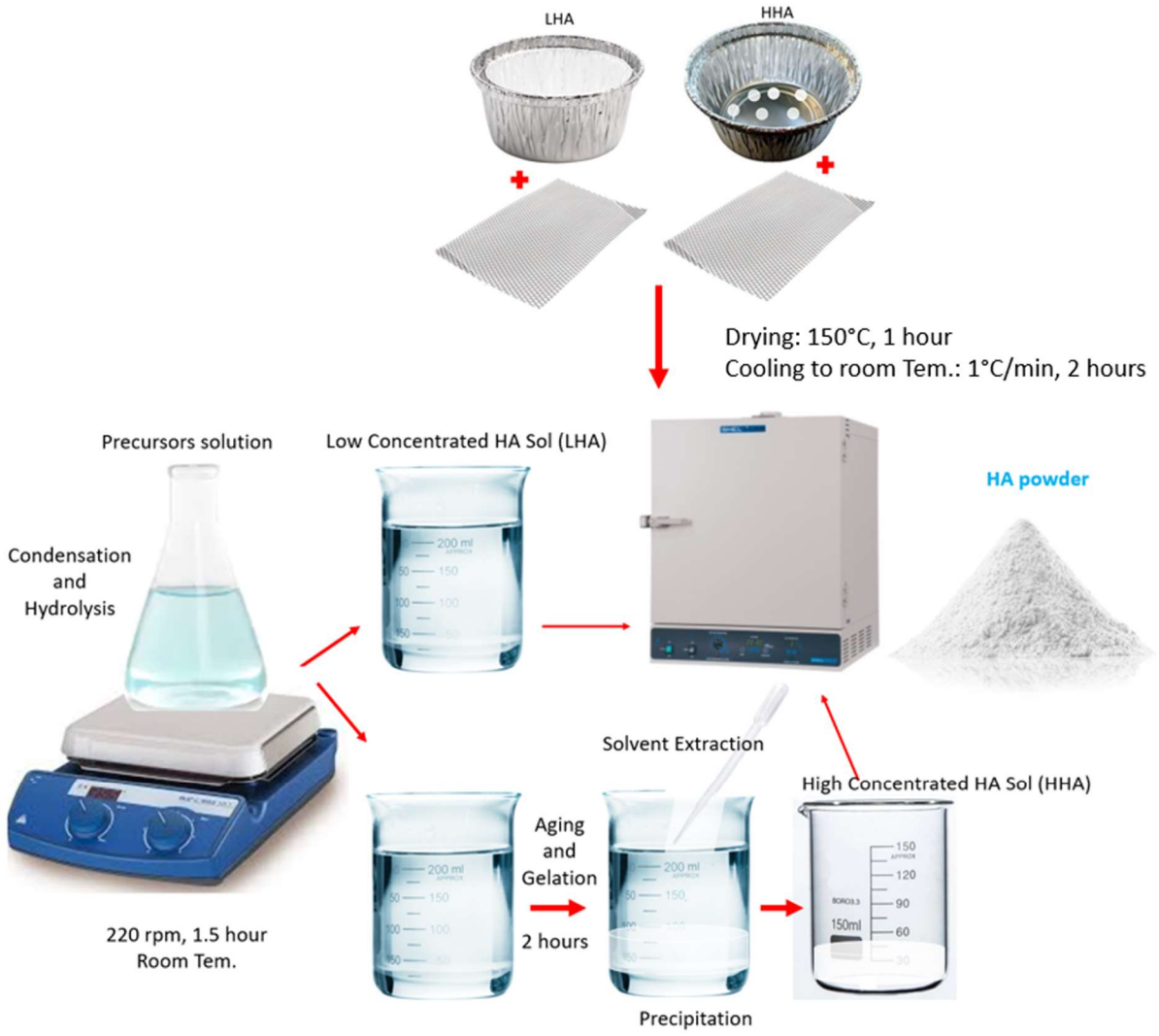

Figure 8.2. HA powder synthesis process.

8.2.2. Characterization

Characterization techniques were discussed in details in Chapter 5, section 5.2. The crystalline structure and morphology of the synthesized HA powders, as well as their residue on the different beds, were characterized through X-ray diffraction (XRD), high-resolution transmission electron microscopy (HR-TEM), field emission electron microscopy (FE-SEM), contact angle measurements (as described in Chapter 3, section 3.2), and high precision scale

(order of 10^{-4} gram). The weigh measurements were done for 3 various samples, and repeated for 3 times for each sample

8.3. Results and discussion

8.3.1. Structural and compositional analysis

A detailed description of phase formation and related peak planes was provided in chapter 5, section 5.3.1. XRD results show pure HA (the peaks with numbers) was synthesized from HHA solution on all bed types, and from LHA solution on Ti mesh substrate. Pure HA as major phase with β-TCP and CaO from LHA solution derived from glass beaker and aluminum cup. It is assumed that pure HA was synthesized from LHA solution on Ti mesh for the following reason: after coating and in the early stage of drying in the oven, the excess solvent was filtered through the mesh then evaporated, and a denser solution containing HA particles remained on the surface. Thus, LHA solution transformed to HHA solution during drying, and resulted in production of pure HA on Ti mesh.

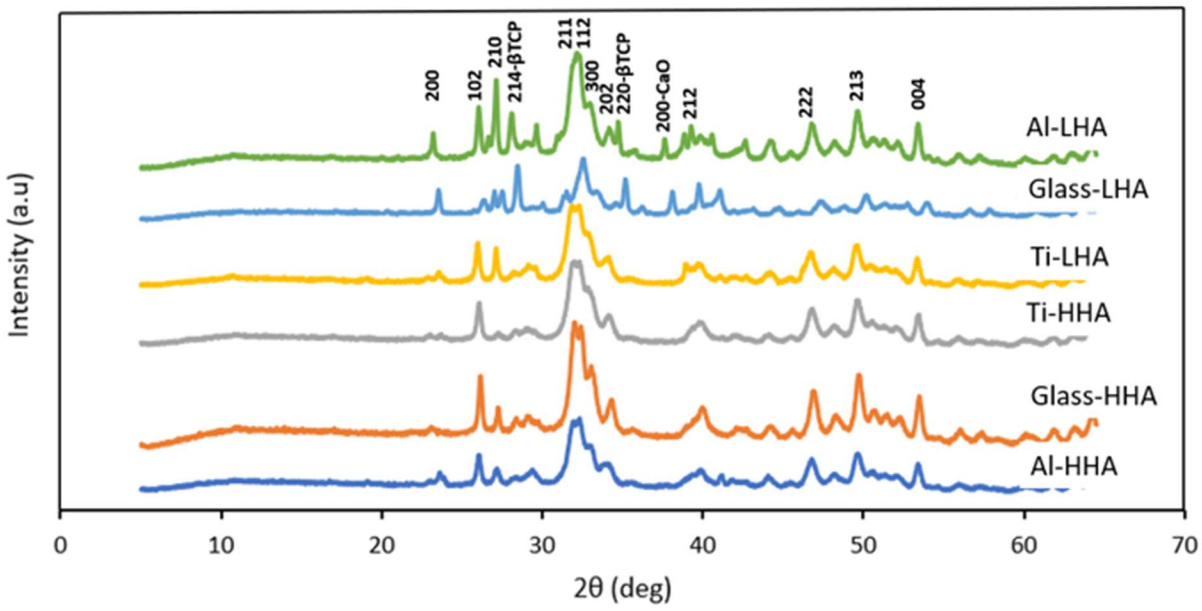

Figure 8.3. XRD patterns for HHA and LHA solutions dried on different substrates at 150 °C for one hour.

Figure 8.4 shows TEM pictures of HA powder derived from HHA or LHA solution on different bed substrates. Nanorods of pure HA as major phase with lengths from 20 nm to 80 nm, and diameters from 5 nm to10 nm, were derived from both HHA and LHA on all beds. The most brilliant planes for pure HA were d = 0.34 nm (002) (Figure 8.4g), d = 0.31 nm (102) (Figure 8.4h), and d = 0.81 nm (100) (Figure 8.4h). For the range of drying bed types and initial solutions investigated in this study, crystal structure and size were not affected. However, as shown in previous study and literature, drying temperature may affect crystal structure and size [153,160].

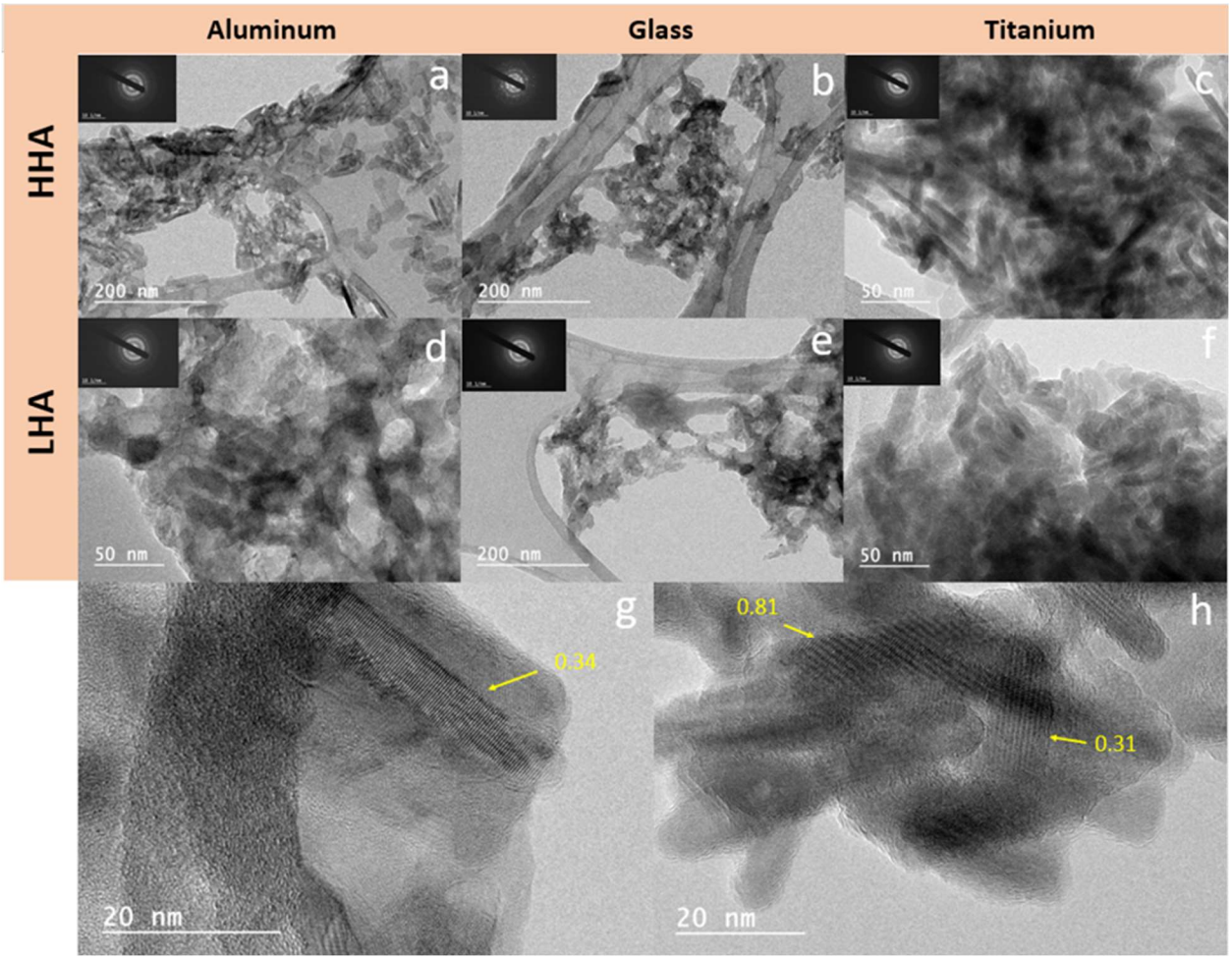

Figure 8.4. TEM pictures of HA powder derived from HHA solution on a) aluminum, b) glass, c) titanium, and from LHA solution on d) aluminum, e) glass, f) titanium. Representative images of HA powder to show plane indices (g and h).

8.3.2. Morphology and elemental distribution

Figure 8.5 shows FE-SEM pictures of HA-derived powder on various bed materials and types. Aluminum and titanium, as metals, have higher thermal conductivity than glass (Alu: 239 $Wm^{-1}k^{-1}$, Ti: 17 $Wm^{-1}k^{-1}$, Pyrex glass: 1.30 $Wm^{-1}k^{-1}$, and hydroxyapatite: 1.2 $Wm^{-1}k^{-1}$) [211,212]. Higher thermal conductivity leads to more nucleation sites on the bed surface for sol, creating a powder with smaller particle size and denser structure on the surface for aluminum. In contrast with aluminum, HA powder synthesis on Pyrex glass beaker has the same particle size but the nano particles are accumulated on top of each other (as thermal conductivity for both glass and hydroxyapatite are the same), make a big sphere with 8µm diameter (Figure 8.5b). As sintering does not happen at low temperature (150 °C), the particle size only depends on nucleation sites and particle growth. In general, HA powder with the same morphology was derived on various beds. This shows the bed can affect the porosity of HA powders. Homogeneous elemental distribution for Ca and P in HA powder from HHA and LHA sol derived from all beds is shown in Figure 8.6, confirming uniform HA existence in all powders.

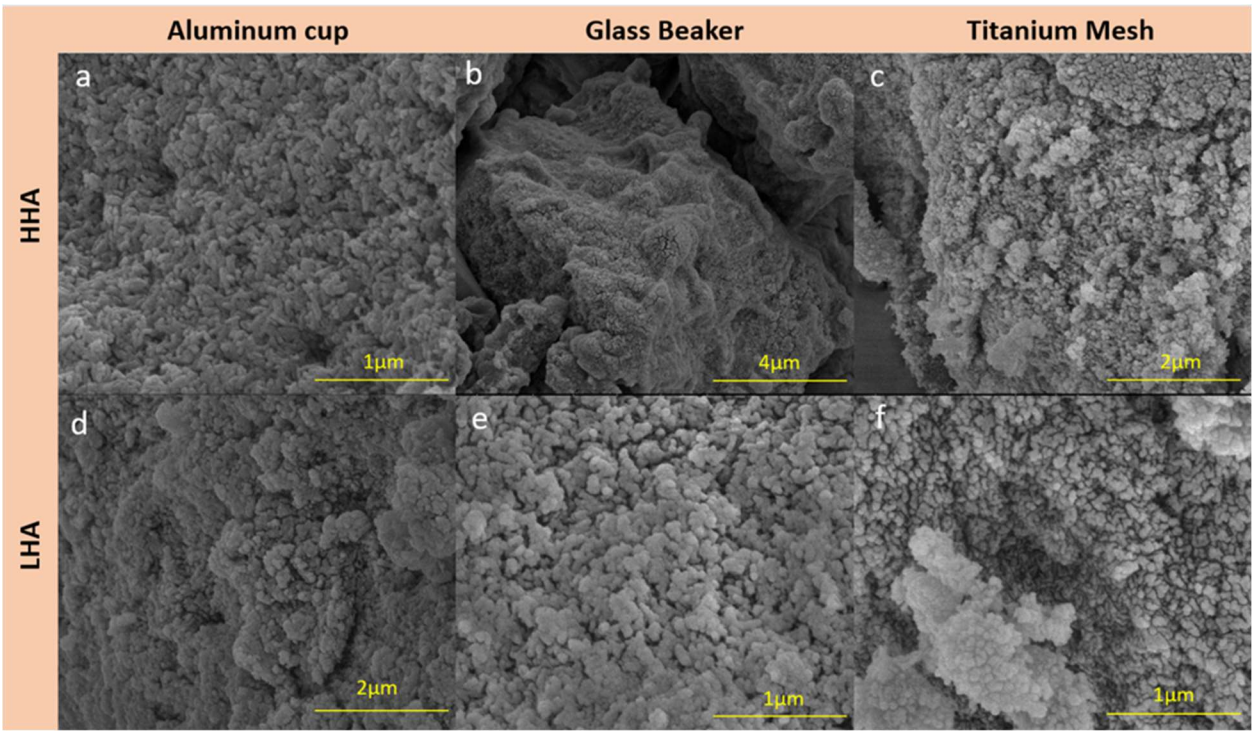

Figure 8.5. FESEM pictures of HA powder derived from HHA solution on a) aluminum, b) glass, c) titanium, and from LHA solution on d) aluminum, e) glass, and f) titanium.

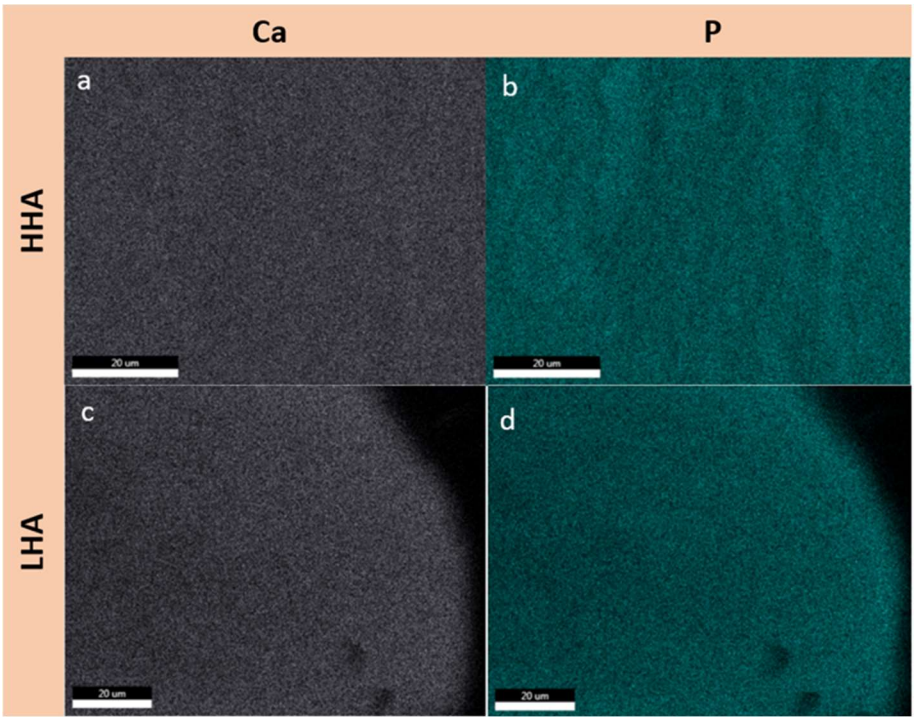

Figure 8.6. Representative EDX elemental distribution of calcium (Ca) and phosphorus (P) in HA powder got from (a and b) HHA solution on any substrate, and (c and d) LHA solution on any substrate.

8.3.3. Contact angle and powder residue

Contact angle between liquid and the solid bed is a good predictor for coating or powder adhesion on a substrate after drying. Thus, wetting contact angle is a key factor to determine if there will be a residue. Table 8.1 presents initial contact angle, between the liquid sol and the substrate right after depositing drops of sol on the substrate. Wetting contact angle is the contact angle between liquid sol and substrate after five minutes, which remained stable before putting the samples in the oven. Mass residue (%) shows the percentage of powder attached to the substrates after scratching and removing all HA powder from the bed. Wetting contact angle was 0^{o} for both HHA and LHA on glass beaker and titanium mesh, but glass beaker has lower mass residue (about 20% lower) than titanium mesh. Titanium mesh had the highest residue due to surface morphology with open areas between wires. LHA and HHA powder dried on the aluminum cup had the lowest

mass residue among all beds, 1.8% and 34%, respectively. Therefore, aluminum cups would be recommended as a substrate for highest HA powder production efficiency. Considering the results for initial and wetting contact angle, and mass residue, it seems that alongside the wetting contact angle, surface topography, morphology and roughness should be considered.

Table 8.1. Initial contact angle, wetting contact angle and HA powder mass residue on bed substrates after powder collection.

Bed substrate	Initial contact angle		Wetting contact angle		Mass residue (%)	
	HHA	LHA	HHA	CHA	HHA	LHA
Aluminum cup	77°	0°	67°	0°	1.8	34
Glass beaker	65°	49°	0°	0°	45	56
Titanium mesh	93°	118°	0°	0°	76	73

8.4. Conclusion

Solution concentration (LHA and HHA) can affect pure or biphasic synthesis of HA powder, as the pH is different in those sols. It was concluded that nanorods pure and biphasic hydroxyapatite were derived from precipitated and calcium deficient HA sol (HHA and LHA) at low temperature from all drying bed types. Bed type was shown to affect crystal structure for Titanium mesh substrates. As they acted as a filter, pure HA was synthesized from both precipitated and calcium deficient HA sol at 150°C. Lowest HA powder residue was 1.8%, obtained on aluminum bed for high concentration sol (HHA). While glass beaker is the most popular substrate in laboratories for powder synthesis, it led to about 50% powder production efficiency for both sols.

Therefore, it is recommended to choose aluminum as a drying bed type for low temperature synthesis based on high HA powder production efficiency (> 98%) and desired crystal structure.

Chapter 9 . Conclusion

The overarching goal of this research work was to further understand how coating process parameters affect coating characteristics and performance of substrates. This is important for appropriate design toward specific applications. Two specific applications for ceramic coatings were targeted and investigated: 1) antistatic/antidust applications, and 2) biomaterial implant applications. Low cost materials and coating methods were prioritized, while focusing on thin film adhesion on the substrates and modification of application-specific properties.

9.1. Antistatic/antidust applications

Based on research questions established in Chapter 1 of this thesis, the main observations for Chapter 3 can be summarized as follows:

1. Dip-coating sol-gel method, with a solution of $ZrCl_4$ as precursor and isopropanol as solvent, is a simple, low-cost coating method, which can produce zirconia thin films on glass and polymer composite substrates.

2. Relative humidity did not affect film thickness, hardness and surface electrical resistivity. However, an increase in relative humidity decreased ZrO_2 fiber thickness and substrates wettability. A decrease in solution concentration decreased film thickness, coating hardness and wettability, but increased ZrO_2 fiber thickness, and did not affect surface electrical resistivity.

In summary, the least expensive zirconia thin film for antistatic/antidust applications can be achieved from a solution with 15 g/L $ZrCl_4$ in isopropanol, prepared by dip coating sol-gel method at 50% relative humidity and dried at 80 °C for 1 hour. Reducing precursor concentration, drying temperature, and drying time while preparing the coating at 50% relative humidity (in the range of ambient humidity) decreased the cost of antistatic thin film manufacturing.

9.2. Biomaterial implant applications

Based on research questions established in Chapter 1 of this thesis for hydroxyapatite coating on metallic (Chapter 5) and polymeric (Chapter 6) mesh substrates, the following observations were made:

1. A stable, adhesive hydroxyapatite coating covering both sides of mesh substrates can be derived by the sol-gel method. Pure or biphasic hydroxyapatite was obtained from the sol-gel method with drying temperatures at 90 °C or 150 °C, regardless of solution or substrate material. This showed suitability of the coating method for all substrate materials, including polymers with melting or glass transition temperature < 300 ^{o}C.

2. Decreasing HA solution concentration increased uniformity and coverage of HA coating. The dip coating process created more uniform coverage, while the drop casting method increased coating coverage (less than 10% open areas). Increasing number of layers increased coating coverage (above 50%) and thickness. Smaller mesh size (200 vs 100) increased coating coverage. Out of all substrate materials, stainless steel had more uniform HA coverage than titanium, PEEK, and cellulose-based mesh fabrics. For cellulose mats, HA coverage was not clearly distinguishable, but HA blocks were observed between the fibers. Overall, HA coating improved corrosion protection of stainless steel with 200 mesh size, similarly to titanium grade 1 substrates.

3. For metallic mesh substrates, HA coating reduced modulus of elasticity, in the range of human skull. HA coating was adhesive and hard enough to remain on substrates for a long time. Elastic modulus and tensile strength of polymeric mesh substrates were affected by substrate material, but HA coating did not affect the mechanical behavior of most substrates. Generally, among polymer meshes investigated in this study, PEEK is the most promising with highest mechanical properties with consistent mechanical behavior under tensile loads.

4. Open areas and HA coating on metallic mesh substrates had the most important effect on biocompatibility, and ECM formation and coverage. HA-coated samples with 20% to 30% open area derived from the dip coating method from any solution with 1 or 2 HA layers showed the highest biocompatibility (ECM coverage above 98%). 3D ECM containing bone cells was achieved after 21 days in osteogenesis media with more than 93% coverage area on both sides for HA-coated mesh substrates. For polymeric substrates, PEEK was the only substrate which displayed bone formation after 21 days, but to a lower extent than metallic substrates. All other polymeric substrates did not have live cells after two weeks, likely due to more limited food circulation through the scaffold and uneven HA coating.

5. Bed substrate material affected HA powder production efficiency. Wetting angle, related to surface roughness and HA solution concentration, could provide an indication of powder residue and manufacturing process efficiency. Overall, HA powder derived from high concentrated HA solution on aluminum had the highest efficiency (~98%).

9.3. Future work and recommendations

Based on the outcomes from the research work, the following recommendations for future work are presented:

1. For zirconia antistatic coatings, up-scaling the coating method for larger applications (e.g., home applications, large-scale composites) should be considered. It might require the use of additives (such as coupling agent) to facilitate the coating process for larger surface areas.

2. For biomaterial implant applications, future work should include *in* vivo studies for the most promising composite meshes (stainless steel and titanium meshes with ECM coverage above 98%). Moreover, PEEK meshes showed potential as polymeric implants, but further research should be performed to tailor mesh structure and mechanical properties (e.g., annealing of woven

mesh, customized weaving, exploration of 3D printing method with carbon fiber-reinforced PEEK filaments).

Appendix. Copyright Information

Copyright Information for Chapter 3

A.1. Reprint permission from the publisher for chapter 3.

Copyright Information for Chapter 5 and Chapter 7

request permission to reuse the article in PhD dissertation
1 message

IT Service Desk <support@services.acs.org> Mon, Aug 9, 2021 at 5:14 AM
Reply-To: support@services.acs.org
To: anader2@lsu.edu

Dear Dr. Naderi,

Thank you for contacting ACS Publications Support.

Your permission requested is granted and there is no fee for this reuse. In your planned reuse, you must cite the ACS article as the source, add this direct link https://pubs.acs.org/doi/abs/10.1021/acsami.1c09034, and include a notice to readers that further permissions related to the material excerpted should be directed to the ACS.

If you need further assistance, please let me know.

Best regards,
Ranjith Alexander

Ranjith Alexander
ACS Publications Support
Customer Services & Information
Website: https://acs.service-now.com/acs
Email: support@services.acs.org
Phone: 800-227-9919 | 202-872-(HELP) 4357

On August 6, 2021 4:43:50 PM PDT, 'anader2@lsu.edu' wrote:

> Dear Sir/Madam
>
> As the first author, I would like to request to reuse my published work in my dissertation, which is:
>
> The published work: https://pubs.acs.org/doi/abs/10.1021/acsami.1c09034
>
> To use the whole article
>
> In my PhD dissertation at LSU.
>
> Please let me know if it is possible.
>
> Regards
>
> Armaghan Naderi

A.2. Reprint permission from the publisher for chapter 5 and chapter 7.

References

[1] P.A. Dearnley, Surface Engineering Basics, in: Introd. to Surf. Eng., Cambridge University Press, 2017: pp. 4–34. doi:10.1017/9781139031509.003.

[2] M. Kutz, ed., Part Two: Types of Degradation, in: Handb. Environ. Degrad. Mater. (Second Ed., Second Edi, William Andrew Publishing, Oxford, 2012: pp. 887–910. doi:https://doi.org/10.1016/B978-1-4377-3455-3.00037-7.

[3] N. Birks, G.H. Meier, F.S. Pettit, Protective coatings, in: Introd. to High Temp. Oxid. Met., 2nd ed., Cambridge University Press, 2006: pp. 271–305. doi:10.1017/CBO9781139163903.012.

[4] C.C. Chang, F.H. Hwang, C.Y. Hsieh, C.C. Chen, L.P. Cheng, Preparation and characterization of polymer/zirconia nanocomposite antistatic coatings on plastic substrates, J. Coatings Technol. Res. 10 (2013) 73–78. doi:10.1007/s11998-012-9427-5.

[5] G.A. Howarth, H.L. Manock, Water-borne polyurethane dispersions and their use in functional coatings, Surf. Coatings Int. 80 (1997) 324–328. doi:10.1007/BF02692680.

[6] M. Samykano, M.R. Raza, N.A.C. Lah, W.S.W. Harun, F. Tarlochan, S.A.C. Ghani, R.I.M. Asri, Corrosion and surface modification on biocompatible metals: A review, Mater. Sci. Eng. C. 77 (2017) 1261–1274. doi:10.1016/j.msec.2017.04.102.

[7] E. Neovius, T. Engstrand, Craniofacial reconstruction with bone and biomaterials: Review over the last 11 years, J. Plast. Reconstr. Aesthetic Surg. 63 (2010) 1615–1623. doi:10.1016/j.bjps.2009.06.003.

[8] M. Mzoughi, W.W. Anku, S.O.B. Oppong, S.K. Shukla, E.S. Agorku, P.P. Govender, Neodymium Doped ZrO2-graphene Oxide Nanocomposites: A Promising Photocatalyst for Photodegradation of Eosin Y Dye, Adv. Mater. Lett. 7 (2016) 946–950. doi:10.5185/amlett.2016.6497.

[9] A.M. Shah, H. Jung, S. Skirboll, Materials used in cranioplasty: a history and analysis, Neurosurg. Focus. 36 (2014) E19. doi:10.3171/2014.2.focus13561.

[10] D. Zang, X. Xun, Ceramics Coated Metallic Materials: Methods, Properties and Applications, in: M. Mhadhbi (Ed.), Adv. Ceram. Mater., 2020. doi:10.5772/intechopen.93814.

[11] R. Yadav, M. Tirumali, X. Wang, M. Naebe, B. Kandasubramanian, Polymer composite for antistatic application in aerospace, Def. Technol. (2019). doi:10.1016/j.dt.2019.04.008.

[12] M. Gagné, D. Therriault, Progress in Aerospace Sciences Lightning strike protection of composites, Prog. Aerosp. Sci. 64 (2014) 1–16. doi:10.1016/j.paerosci.2013.07.002.

[13] M. Barletta, A. Gisario, Electrostatic spray painting of carbon fibre-reinforced epoxy composites, Prog. Org. Coatings. 64 (2009) 339–349. doi:10.1016/j.porgcoat.2008.07.020.

[14] A. Naderi, A. Dolati, A. Afshar, G. Palardy, A simple route to synthesize zirconia antistatic thin films on glass substrates and their application to polymer-based composites, Mater. Chem. Phys. 244 (2020) 122696. doi:10.1016/j.matchemphys.2020.122696.

[15] F. Corduas, D.A. Lamprou, E. Mancuso, Next-generation surgical meshes for drug delivery and tissue engineering applications: materials, design and emerging manufacturing technologies, Bio-Design Manuf. 4 (2021) 278–310. doi:10.1007/s42242-020-00108-1.

[16] L. Zhu, P. Schuster, U. Klinge, Mesh implants : An overview of crucial mesh parameters, World J. Gastrointest. Surg. 7 (2015) 226–236. doi:10.4240/wjgs.v7.i10.226.

[17] A. Naderi, G. Palardy, Low-cost synthesis of hydroxyapatite on different bed materials: crystalline structure, morphology and process efficiency (poster presentation), in: 11th World Biomater. Congr., n.d.

[18] L.E. Walp, Antistatic Agents, in: M. Howe-Grant (Ed.), Kirk-Othmer Encycl. Chem. Technol., Vol. 3 (4t, John Wiley & Sons, inc., New York, 1992.

[19] J. Pionteck, Introduction, in: Handb. Antistatics (Second Ed., 2016: pp. 1–15. doi:10.1016/B978-1-895198-95-9.50003-0.

[20] Tribocharging, Corrosionpedia. (2013). https://www.corrosionpedia.com/definition/250/tribocharging.

[21] K. Robinson, W. Durkin, Electrostatic Issues in Roll-to-Roll Manufacturing Operations, IEEE Trans. Ind. Appl. 46 (2010) 2172–2178. doi:10.1109/TIA.2010.2071270.

[22] H.B. Garrett, A.C. Whittlesey, Spacecraft charging, an update, IEEE Trans. Plasma Sci. 28 (2000) 2017–2028. doi:10.1109/27.902229.

[23] J.H. Kassebaum, R.A. Kocken, Controlling static electricity in hazardous (classified) locations, in: Ind. Appl. Soc. 42nd Annu. Pet. Chem. Ind. Conf., 1995: pp. 105–113. doi:10.1109/PCICON.1995.523945.

[24] J.P. Wagner, F. Rangel Clavijo, Electrostatic charge generation during impeller mixing of used transformer oil, J. Electrostat. 50 (2000) 31–47. doi:https://doi.org/10.1016/S0304-3886(00)00019-X.

[25] X. Yang, Z. Ni, X. Xu, J. Yang, Novel preparation of anti-static zirconia ceramic by iron infiltration at high temperature, Ceram. Int. 43 (2017) 1227–1230.

doi:10.1016/j.ceramint.2016.10.068.

[26] E. Hanatziv, No Title, (n.d.). palziv.com.

[27] M. Tolinski, 6 - Additives for Modifying Electrical Properties, in: M. Tolinski (Ed.), Addit. Polyolefins (Second Ed., Second Edition, William Andrew Publishing, Oxford, 2015: pp. 57–67. doi:https://doi.org/10.1016/B978-0-323-35884-2.00006-5.

[28] ANTI-STATIC ADDITIVES FOR POLYETHYLENE, (n.d.). https://daiaplastic.com/en/anti-static-additives-for-polyethylene/.

[29] H. Frederick, W. Li, G. Palardy, Disassembly Study of Ultrasonically Welded Thermoplastic Composite Joints via Resistance Heating, Materials (Basel). 14 (2021). doi:10.3390/ma14102521.

[30] P.-C. Ma, N.A. Siddiqui, G. Marom, J.-K. Kim, Dispersion and functionalization of carbon nanotubes for polymer-based nanocomposites: A review, Compos. Part A Appl. Sci. Manuf. 41 (2010) 1345–1367. doi:https://doi.org/10.1016/j.compositesa.2010.07.003.

[31] S. Liu, W. Yang, J. Lei, C. Zhou, Properties of nanoparticles filled soft poly (vinyl chloride) composites including antistatic plasticizer, J. Appl. Polym. Sci. 127 (2013) 3221–3227. doi:https://doi.org/10.1002/app.37753.

[32] M. Mohiuddin, Effect of Pressure and Temperature on Electrical Conductivity of CNT-PEEK Composites, in: 2012.

[33] C. Fontanesi, C. Leonelli, T. Manfredini, C. Siligardi, G. Carlo Pellacani, Characterisation of the surface conductivity of glassy materials by means of impedance spectroscopy measurements, J. Eur. Ceram. Soc. 18 (1998) 1593–1598. doi:https://doi.org/10.1016/S0955-2219(98)00072-7.

[34] R.C. GARVIE, R.H. HANNINK, R.T. PASCOE, Ceramic steel?, Nature. 258 (1975) 703–704. doi:10.1038/258703a0.

[35] R.B. Heimann, Electroceramic Materials, in: Class. Adv. Ceram., John Wiley & Sons, Ltd, 2010: pp. 253–318. doi:https://doi.org/10.1002/9783527630172.ch8.

[36] T.O. Mason, Conductive ceramics, Encycl. Br. (2008). https://www.britannica.com/technology/conductive-ceramics. Accessed 12 July 2021.

[37] A. Sinhamahapatra, J.-P. Jeon, J. Kang, B. Han, J.-S. Yu, Oxygen-Deficient Zirconia (ZrO2−x): A New Material for Solar Light Absorption, Sci. Rep. 6 (2016) 27218. doi:10.1038/srep27218.

[38] A.S. Keiteb, E. Saion, A. Zakaria, N. Soltani, Structural and Optical Properties of

Zirconia Nanoparticles by Thermal Treatment Synthesis, J. Nanomater. 2016 (2016) 1913609. doi:10.1155/2016/1913609.

[39] G.K. Paul, S. Bandyopadhyay, S.K. Sen, S. Sen, Structural, optical and electrical studies on sol–gel deposited Zr doped ZnO films, Mater. Chem. Phys. 79 (2003) 71–75.

[40] X. Wang, L. Li, X. Duan, Effects of Zr Doping on Properties of ATO Nanometer Powder, Rare Met. Cem. Carbides. 32 (2004) 4–6.

[41] B. Zhang, X. Dong, X. Xu, P. Zhao, J. Wu, Effect of annealing treatment on properties of ITO and ITO: Zr thin films, CHINESE J. NONFERROUS Met. 18 (2008) 48.

[42] J. XUE, W. LIN, R. MA, B. KANG, Z. WU, Structural, optical and electrical properties of Al-Zr codoped ZnO Transparent conductive thin films, Chinese J. Liq. Cryst. Displays. 22 (2007) 560–564.

[43] N.H. Burlingame, ELECTRO-STATIC DISSIPATIVE ZIRCONIA, 6,136,232, 2000.

[44] B. Gornika, M. Mazur, K. Sieradzka, E. Prociow, M. Lapinski, Antistatic Properties of Nanofilled Coatings, Acta Phys. Pol. A. 117 (2010) 869–872.

[45] J. Pionteck, antistatic agents in various inductrial products, in: Handb. Antistatics (Second Ed., 2016: pp. 287–357.

[46] W.D. Schindler, P.J. Hauser, 10 - Antistatic finishes, in: W.D. Schindler, P.J. Hauser (Eds.), Chem. Finish. Text., Woodhead Publishing, 2004: pp. 121–128. doi:https://doi.org/10.1533/9781845690373.121.

[47] W. Khan, P. Saini, R. Sharma, Carbon Nanotube-Based Polymer Composites: Synthesis, Properties and Applications, in: Carbon Nanotub. - Curr. Prog. Their Polym. Compos., Intech Open, 2015. doi:10.5772/62497.

[48] M.Z. Al-badra, M.S. Abd-elhady, H.A. Kandil, A novel technique for cleaning PV panels using antistatic coating with a mechanical vibrator, Energy Reports. 6 (2020) 1633–1637. doi:10.1016/j.egyr.2020.06.020.

[49] B.W.N.H. Hemasiri, J.-K. Kim, J.-M. Lee, Fabrication of highly conductive graphene/ITO transparent bi-film through CVD and organic additives-free sol-gel techniques, Sci. Rep. 7 (2017) 17868. doi:10.1038/s41598-017-18063-w.

[50] Y.-J. Lin, C.-J. Wu, The properties of antimony-doped tin oxide thin films from the sol-gel process, Surf. Coatings Technol. 88 (1997) 239–247.

[51] M. Wasim, M.R. Khan, M. Mushtaq, A. Naeem, M. Han, Q. Wei, Surface modification of bacterial cellulose by copper and zinc oxide sputter coating for UV-resistance/antistatic/antibacterial characteristics, Coatings. 10 (2020) 364.

[52] S. Zinatloo-ajabshir, M. Salavati-niasari, A Sonochemical-Assisted Synthesis of Pure Nanocrystalline Tetragonal Zirconium Dioxide Using Tetramethylethylenediamine, 662 (2014) 654–662. doi:10.1111/ijac.12269.

[53] W. Chi, S. Sampath, H. Wang, Microstructure–Thermal Conductivity Relationships for Plasma-Sprayed Yttria-Stabilized Zirconia Coatings, J. Am. Ceram. Soc. 91 (2008) 2636–2645.

[54] S.M. Chang, R.A. Doong, ZrO2 thin films with controllable morphology and thickness by spin-coated sol-gel method, Thin Solid Films. 489 (2005) 17–22. doi:10.1016/j.tsf.2005.04.076.

[55] M. Sagmeister, U. Brossmann, E.J.W. List, R. Ochs, D. V. Szabó, R. Saf, W. Grogger, E. Tchernychova, R. Würschum, Synthesis and optical properties of organic semiconductor: Zirconia nanocomposites, J. Nanoparticle Res. 12 (2010) 2541–2551. doi:10.1007/s11051-009-9823-7.

[56] I.J. Berlin, V.S. Anitha, P. V. Thomas, K. Joy, Influence of oxygen atmosphere on the photoluminescence properties of sol-gel derived ZrO2thin films, J. Sol-Gel Sci. Technol. 64 (2012) 289–296. doi:10.1007/s10971-012-2856-x.

[57] B.D. Agarwal, L.J. Broutman, K. Chandrahekhare, Analysis and Performance of Fiber Composites, 4th ed., John Wiley & Sons, inc., 2017.

[58] M. Barletta, A. Gisario, V. Tagliaferri, Electrostatic spray deposition (ESD) of polymeric powders on thermoplastic (PA66) substrate, Surf. Coatings Technol. 201 (2006) 296–308. doi:10.1016/j.surfcoat.2005.11.120.

[59] M.L. Herring, B.L. Fox, The effect of a rapid curing process on the surface finish of a carbon fibre epoxy composite, Compos. Part B. 42 (2011) 1035–1043. doi:10.1016/j.compositesb.2011.03.014.

[60] M.L. De Souza, B.L. Fox, The Surface Finish of Thermally Aged Carbon Fibre Reinforced Composites Using E-glass as a Surface Barrier, Appl. Compos. Mater. 22 (2015) 573–582. doi:10.1007/s10443-014-9424-1.

[61] F. Heshmatpour, R.B. Aghakhanpour, Synthesis and characterization of nanocrystalline zirconia powder by simple sol-gel method with glucose and fructose as organic additives, Powder Technol. 205 (2011) 193–200. doi:10.1016/j.powtec.2010.09.011.

[62] L. Liang, Y. Xu, D. Wu, Y. Sun, A simple sol-gel route to ZrO2 films with high optical performances, Mater. Chem. Phys. 114 (2009) 252–256. doi:10.1016/j.matchemphys.2008.09.007.

[63] S. Zinatloo-ajabshir, N. Ghasemian, M. Salavati-niasari, Green synthesis of Ln 2 Zr 2 O 7 (Ln = Nd , Pr) ceramic nanostructures using extract of green tea via a facile route and

their efficient application on propane-selective catalytic reduction of NO x process, Ceram. Int. 46 (2020) 66–73. doi:10.1016/j.ceramint.2019.08.231.

[64] N. Chandra, D.K. Singh, M. Sharma, R.K. Upadhyay, S.S. Amritphale, S.K. Sanghi, Journal of Colloid and Interface Science Synthesis and characterization of nano-sized zirconia powder synthesized by single emulsion-assisted direct precipitation, J. Colloid Interface Sci. 342 (2010) 327–332. doi:10.1016/j.jcis.2009.10.065.

[65] ASTM D3363-20, Standard Test Method for Film Hardness by Pencil Test, in: B. Stand., ASTM International, West Conshohocken, PA, 2020. doi:10.1520/D3363-20.

[66] ASTM D257-14(2021)e1, Standard Test Methods for DC Resistance or Conductance of Insulating Materials, in: B. Stand., ASTM International, West Conshohocken, PA, 2021. doi:10.1520/D0257-14R21E01.

[67] K.H. Haas, S. Amberg-Schwab, K. Rose, Functionalized coating materials based on inorganic-organic polymers, Thin Solid Films. 351 (1999) 198–203. doi:10.1016/S0040-6090(99)00203-5.

[68] F. Monte, W. Larsen, J.D. Mackenzie, Chemical interactions promoting the ZrO2 tetragonal stabilization in ZrO 2 – SiO 2 Binary Oxides, J. Am. Ceram. Soc. 12 (2000) 1506–1512.

[69] S. Chen, Y. Yin, D. Wang, Y. Liu, X. Wang, Structures, growth modes and spectroscopic properties of small zirconia clusters, J. Cryst. Growth. 282 (2005) 498–505. doi:10.1016/j.jcrysgro.2005.05.017.

[70] B. Babiarczuk, A. Szczurek, A. Donesz-Sikorska, I. Rutkowska, J. Krzak, The influence of an acid catalyst on the morphology, wettabillity, adhesion and chemical structure properties of TiO2 and ZrO2 sol-gel thin films, Surf. Coatings Technol. 285 (2016) 134–145. doi:10.1016/j.surfcoat.2015.11.030.

[71] L.F. Cueto, E. Sánchez, L.M. Torres-Martínez, G.A. Hirata, On the optical, structural, and morphological properties of ZrO2 and TiO2 dip-coated thin films supported on glass substrates, Mater. Charact. 55 (2005) 263–271. doi:10.1016/j.matchar.2005.05.004.

[72] S.-G. Sun, Y. Lin, Kinetics of isopropanol oxidation on Pt(111), Pt(110), Pt(100), Pt(610) and Pt(211) single crystal electrodes -, Electrochim. Acta. 44 (1998) 1153–1162. doi:10.1016/s0013-4686(98)00218-7.

[73] A.F. Mavrogenis, R. Dimitriou, J. Parvizi, G.C. Babis, Biology of implant osseointegration, J. Musculoskelet. Neuronal Interact. 9 (2009) 61–71. doi:10.1016/j.joms.2007.05.013.

[74] K. Brinkiene, J. Česniene, R. Keželis, V. Matulioniene, V. Mečius, Investigation of plasma coatings manufactured from synthesized zirconia, Medziagotyra. 14 (2008) 138–

142.

[75] S. Zinatloo-ajabshir, Z. Zinatloo-ajabshir, M. Salavati-niasari, S. Bagheri, S. Bee, A. Hamid, Facile preparation of Nd 2 Zr 2 O 7 – ZrO 2 nanocomposites as an effective photocatalyst via a new route, 26 (2017) 315–323. doi:10.1016/j.jechem.2016.11.005.

[76] Z.N. Kayani, A. Kamran, Z. Saddiqe, S. Riaz, S. Naseem, Probe of ZrTiO2 thin films with TiO2-ZrO2 binary oxides deposited by dip coating technique, J. Photochem. Photobiol. B Biol. 183 (2018) 357–366. doi:10.1016/j.jphotobiol.2018.04.051.

[77] A. Smieszek, A. Donesz-sikorska, J. Grzesiak, J. Krzak, K. Marycz, Biological effects of sol – gel derived ZrO 2 and SiO 2 / ZrO 2 coatings on stainless steel surface — In vitro model using mesenchymal stem cells, 29 (2014) 699–714. doi:10.1177/0885328214545095.

[78] N. Hameed, S.P. Thomas, R. Abraham, S. Thomas, Morphology and contact angle studies of poly (styrene-co-acrylonitrile) modified epoxy resin blends and their glass fibre reinforced composites, 1 (2007) 345–355. doi:10.3144/expresspolymlett.2007.49.

[79] R. Radha, D. Sreekanth, Insight of magnesium alloys and composites for orthopedic implant applications – a review, J. Magnes. Alloy. 5 (2017) 286–312. doi:https://doi.org/10.1016/j.jma.2017.08.003.

[80] Orthopedic Biomaterials Market Size, Share & Trends Analysis Report By Material Type (Ceramics & Bioactive Glasses, Polymers), By Application (Orthobiologics, Orthopedic Implants), By Region, And Segment Forecasts, 2019 - 2025, San Francisco, 2019. https://www.grandviewresearch.com/industry-analysis/orthopedic-biomaterials-market.

[81] N.J. Hallab, J.J. Jacobs, Orthopedic Applications, Fourth Edition, Elsevier, n.d. doi:10.1016/B978-0-12-816137-1.00071-4.

[82] X. Liu, M. Li, Y. Zhu, K.W.K. Yeung, P.K. Chu, S. Wu, The modulation of stem cell behaviors by functionalized nanoceramic coatings on Ti-based implants, Bioact. Mater. 1 (2016) 65–76. doi:https://doi.org/10.1016/j.bioactmat.2016.09.001.

[83] A. Sanan, S.J. Haines, Repairing holes in the head: a history of cranioplasty., Neurosurgery. 40 (1997) 588–603. doi:10.1097/00006123-199703000-00033.

[84] A. Aciduman, D. Belen, The earliest document regarding the history of cranioplasty from the Ottoman era., Surg. Neurol. 68 (2007) 343–349. doi:10.1016/j.surneu.2006.10.073.

[85] D. Stula, Cranioplasty Indications, Techniques, and Results, Springer International Publishing, 1984.

[86] S. Aydin, O. Training, B. Kucukyuruk, S. Aydin, G.Z. Sanus, Cranioplasty : Review of materials and techniques, J. Neurosci. Rural Pract. 2 (2011) 162–167. doi:10.4103/0976-

3147.83584.

[87] T.T. Roberts, A.J. Rosenbaum, Bone grafts , bone substitutes and orthobiologics The bridge between basic science and clinical advancements in fracture healing, Organogenesis. 8 (2012) 114–124.

[88] national center for injury prevention and control (CDC) center for disease control and prevention, SURVEILLANCE OF TBI - RELATED EMERGENCY DEPARTMENT VISITS , 2010.

[89] Head injury, (n.d.). https://www.columbianeurology.org/neurology/staywell/document.php?id=33918.

[90] J.P. Posti, Cranioplasty After Severe Traumatic Brain Injury : Effects of Trauma and Patient Recovery on Cranioplasty Outcome, 9 (2018). doi:10.3389/fneur.2018.00223.

[91] N. Acciarri, F. Nicolini, M. Martinoni, Cranioplasty : Routine Surgical Procedure or Risky Operation ?, World J. Surg. Res. 5 (2016) 22–33.

[92] W.M.A. Abd El-Ghani, Cranioplasty with polymethyl methacrylate implant: solutions of pitfalls, Egypt. J. Neurosurg. 33 (2018) 2–5. doi:10.1186/s41984-018-0002-y.

[93] A. Tasiou, K. Vagkopoulos, I. Georgiadis, A.G. Brotis, H. Gatos, K.N. Fountas, Cranioplasty optimal timing in cases of decompressive craniectomy after severe head injury: A systematic literature review, Interdiscip. Neurosurg. Adv. Tech. Case Manag. 1 (2014) 107–111. doi:10.1016/j.inat.2014.06.005.

[94] D. Wachter, K. Reineke, T. Behm, V. Rohde, Cranioplasty after decompressive hemicraniectomy : Underestimated surgery-associated complications ?, Clin. Neurol. Neurosurg. 115 (2013) 1293–1297. doi:10.1016/j.clineuro.2012.12.002.

[95] K.N. Evans, J.A. Forsberg, B.K. Potter, J.S. Hawksworth, T.S. Brown, R. Andersen, J.R. Dunne, D. Tadaki, E.A. Elster, Inflammatory Cytokine and Chemokine Expression is Associated With Heterotopic Ossification in High-Energy Penetrating War Injuries, J. Orthop. Trauma. 26 (2012) 204–213.

[96] S.A.X. Stango, D. Karthick, S. Swaroop, U.K. Mudali, U. Vijayalakshmi, Development of hydroxyapatite coatings on laser textured 316 LSS and Ti-6Al-4V and its electrochemical behavior in SBF solution for orthopedic applications, Ceram. Int. 44 (2018) 3149–3160. doi:10.1016/j.ceramint.2017.11.083.

[97] D. Qiu, L. Yang, Y. Yin, A. Wang, Preparation and characterization of hydroxyapatite/titania composite coating on NiTi alloy by electrochemical deposition, Surf. Coatings Technol. 205 (2011) 3280–3284. doi:10.1016/j.surfcoat.2010.11.049.

[98] M. Tlotleng, E. Akinlabi, M. Shukla, S. Pityana, Microstructures, hardness and

bioactivity of hydroxyapatite coatings deposited by direct laser melting process, Mater. Sci. Eng. C. 43 (2014) 189–198. doi:10.1016/j.msec.2014.06.032.

[99] R. Datti, G. Cavagnaro, S. Camici, Stainless steel wire mesh cranioplasty: ten years' experience with 183 patients (100 followed up)., Acta Neurochir. (Wien). 78 (1985) 133–135. doi:10.1007/BF01808692.

[100] N. Eliaz, Corrosion of metallic biomaterials: A review, Materials (Basel). 12 (2019). doi:10.3390/ma12030407.

[101] P.K. Vallittu, Bioactive glass-containing cranial implants: an overview, J. Mater. Sci. 52 (2017) 8772–8784. doi:10.1007/s10853-017-0888-x.

[102] T. Mikami, K. Miyata, K. Komatsu, K. Yamashita, M. Wanibuchi, N. Mikuni, Exposure of titanium implants after cranioplasty: A matter of long-term consequences, Interdiscip. Neurosurg. Adv. Tech. Case Manag. 8 (2017) 64–67. doi:10.1016/j.inat.2017.01.015.

[103] J. Parthasarathy, 3D modeling, custom implants and its future perspectives in craniofacial surgery., Ann. Maxillofac. Surg. 4 (2014) 9–18. doi:10.4103/2231-0746.133065.

[104] R. de S. LEÃO, J.R.S. MAIOR, C.A. de A. LEMOS, B.C. do E. VASCONCELOS, M.A.J.R. MONTES, E.P. PELLIZZER, S.L.D. MORAES, R. de S. LEÃO, J.R.S. MAIOR, C.A. de A. LEMOS, B.C. do E. VASCONCELOS, M.A.J.R. MONTES, E.P. PELLIZZER, S.L.D. MORAES, Complications with PMMA compared with other materials used in cranioplasty: a systematic review and meta-analysis, Braz. Oral Res. 32 (2018) 1–12. doi:10.1590/1807-3107bor-2018.vol32.0031.

[105] F.A. Muller, L. Muller, I. Hofmann, P. Greil, M.M. Wenzel, R. Staudenmaier, Cellulose-based scaffold materials for cartilage tissue engineering, Biomaterials. 27 (2006) 3955–3963. doi:10.1016/j.biomaterials.2006.02.031.

[106] P.S.D. Urso, W.J. Earwaker, T.M. Barkert, M.J. Redmond, R.G.T.D.J. Effeney, E.H. Tomlinson, Custom cranioplasty using stereolithography and acrylic, (2000) 200–204. doi:10.1054/bjps.

[107] Z.M. Qian, P. Fan, Xianqun MD, The Application and Progress of High-Density Porous Polyethylene in the Repair of Orbital Wall Defect, J. Craniofac. Surg. 25 (n.d.) 1451–1453.

[108] B. Kim, K. Hong, D. Ph, K. Park, D. Ph, D. Park, D. Ph, Y. Chung, D. Ph, Customized Cranioplasty Implants Using Three-Dimensional Printers and Polymethyl-Methacrylate Casting, (2012) 541–546.

[109] D. Garcia-Gonzalez, S. Garzon-Hernandez, A. Arias, A new constitutive model for polymeric matrices: Application to biomedical materials, Compos. Part B Eng. 139 (2018) 117–129. doi:10.1016/j.compositesb.2017.11.045.

[110] S. Verma, N. Sharma, S. Kango, S. Sharma, Developments of PEEK (Polyetheretherketone) as a biomedical material: A focused review, Eur. Polym. J. 147 (2021) 110295. doi:https://doi.org/10.1016/j.eurpolymj.2021.110295.

[111] M. Punchak, L.K. Chung, C. Lagman, T.T. Bui, J. Lazareff, K. Rezzadeh, R. Jarrahy, I. Yang, Outcomes following polyetheretherketone (PEEK) cranioplasty : Systematic review and meta-analysis, J. Clin. Neurosci. 41 (2017) 30–35. doi:10.1016/j.jocn.2017.03.028.

[112] D. Garcia-Gonzalez, J. Jayamohan, S.N. Sotiropoulos, S.H. Yoon, J. Cook, C.R. Siviour, A. Arias, A. Jérusalem, On the mechanical behaviour of PEEK and HA cranial implants under impact loading, J. Mech. Behav. Biomed. Mater. 69 (2017) 342–354. doi:10.1016/j.jmbbm.2017.01.012.

[113] Unfilled Polyetheretherketone (PEEK), (n.d.). polymerdatabase.com.

[114] AZoM, Polymethylmethacrylate - Acrylic - PMMA General Purpose, (2001). azom.com.

[115] R. Ma, D. Guo, Evaluating the bioactivity of a hydroxyapatite-incorporated polyetheretherketone biocomposite, J. Orthop. Surg. Res. 14 (2019) 32. doi:10.1186/s13018-019-1069-1.

[116] A.M. Borba, M. Miloro, A.H. Borges, F.L.M. Pedro, A.L. Fernandes da Silva, N.R. Simão, Customized Polymethyl Methacrylate Implants for the Reconstruction of Craniofacial Osseous Defects, Case Rep. Surg. 2014 (2014) 1–8. doi:10.1155/2014/358569.

[117] A.L. Ko, J.D. Nerva, J.J.J. Chang, R.M. Chesnut, Peer-Review Short Reports Traumatic Fracture of a Polymethyl Methacrylate Patient-Specific Cranioplasty Implant, World Neurosurg. 82 (2013) 536.e11-536.e13. doi:10.1016/j.wneu.2013.09.025.

[118] A.A. Abdel-wahab, S. Ataya, V. V Silberschmidt, Temperature-dependent mechanical behaviour of PMMA : Experimental analysis and modelling, Polym. Test. 58 (n.d.) 86–95. doi:10.1016/j.polymertesting.2016.12.016.

[119] R.I.M. Asri, W.S.W. Harun, M. Samykano, N.A.C. Lah, S.A.C. Ghani, F. Tarlochan, M.R. Raza, Corrosion and surface modi fi cation on biocompatible metals : A review, Mater. Sci. Eng. C. 77 (2017) 1261–1274. doi:10.1016/j.msec.2017.04.102.

[120] E. Nout, M.Y. Mommaerts, Considerations in computer-aided design for inlay cranioplasty: technical note, Oral Maxillofac. Surg. 22 (2018) 65–69. doi:10.1007/s10006-017-0668-4.

[121] P. Pooyan, R. Tannenbaum, H. Garmestani, Mechanical behavior of a cellulose-reinforced scaffold in vascular tissue engineering, J. Mech. Behav. Biomed. Mater. 7 (2012) 50–59. doi:10.1016/j.jmbbm.2011.09.009.

[122] Y. Yang, Y. Lu, K. Zeng, T. Heinze, T. Groth, K. Zhang, Recent Progress on Cellulose-Based Ionic Compounds for Biomaterials, Adv. Mater. 2000717 (2020). doi:10.1002/adma.202000717.

[123] K. Yamaguchi, M. Prabakaran, M. Ke, X. Gang, I.M. Chung, I.C. Um, M. Gopiraman, I.S. Kim, Highly dispersed nanoscale hydroxyapatite on cellulose nanofibers for bone regeneration, Mater. Lett. 168 (2016) 56–61. doi:https://doi.org/10.1016/j.matlet.2016.01.010.

[124] R.J. Hickey, A.E. Pelling, Cellulose Biomaterials for Tissue Engineering, Front. Bioeng. Biotechnol. 7 (2019) 1–15. doi:10.3389/fbioe.2019.00045.

[125] R.M.A. Domingues, M.E. Gomes, R.L. Reis, The Potential of Cellulose Nanocrystals in Tissue Engineering Strategies, Biomacromolecules. 15 (2014) 2327–2346. doi:dx.doi.org/10.1021/bm500524s | Biomacromolecules.

[126] D. Ciecholewska-ju, A. Zywicka, A. Junka, P. Sobolewski, U. Kowalska, M. Toporkiewicz, K. Fija, Superabsorbent crosslinked bacterial cellulose biomaterials for chronic wound dressings, Carbohydr. Polym. 253 (2021). doi:10.1016/j.carbpol.2020.117247.

[127] R. Riahipour, A.A. Sahraei, N. Van De Werken, M. Tehrani, mechanical properties of an epoxy using halogen-free fillers, Sci Eng Compos Mater. 25 (2018) 939–946.

[128] B. Stawarczyk, S. Taufall, M. Roos, P.R. Schmidlin, N. Lümkemann, Bonding of composite resins to PEEK : the influence of adhesive systems and air-abrasion parameters, Clin Oral Invest. 22 (2018) 763–771. doi:10.1007/s00784-017-2151-x.

[129] E.B.O. Reilly, S. Barnett, C. Madden, B. Welch, B. Mickey, S. Rozen, Computed-tomography modeled polyether ether ketone (PEEK) implants in revision cranioplasty, Br. J. Plast. Surg. 68 (2015) 329–338. doi:10.1016/j.bjps.2014.11.001.

[130] A. Yelten-Yilmaz, S. Yilmaz, Wet chemical precipitation synthesis of hydroxyapatite (HA) powders, Ceram. Int. 44 (2018) 9703–9710. doi:10.1016/j.ceramint.2018.02.201.

[131] S. V. Dorozhkin, Bioceramics of calcium orthophosphates, Biomaterials. 31 (2010) 1465–1485. doi:10.1016/j.biomaterials.2009.11.050.

[132] I. Denry, L.T. Kuhn, Design and characterization of calcium phosphate ceramic scaffolds for bone tissue engineering, Dent. Mater. 32 (2016) 43–53. doi:10.1016/j.dental.2015.09.008.

[133] L. Zaccaria, S. Tharakan, S. Altermatt, Hydroxyapatite ceramic implants for cranioplasty in children: a single-center experience, Child's Nerv. Syst. 33 (2016) 343–348.

[134] R.I.M. Asri, W.S.W. Harun, M.A. Hassan, S.A.C. Ghani, Z. Buyong, A review of

hydroxyapatite-based coating techniques: Sol-gel and electrochemical depositions on biocompatible metals, J. Mech. Behav. Biomed. Mater. 57 (2016) 95–108. doi:10.1016/j.jmbbm.2015.11.031.

[135] R.I.M. Asri, S.A.C. Ghani, J. Alias, J.H.M. Shariffuddin, F.H. Zulkifli, W.S.W. Harun, K. Kadirgama, A comprehensive review of hydroxyapatite-based coatings adhesion on metallic biomaterials, Ceram. Int. 44 (2017) 1250–1268. doi:10.1016/j.ceramint.2017.10.162.

[136] A. Szcześ, L. Hołysz, E. Chibowski, Synthesis of hydroxyapatite for biomedical applications, Adv. Colloid Interface Sci. 249 (2017) 321–330. doi:10.1016/j.cis.2017.04.007.

[137] Y. Ducic, Titanium mesh and hydroxyapatite cement cranioplasty: a report of 20 cases, J. Oral Maxillofac. Surg. 60 (2002) 272–276.

[138] A. Matbouei, A. Fathi, S.M. Rabiee, M. Shirzad, Layered manufacturing of a three-dimensional polymethyl methacrylate (PMMA) scaffold used for bone regeneration, Mater. Technol. 34 (2019) 167–177. doi:10.1080/10667857.2018.1541212.

[139] K. Rahmani-Monfard, A. Fathi, S.M. Rabiee, Three-dimensional laser drilling of polymethyl methacrylate (PMMA) scaffold used for bone regeneration, Int. J. Adv. Manuf. Technol. 84 (2016) 2649–2657. doi:10.1007/s00170-015-7917-1.

[140] B.A. Khader, M.R. Towler, Materials and techniques used in cranioplasty fi xation : A review, Mater. Sci. Eng. C. 66 (2016) 315–322. doi:10.1016/j.msec.2016.04.101.

[141] S.L. Edwards, J.A. Werkmeister, Mechanical evaluation and cell response of woven polyetheretherketone scaffolds., J. Biomed. Mater. Res. A. 100 (2012) 3326–3331. doi:10.1002/jbm.a.34286.

[142] P. Amrollahi, J.S. Krasinski, R. Vaidyanathan, L. Tayebi, D. Vashaee, Electrophoretic Deposition (EPD): Fundamentals and Applications from Nano- to Microscale Structures, in: M. Aliofkhazraei, A.S.H. Makhlouf (Eds.), Handb. Nanoelectrochemistry Electrochem. Synth. Methods, Prop. Charact. Tech., Springer International Publishing, Cham, 2016: pp. 561–591. doi:10.1007/978-3-319-15266-0_7.

[143] I. Gurrappa, L. Binder, Electrodeposition of nanostructured coatings and their characterization—A review, Sci. Technol. Adv. Mater. 9 (2008) 43001. doi:10.1088/1468-6996/9/4/043001.

[144] B. Priyadarshini, M. Rama, Chetan, U. Vijayalakshmi, Bioactive coating as a surface modification technique for biocompatible metallic implants: a review, J. Asian Ceram. Soc. 7 (2019) 397–406. doi:10.1080/21870764.2019.1669861.

[145] C.A.D. Rodriguez, G. Tremiliosi-Filho, Electrochemical Deposition, in: Q.J. Wang, Y.-

W. Chung (Eds.), Encycl. Tribol., Springer US, Boston, MA, 2013: pp. 918–922. doi:10.1007/978-0-387-92897-5_700.

[146] D. DeMeo, S. Macnaughton, S. Sonkusale, T. Vandervelde, Electrodeposited Copper Oxide and Zinc Oxide Core-Shell Nanowire Photovoltaic Cells, in: 2011. doi:10.5772/17644.

[147] S.R.V.S. Prasanna, K. Balaji, S. Pandey, S. Rana, Chapter 4 - Metal Oxide Based Nanomaterials and Their Polymer Nanocomposites, in: N. Karak (Ed.), Nanomater. Polym. Nanocomposites, Elsevier, 2019: pp. 123–144. doi:https://doi.org/10.1016/B978-0-12-814615-6.00004-7.

[148] A.J. Ruys, B.A. Sutton, 9 - Metal-ceramic functionally graded materials (FGMs), in: A.J. Ruys (Ed.), Met. Ceram., Woodhead Publishing, 2021: pp. 327–359. doi:https://doi.org/10.1016/B978-0-08-102869-8.00009-4.

[149] K. Hung, H. Lai, Y. Yang, H. Feng, Characterization of Hydroxyapatite (HA) Sputtering Targets by APS Methods, (2017) 1–13. doi:10.3390/coatings7110197.

[150] C. Hu, F. Li, D. Qu, Q. Wang, R. Xie, H. Zhang, S. Peng, Y. Bao, Y. Zhou, 8 - Developments in hot pressing (HP) and hot isostatic pressing (HIP) of ceramic matrix composites, in: I.M. Low (Ed.), Adv. Ceram. Matrix Compos. (Second Ed., Second Edition, Woodhead Publishing, 2014: pp. 177–202. doi:https://doi.org/10.1016/B978-0-08-102166-8.00008-6.

[151] S. Najeeb, M.S. Zafar, Z. Khurshid, F. Siddiqui, Applications of polyetheretherketone (PEEK) in oral implantology and prosthodontics, J. Prosthodont. Res. 60 (2016) 12–19. doi:https://doi.org/10.1016/j.jpor.2015.10.001.

[152] N. Koju, P. Sikder, Y. Ren, H. Zhou, S.B. Bhaduri, Biomimetic coating technology for orthopedic implants, Curr. Opin. Chem. Eng. 15 (2017) 49–55. doi:https://doi.org/10.1016/j.coche.2016.11.005.

[153] S. Arul Xavier Stango, U. Vijayalakshmi, Synthesis and characterization of hydroxyapatite/carboxylic acid functionalized MWCNTS composites and its triple layer coatings for biomedical applications, Ceram. Int. 45 (2019) 69–81. doi:10.1016/j.ceramint.2018.09.135.

[154] D. Sidane, D. Chicot, S. Yala, S. Ziani, A. Iost, X. Decoopman, Study of the mechanical behavior and corrosion resistance of hydroxyapatite sol – gel thin coatings on 316 L stainless steel pre-coated with titania fi lm, Thin Solid Films. 593 (2015) 71–80. doi:10.1016/j.tsf.2015.09.037.

[155] B.A.E. Ben-arfa, I.M.M. Salvado, J.M.F. Ferreira, R.C. Pullar, Novel route for rapid sol-gel synthesis of hydroxyapatite , avoiding ageing and using fast drying with a 50-fold to 200-fold reduction in process time, Mater. Sci. Eng. C. 70 (2017) 796–804.

doi:10.1016/j.msec.2016.09.054.

[156] B. Beig, U. Liaqat, M.F.K. Niazi, I. Douna, M. Zahoor, M.B.K. Niazi, Current Challenges and Innovative Developments in Hydroxyapatite-Based Coatings on Metallic Materials for Bone Implantation: A Review, Coatings. 10 (2020). doi:10.3390/coatings10121249.

[157] S. Chahal, F.S.J. Hussain, M.M. Yusoff, M.S.B.A. Rasad, A. Kumar, Nanohydroxyapatite-coated hydroxyethyl cellulose/poly (vinyl) alcohol electrospun scaffolds and their cellular response, Int. J. Polym. Mater. Polym. Biomater. 66 (2017) 115–122. doi:10.1080/00914037.2016.1190926.

[158] L. Wang, L. Weng, S. Song, Q. Sun, Mechanical properties and microstructure of polyetheretherketone–hydroxyapatite nanocomposite materials, Mater. Lett. 64 (2010) 2201–2204. doi:https://doi.org/10.1016/j.matlet.2010.06.067.

[159] F. Mazaheri, N. Shafiei, F. Mohandes, B. Dolatyar, N. Zandi, B. Zeynali, A. Simchi, Glucose cross-linked hydrogels conjugate HA nanorods as bone scaffolds : Green synthesis , characterization and in vitro studies, Mater. Chem. Phys. 242 (2020) 122515. doi:10.1016/j.matchemphys.2019.122515.

[160] J.P. Lopez, F. Vilaseca, L. Barberà, R.J. Bayer, M.A. Pèlach, P. Mutjé, Processing and properties of biodegradable composites based on Mater-Bi®and hemp core fibres, Resour. Conserv. Recycl. 59 (2012) 38–42. doi:10.1016/j.resconrec.2011.06.006.

[161] M. Leena, D. Rana, T.J. Webster, M. Ramalingam, Accelerated synthesis of biomimetic nano hydroxyapatite using simulated body fluid, Mater. Chem. Phys. 180 (2016) 166–172. doi:10.1016/j.matchemphys.2016.05.060.

[162] I. Mobasherpour, M.S. Heshajin, A. Kazemzadeh, M. Zakeri, Synthesis of nanocrystalline hydroxyapatite by using precipitation method, 430 (2007) 330–333. doi:10.1016/j.jallcom.2006.05.018.

[163] S. Gao, K. Sun, A. Li, H. Wang, Synthesis and characterization of hydroxyapatite nanofiber by chemical precipitation method using surfactants, Mater. Res. Bull. 48 (2013) 1003–1006. doi:10.1016/j.materresbull.2012.11.090.

[164] M.A. Goldberg, P. V Protsenkob, V. V Smirnova, O.S. Antonovaa, S. V Smirnov, A.A. Konovalov, K.G. Vorckachev, E.A. Kudryavtsev, S.M. Barinov, V.S. Komlev, The enhancement of hydroxyapatite thermal stability by Al doping, J. Mater. Res. Technol. 9 (2020) 76–88. doi:10.1016/j.jmrt.2019.10.032.

[165] ASTM D638-14, Standard Test Method for Tensile Properties of Plastics, in: B. Stand., ASTM International, West Conshohocken, PA, 2014. doi:0.1520/D0638-14.

[166] ASTM F1147-05(2017)e1, Standard Test Method for Tension Testing of Calcium

Phosphate and Metallic Coatings, in: B. Stand., ASTM International, West Conshohocken, PA, 2017. doi:10.1520/F1147-05R17E01.

[167] R. Chakraborty, M.S. Raza, S. Datta, P. Saha, Synthesis and characterization of nickel free titanium–hydroxyapatite composite coating over Nitinol surface through in-situ laser cladding and alloying, Surf. Coatings Technol. 358 (2019) 539–550. doi:10.1016/j.surfcoat.2018.11.036.

[168] T.M. Sridhar, U.K. Mudali, M. Subbaiyan, Preparation and characterisation of electrophoretically deposited hydroxyapatite coatings on type 316L stainless steel, 45 (2003) 237–252.

[169] S. Shaik, E.C. Martin, D.J. Hayes, J.M. Gimble, R. V Devireddy, Transcriptomic Profiling of Adipose Derived Stem Cells Undergoing Osteogenesis by RNA-Seq, Sci. Rep. (2019) 1–17. doi:10.1038/s41598-019-48089-1.

[170] S. Shaik, X. Wu, J. Gimble, R. Devireddy, Effects of Decade Long Freezing Storage on Adipose Derived Stem Cells Functionality, Sci. Rep. (2018) 1–12. doi:10.1038/s41598-018-26546-7.

[171] C. Heitmann, G. Felmerer, B.M. Durmus, G. Ingianni, Anatomical features of perforator blood vessels in the deep inferior epigastric perforator flap., Br. J. Plast. Surg. 53 (2000) 200–204. doi:10.1054/bjps.

[172] S. Thirumala, X. Wu, J.M. Gimble, R. V Devireddy, Evaluation of polyvinylpyrrolidone as a cryoprotectant for adipose tissue-derived adult stem cells, Tissue Eng. Part C Methods. 16 (2009) 783–792.

[173] R. Florencio-silva, G. Rodrigues, E. Sasso-cerri, M.J. Simões, P.S. Cerri, B. Cells, Biology of Bone Tissue : Structure , Function , and Factors That Influence Bone Cells, Biomed Res. Int. 2015 (2015). doi:10.1155/2015/421746.

[174] M.A. El-ganzuri, R. Rashad, E. Muhammad, Annals of Cytology and Pathology Regulatory Mechanisms of Bone Development and Function, Ann. Cytol. Pathol. 1 (2015) 5–17.

[175] B. St-Jacques, M. Hammerschmidt, A.P. McMahon, Indian hedgehog signaling regulates proliferation and differentiation of chondrocytes and is essential for bone formation, Genes Dev. 13 (1999) 2072–2086.

[176] T. Kasuga, M. Nogami, M. Niinomi, T. Hattori, Bioactive calcium phosphate invert glass-ceramic coating on β-type Ti–29Nb–13Ta–4.6Zr alloy, Biomaterials. 24 (2003) 283–290. doi:https://doi.org/10.1016/S0142-9612(02)00316-2.

[177] C. Gao, S. Peng, P. Feng, C. Shuai, Bone biomaterials and interactions with stem cells, Bone Res. 5 (2017) 17059. doi:10.1038/boneres.2017.59.

[178] T. Kokubo, H. Kushitani, S. Sakka, T. Kitsugi, T. Yamamuro, Solutions able to reproduce in vivo surface-structure changes in bioactive glass-ceramic A-W, J. Biomed. Mater. Res. 24 (1990) 721–734.

[179] P. Wang, C. Li, H. Gong, X. Jiang, H. Wang, K. Li, Effects of synthesis conditions on the morphology of hydroxyapatite nanoparticles produced by wet chemical process, Powder Technol. 203 (2010) 315–321. doi:10.1016/j.powtec.2010.05.023.

[180] R.G. Carrodeguas, S. De Aza, a -Tricalcium phosphate : Synthesis , properties and biomedical applications, Acta Biomater. 7 (2011) 3536–3546. doi:10.1016/j.actbio.2011.06.019.

[181] I.M. Manjubala, T.P.S. Astry, Bone In-growth Induced by Ceramic in Femoral Defect of Dogs, J. Biomater. Appl. 19 (2005) 341–360. doi:10.1177/0885328205048633.

[182] T. Mitsionis, Anastasios Vaimakis, C. Trapalis, N. Todorova, R. Bahnemann, Detlef Dillert, Hydroxyapatite/titanium dioxide nanocomposites for controlled photocatalytic NO oxidation, Appl. Catal. B Environ. 106 (2011) 398–404.

[183] P. Chavoshnejad, O. Alsmairat, C. Ke, M.J. Razavi, Effect of the Interfiber Bonding on the Mechanical Behavior of Electrospun Fibrous Mats, J. Phys. D. Appl. Phys. 54 (2021) 025302. doi:10.1038/s41598-020-64735-5.

[184] G. Choi, L.A. Evans, A review : Recent advances in sol-gel-derived hydroxyapatite nanocoatings for clinical applications, J. Am. Ceram. Soc. 103 (2020) 5442–5453. doi:10.1111/jace.17118.

[185] E. Mohseni, E. Zalnezhad, A.R. Bushroa, Comparative investigation on the adhesion of hydroxyapatite coating on Ti – 6Al – 4V implant : A review paper International Journal of Adhesion & Adhesives Comparative investigation on the adhesion of hydroxyapatite coating on Ti – 6Al – 4V implant : A review paper, Int. J. Adhes. Adhes. 48 (2014) 238–257. doi:10.1016/j.ijadhadh.2013.09.030.

[186] A. Naderi, B. Zhang, J.A. Belgodere, K. Sunder, G. Palardy, Improved Biocompatible, Flexible Mesh Composites for Implant Applications via Hydroxyapatite Coating with Potential for 3-Dimensional Extracellular Matrix Network and Bone Regeneration, ACS Appl. Mater. Interfaces. 13 (2021) 26824–26840. doi:10.1021/acsami.1c09034.

[187] ASTM D3822 / D3822M-14(2020), Standard Test Method for Tensile Properties of Single Textile Fibers, in: B. Stand., ASTM International, West Conshohocken, PA, 2020. doi:10.1520/D3822_D3822M-14R20.

[188] P.A. Eutionnat-Diffo, Y. Chen, J. Guan, A. Cayla, C. Campagne, X. Zeng, V. Nierstrasz, Stress, strain and deformation of poly-lactic acid filament deposited onto polyethylene terephthalate woven fabric through 3D printing process, Sci. Rep. 9 (2019) 14333. doi:10.1038/s41598-019-50832-7.

[189] H. Xuan, Y. Hu, Y. Wu, Z. He, Containment ability of Kevlar 49 composite case under spinning impact, J. Aerosp. Eng. 31 (2018) 4017096.

[190] S. Sun, J.R. Mitchell, W. MacNaughtan, T.J. Foster, V. Harabagiu, Y. Song, Q. Zheng, Comparison of the Mechanical Properties of Cellulose and Starch Films, Biomacromolecules. 11 (2010) 126–132. doi:10.1021/bm900981t.

[191] Y. Elmogahzy, R. Farag, 7 - Tensile properties of cotton fibers: Importance, research, and limitations, in: A.R. Bunsell (Ed.), Handb. Prop. Text. Tech. Fibres (Second Ed., Second Edition, Woodhead Publishing, 2018: pp. 223–273. doi:https://doi.org/10.1016/B978-0-08-101272-7.00007-9.

[192] R. Sinha, S. Janaswamy, A. Prasad, Enhancing mechanical properties of Electrospun Cellulose Acetate Fiber Mat upon Potassium Chloride exposure, Materialia. 14 (2020) 100881. doi:https://doi.org/10.1016/j.mtla.2020.100881.

[193] S. Singh, C. Prakash, S. Ramakrishna, 3D printing of polyether-ether-ketone for biomedical applications, Eur. Polym. J. 114 (2019) 234–248. doi:https://doi.org/10.1016/j.eurpolymj.2019.02.035.

[194] Y. Wang, W.-D. Müller, A. Rumjahn, A. Schwitalla, Parameters Influencing the Outcome of Additive Manufacturing of Tiny Medical Devices Based on PEEK., Mater. (Basel, Switzerland). 13 (2020). doi:10.3390/ma13020466.

[195] A.R. Zanjanijam, I. Major, J.G. Lyons, U. Lafont, D.M. Devine, Fused Filament Fabrication of PEEK: A Review of Process-Structure-Property Relationships., Polymers (Basel). 12 (2020). doi:10.3390/polym12081665.

[196] D. Yang, Y. Cao, Z. Zhang, Y. Yin, D. Li, Effects of crystallinity control on mechanical properties of 3D-printed short-carbon-fiber-reinforced polyether ether ketone composites, Polym. Test. 97 (2021) 107149. doi:https://doi.org/10.1016/j.polymertesting.2021.107149.

[197] S. Shaik, D. Hayes, J. Gimble, R. V Devireddy, Inducing heat shock proteins enhances the stemness of frozen–thawed adipose tissue-derived stem cells, Stem Cells Dev. 26 (2017) 608–616.

[198] M.S. Shaik, X. Wu, J. Gimble, R. Devireddy, Development Of Cyroprotective Media For Frozen Storage Of Human Lipoaspirates., Cryobiology. 91 (2019) 152–153.

[199] W. Strober, Trypan blue exclusion test of cell viability., Curr Protoc Immunol. (n.d.) Appendix 3:Appendix 3B. doi:10.1002/0471142735.ima03bs21.

[200] M.K. Reumann, C. Linnemann, R.H. Aspera-werz, S. Arnold, M. Held, C. Seeliger, A.K. Nussler, S. Ehnert, Donor Site Location Is Critical for Proliferation , Stem Cell Capacity , and Osteogenic Differentiation of Adipose Mesenchymal Stem / Stromal Cells :

Implications for Bone Tissue Engineering, Int. J. Mol. Sci. 19 (2018) 1868. doi:10.3390/ijms19071868.

[201] G. Baschek, G. Hartwig, F. Zahradnik, Effect of water absorption in polymers at low and high temperatures, Polymer (Guildf). 40 (1999) 3433–3441. doi:https://doi.org/10.1016/S0032-3861(98)00560-6.

[202] M. N'Diaye, F. Pascaretti-Grizon, P. Massin, M.F. Baslé, D. Chappard, Water absorption of poly(methyl methacrylate) measured by vertical interference microscopy., Langmuir. 28 (2012) 11609–11614. doi:10.1021/la302260a.

[203] R. Naomi, R. Bt Hj Idrus, M.B. Fauzi, Plant- vs. Bacterial-Derived Cellulose for Wound Healing: A Review, Int. J. Environ. Res. Public Health. 17 (2020) 6803. doi:10.3390/ijerph17186803.

[204] K. Marra, J. Rubin, The potential of adipose-derived stem cells in craniofacial repair and regeneration., Birth Defects Res C Embryo Today. 96 (2012) 95–97. doi:10.1002/bdrc.21001.

[205] M. Blaskovic, D. Gabri, N.J. Coleman, I.J. Slipper, M. Mladenov, Bone Healing Following Different Types of Osteotomy : Scanning Electron Microscopy (SEM) and Three-Dimensional SEM Analyses, Microsc Microanal. 22 (2016) 1170–1178. doi:10.1017/S1431927616011971.

[206] J.Z. Paxton, L. Grover, K. Baar, Engineering an In Vitro Model of a Functional Ligament from Bone to Bone, Tissue Eng. Part A. 16 (2010) 3515–3525. doi:10.1089/ten.TEA.2010.0039.

[207] L.F. Coutinho, J. Batista, É. Brito, E.F. Martinez, V.A.M. Montalli, J.L. Cintra, V.C. De Araújo, M.H. Napimoga, Presence of Cells in Fresh- Frozen Allogenic Bone Grafts from Different Tissue Banks, Braz. Dent. J. 28 (2017) 1–6. doi:http://dx.doi.org/10.1590/0103-6440201701206.

[208] Ceramic scaffold, (n.d.). https://www.sigmaaldrich.com/US/en/product/aldrich/z682012.

[209] Hydroxyapatite powder, (n.d.). https://www.sigmaaldrich.com/US/en/product/aldrich/900203.

[210] Metallic scaffold, (n.d.). https://www.medicaldevice-developments.com/features/featurebuilt-for-you-7533999//featurebuilt-for-you-7533999-502617.html.

[211] A.C. Bento, D.P. Almond, S.R. Brown, I.G. Turner, Thermal and optical characterization of the calcium phosphate biomaterial hydroxyapatite, J. Appl. Phys. 79 (1996) 6848–6852.

[212] J. Carvill, 3 - Thermodynamics and heat transfer, in: J. Carvill (Ed.), Mech. Eng. Data Handb., Butterworth-Heinemann, Oxford, 1993: pp. 102–145. doi:https://doi.org/10.1016/B978-0-08-051135-1.50008-X.

Vita

Armaghan Naderi, born in Tehran, Iran, got her bachelor's degree from Amirkabir University of Technology. She had a work experience as an intern for three months in jewelry industry as a senior. Following her bachelor' study, she started her master's program in corrosion and protection in an elite program. She received her master's degree from Sharif university of Technology in Iran. To complete her studies in materials science and engineering, she joined the department of Mechanical and Industrial Engineering at Louisiana State University one year after completion of her master's degree. Upon completion of her PhD degree, she will join biomaterial industry.